Probabilistic Inference of Tensorial Stress in the Earth's Seismogenic Crust

by

Olivia Leigh Walbert

A dissertation submitted in partial fulfillment
of the requirements for the degree of
Doctor of Philosophy
(Earth and Environmental Sciences and Scientific Computing)
in the University of Michigan
2023

Doctoral Committee:

Associate Professor Eric Hetland, Chair
Professor Seth Guikema
Associate Professor Yihe Huang
Professor Jeroen Ritsema

Olivia Leigh Walbert
ohelprin@umich.edu
ORCID ID: 0000-0002-6026-5014

For Jared

ACKNOWLEDGMENTS

I am honored to have the opportunity to express my deepest gratitude for the guidance, support, and encouragement I have received from many people that have been vital to my studies at the University of Michigan. First and foremost, I am incredibly grateful to my advisor, Eric Hetland, for allowing me to work with him and receive mentorship in research and teaching. I am also indebted to my dissertation committee members, Seth Guikema, Yihe Huang, and Jeroen Ritsema, whose thoughtful feedback and guidance have helped shape this work. I owe many thanks to the outstanding administrative staff of the Department of Earth and Environmental Sciences, including Anne Hudon, Paula Frank, Chrissy Zigulis, Nico Spraggins, Carla Huhn, Courtney Hooper, and Craig Delap, and the Michigan Institute for Computational Discovery and Engineering, including Ken Powell, Heidi Bennett, JoAnne Kerr, and Sarah McNitt. Additionally, I am grateful to the National Science Foundation (grant EAR-1722994 awarded to Eric Hetland) and the Department of Earth and Environmental Sciences for supporting this research through their funding.

I have been incredibly fortunate to have had many outstanding teachers who fostered my curiosity, critical thinking, and courage throughout my education. I am grateful for every professor I have had the opportunity to learn from at the University of Michigan. Additionally, many of the best teachers in my life have come in the form of my peers, and for that, I owe a significant debt to my fellow graduate students, who have inspired me with their creativity, passion, and dedication to learning. In particular, I would like to thank the past and present residents of the geophysics lab and my co-graduate student mentors, including Jing Ci, Meredith, Marlon, Prithvi, Sam, Eric, Meichen, María, Seoyoung, Sydney, Yaolin, Yang, Leo, Amir, Dongdong, Andrés, Peng, Allison, and Madelyn, whose friendship and support have meant more than they could know.

Finally, I want to express my heartfelt appreciation to my family for their love. I am blessed with a supportive spouse, siblings, parents, step-parents, in-laws, aunts, uncles, and grandparents. I am so fortunate to continue to get to know, understand, and love you all more with the passing years. All of my efforts are always for you.

TABLE OF CONTENTS

Chapter

LIST OF TABLES

LIST OF FIGURES

ABSTRACT

Stress in Earth's crust is a fundamental physical quantity for understanding solid Earth processes and seismic hazards. While the connection between crustal stress and seismic hazards is well-established, directly measuring crustal stress remains challenging. Earthquakes are most commonly used only to probe the stress changes during the earthquakes, although they also provide insight into the crustal stresses that preceded them. This dissertation proposes a probabilistic framework to constrain the crustal stress tensor from earthquake models. This framework allows us to investigate regional transitions in crustal stress in South Island, New Zealand, and the East African Rift System.

In Chapter 2, we describe a novel Bayesian Markov Chain Monte Carlo strategy for estimating tensorial seismogenic stress. We apply this method to several published coseismic slip models of the 2016 $M_w 7.8$ Kaikōura, New Zealand earthquake, constraining the most likely orientation and relative magnitudes of the principal stress components that preceded this large and complicated earthquake. Furthermore, it supports that slip pattern variations over large earthquakes do not necessarily imply that the background seismogenic stresses were heterogeneous over the earthquake's spatial extent. We find that the pre-earthquake stress in the Kaikōura earthquake region is consistent with a thrust stress regime and a near-horizontal most compressive stress trending WNW–ESE.

In Chapter 3, we estimate the seismogenic tensorial stress preceding the 2010 $M_w 7.2$ Darfield and February 2011 $M_w 6.2$ Christchurch earthquakes, that occurred in the Canterbury Plains to the south of the Kaikōura earthquake. We find that the pre-earthquake stress in the Canterbury Plains region is consistent with a strike-slip stress regime and a

near-horizontal most compressive stress trending NW–SE. We investigate the transition of the upper crustal stress, from the thrust regime we infer from the Kaikōura earthquake to the strike-slip regime we infer in the Canterbury Plains, through a mechanical model where loading due to sediment deposition in the Canterbury Plains is sufficient for the observed rotation of the principal components of stress. This mechanical model allows us to constrain the absolute magnitude of tectonic stress for northeastern South Island, New Zealand. Our constraint is one of the few quantifications of absolute stress, not just for this active tectonic setting, but globally. Additionally, we provide arguments from a culmination of studies on the state of stress for the South Island that supports a highly oblique thrust slip mechanism for the Alpine Fault, the South Island's on-shore plate boundary. Our predicted slip mechanism for the Alpine Fault, which has been seismically quiescent throughout instrumental history, contradicts the predominantly strike-slip mechanism commonly assumed as the most likely mechanism of a potential future earthquake on the Alpine Fault.

In Chapter 4, we determine models of tensorial stress consistent with seismic observations from focal mechanism catalogs for the region surrounding the Afar depression, including the Red Sea, Gulf of Aden, and Main Ethiopian Rift. We propose an unsupervised clustering procedure that includes both the geodesic distance between earthquakes and the similarity of the posterior probability density functions of stress estimated from the focal mechanisms of those earthquakes. We determine crustal stresses at regional scales, resolving two clusters that infer a normal stress regime with a 47° counter-clockwise rotation of the principal horizontal components of stress from west to east. The boundary between our clusters coincides with the Danakil Block, a structure geodetically observed to be undergoing a similar counter-clockwise rotation.

CHAPTER 1

Introduction

Stress is a fundamental physical quantity, mathematically represented as a tensor, which describes symmetric tractions acting upon a finite volume within a material. In Earth's crust, forces are generated by a number of mechanisms, from large scale tectonics (*e.g.*, *Forsyth and Uyeda*, 1975) to localized sources of loading. The accumulation of stresses results in crustal deformation, including earthquakes. While direct measurement of the stresses within Earth's crust remains challenging, observations of earthquakes as stress phenomena provide a means of making inferences of stresses within Earth's seismogenic crust.

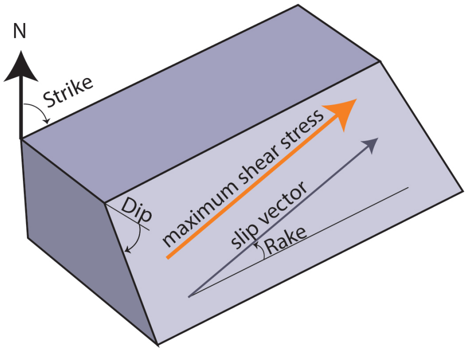

Figure 1.1: Illustration of the Wallace-Bott assumption for a fault plane defined by strike, dip, and rake angular geometries (Wallace, 1951; Bott, 1959). Strike is measured clockwise from North, dip is measured from horizontal to the fault surface, and rake is measured counter-clockwise from strike-linear to the direction of motion along the fault's face (i.e., to the slip vector). The Wallace-Bott assumption equates the orientation of the slip vector to the maximum shear stress in Earth's crust preceding the earthquake that allowed for slip along this pre-existing fault plane.

In this dissertation, we propose a methodology to infer stresses within Earth's crust, following previous stress estimation strategies that rely on the Wallace-Bott assumption (Fig. 1.1). The Wallace-Bott assumption equates the orientation of slip observed during an earthquake to the angle of maximum shear stress on a fault plane before the earthquake initiated (*e.g.*, *McKenzie*, 1969; *Michael*, 1984; *Hardebeck and Michael*, 2006; *Arnold and Townend*, 2007; *Medina Luna and Hetland*, 2013). From this assumption, and given an observation of the orientation of the fault plane and slip during an earthquake, a model of the seismogenic stress can be inferred. The probabilistic framework we develop is distinct from many of the past methods in that it provides complete posterior probability density functions of tensorial stresses consistent with the observations of earthquake slip. Our Bayesian probabilistic method allows for the inclusion of data and model uncertainties, flexibility to consider multiple conflicting data observations, and evaluation of the mechanical consistency of non-unique data observations. Through this probabilistic framework, we seek to understand spatial relationships of crustal stress through multiple tectonic environments.

In this dissertation, we utilize our approach to constrain crustal stress tensors from geodetically and seismically derived observations of earthquake slip. One data source we use is coseismic slip models, which are planar or listric representations of one or more finite faults in Earth's subsurface that experienced slip during an earthquake. Geodetic observations of the crustal deformation associated with an earthquake, such as measurements from the global navigation satellite system (GNSS) and interferometric synthetic aperture radar (InSAR), inform the modeling of these finite faults and their slip distributions. Coseismic slip models assume an elastic half-space and often follow from the solution presented by *Okada* (1985) to estimate parameters descriptive of an earthquake's slip surface, including fault plane geometries and locations. Due to the under-determined nature of the problem, additional observations of the earthquake, including from geologic, seismic, or tsunami data, can be used for better constraining some of the coseismic slip model parameters. Coseismic slip models are an advantageous source of earthquake slip data as they provide an image of an earthquake's slip distribution resolved on a sub-fault scale. However, the availability of these models is limited to earthquakes of moderate magnitudes and larger, require considerable effort to produce, and are not fully unique. We preferentially utilize coseismic slip models as slip data for large earthquakes with varying fault and slip geometries to determine highly constrained estimates on seismogenic crustal stress tensors.

A second form of earthquake slip data we use in this dissertation is earthquake focal mechanisms. Earthquake focal mechanisms are point-source fault plane solutions that provide geometries describing two ambiguous, conjugate nodal planes, where one represents an earthquake's slip surface, and the other is an auxiliary plane. Focal mechanisms are derived from first motions recorded by an array of seismic instruments or full wave-form inversions. It is not possible to determine which of the two nodal planes is the slip surface and which is the auxiliary plane from the focal mechanism alone, and regional geologic evidence or geodetic data must be leveraged in inferring a fault plane from a focal mechanism. Due to this nodal plane ambiguity, taking focal mechanisms as earthquake slip data requires considering both nodal planes as the possible slip surface, imparting uncertainty on the fault plane geometry and resulting in less constrained estimates of the stress that preceded the earthquake. Instead, focal mechanisms of multiple earthquakes are often inverted for a joint solution to determine regional stress consistent with each focal mechanism observation.

The first two science chapters included in this body of work, Chapters 2 and 3, seek to resolve transitions in stress in the transpressive tectonic setting of South Island, New Zealand. These chapters rely on published coseismic slip models as observations of earthquake slip with a known, multi-segment slip surface for large earthquakes in New Zealand's South Island. Chapter 2 provides the exposition of our Bayesian Markov Chain Monte Carlo estimation technique, including synthetic test cases and a procedure for quantifying uncertainties on the observed fault plane's geometry. Applying our methodology to several coseismic slip models of the 2016 $M_w 7.8$ Kaikōura earthquake yields a well-constrained stress posterior for this large and complicated earthquake. Chapter 3 further applies this estimation technique to coseismic slip models for earthquakes within the Canterbury Plains of South Island, just south of the Kaikōura earthquake region from Chapter 2. We note a dramatic rotation of the principal components of stress resolved for the Kaikōura earthquake and the Canterbury Plain's earthquakes, prompting an exploration of potential sources of vertical loading in the Canterbury Plains relative to the Kaikōura earthquake's tectonic setting within the Marlborough Fault System that actively accommodates compression from the Hikurangi Subduction Zone. We propose a mechanical model of crustal loading from sedimentation in the Canterbury Plains to explore the rotation of the stress tensor. Through this model, we bound a seldom-made constraint on the absolute magnitude of tectonic stress.

A strategy commonly used in inferring regional stress is determining a state of stress consistent with multiple observations of earthquake slip as an averaged regional stress; however, the selection of data and means of grouping this data leaves the potential for bias in inferences of these stresses. We expand our methodology in Chapter 4 to include the inversion of focal mechanisms to study regional tectonics of the Afar Triple Junction. From a dataset of 316 focal mechanisms for earthquakes that have occurred in the crust over the past five decades, we propose an unsupervised clustering procedure informed by geodesic and stress-based distance metrics to determine similarities in regional stress between earthquakes from our calculated stress posteriors. This clustering procedure reduces bias when grouping earthquakes to infer regional stresses. Additionally, it relates the similarity among earthquakes to a physically causative attribute. Our clustering procedure allows us to determine broad, regional stresses with transitions in the regional stress related to physical mechanisms in Earth's crust.

The results of this dissertation reveal that probabilistic inference from earthquake slip observations allows for constrained stress posterior probability density functions that characterize seismogenic stresses for individual earthquakes and regional-scale crustal stresses. These inferences do not necessitate informed priors or data selectivity that may lead to subjective biases in inference and interpretation, and they allow for the quantification of data and model uncertainties. Our work provides insights into regional transitions of crustal stresses for compressional and extensional tectonic settings, and it investigates observed rotations in stress that result from both localized sources of loading (*e.g.*, the burial of bedrock by sediment deposition in Chapter 3) and tectonic drivers (*e.g.*, distinctions in triple junction kinematics in Chapter 4).

CHAPTER 2

Bayesian Inference of Seismogenic Stress for the 2016 $M_w 7.8$ Kaikōura, New Zealand, Earthquake [*]

Abstract

We use a Bayesian Markov Chain Monte Carlo estimation strategy to estimate the state of pre-earthquake stress from eight published coseismic slip models (CSMs) of the 2016 $M_w 7.8$ Kaikōura, New Zealand earthquake. Our estimation relies on the Wallace-Bott assumption, which equates the direction of slip and the orientation of maximum shear stress along a fault plane, and is analogous to methods that infer stress from focal mechanisms. We infer the orientations and relative magnitudes of the principal components of tensorial stress preceding the 2016 $M_w 7.8$ Kaikōura, New Zealand earthquake as stress posterior probability density functions (PDFs). We find that the orientations of the principal stresses are well resolved, with weaker to no resolution of the relative magnitudes of the principal stresses. We form a non-mutually exclusive composite posterior PDF as an aggregate of the individual posterior PDFs estimated from each CSM, which allows for the true coseismic slip to be included in any or all of the CSMs. We find that the Kaikōura earthquake can be described by a homogeneous pre-earthquake tensorial stress, despite the complex pattern of slip on multiple fault segments. This state of crustal stress is best represented by an Andersonian thrust regime with a WNW-ESE trending, horizontal most compressive stress. In addition to describing the state of pre-earthquake stress, the non-mutually exclusive composite posterior PDF allows for the evaluation of the mechanical consistency of the features within CSMs, both individually and as an ensemble. The estimated stress posteriors allow

---

[*] Chapter 2 is published in *Bulletin of the Seismological Society of America* as Walbert, O.L., and E. A. Hetland (2022). Bayesian Inference of Seismogenic Stress for the 2016 $M_w 7.8$ Kaikōura, New Zealand, Earthquake, *Bull. Seismol. Soc. Am.* 112 (4): 1894–1907, doi: 10.1785/0120210173.

testing of the CSMs for consistency with known slip mechanisms on the Hope Fault, as well as arbitration between differences in inferred slip presented by the CSMs.

2.1 Introduction

At the top of the South Island of New Zealand, the Marlborough Fault System (MFS) links the Alpine fault transpressional plate boundary in the center of the South Island to the Hikurangi trench in the northeast of the South Island (Fig. 2.1). The MFS is characterized by a network of southwest to northeast striking, predominately right-lateral strike-slip faults with varying dips (*Litchfield et al.*, 2014, 2018). The 2016 $M_w 7.8$ Kaikōura earthquake initiated along immature, disconnected faults at the southeastern edge of the MFS (*Kaiser et al.*, 2017), and continued to rupture relatively mature faults in a northeasterly progression through the MFS (*Litchfield et al.*, 2018; *Little et al.*, 2018), with possible slip along the Hikurangi Trench interface (Fig. 2.1; *Bai et al.*, 2017; *Hollingsworth et al.*, 2017; *Hamling et al.*, 2017). In total, the Kaikōura earthquake ruptured at least 20 faults along an approximately 180 km extent striking southwest to northeast (*e.g.*, *Hamling et al.*, 2017; *Langridge et al.*, 2018; *Litchfield et al.*, 2018; *Nicol et al.*, 2018; *Williams et al.*, 2018). A wide spectrum of faulting mechanisms was observed along the complicated fault geometries involved (*Kearse et al.*, 2018; *Litchfield et al.*, 2018), with the rupture initiating on a strike-slip fault, releasing maximum seismic moment along reverse faults, and transitioning to transpressional faulting (*e.g.*, *Cesca et al.*, 2017).

The complicated rupture patterns of the Kaikōura earthquake have been well studied and several coseismic slip models have been published (*e.g.*, *Clark et al.*, 2017; *Hamling et al.*, 2017; *Holden et al.*, 2017; *Wang et al.*, 2018; *Xu et al.*, 2018). While all of these models have some features in common, there is a limited consensus on the overall pattern of coseismic slip and the slip surfaces involved in the earthquake. Indeed, several authors published more than one model that can reasonably explain the observations. Despite this lack of consensus on the details of the coseismic slip models, the complexity of the coseismic slip during the Kaikōura earthquake, involving disparate slip mechanisms on a host of faults, makes it particularly apt to infer seismogenic stresses, as has been done for similarly complicated earthquakes (*e.g.*, *Medina Luna and Hetland*, 2013; *Styron and Hetland*, 2015; *Douilly et al.*, 2015; *Zhang et al.*, 2016). While there have been several past studies inferring seismogenic stresses from focal mechanisms of earthquakes for the South Island of New Zealand (*e.g.*, *Townend et al.*, 2012; *Michailos et al.*, 2020), to our knowledge, the coseismic slip models of the Kaikōura earthquake have not been used to infer seismogenic stresses, which can provide important constraints for validating specific features of the individual slip models.

We estimate the seismogenic stress that led to the Kaikōura earthquake from eight published coseismic slip models (Fig. 2.1; *Clark et al.*, 2017; *Hamling et al.*, 2017; *Holden et al.*, 2017; *Wang et al.*, 2018; *Xu et al.*, 2018). We use a Bayesian Markov Chain Monte Carlo (MCMC) stress estimation strategy, which is based on, but modified from previous work (*Medina Luna and Hetland*, 2013; *Styron and Hetland*, 2015; *Zhang et al.*, 2016). Our stress estimation builds directly from the work of *Angelier et al.* (1982), and is analogous to methods to infer stress from focal mechanisms (*e.g.*, *McKenzie*, 1969; *Michael*, 1984; *Hardebeck and Michael*, 2006; *Arnold and Townend*, 2007). In our MCMC estimation, we determine posterior probability density functions (PDFs) of the seismogenic stress for the Kaikōura earthquake. We find that the orientations of the principal stresses are well resolved, with weaker to no resolution of the relative magnitudes of the principal stresses (inversion of earthquake slip data is insensitive to the absolute magnitude of stress; *McKenzie*, 1969).

Our aim in determining these posteriors is to assess the level of heterogeneity of the seismogenic stress in the region of the earthquake, and to quantify its orientations and relative magnitudes as a stress tensor. We find that the Kaikōura coseismic slip models are more consistent with an Andersonian thrust regime with a sub-horizontal, near E-W trending most compressive stress. We find that our stress inferences give a basis with which to assess coseismic slip models in an aggregate form, which can be interrogated to validate individual coseismic slip models or features of those models.

2.2 Coseismic slip models

We use eight coseismic slip models of the Kaikōura earthquake (Table 2.1; *Clark et al.*, 2017; *Hamling et al.*, 2017; *Holden et al.*, 2017; *Wang et al.*, 2018; *Xu et al.*, 2018). While there are additional studies of these earthquakes, we limit ourselves to studies that openly disseminated their full coseismic slip models. We discuss features of these models that are pertinent to our analysis here, and we refer readers to those studies for full details on how the models were constructed and all of their features.

With the exception of *Wang et al.* (2018), the coseismic slip model studies we consider all published alternative models, and rather than choosing which of those alternative models are more representative of the Kaikōura earthquake, we consider all of the proposed coseismic slip models as equally plausible representations of the true coseismic slip of the Kaikōura earthquake. *Wang et al.* (2018) only proposed a single coseismic slip model for Kaikōura, Wang-K, which was constrained by GPS, InSAR, strong motion, and teleseismic waves. Wang-K includes both crustal faults and the Hikurangi Trench. The two alternative models proposed by *Hamling et al.* (2017), Hamling-Ka and Hamling-Kb, were both constrained using InSAR, GPS and coastal uplift data, with Hamling-Ka including crustal fault segments and the Hikurangi Trench, while Hamling-Kb only considered crustal fault segments (Table 2.1). *Holden et al.* (2017) published two coseismic slip models of the Kaikōura earthquake, Clark/Holden-K and Holden-K, both with rakes constrained with strong-motion and high-rate GPS data, using fault geometries and final slip informed by the work of *Clark et al.* (2017). Clark/Holden-K includes crustal faults and the Hikurangi Trench, while Holden-K includes a small subset of the crustal faults included in Clark/Holden-K that were determined to contribute to recorded ground motions through a kinematic source inversion. *Xu et al.* (2018) proposed three alternative coseismic slip models of the Kaikōura earthquake, Xu-Ka, Xu-Kb, and Xu-Kc, all of which were constrained by GPS, InSAR, and SAR pixel offsets, and included the same crustal faults, which were assumed to have listric geometries. Xu-Ka only included the crustal faults, while Xu-Kb also included the Hikurangi Trench (Table 2.1). Their third alternative model, Xu-Kc, included the mostly off-shore Pt. Kean fault in addition to the crustal faults.

Despite the approximately 12 meters of maximum net slip and 8 meters of estimated throw along the Papatea fault measured during mapping (*Langridge et al.*, 2018), both *Hamling et al.* (2017) and *Holden et al.* (2017) omitted the Papatea fault from their coseismic slip models (Table 2.1). *Hamling et al.* (2017) argued that the geodetically observed coseismic surface deformation around the Papatea fault was not consistent with an elastic dislocation, an inference agreed upon by *Diederichs et al.* (2019). Similarly, *Holden et al.* (2017) were unable to isolate seismic signals in the seismograms distinct from those resulting from slip on neighboring ruptured faults. In contrast, both *Wang et al.* (2018) and *Xu et al.* (2018) included the Papatea fault in their coseismic slip models (Table 2.1).

2.3 Inversion of slip data

We seek to constrain tensorial stress from coseismic slip models, excluding some scalar magnitude, following the approach of *Medina Luna and Hetland* (2013) and others (*e.g.*, *Arnold and Townend*, 2007; *Styron and Hetland*, 2015). We use a Bayesian estimation strategy to invert coseismic slip models for the orientations and relative magnitudes of the principal components of seismogenic stress in the region of the Kaikōura earthquake. We use an MCMC random walk scheme to solve for the posterior PDFs over the model state, composed of the relative magnitudes of the principal stresses and the Euler angles of the stress tensor. We denote the magnitudes of the most, intermediate, and least compressive stresses as σ_1, σ_2, and σ_3, respectively, and refer to those principal stresses as the MCS, ICS, and LCS. The orientation of the stress tensor can be described by the three Euler angles, ϕ, θ, and ρ. Here we take ϕ and θ to be the trend and plunge of the MCS, while ρ describes a rotation of ICS and LCS about MCS (Fig. 2.2a). As the maximum shear stress along a fault segment, $\tau_{\max}$, does not depend on the absolute magnitude of stress (*e.g.*, *McKenzie*, 1969), we do not directly include σ_1, σ_2 or σ_3 in the model state. Rather, we describe the relative magnitudes of the principal stresses with δ (*e.g.*, *Angelier*, 1979) and ς, which are defined as

$$\delta = \frac{\sigma_2 - \sigma_3}{\sigma_1 - \sigma_3}, \tag{2.1}$$

and

$$\varsigma = \frac{\sigma_3}{\sigma_1}. \tag{2.2}$$

We use m to denote the model state, which is the collection of ϕ, θ, ρ, δ, and ς. The Bayesian posterior PDF, hereafter referred to simply as the posterior, f_{post}, can be expressed as

$$f_{\text{post}}\left(m|\lambda\right) = wL_{\text{obs}}\left(\lambda|m\right) f_{\text{prior}}\left(m\right), \tag{2.3}$$

where λ denotes the observed slip rake on each fault segment in a given coseismic slip model, and w is a scaling factor. L_{obs} is a likelihood function that we discuss in greater detail below. The Bayesian prior PDF, f_{prior}, is knowledge of m independent of the coseismic slip models.

We assume non-informative priors for the Euler angles of the stress tensor, as well as for δ. Our prior for ς is that any value is equally likely within the bounds of 0.21 to 0.89. $\varsigma = 0.21$ is such a strongly deviatoric stress tensor that an optimally oriented fault with a coefficient of friction of 0.85 would fail, which corresponds to the empirically determined friction for intact rock to fail at normal stresses below 200 MPa (*Byerlee*, 1978). The bound of $\varsigma = 0.89$ is imposed to avoid near isotropic stresses, which are inconsistent with faulting at finite frictional strength. This value is associated with a stress state in which an optimally oriented fault plane with a coefficient of friction of 0.06 would fail, a friction that corresponds to empirical estimates for wet montmorillonite (*Klima et al.*, 1988), a conservative approximation for a potential fault gouge material. While it is conceivable that a mature fault may indeed have a friction this low, we do not *a priori* feel that it is likely that all of the fault segments that slipped during the earthquake have such a low frictional strength. We apply an additional constraint such that we reject models that result in two principal stress components lying parallel to any of the fault segments (*i.e.*, stress tensors that would produce vanishingly small shear stress on the fault segment). Specifically, any trial stresses that predict $\tau_{max}/\sigma_N < 0.002$ on at least one fault segment, where σ_N denotes the normal stress on the fault segment, are rejected. Note that this condition is different from the prior upper bound on ς, as one could have a deviatoric stress that still produces a near-zero shear stress on a fault if that fault is perfectly orthogonal to one of the principal components of stress.

Before moving on to discuss the likelihood function we assume in the MCMC, it is worthwhile to reiterate the data that we use to inform the MCMC. The coseismic slip models we consider are composed of a collection of fault segments, each of which are broken down into a number of sub-faults, where most, but not all, of the fault segments are planar. The standard operating procedure in coseismic slip model studies is to determine the fault segment geometries separately before imaging the distribution of coseismic slip on those segments, with segment geometries informed by mapped surface traces, aftershocks, and other data, in addition to the geodetic/seismic data which is then used to image the coseismic slip (*e.g.*, *Fielding et al.*, 2013; *Douilly et al.*, 2015; *He et al.*, 2017). Each segment is discretized into sub-faults, and coseismic slip is estimated on each of the sub-faults, with added regularization of the slip on each of the fault segments in the inversion.

Motivated by the fact that the fault slip of the sub-faults within each segment share a common regularization, we do not treat the slip rake of each sub-fault as independent information. Rather, we take the average slip rakes across each of the fault segments to be the data in our MCMC. As there is no regularization of the fault slip across fault segments in a single coseismic slip model, we treat each fault segment in the coseismic slip models as independent. We denote the weighted, angular average strike, dip, and rake of the sub-faults within fault segment i as φ_i, ϑ_i, and λ_i, respectively. We weight the averages by the potency of the imaged slip in each sub-fault, calculating the weighted averages as

$$\alpha_i = \arctan\left(\frac{\sum_j p_i^j \sin\tilde{\alpha}_i^j}{\sum_j p_i^j \cos\tilde{\alpha}_i^j}\right), \tag{2.4}$$

where α_i is either φ_i, ϑ_i, or λ_i, p_i^j is the potency (*i.e.*, the product of the area and slip) of sub-fault j, and $\tilde{\alpha}_i^j$ is the angle corresponding to the sub-fault. Weighting by potency has the effect that sub-faults with larger magnitudes of slip are more important on the averages. λ_i takes the role of the data in our MCMC, while φ_i and ϑ_i are model parameters, which we refer to as the data context. We discuss our quantification of the uncertainties on φ_i, ϑ_i, and λ_i below, providing further details in the electronic supplement.

We relate the stress tensor associated with m to the slip observed on each fault segment of a slip model using the Wallace-Bott assumption, which is that coseismic slip along a fault is collinear to the direction of the maximum shear stress on the fault prior to failure (*Wallace*, 1951; *Bott*, 1959). We determine the shear stresses projected along fault strike and dip directions by rotating the stress tensor associated with m into fault coordinates. The predicted rake on segment i is then

$$\hat{\lambda}_i = \arctan\left(\frac{\tau_{\vartheta_i}}{\tau_{\varphi_i}}\right), \tag{2.5}$$

where τ_{ϑ_i} and τ_{φ_i} are the dip-slip and strike-slip components of the shear stress along the fault segment, respectively.

L_{obs} determines the likelihood of model predicted rakes given the observed rakes and their ascribed uncertainties. Assuming that the slip rakes on the segments are uncorrelated, the likelihood function is

$$L_{\text{obs}}\left(\hat{\lambda}|m\right) = \prod_i L_i\left(\hat{\lambda}_i|m\right), \tag{2.6}$$

where L_i is the likelihood of a model predicted rake on segment i given $\hat{\lambda}_i$ computed for that segment. We acknowledge that it is possible that the slip rakes are correlated across the fault segments within a coseismic slip model, although as the degree to which they may be correlated is unknown, we feel that potential correlations of rake across segments are less important than their uncertainties, which are also not well established. Hence, we ignore any potential correlations in fault slip rake within the coseismic slip models and concern ourselves instead with quantifying the uncertainties on the observed slip rakes on the fault segments, in addition to the model prediction errors due to uncertainties in segment geometries. Accounting for uncertainties in both λ_i and $\hat{\lambda}_i$, the likelihood function is

$$L_i = \int f(\tilde{\lambda};\lambda,\chi_\lambda)\, f(\tilde{\lambda};\hat{\lambda},\chi_{\hat{\lambda}})\partial\tilde{\lambda}, \tag{2.7}$$

where $\tilde{\lambda}$ denotes all possible predicted rakes, χ_λ and $\chi_{\hat{\lambda}}$ denote measures of the uncertainties of λ and $\hat{\lambda}$, respectively (*e.g.*, *Tarantola*, 2005).

Since the rake directions are angular values, the PDFs in Eq. 7 are correctly cast as von Mises PDFs (Appendix A), as noted by *Styron and Hetland* (2015). However, Eq. 7 is not straightforward to implement for von Mises PDFs — *Styron and Hetland* (2015) did not consider uncertainties in fault segment geometries. For rake uncertainties less than approximately 30°, a von Mises PDF is well represented by a Gaussian PDF with limited loss of information (Appendix A). As context, Fig. 2.A1a shows the approximation of von Mises PDFs with Gaussian PDFs for $\sigma = 30°$, $\sigma = 36°$, and $\sigma = 50°$. The uncertainties of the coseismic slip models are not fully quantified in the images of coseismic slip that we use, and we feel that the level of statistical rigor provided from using von Mises PDFs, at the expense of computational ease, is not warranted. By assuming Gaussian PDFs to describe the uncertainties of λ_i and $\hat{\lambda}_i$, L_i becomes

$$L_i(\hat{\lambda}_i|m, \lambda_i) \approx e^{-\frac{1}{2}(\lambda_i - \hat{\lambda}_i)^2/(s^2_{\lambda_i} + s^2_{\hat{\lambda}_i})} \tag{2.8}$$

where s_{λ_i} and $s_{\hat{\lambda}_i}$ are the data uncertainties and error propagated uncertainties, respectively (*Tarantola*, 2005). We discuss our uncertainty quantification of s_{λ_i} and $s_{\hat{\lambda}_i}$ in detail in the electronic supplement.

2.3.1 MCMC lattice sampling

We use a lattice random walk MCMC to sample the posterior for each coseismic slip model considered. The lattice is a discretization of the prior over the model space, and the random walk (RW) only visits those discrete sites (*e.g.*, *Mosegaard and Tarantola*, 1995). The condition of detailed balance is satisfied using a lattice RW, which is necessary for the equilibration to the true probabilities of the sampled model space and an indifference to the starting position of the random walk (*Metropolis et al.*, 1953). Lattice RWs are convenient to implement, and the equilibrium probabilities are merely the frequency with which each lattice point is visited. Moreover, when using a common lattice, posterior samples from multiple MCMCs can be directly compared to each other. The use of a lattice RW is a departure from previous works of *Medina Luna and Hetland* (2013) and *Styron and Hetland* (2015). Both of those studies did not use an MCMC, but rather a naive Bayesian rejection strategy. Within the MCMC, every visited model state is retained, and the frequency in which the RW sampled a particular m within the lattice is an estimate of the equilibrium probability of the m.

There are four sets of Euler angles that describe the same stress tensor. The same MCS orientation can be described by both (ϕ, θ, ρ) and ($\phi \pm \pi$, -θ, -ρ). Furthermore, ρ and $\rho \pm \pi$ describe the same LCS and ICS orientations for a given ϕ and θ. Rather than attempting to construct the lattice to include these symmetries, we construct our lattice so that it completely spans the range of all Euler angles, which is a 3-sphere (*i.e.*, a sphere in four dimensions), and replicate samples based on the symmetries at the end of the RW. As we assume non-informative priors of the Euler angles, the lattice points are roughly evenly spaced on the 2-sphere describing ϕ and θ, with a lattice point spacing of 2° in ϕ for $\theta = 0$ (Fig. 2.2b). The lattice points are evenly spaced over $-\pi \leq \rho \leq \pi$, with spacing of 2°. Similarly, we assume uniformly spaced lattice points within the prior ranges on δ and

ς. The lattice points along the sphere are connected to their radially nearest lattice points (Fig. 2.2b), while ρ, δ, and ς are connected to the linearly nearest lattice points. Note that when the RW is at a bounding value of δ and/or ς, trial models are never selected outside of the bounds, leading to under sampling of the bounding values of those parameters.

We use a Metropolis algorithm to guide the RW in the MCMC. A trial model is randomly chosen from the lattice nodes connected to the current model state at each step of the RW. These connected states include the neighboring states in addition to the current state. At step $k+1$, predictions of rake, $\hat{\lambda}^{k+1}$, are calculated from the trial model. This trial model is selected as the next step in the random walk in proportion to the relative likelihood of the trial model compared to the current model at step k, given by

$$LR = \prod_{i} \frac{L_i\left(\hat{\lambda}_i^{k+1} \,|\, m^{k+1},\, \lambda_i\right)}{L_i\left(\hat{\lambda}_i^{k} \,|\, m^{k},\, \lambda_i\right)}, \tag{2.9}$$

where $\hat{\lambda}^k$ is the rake predicted by the current model state. Eq. 9 is the Metropolis criterion *Metropolis et al.* (1953), and as we assume that all of the model states comprising the lattice are equally likely *a priori*, we do not include the prior probabilities of m_k or m_{k+1} in LR. As an aside, we note that since each trial model is chosen with equal likelihood, there is no propositional distribution, and LR follows the Metropolis algorithm and not the Metropolis-Hastings algorithm (*Hastings*, 1970). If m_{k+1} is as, or more likely than, m_k, $LR \geq 1$ and the trial will always be chosen as the next step in the MCMC. If m_{k+1} is less likely than m_k, $LR < 1$ and m_{k+1} is accepted with probability LR. If m_{k+1} is rejected, then the current model state is replicated in the RW sequence (*i.e.*, $m_{k+1} = m_k$). The MCMC continues in this fashion until a predetermined number of steps are completed.

2.3.2 Composite posterior

We take the non-mutually exclusive (NME) union of the posteriors calculated for each of the coseismic slip models as the composite posterior of the stress estimates for the Kaikōura earthquake, hereafter just referred to as the composite posterior. Forming the composite posterior in this manner is a departure from the previous work of *Medina Luna and Hetland* (2013) and *Styron and Hetland* (2015), where they computed the joint posterior as the final composite posterior for an earthquake. The joint posterior represents the model states that are consistent with all of the coseismic slip models, and hence by combining solutions from individual coseismic slip models through the joint implicitly assumes that only the commonalities of the slip models represent the true coseismic slip. Here we take the position that any, or all, of the coseismic slip models may be an accurate depiction of the true coseismic slip, rather than considering that the true solution is in each of the coseismic slip models. Where a joint posterior will not include features that are only within one of the constituent posteriors, the NME union composite posterior will include all features of all of the constituent posteriors, where common features are amplified, while features unique to one or a few posteriors are minimized. Using the NME union for the composite posterior is crucial here, as several of the studies that we consider published alternate coseismic slip models, and we can consider all of these alternate models without attempting to *a priori* determine which of the alternates are better representations of the Kaikōura earthquake.

In the case of two posteriors derived from two coseismic slip models of the same earthquake, either alternative models presented in the same study or models from two studies, the composite posterior is

$$f_C\left(\sigma \,|\, CS_A \text{ or } CS_B\right) = f_A\left(\sigma \,|\, CS_A\right) + f_B\left(\sigma \,|\, CS_B\right) - f_J\left(\sigma \,|\, CS_A \,\&\, CS_B\right), \quad (2.10)$$

where f_A and f_B are the individual posteriors for the two coseismic slip models CS_A and CS_B, respectively, and f_J is the joint of the two posteriors (*i.e.*, the features that are common to both f_A and f_B). We illustrate the construction of f_C using synthetic coseismic slip models in the electronic supplement.

2.4 Earthquake composite posteriors

We present the composite posterior for the Kaikōura earthquake below, describing the individual posteriors resulting from each of the eight coseismic slip models in the electronic supplement. The most likely estimates for the trend/plunge of the principal stress directions are $100°/0°$ for MCS, $184°/12°S$ for ICS, and $350°/72°N$ for LCS. To display the posteriors over the 5-dimensional model space, we show histograms of δ and ς (*i.e.*, the marginals of δ and ς) and the directions of the principal stress orientations. The stress orientation of MCS is given directly by ϕ and θ and is the number of times the MCMC visited the lattice over these parameters on a 2-sphere (Fig. 2.2b). The orientations of ICS and LCS require consideration of ρ in addition to ϕ and θ, resulting in the orientations of these two principal components not corresponding to the same regular spherical lattice as the MCS orientation. To standardize the display for all components, we map ICS and LCS orientations onto the same lattice we use for MCS, by counting directions of both ICS and LCS visited in the RW to the nearest point on the (ϕ, θ) lattice over the 2-sphere (Fig. 2.2b). We use a Lambert projection of the lower-hemisphere piercing points of those directions to display the orientations. Using MCS as an example, "lower hemisphere piercing points" refer to the two sets of ϕ and θ that equivalently describe the same principal stress orientation, from which we take the angles associated with positive dip (note that in the case where $\theta = 0$, we show both ϕ angles on the posterior plots). As the Lambert projection is conformal and the distance between $0°$ and $10°$ is the same as between $80°$ and $90°$ in the Lambert projected plane, we prefer to use a Lambert projection to display the posteriors rather than a stereographic projection in this paper.

For all CSMs considered, we find that the marginals of ς (*i.e.*, the ratio between σ_1 and σ_3)) are non-informative (*cf.*, Fig. 2.S11 in the electronic supplement; note that the lower likelihood of ς at the extremes is due to the under-sampling of the edges of the prior, as noted above). We also do not find any clear correlations between ς and any of the other model parameters. These results use a fairly coarse ς discretization, although we repeated a few of the MCMCs using a denser ς discretization and found the same lack of constraint on ς. Due to the lack of information in the marginal for ς, we do not discuss it further. We find that the marginal for δ (*i.e.*, the ratio between the difference of σ_2 and σ_3 versus σ_1 and σ_3) is moderately resolved from the coseismic slip models (*cf.*, Fig. 2.S10 in the electronic supplement), and that it lacks any strong correlations with the other model parameters. As our main focus is the interpretation of the principal stress directions, we do not include the marginals of δ for the individual slip models in the main text.

Our composite posterior for the Kaikōura earthquake reveals several concentrations of orientations of principal stress directions with moderate to high likelihoods (Fig. 2.3). Each of these features can be connected to particular coseismic slip models. The concentration associated with the highest likelihood of the posterior, labeled "A" in Fig. 2.3, is characterized by a sub-horizontal, ESE-WNW trending MCS, near-vertical LCS, and a NNE-SSW trending ICS with a shallow to moderate plunge. This facet of the composite posterior is due to the high likelihood features in the Hamling-Ka, Hamling-Kb, and Clark/Holden-K individual posteriors (*cf.* Fig. 2.3 with 2.S2–2.S4 in the electronic supplement). These three models all excluded the Papatea fault, with Hamling-Kb not including slip on the Hikurangi Trench (Fig. 2.1; Table 2.1).

The concentration of orientations associated with the second highest likelihood in the Kaikōura composite, labeled "B" in Fig. 2.3 is due to the posteriors from the *Xu et al.* (2018) models (*cf.*, Fig. 2.3 with 2.S7–2.S9 in the electronic supplement). The commonality of each of these models is the inclusion of a fault segment representing coseismic deformation on the Papatea fault. This facet of the composite posterior is characterized by a sub-horizontal, NNE-SSW trending MCS, a sub-horizontal, roughly E-W trending ICS, and an LCS steeply plunging to the SE. It is worth noting that the ICS and MCS in features

"B" and "A", respectively, have similar trends, with LCS of both features having a high dip. The last feature in the Kaikōura composite posterior, labeled "C" in Fig. 2.3, is due to Wang-K (*cf.*, Fig. 2.3 with Fig. 2.S6 in the electronic supplement). Feature "C" is most typified by a near-vertical ICS, and an LCS plunging to the SW. The Holden-K posterior has an LCS similarly plunging to the SW and a steeply plunging ICS as the Wang-K model (*cf.*, Fig. 2.3 with Figs. 2.S5 & 2.S6 in the electronic supplement).

The posteriors that contribute to facet "A" of the Kaikōura posterior all have lower δ values, signifying that ICS and LCS are similar in relative magnitude (see Fig. 2.S10 in the electronic supplement). The other coseismic slip models are typified by larger δ values, although several models poorly constrain δ (see Fig. 2.S10 in the electronic supplement). Considered in total, the Kaikōura composite posterior shows highest likelihoods of δ less than about 0.5 (Fig. 2.4).

The majority of λ_i are well described by the stress posteriors of the individual coseismic slip models. We use the Jensen-Shannon (JS) divergence to compare the distribution of the posterior predicted $\hat{\lambda}_i$ to the Gaussian distribution parameterized by λ_i and its uncertainty, s_{λ_i}. The JS divergence is described in Appendix A1, and here we use it to quantify the aggregate level of fit of the posterior stress models for each of the fault segments. To provide a context for interpreting the JS divergence, Fig. 2.A1b compares three sets of Gaussian and equivalent von Mises (*i.e.*, with $\kappa = \sigma^{-2}$) PDFs, with JS divergences of the three sets of 0.17, 0.40, and 1.0. 36 of the 102 fault segments have JS$\leq$0.17, and 19 have JS$>$0.4 (Table 2.S1 in the electronic supplement). The largest JS divergence of the fits is 0.64, which corresponds to segments 4 and 6 of Holden-K (see Table 2.S1 and Fig. 2.S16 in the electronic supplement). Most of the fault segments for which λ_i is not well described by the stress posteriors are segments with either low potency and low maximum slip (see Table 2.S1 in the electronic supplement), or are segments that do not have consensus across slip models. There is no spatial pattern in these misfitted fault segments, and hence do not challenge the notion that a single state of stress is consistent with each of the coseismic slip models.

The rakes predicted by the posterior stress models for the Kaikōura coseismic slip models broadly agree with the vast majority of segments (Table 2.S1 in the electronic supplement). Fig. 2.5 demonstrates this agreement as a rose plot of the predicted versus observed rakes for the segments of Xu-Ka and includes the percent potency and maximum slip observed for each segment. Rose plots for additional models are provided in the electronic supplement (Figs. 2.S13–2.S20). The only coseismic slip model in which the majority of segments are poorly described is in the seven-segment Holden-K model. Holden-K only includes a subset of segments from Clark/Holden-K that are required to fit local strong motion data. At face value, that the majority of the segments in Holden-K are not well-described by a homogeneous stress model might suggest that uniform stress is inconsistent with the Kaikōura earthquake; however, given the simplicity of Holden-K and the fact that the other coseismic slip models for Kaikōura do not have a similar level of misfit across all segments, we believe that the inability to fit Holden-K does not challenge a homogeneous pre-earthquake stress. The overwhelming majority of the misfit segments from the seven other models are low potency segments. For example, the three highest misfit segments belonging to Wang-K have the smallest relative potencies of the entire 12-segment model. Additionally, the three segments with the highest misfit shared by both Hamling-Ka and Hamling-Kb (see segments 4, 9, and 15 in Table 2.S1 and Fig. 2.S13–2.S14 in the electronic supplement) have low relative potencies. The average slip rakes on all of the segments in Xu-Ka and Xu-Kc are consistent with the rakes predicted by the posteriors, with a very strong agreement in predicted and observed rakes on all segments in Xu-Ka. The introduction of the Hikurangi Trench in Xu-Kb and the Pt. Kean fault in Xu-Kc results in a decrease in fit of segment 0. Segment 0 is a high potency, high slip, central segment that is representative of the Needles fault and Kekerengu fault, among others, and is common to all the Xu coseismic slip models. In Xu-Ka, the JS divergence of this segment is only 0.08, although in Xu-Kb and Xu-Kc, the JS divergence approaches 0.3. Additionally, the average rake on the southernmost segment of the Xu models (segment 4 in Xu-Kc) is not well described by the posterior stress models, but the predicted rakes are about 30° of the observed λ_i.

2.5 Discussion

In the following subsections, we discuss our uncertainty model and its effect on the posteriors. We explore the goodness of fit of our rake predictions and what we can learn from their residuals. Finally, we compare our results to independent information and determine which features of our posteriors, or the associated coseismic slip models, are robust to external indications of stress in the area of the Kaikōura earthquake.

2.5.1 Assessment of uncertainty model

It is crucial to have quantified uncertainties when using a Bayesian estimation strategy. Our scheme to quantify the uncertainties of λ_i is based on the degree to which slip rake varies across a fault segment, and takes into account the potency of that segment relative to the total potency of the coseismic slip model. The former aspect of our scheme has the effect that coseismic slip rake on segments with a large variation in imaged rakes is less certain than that on segments with low variation of rakes, segment potency being equal, and thus segments with low variance in imaged coseismic slip rake have a greater influence on the solution. However, the distribution of imaged slip across a fault segment is regularized to varying degrees, with slip constrained to be smooth and/or with rake constrained. A high degree of regularization and/or a heavily constrained coseismic slip model can result in exceedingly little variation of slip rake across a segment, which could be mistaken for high certainty of λ_i. To avoid conflating overly constrained images of coseismic slip with highly certain images of coseismic slip, we arbitrarily set the uncertainty to 25° when the rake variance across a segment is less than 3°.

At the other extreme, when the variation of coseismic rake on a segment is high, the scaled variance can be quite large. Likewise, when the segment potency is low, our scheme results in a large uncertainty of λ_i. The fact that we are using Gaussian PDFs to approximate distributions for angular values, motivates us to cap the uncertainties at 30° (see Appendix A; 32 of the 102 segments were capped with an uncertainty of 30°). An uncertainty of 30° is stating that there is a 68% probability that the true coseismic rake is $\lambda_i \pm 30^\circ$ (66% in the equivalent von Mises PDF), and a 95% probability rake is $\lambda_i \pm 60^\circ$ (94% in the equivalent von Mises PDF). In other words, with our posited maximum cap on uncertainty, we are assuming that a coseismic slip model can in the least resolve the difference between dip-slip and strike-slip faulting mechanisms at about 95% confidence. For instance, if the imaged coseismic slip model resolved pure reverse slip on a segment, the rake would be 90°, with oblique-reverse rakes of 30°–150° at 95% confidence. Aside from the issue of approximating von Mises PDFs with Gaussian PDFs (see Appendix A), we believe that this upper bound of rake uncertainty is reasonable under the premise that coseismic slip models can in the least discern dip-slip from strike-slip motion.

In our scheme, s_{λ_i} ranges from 3° to 30°, with a median of 25°. Only 33 fault segments have uncertainties on λ_i less than 20°. From the fits of the posterior stress models to λ_i (see Table 2.S1 and Figs. 2.S13–S20 in the electronic supplement), no clear patterns indicate that high-potency segments are fit better by our predictions than low-potency segments, or that segments with low s_{λ_i} are fit better than those with higher s_{λ_i}. If these patterns were present, they would indicate that our uncertainty model is driving the solution; however, we find that this is not the case. For instance, in Hamling-Kb (see Table 2.S1 and Figs. 2.S13 & 2.S14 in the electronic supplement), the degree of fit to segments with low s_{λ_i} varies substantially (*cf.*, segments 1 and 4 for Hamling-Kb). Likewise, the degree of fit does not vary with the potency of the segment (*cf.*, segments 1 and 8 for Hamling-Kb).

2.5.2 Fit residuals

For the majority of the fault segments, the predictions of our posteriors are consistent with λ_i. Segments for which predictions misfit λ_i are segments with low potency or low maximum slip, or are segments that lack consensus between coseismic slip models. Both the coseismic slip on and the geometry of segments with low potency and/or low maximum slip are inherently harder to constrain owing to the lower geodetic or seismic signals. For example, the poorly fit fault segments within the coseismic slip models discussed in our results are low potency segments. However, it is important to note that there are many segments with low potency and low maximum slip that are well fit by the posterior. We also find that some segments which are not represented in all, or most, of the coseismic slip models are poorly fit. In that, misfits between the posterior stress models and individual segments present a method to test the compatibility of segments with other coseismic slip models.

The single posterior we determined represents a single state of pre-earthquake stress, or at least a pre-earthquake stress which varies less than the variance of the posterior. Variation in rake across all of the fault segments in a coseismic slip model is then due simply to variation in fault segment geometry. The uncertainties of slip rake and fault geometries that we use capture the degree to which that information is known, but those uncertainties could also be interpreted to describe the variation of slip rake or geometry of that segment within a coseismic slip model. If systematic spatial variations of the residuals were observed for multi-segment slip models, this might indicate that a heterogeneous stress would be required to describe variations of slip rakes on the segments across the earthquake; however, we do not find such evidence of spatially systematic misfits.

We acknowledge that it is possible that the pre-earthquake stress in the region surrounding individual, poorly fit fault segments differs from the near-homogeneous stress elsewhere, with no systematic spatial variation of the stress field. Alternatively, it could simply be that the λ_i, which is based on the imaged coseismic slip rakes, on these poorly fit segments are not accurate descriptions of the true earthquake slip. As we can not fully determine which of these possibilities is the cause of the misfitting rakes, we feel that there would be limited knowledge gained by exploring *ad hoc* stress models, where stress is allowed to vary arbitrarily to perfectly capture the imaged slip rake on all of the segments. Moreover, as there is no clear evidence that the coseismic slip models require a systematic heterogeneous stress, we see no compelling reason to explore heterogeneous pre-earthquake stress models. The fact that several stress estimations from earthquake focal mechanisms also conclude homogeneous stress for New Zealand's South Island (*e.g.*, *Balfour et al.*, 2005; *Boese et al.*, 2012; *Townend et al.*, 2012; *Holt et al.*, 2013; *Michailos* *et al.*, 2020), lends support to our decision to only consider homogeneous pre-earthquake stress models.

2.5.3 Testing the consistency of coseismic slip models

As we consider all of the coseismic slip models as possible representations of the true coseismic slip in the Kaikōura earthquake, our resulting posteriors are estimates of varied, and, in some cases, conflicting representations of the true earthquake slip. In this subsection, we investigate which features of our posteriors are robust reflections of the seismogenic state of stress by testing the posteriors against independent information. We interrogate the Kaikōura composite posterior for its consistency with the known sense of slip along the Hope Fault, a prominent fault in the MFS. Furthermore, in cases where different features of the composite posteriors can be clearly identified within the coseismic slip models, we indirectly test the coseismic slip models themselves against external information through our composite stress posteriors.

The Kaikōura composite posterior has a primary, high probability MCS solution trending approximately E-W (labeled “A” in Fig. 2.3), and a secondary, lower probability, solution trending near N-S (labeled “B” in Fig. 2.3). The near E-W trending MCS facet of the composite posterior is contributed to by the Hamling-Ka, Hamling-Kb, and Clark/Holden-K posteriors, while the near N-S trending MCS facet results from the three *Xu et al.* (2018) models. Wang-K contributes an even lower probability solution of MCS in the composite posterior that trends between these two end-members (labeled “C” in Fig. 2.3).

An important difference between the E-W trending and the N-S trending MCS solutions is the respective omission versus inclusion of the Papatea fault in the coseismic slip models constraining these facets of the posterior. The Papatea fault was observed by *Litchfield et al.* (2018) through field mapping to have slipped 12 meters. Given that their coseismic slip models are based on the elastic dislocation solution of *Okada* (1985), *Clark et al.* (2017), and *Hamling et al.* (2017) chose to ignore this highly offset feature as they were unable to model the observed deformation elastically, and instead excluded data surrounding the Papatea fault while constraining their models. *Holden et al.* (2017) also excluded this region of deformation from the Holden-K model due to a lack of sufficient strong-motion and high-rate GPS stations. Additionally, *Diederichs et al.* (2019) concluded that the Papatea fault deformed anelastically as a result of the displacement of surrounding faults minimizing available space, rather than through the release of stored strain energy, a conclusion supported by *Hamling* (2019). They further posit that the traditional modeling of slip along planar segments in an elastic half-space may not be appropriate. In contrast, the slip models that did include the Papatea fault, those of *Wang et al.* (2018) and *Xu et al.* (2018), did not report similar challenges with modeling the deformation around the Papatea fault, and hence included this fault in their proposed coseismic slip models.

We can test the level of compatibility with the estimated posterior stress directions of the N-S MCS trending solutions and the E-W MCS trending solutions against the known sense of slip of the Conway segment of the Hope fault. The Conway segment runs through the Kaikōura coseismic slip region (Fig. 2.1) and was observed to undergo minor surface displacement, with a net displacement of 1.5 m, during the Kaikōura earthquake (*Litchfield et al.*, 2018). However, geodetic data did not indicate that the Hope fault slipped to a significant enough degree to be captured in the coseismic slip models (*e.g.*, *Clark et al.*, 2017), and the lack of involvement of the greater extent of the Hope Fault has been a persisting question (*e.g.*, *Litchfield et al.*, 2018). The Conway segment of the Hope Fault has been evaluated to have a heightened seismic hazard, in part due to a short recurrence interval of 180-310 years and very high right-lateral slip rate of 23 ± 4 mm/year (*e.g.*, *Langridge et al.*, 2003). We forward predict rakes on a fault segment striking 73° and dipping 70° to the north, which are the best estimates of the strike and dip of the Conway segment recorded by paleoseismic observations (*Van Dissen and Yeats*, 1991; *Langridge et al.*, 2003; *Litchfield et al.*, 2014). We find that the median sense of motion predicted on the Conway segment for a N-S trending MCS is left-lateral, while an E-W trending MCS would result in a right-lateral faulting mechanism, which is compatible with the paleoseismic observations. In other words, the decision to exclude the deformation surrounding the Papatea fault, as made by *Hamling et al.* (2017) and *Holden et al.* (2017), results in coseismic slip models that are consistent with a state of stress that agrees with observations of the long-term slip mechanisms on the Conway segment. That the N-S trending MCS characteristic of the Papatea-including models from *Xu et al.* (2018) is inconsistent with dextral slip on the Hope Fault lends further support to the assertion that the deformation around the Papatea should not be included in the coseismic slip models, in addition to it not being suited for elastic dislocation modeling. While the Papatea Fault has large slip in their models, it is important to emphasize that it is not just the Papatea fault that results in the inference of a N-S oriented MCS, but rather the entirety of the coseismic slip models that contain the Papatea fault, including choices in representation of slip elsewhere in the earthquake. Indeed, *Wang et al.* (2018) included a Papatea fault but found a MCS trending between the E-W and N-S trends we considered above.

Another point of disagreement among the coseismic slip models is whether the Hikurangi Trench slipped during the Kaikōura earthquake. Three of the four publications in which we source coseismic slip models provided alternative models where the key difference was whether the Hikurangi Trench was included in the coseismic slip model (Table 2.1). *Hamling et al.* (2017) found that the inclusion of the Hikurangi Trench in their Hamling-Ka model improved the fit of observed inland subsidence. However, their Hamling-Kb model minimized residuals observed near the Kekerengu fault. Additionally, both Hamling-Ka and Hamling-Kb produced similar tsunami models. The authors found that they needed to add a constraint on the total moment to determine the contribution of slip along the Hikurangi Trench, but could not conclusively establish whether Hikurangi Trench slip was needed based on the geodetic data. *Holden et al.* (2017) found that the inclusion of the Hikurangi Trench did not contribute to modeled ground motion, and thus they omitted the Hikurangi Trench, along with several other major fault segments, in the Holden-K model. Finally, *Xu et al.* (2018) found that both their coseismic slip model that included the Hikurangi Trench, Xu-Kb, and their slip model that included the offshore Pt. Kean fault instead of the Hikurangi Trench, Xu-Kc, had similar slip distributions on crustal fault segments common to the two models. This similarity of imaged slip on crustal faults indicates that the data can not discriminate whether slip occurred on the Hikurangi Trench or Pt. Kean structures, and indeed *Xu et al.* (2018) found a similar lack of resolution on both the Hikurangi Trench and Pt. Kean segments in checkerboard tests.

Features within the Kaikōura composite posterior that are common to coseismic slip models that either contain or neglect slip on the Hikurangi Trench can be identified; however, the differences in these features are less pronounced than in the Papatea case discussed above. Just focusing on the *Xu et al.* (2018) models, Xu-Kb results in a near-vertical LCS (Fig. 2.S8 in the electronic supplement), while their coseismic slip models neglecting the Hikurangi Trench, Xu-Ka and Xu-Kc, are consistent with an off-vertical LCS dipping to the southeast (Fig. S7 & S9 in the electronic supplement). In contrast, the *Hamling et al.* (2017) models with or without the Hikurangi Trench are both consistent with similar orientations of principal stress directions (Figs. 2.S2 & 2.S3 in Supplementary Material). Wang-K, which does contain slip on the Hikurangi Trench, is consistent with a SW plunging LCS (Fig. 2.S6 in electronic supplement).

2.6 Conclusions

We invert coseismic slip models to obtain the orientations and relative magnitudes of principal stress for the 2016 Kaikōura earthquake through a Bayesian Markov Chain Monte Carlo (MCMC) estimation strategy. We consider eight coseismic slip models of the Kaikōura earthquake (*Clark et al.*, 2017; *Hamling et al.*, 2017; *Holden et al.*, 2017; *Wang et al.*, 2018; *Xu et al.*, 2018). Rather than *a priori* determining which model is a better representation of the true earthquake slip or assuming that the true earthquake slip is some average of all proposed models, we allow for the possibility that any or all of the coseismic slip models are the true representation of the Kaikōura earthquake. We calculate posteriors of stress for each coseismic slip model independently, and then form the non-mutually exclusive union of all of the posteriors as the composite stress posterior for the Kaikōura earthquake.

Our composite posterior for the Kaikōura earthquake is characterized by well defined orientations of the principal components of stress, with little to no constraints on the relative magnitudes of the principal stresses. The composite posterior reveals a most likely stress orientation with MCS trending WNW-ESE and near-horizontal, ICS trending ENE-WSW and plunging shallowly, and LCS plunging near-vertical, consistent with an Andersonian thrust stress regime. We find that this state of pre-earthquake stress is consistent with independent paleoseismic observations of the slip mechanism of the nearby Conway segment of the Hope Fault.

Our analysis provides a means for determining whether coseismic slip models of the same earthquake are mechanically consistent, either in facets of those models or in the entire model. Additionally, our analysis provides a means to determine whether coseismic slip models are mechanically consistent with nearby faults or known deformation patterns. In that, the inversion of coseismic slip models for stress has potential application to the arbitration between differences in features across multiple slip models of the same earthquake.

2.7 Data and resources

Data used in this paper came from published sources listed in the references. The code used for the MCMC stress inversions is available from . Fault traces for major faults in Fig. 2.1 are sketches of active fault traces from *Langridge et al.* (2016) and *Stirling et al.* (2012). Focal mechanism in Fig. 2.1 is the best double couple solution from the Global Centroid Moment Tensor Project database (last accessed on June 2021). Figs. 2.1 and 2.4 were made using the Generic Mapping Tools version 6.1.1 (www.generic-mapping-tools.org; *Wessel et al.*, 2019). The electronic supplement includes: supplemental text that describes the uncertainty on rake, as well as a demonstration of our methods for synthetic slip models; a table that provides details regarding segments in the coseismic slip models; figures of the results of our synthetic models, the orientations of principal stresses for the posteriors obtained for each of the coseismic slip models, the marginals of δ and ς, and comparisons of the predicted and observed rakes on each segment.

2.8 Acknowledgments

This research was funded by NSF grant EAR 1722994. We are grateful for the thorough reviews provided by Chris Rollins, Rich Koehler, and an anonymous reviewer, as well as comments from Associate Editor Mark Stirling, whose contributions have improved the quality of this paper. Former University of Michigan graduate student Russel Wilcox-Cline worked on an earlier version of the MCMC stress inversion method, and although this research does not include any component of his work, we gratefully acknowledge that his efforts influenced the direction of this work.

2.9 Appendix

Approximation of von Mises PDF with a Gaussian PDF

Uncertainties of angular values, such as fault strike, dip or rake, are correctly cast with a von Mises PDF,

$$f_{\mathrm{vM}}(\alpha;\bar{\alpha},\kappa) = Ae^{\kappa\cos(\bar{\alpha}-\alpha)}, \tag{2.A1}$$

where A is a normalization factor, α is an angular value, $\bar{\alpha}$ is the most likely angle, and κ is a concentration parameter that determines the spread of the distribution. A Gaussian PDF of the same angular value is

$$f_{\mathrm{G}}(\alpha;\bar{\alpha},\sigma) = Be^{-\frac{1}{2}\frac{(\alpha-\bar{\alpha})^2}{\sigma^2}}, \tag{2.A2}$$

where B is a normalization factor and σ^2 is the variance. For large κ, f_{vM} is approximately f_{G} with a variance of κ^{-1}.

Here we seek to determine a value of σ in which f_{vM} can be approximated by f_{G} as

$$f_{\mathrm{vM}}(\alpha;\bar{\alpha},\kappa=\sigma^{-2}) \approx f_{\mathrm{G}}(\alpha;\bar{\alpha},\sigma). \tag{2.A3}$$

We use the Jensen-Shannon (JS) divergence, $\mathcal{D}_{\mathrm{JS}}$, to quantify the distance between these two PDFs. The JS divergence is a symmetric distance measure between PDFs based on the Kullbach-Liebler (KL) divergence, $\mathcal{D}_{\mathrm{KL}}$, defined as

$$\mathcal{D}_{\mathrm{JS}}\left(f_{\mathrm{vM}}, f_{\mathrm{G}}\right) = \frac{1}{2}\left(\mathcal{D}_{\mathrm{KL}}\left(f_{\mathrm{vM}} \| f_{\mu}\right) + \mathcal{D}_{\mathrm{KL}}\left(f_{\mathrm{G}} \| f_{\mu}\right)\right), \tag{2.A4}$$

where f_μ is the average of f_{vM} and f_{G} and

$$\mathcal{D}_{\mathrm{KL}}\left(f_X \| f_\mu\right) = \int f_X(x) \log \frac{f_X(x)}{f_\mu(x)} dx. \tag{2.A5}$$

Fig. 2.A1a shows the JS divergence between these two PDFs for increasing σ. For $\sigma \leq 30°$, $\mathcal{D}_{\mathrm{JS}} \leq 0.17$, and the two PDFs are quite similar (Fig. 2.A1b). We take $\sigma = 30°$ to be the limit at which we allow a von Mises PDF to be approximated by a Gaussian PDF. At the upper bound of $\sigma = 30°$, the 99.99% confidence of a Gaussian (*i.e.*, the 4-σ bounds) is $\pm 120°$, which is within $[-180°, 180°]$.

Table 2.1: Number of fault segments and whether the Hikurangi Trench or Papatea Fault were included in each coseismic slip model.

Slip Model	Number of Faults	Hikurangi	Papatea
Hamling-Ka	20	x	
Hamling-Kb	19		
Clark/Holden-K	25	x	
Holden-K	7		
Wang-K	12	x	x
Xu-Ka	6		x
Xu-Kb	7	x	x
Xu-Kc	7		x

2.10 Figures - Chapter 2

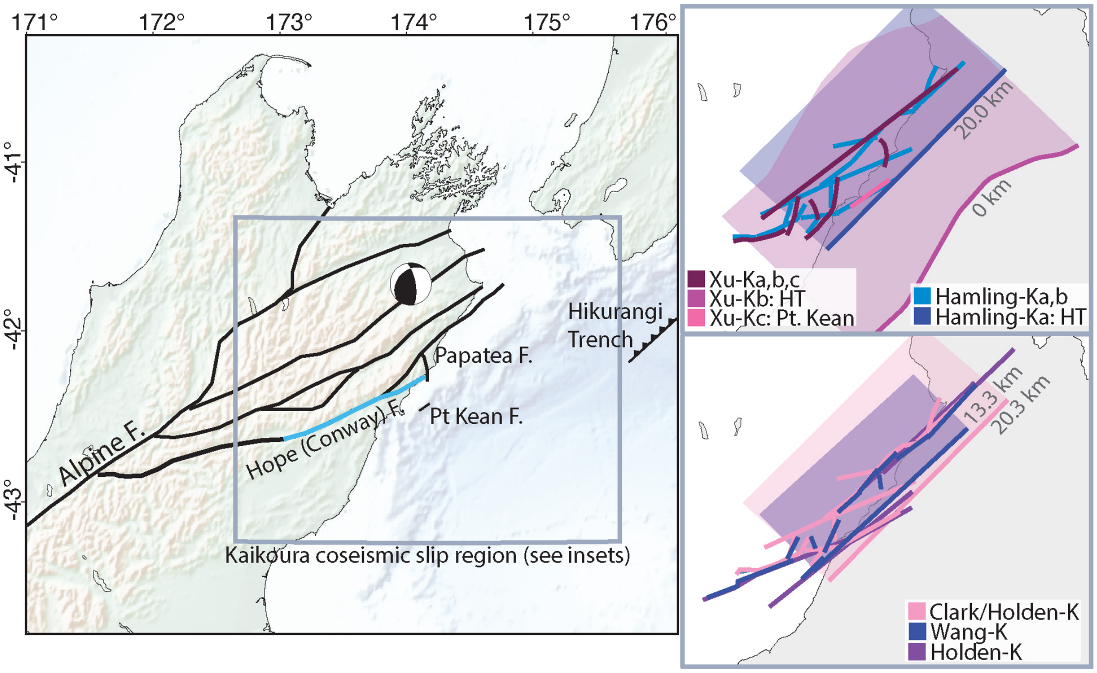

Figure 2.1: (left) Map of the top of New Zealand's South Island with idealized sketches of major active faults (thin lines) from Langridge et al. (2016) and the southwestern extent of the Hikurangi Trench from Stirling et al. (2012). The Global Centroid Moment Tensor (GCMT) double-couple focal mechanism solution for the 2016 $M_w 7.8$ Kaikōura earthquake is shown at the centroid location (see Data and Resources Section). (right) Figure insets show the fault segment traces for the coseismic slip models that we consider in this study: Hamling-Ka and Hamling-Kb (Hamling et al., 2017); Clark/Holden-K (Clark et al., 2017; Holden et al., 2017); Holden-K (Holden et al., 2017); Wang-K (Wang et al., 2018); Xu-Ka, Xu-Kb, and Xu-Kc (Xu et al., 2018). Segments associated with the Hikurangi Trench are shown as surface projections of the segment surface in the coseismic slip models, with indicated depths of the top edge of the segment.

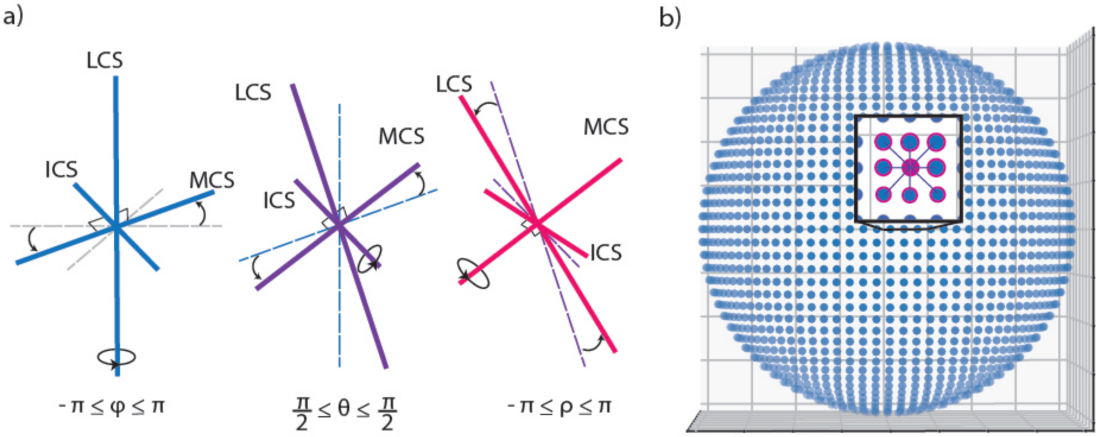

Figure 2.2: (a) Illustration of the rotation axes defined by the Euler angles, ϕ, θ, and ρ, describing the orientations of the principal components of stress. (b) The spherical lattice of the (ϕ, θ) model space, highlighting the connectivity between one lattice point and the radially nearest nodes.

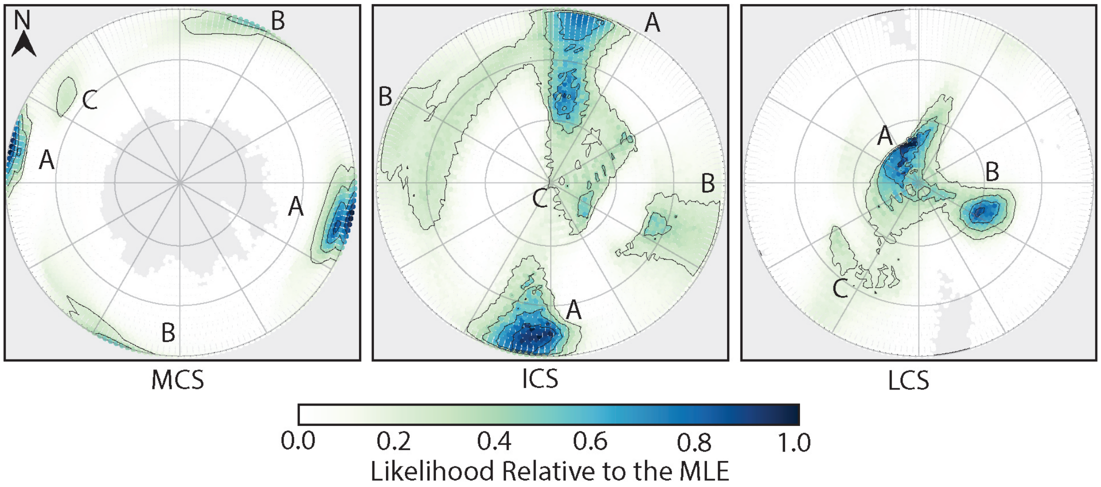

Figure 2.3: Lambert projection of the lower hemisphere piercing points for the non-mutually exclusive union composite posterior determined from the Kaikōura coseismic slip models. The relative likelihood of each principal component is represented by a colormap normalized by the likelihood of the most likely estimate and by contours with intervals of 0.2 of the most likely estimate. Top of the page is oriented towards geographic North (equivalent to a trend of 0°; grid-lines indicate 30° intervals of trend and plunge, where the outermost circle represents a plunge of 0° and the center of the circle a plunge of 90°. Annotations indicate facets of the posterior discussed in the main text: “A” corresponds to the highest likelihood solutions and are orientations consistent with right-lateral slip on the Conway segment of the Hope Fault; “B” and “C” are lower likelihood solutions that are inconsistent with right-lateral slip on the Conway segment.

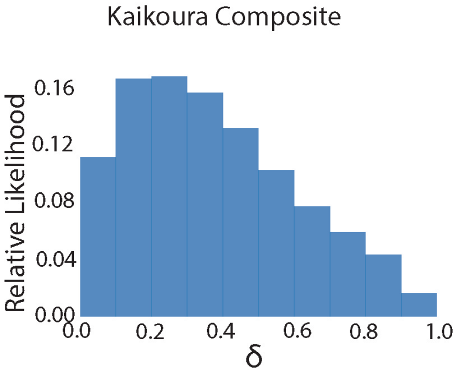

Figure 2.4: Histogram of δ (*i.e.*, the marginal of δ) for the Kaikōura composite posterior.

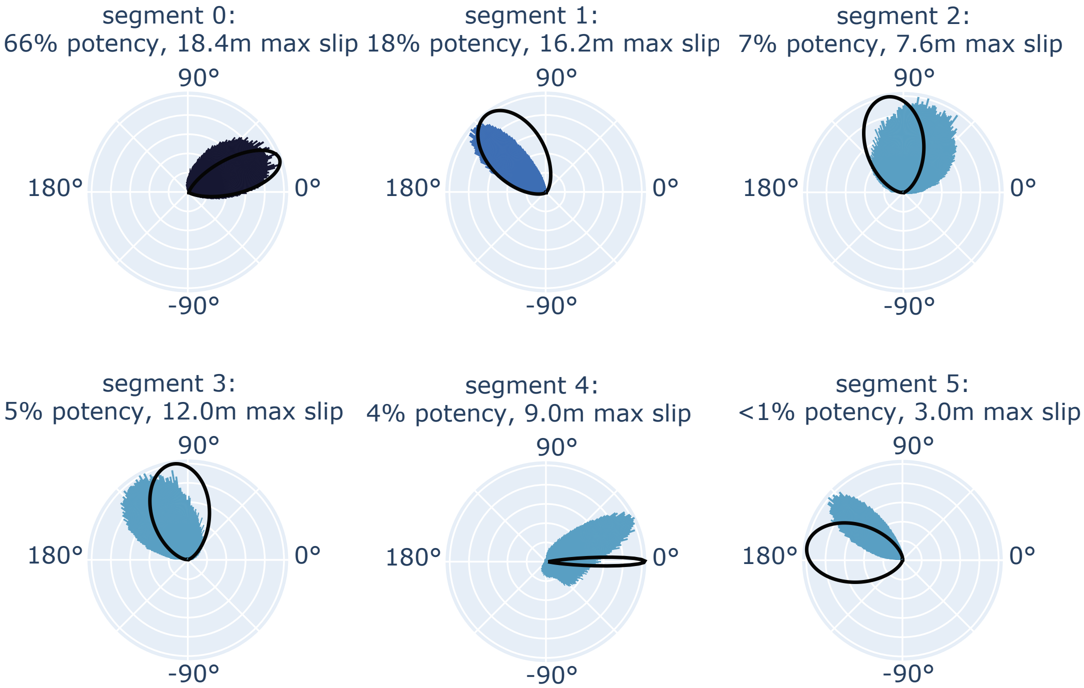

Figure 2.5: Rose plots of predicted (bars) *vs.* observed (black line) rake for the segments of the Xu-Ka coseismic slip model (Xu et al., 2018). The percent potency and maximum slip observed for each segment is given in each rose plot's subtitle.

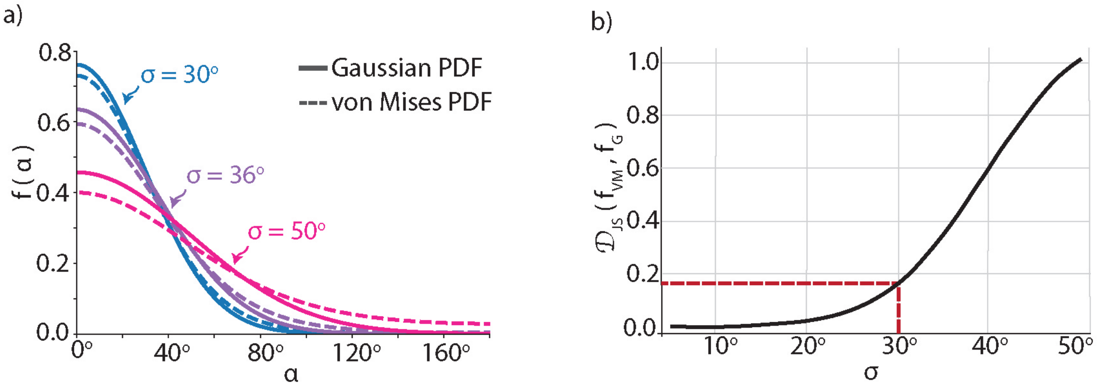

Figure 2.A1: (a) Approximation of von Mises PDFs (dashed lines) with Gaussian PDFs (solid lines) for increasing $\sigma = 30^{\circ}$, $\sigma = 36^{\circ}$, and $\sigma = 50^{\circ}$. (b) Jensen-Shannon (JS) divergence between von Mises PDFs and Gaussian PDFs for increasing σ.

2.11 Supplemental material - Chapter 2

2.11.S1 Description of the supplemental material

The supplemental text includes a demonstration of our methods on two synthetic coseismic slip models, as well as a description of our quantification of the uncertainties on rake that we implement in the calculation of our likelihood ratios.

Table 2.S1 provides data used in our inversions for all of the segments for each coseismic slip model, including the percent potency of a segment relative to the coseismic slip model's total potency, the maximum slip resolved along the segment, and the Jensen-Shannon (JS) divergence between the Gaussian distribution defined by the segment's observed rake and it's quantified uncertainty with the distribution of predicted rake values associated with the posterior.

Figure 2.S1 shows the results of our methods for two synthetic coseismic slip models.

Figures 2.S2–2.S9 show the orientations of principal stresses from the posteriors obtained for each of the coseismic slip models considered. The stress orientation of the most compressive stress (MCS) is given directly by ϕ and θ, and is the number of times the MCMC visited the random walk (RW) lattice over these parameters on a 2-sphere. To standardize the display of the posteriors of the principal stress orientations for all components, we map the intermediate compressive stress (ICS) and least compressive stress (LCS) orientations onto the same lattice we use for MCS, by counting directions of ICS/LCS visited in the RW to the nearest point on the (ϕ, θ) lattice over the 2-sphere. We use a Lambert projection of the lower-hemisphere piercing points of those directions. The contours in the figures are the contours from the composite posterior (Fig. 2.3).

Figures 2.S10–2.S11 show the histograms of δ and ς (*i.e.*, the marginals of δ and ς) for each of the coseismic slip models considered.

Figure 2.S12 shows the histogram of δ and ς (*i.e.*, the marginals of δ and ς) for the Kaikoura composite posterior.

Figures 2.S13–2.S20 shows the average rake on each fault segment and its assessed uncertainty, along with rose plots of the rakes predicted by the stress models in the posterior obtained from that coseismic slip model. A rake of 0° corresponds to a left-lateral strike-slip faulting mechanism, a rake of 180° corresponds to a right-lateral strike-slip faulting mechanism, a rake of 90° corresponds to a reverse slip faulting mechanism, and a rake of -90° corresponds to a normal slip faulting mechanism.

2.11.S2 Supplemental text

2.11.S2.1 Synthetic slip data posteriors

We consider two synthetic coseismic slip models, which we denote CS_A and CS_B (Fig. 2.S1). Both of these slip models are composed of two fault segments, denoted FS_X^k, where $X = A$ or B is the coseismic slip model and $k = 1$ or 2 is the fault segment (Fig. 2.S1). The posterior from each of the fault segments, denoted $f\left(\sigma \left| FS_X^k\right.\right)$, is estimated from our MCMC strategy, and the joint posterior,

$$f_J\left(\sigma \left| CS_X\right.\right) = f_J\left(\sigma \left| FS_X^1 \,\&\, FS_X^2\right.\right) = f\left(\sigma \left| FS_X^1\right.\right) \cdot f\left(\sigma \left| FS_X^2\right.\right), \tag{2.S1}$$

is then the posterior of stress that is consistent with slip on both of the segments. The joint posteriors only retain features that are common to the posteriors associated with each of the fault segments in that coseismic slip model (Fig. 2.S1). The NME union composite posterior,

$$f_C\left(\sigma \,|\, CS_A \text{ or } CS_B\right) = f_J\left(\sigma \left| CS_A\right.\right) + f_J\left(\sigma \left| CS_B\right.\right) - f_J\left(\sigma \left| CS_A\right.\right) \cdot f_J\left(\sigma \left| CS_B\right.\right), \tag{2.S2}$$

then describes the stresses that are consistent with either or both of the coseismic slip models. The NME union posterior includes regions of high likelihood from both of the individual coseismic slip model posteriors, even if these regions are not shared by both posteriors.

2.11.S2.2 Quantification of uncertainties on rake

The level of uncertainties on either fault slip or segment geometries in the coseismic slip models we use were not established, neither qualitatively nor quantitatively. In addition to the aleatoric uncertainties due to inverting inherently uncertain data, epistemic uncertainties in the coseismic slip models that arise from uncertainties in crustal parameters have been demonstrated to be important (*Duputel et al.*, 2012, 2014; *Ragon et al.*, 2018, 2019; *Langer et al.*, 2020). We recognize the challenges in quantifying the level of uncertainties in the slip models, and are fully aware that not quantifying uncertainties in coseismic models is in no way unique to the published coseismic slip models we use. However, as previously stated, having quantified uncertainties is crucial within a Bayesian estimation framework.

We take the angular variance of rake across the sub-faults in a given segment, weighted by the sub-fault's potency, as an initial proxy for the level of uncertainty on the fault segment's rake. We compute the weighted angular variance, v_{λ_i}, as

$$v_{\lambda_i} = \arctan\left(\frac{\sum_j p_i^j \sin^2(\tilde{\lambda}_i^j - \lambda_i)}{\sum_j p_i^j \cos^2(\tilde{\lambda}_i^j - \lambda_i)}\right), \tag{2.S3}$$

where $\tilde{\lambda}_i^j$ is the observed rake on sub-fault j on fault segment i, and p_i^j is the potency of the sub-fault. v_{λ_i} can be viewed as the degree to which a single λ_i captures the actual coseismic slip rake across that segment, either due to inherent uncertainty in the estimated slip rakes or natural variability of slip rake across the segment.

We recognize that there are two main issues with using v_{λ_i} to quantify the uncertainties of λ_i. (1) Coseismic slip on fault segments with larger potencies are likely much better resolved in a coseismic slip model than slip on fault segments with lower levels of potency, owing to the fact the surface deformation and seismic energy resulting from high potency fault segments can dominate those from low potency segments. (2) The variation in slip across the sub-faults on each segment is heavily influenced by the regularization and/or constraints on rake imposed when determining the coseismic slip models.

In order to address point (1) above, we scale v_{λ_i} by a factor that depends upon the segment potency, p_i, relative to the total potency in that coseismic slip model, p. We calculate a potency scaled variation, s'_{λ_i}, as

$$s'_{\lambda_i} = v_{\lambda_i}\left(1 + e^{-10p_i/p}\right). \tag{2.S4}$$

This scaling has the effect that λ_i on lower potency segments have a higher uncertainty than high potency segments, while still basing the uncertainty on the variation in the coseismic slip models.

With regards to point (2) we find several fault segments with v_{λ_i} very close to zero, resulting in $s'_{\lambda_i} \approx 0$, and in all cases these segments are either heavily regularized or the inferred coseismic slip rake was pinned at the rake constraints imposed when imaging the coseismic slip. To avoid having the rake on these overly-constrained segments to be manifested as highly certain in L_{obs}, and thus drive the solution, we arbitrarily set the final variation of rake, s_{λ_i}, to 25° on segments in which $s'_{\lambda_i} \approx 0$. As we are approximating what should be von Mises PDFs as Gaussian PDFs, we set a maximum on s_{λ_i} of 30°, the limit in which we deem the two PDFs to be approximately equivalent (see Appendix A). For all other fault segments that conform to these two points, $s_{\lambda_i} = s'_{\lambda_i}$.

L_{obs} depends not only s_λ, but also on the uncertainties of the model predicted rake, $s_{\hat{\lambda}_i}$. Since $\hat{\lambda}_i$ depends entirely on φ_i and ϑ_i, $s_{\hat{\lambda}_i}$ depends on the uncertainties of φ_i and ϑ_i, denoted s_{φ_i} and s_{ϑ_i}, respectively. As with the imaged coseismic slip, the uncertainties of the fault segment geometries are not quantified in the published coseismic slip models we use. Since there are no direct features of the coseismic slip models we could use to base our estimation of s_{φ_i} and s_{ϑ_i}, we arbitrarily assume

$$s_{\varphi_i} = s_{\vartheta_i} = 20^\circ e^{-10p_i/p} + 10^\circ. \tag{2.S5}$$

This scaling results in s_{φ_i} and s_{ϑ_i} approaching 30° on fault segments with very low potency relative to the total potency of the model, while segments with higher potency have s_{φ_i} and s_{ϑ_i} about 10°. We propagate the uncertainties of φ_i and ϑ_i into an uncertainty on $\hat{\lambda}_i$ as

$$\begin{bmatrix} s_{\hat{\lambda}_i} \end{bmatrix} = J_{\hat{\lambda}} \begin{bmatrix} s^2_{\varphi_i} & 0 \\ 0 & s^2_{\vartheta_i} \end{bmatrix} J^T_{\hat{\lambda}} \tag{2.S6}$$

where $J_{\hat{\lambda}}$ is the Jacobian of the prediction of rake with respect to φ_i and ϑ_i, evaluated for each fault segment.

2.11.S3 Data and resources specific to the electronic supplement

Data used in this paper came from published sources listed in the references below. Figs. S1–S9 were made using the Generic Mapping Tools version 6.1.1 (www.generic-mapping-tools.org; *Wessel et al.*, 2019).

2.11.S4 Tables

Table 2.S1: The percent potency of each segment in the coseismic slip models relative to the coseismic slip model's total potency, the maximum slip resolved along the segment, and the Jensen-Shannon (JS) divergence between the average rake on that segment and the rakes predicted by the stress models in the posterior for that coseismic slip model.

slip model	segment number	potency (%)	max. slip (m)	JS divergence
Hamling-Ka	1	18	24.2	0.10
	3	18	18.1	0.24
	2	15	24.9	0.35
	0	14	13.1	0.12
	13	10	5.8	0.20
	18	6	4.5	0.15
	19	4	5.3	0.24
	9	4	5.4	0.53
	6	3	8.6	0.27
	14	2	3.9	0.05
	8	2	5.7	0.22
	4	2	3.8	0.52
	7	1	3.5	0.24
	5	1	2.8	0.25
	17	1	2.8	0.38
	12	< 1	1.0	0.21
	11	< 1	1.4	0.29
	10	< 1	1.5	0.17
	15	< 1	0.8	0.25
	16	< 1	2.0	0.06

slip model	segment number	potency (%)	max. slip (m)	JS divergence
Hamling-Kb	1	17	24.0	0.04
	3	17	18.5	0.08
	2	13	24.1	0.29
	13	13	7.1	0.14
	0	12	12.8	0.11
	6	7	8.8	0.22
	18	5	5.3	0.22
	4	3	6.5	0.64
	9	3	4.9	0.57
	17	2	2.3	0.18
	8	2	5.5	0.19
	5	2	2.4	0.23
	7	1	3.5	0.36
	14	1	3.5	0.09
	15	1	2.8	0.43
	11	< 1	1.1	0.29
	10	< 1	1.5	0.13
	12	< 1	0.8	0.21
	16	< 1	1.6	0.02

slip model	segment number	potency (%)	max. slip (m)	JS divergence
Clark/Holden-K	3	15	14.7	0.21
	2	11	21.8	0.30
	20	9	2.0	0.06
	0	9	11.5	0.16
	1	7	21.9	0.17
	14	7	2.9	0.19
	13	7	6.5	0.17
	21	6	8.2	0.15
	19	6	4.9	0.26
	9	4	5.4	0.52
	23	3	10.7	0.57
	22	2	10.1.	0.24
	4	2.	2.9	0.44
	6	2	7.1	0.29
	8	2	5.8	0.25
	7	1	3.5	0.22
	5	1	3.1	0.28
	24	1	9.1	0.21
	15	1	3.6	0.16
	16	1	1.4.	0.41
	10	< 1	1.6	0.11
	11	< 1	1.3	0.27
	17	< 1	1.6	0.13
	18	< 1	2.1	0.03
	12	< 1	0.9	0.18

slip model	segment number	potency (%)	max. slip (m)	JS divergence
Holden-K	5	64	24.8	0.49
	0	18	3.0	0.12
	1	9	5.2	0.48
	6	3	10.1	0.64
	4	2	2.0	0.64
	3	2	4.7	0.23
	2	2	8.8	0.18
Wang-K	11	38	14.2	0.04
	10	11	14.2	0.25
	8	11	12.5	0.50
	7	11	12.5	0.26
	0	7	8.3	0.17
	9	5	7.5	0.23
	6	4	10.5	0.08
	4	4	5.5	0.02
	1	3	6.2	0.02
	3	2	3.8	0.57
	2	2	3.8	0.54
	5	1	4.1	0.46

slip model	segment number	potency (%)	max. slip (m)	JS divergence
Xu-Ka	0	66	18.4	0.08
	1	18	16.2	0.07
	2	7	7	0.07
	3	5	12.0	0.05
	4	4	9.0	0.49
	5	< 1	3.0	0.23
Xu-Kb	0	50	18.6	0.30
	5	24	18.3	0.11
	1	10	17.9	0.04
	2	7	6.5	0.06
	3	5	10.6	0.09
	4	4	10.2	0.62
	6	< 1	2.3	0.20
Xu-Kc	0	60	18.8	0.27
	6	10	11.9	0.40
	1	10	15.5	0.16
	2	8	7.4	0.05
	3	5	10.6	0.07
	4	3	9.0	0.33
	5	< 1	2.3	0.21

2.11.S5 Figures

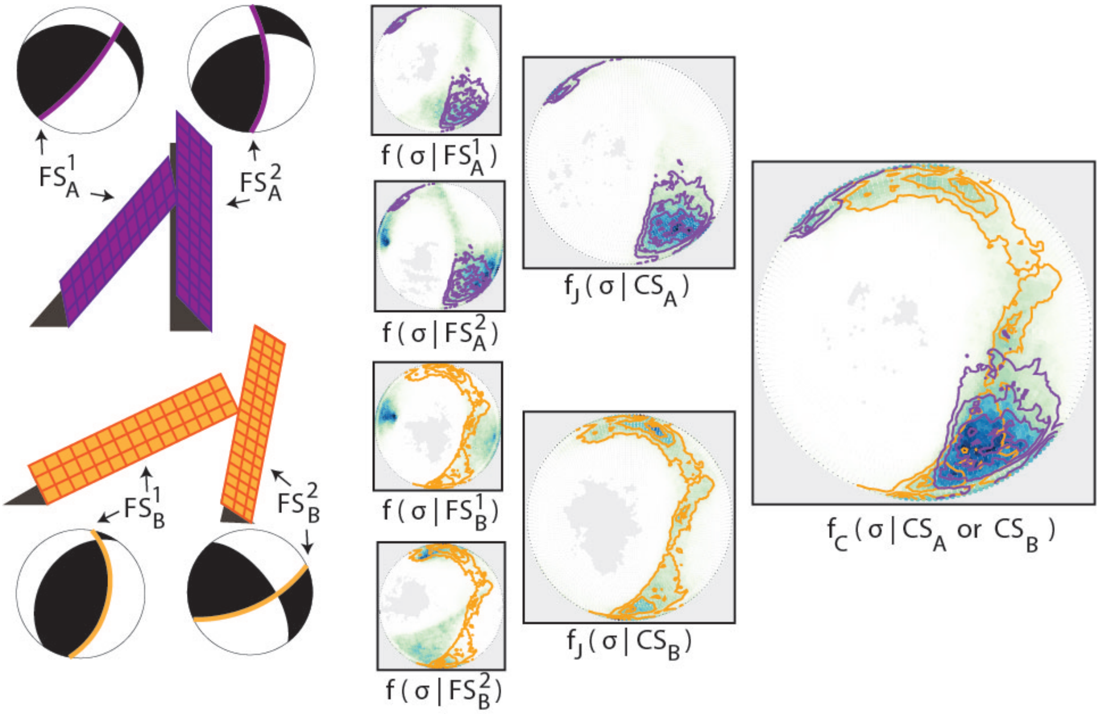

Figure 2.S1: Two synthetic coseismic slip models, CS_A and CS_B, with two fault segments each, FS_X^k with $X = A$ or B, shown as outlined focal mechanism nodal planes and as planar dipping surfaces, along with the associated posteriors of MCS orientation consistent with the fault segments, $f\left(\sigma \left| FS_X^k\right.\right)$ (second from left column), the coseismic slip models, $f_J\left(\sigma \left| CS_X\right.\right)$ (third column), or the NME union composite of both coseismic slip models, $f_C\left(\sigma \left| CS_A \text{ or } CS_B\right.\right)$ (rightmost plot). Likelihood in the posteriors ranges from a white (negligible likelihood) to dark blue (maximum likelihood), and contours are from the joint posteriors.

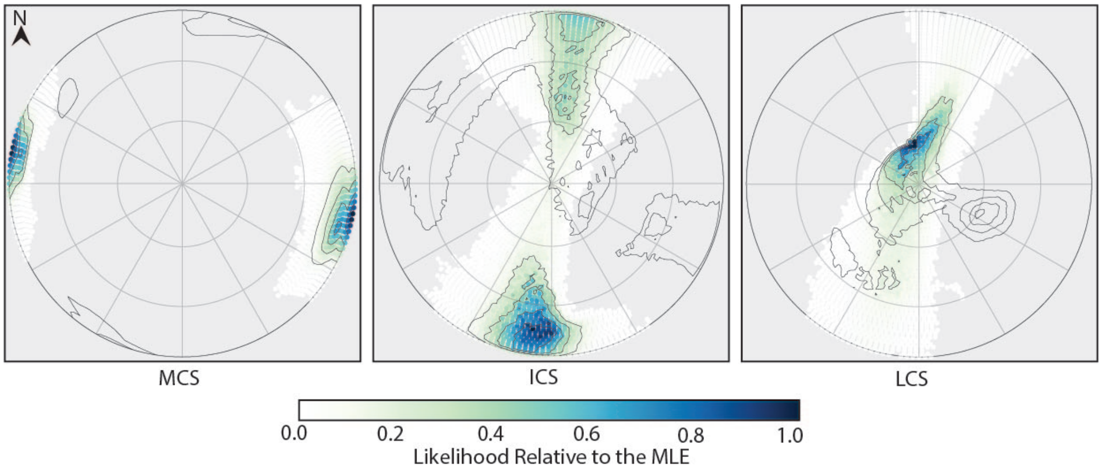

Figure 2.S2: Lambert projection of the lower hemisphere piercing points for the principal components of stress for the Hamling-Ka posterior (Hamling et al., 2017). The relative likelihood of each principal component is represented by a colormap normalized by the likelihood of the most likely estimate. The overlaid contours are the regions of highest likelihood for the Kaikoura composite posterior (Fig. 2.3 in the main text), with intervals of 0.2 of the most likely estimate. Top of the page is oriented towards geographic North (equivalent to a trend of $0°$); grid-lines indicate $30°$ intervals of trend and plunge, where the outermost circle represents a plunge of $0°$ and the center of the circle a plunge of $90°$.

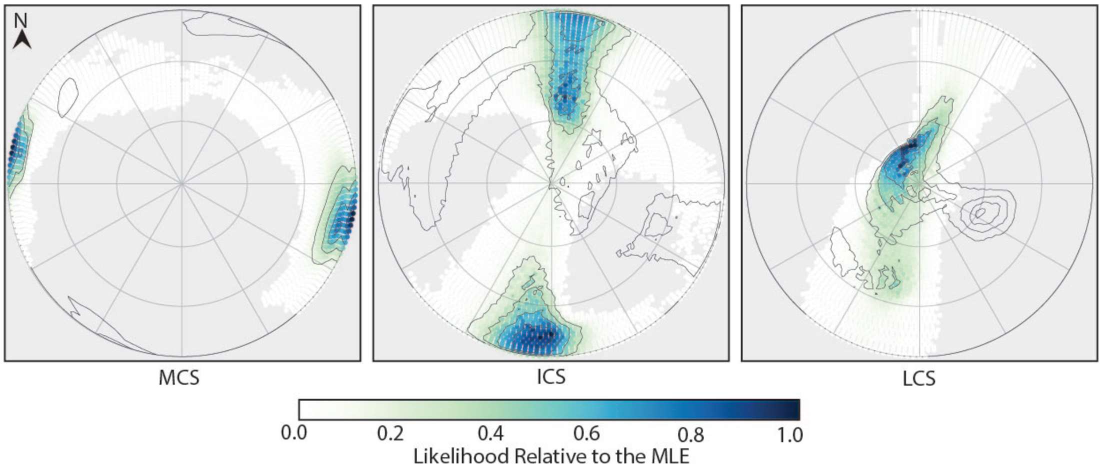

Figure 2.S3: Lambert projection of the lower hemisphere piercing points for the principal components of stress for the Hamling-Kb posterior (Hamling et al., 2017). The relative likelihood of each principal component is represented by a colormap normalized by the likelihood of the most likely estimate. The overlaid contours are the regions of highest likelihood for the Kaikoura composite posterior (Fig. 2.3 in the main text), with intervals of 0.2 of the most likely estimate. Top of the page is oriented towards geographic North (equivalent to a trend of $0°$); grid-lines indicate $30°$ intervals of trend and plunge, where the outermost circle represents a plunge of $0°$ and the center of the circle a plunge of $90°$.

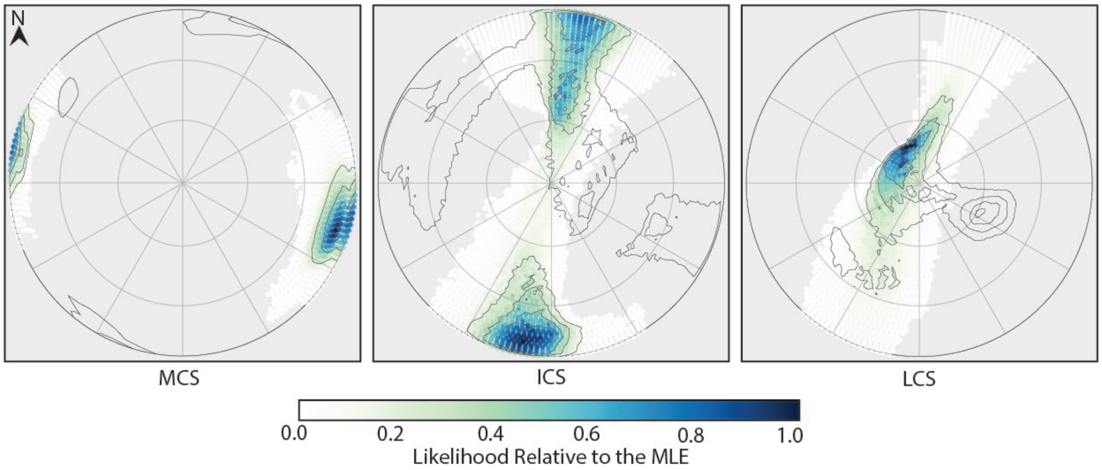

Figure 2.S4: Lambert projection of the lower hemisphere piercing points for the principal components of stress for the Clark/Holden-K posterior (Clark et al., 2017; Holden et al., 2017). The relative likelihood of each principal component is represented by a colormap normalized by the likelihood of the most likely estimate. The overlaid contours are the regions of highest likelihood for the Kaikoura composite posterior (Fig. 2.3 in the main text), with intervals of 0.2 of the most likely estimate. Top of the page is oriented towards geographic North (equivalent to a trend of 0°); grid-lines indicate 30° intervals of trend and plunge, where the outermost circle represents a plunge of 0° and the center of the circle a plunge of 90°.

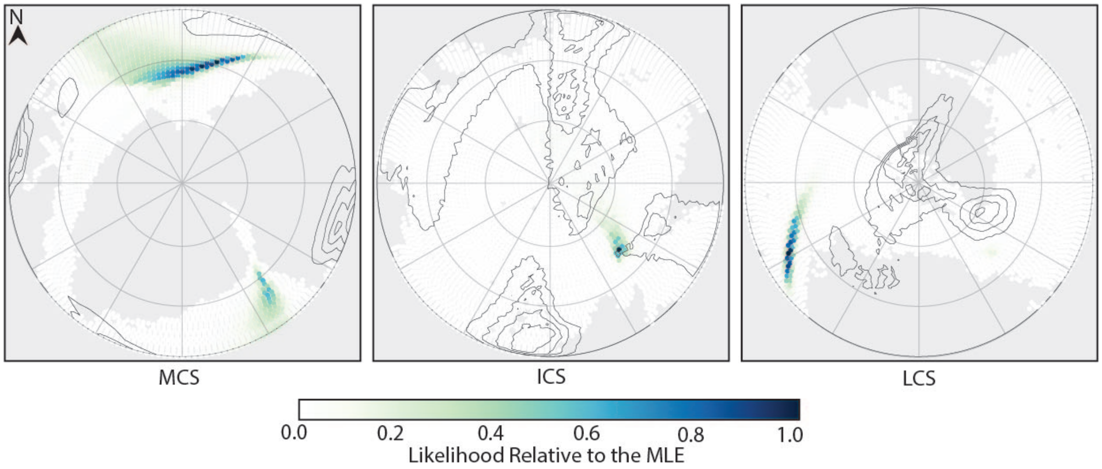

Figure 2.S5: Lambert projection of the lower hemisphere piercing points for the principal components of stress for the Holden-K posterior (Holden et al., 2017). The relative likelihood of each principal component is represented by a colormap normalized by the likelihood of the most likely estimate. The overlaid contours are the regions of highest likelihood for the Kaikoura composite posterior (Fig. 2.3 in the main text), with intervals of 0.2 of the most likely estimate. Top of the page is oriented towards geographic North (equivalent to a trend of 0°); grid-lines indicate 30° intervals of trend and plunge, where the outermost circle represents a plunge of 0° and the center of the circle a plunge of 90°.

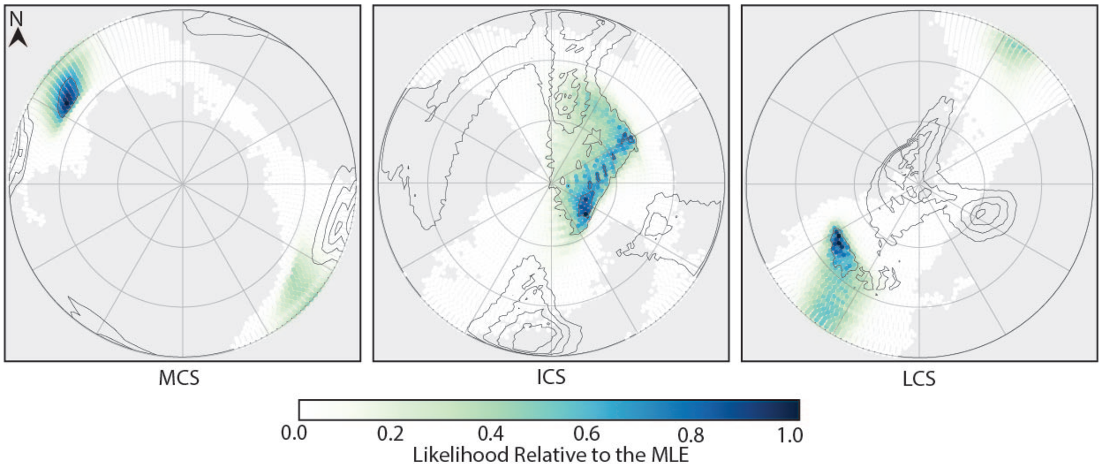

Figure 2.S6: Lambert projection of the lower hemisphere piercing points for the principal components of stress for the Wang-K posterior (Wang et al., 2018). The relative likelihood of each principal component is represented by a colormap normalized by the likelihood of the most likely estimate. The overlaid contours are the regions of highest likelihood for the Kaikoura composite posterior (Fig. 2.3 in the main text), with intervals of 0.2 of the most likely estimate. Top of the page is oriented towards geographic North (equivalent to a trend of 0°); grid-lines indicate 30° intervals of trend and plunge, where the outermost circle represents a plunge of 0° and the center of the circle a plunge of 90°.

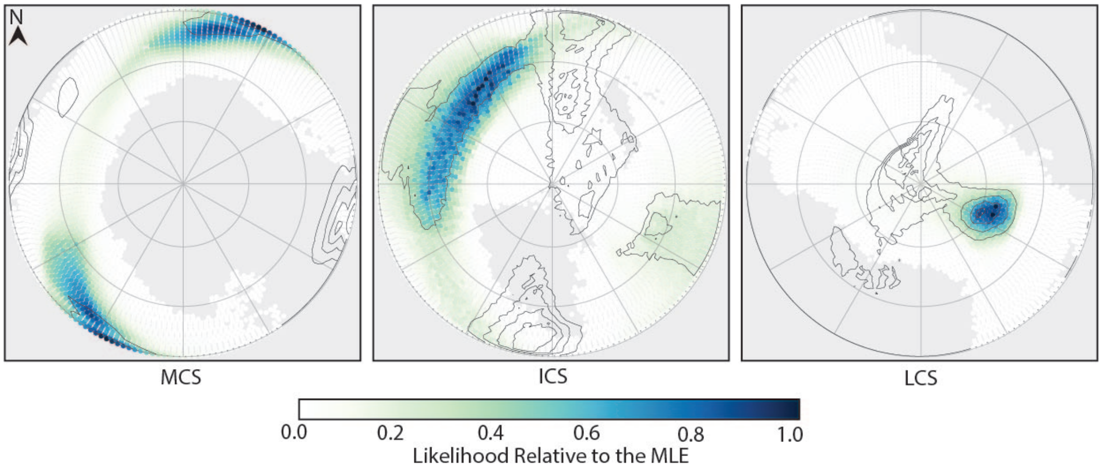

Figure 2.S7: Lambert projection of the lower hemisphere piercing points for the principal components of stress for the Xu-Ka posterior (Xu et al., 2018). The relative likelihood of each principal component is represented by a colormap normalized by the likelihood of the most likely estimate. The overlaid contours are the regions of highest likelihood for the Kaikoura composite posterior (Fig. 2.3 in the main text), with intervals of 0.2 of the most likely estimate. Top of the page is oriented towards geographic North (equivalent to a trend of 0°); grid-lines indicate 30° intervals of trend and plunge, where the outermost circle represents a plunge of 0° and the center of the circle a plunge of 90°.

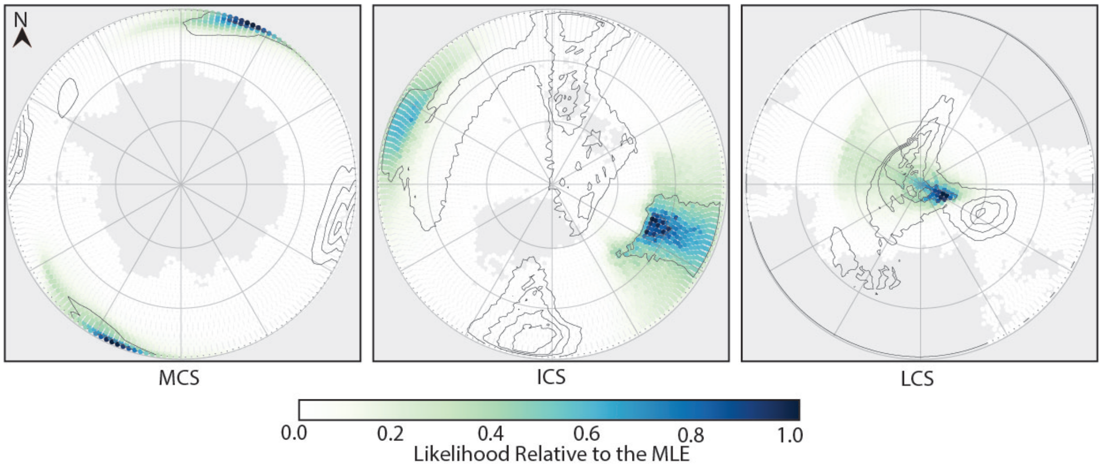

Figure 2.S8: Lambert projection of the lower hemisphere piercing points for the principal components of stress for the Xu-Kb posterior (Xu et al., 2018). The relative likelihood of each principal component is represented by a colormap normalized by the likelihood of the most likely estimate. The overlaid contours are the regions of highest likelihood for the Kaikoura composite posterior (Fig. 2.3 in the main text), with intervals of 0.2 of the most likely estimate. Top of the page is oriented towards geographic North (equivalent to a trend of 0°); grid-lines indicate 30° intervals of trend and plunge, where the outermost circle represents a plunge of 0° and the center of the circle a plunge of 90°.

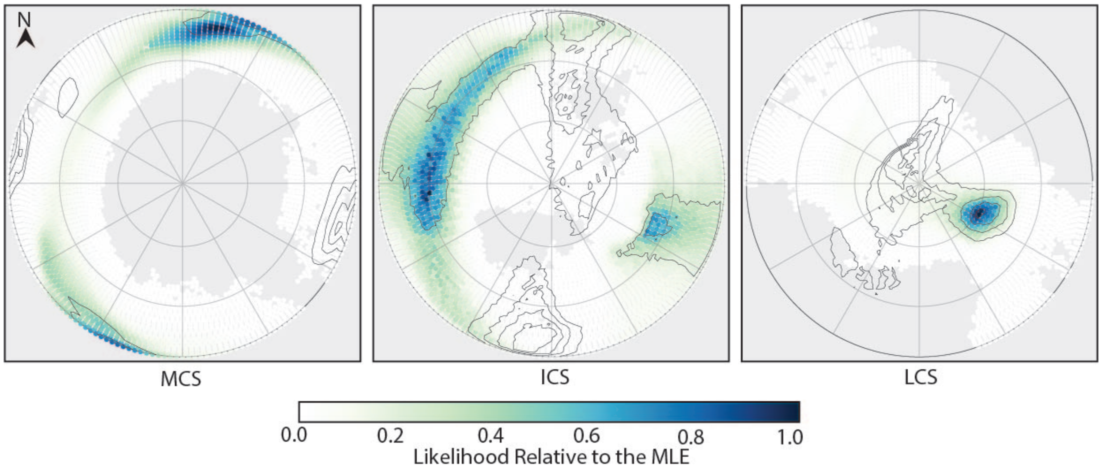

Figure 2.S9: Lambert projection of the lower hemisphere piercing points for the principal components of stress for the Xu-Kc posterior (Xu et al., 2018). The relative likelihood of each principal component is represented by a colormap normalized by the likelihood of the most likely estimate. The overlaid contours are the regions of highest likelihood for the Kaikoura composite posterior (Fig. 2.3 in the main text), with intervals of 0.2 of the most likely estimate. Top of the page is oriented towards geographic North (equivalent to a trend of 0°); grid-lines indicate 30° intervals of trend and plunge, where the outermost circle represents a plunge of 0° and the center of the circle a plunge of 90°.

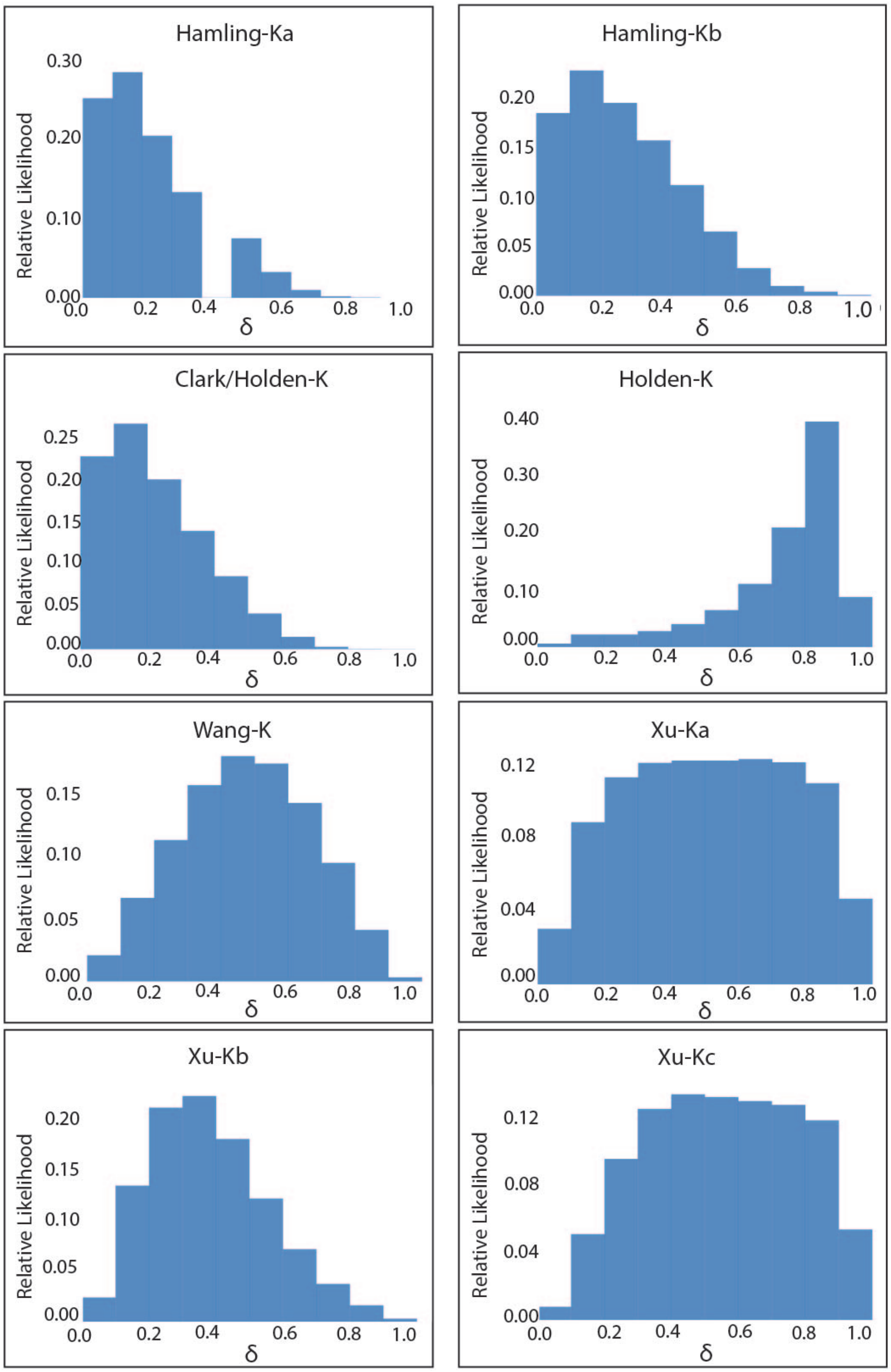

Figure 2.S10: Histograms of δ (*i.e.*, the marginal of δ) for each of the coseismic slip models considered.

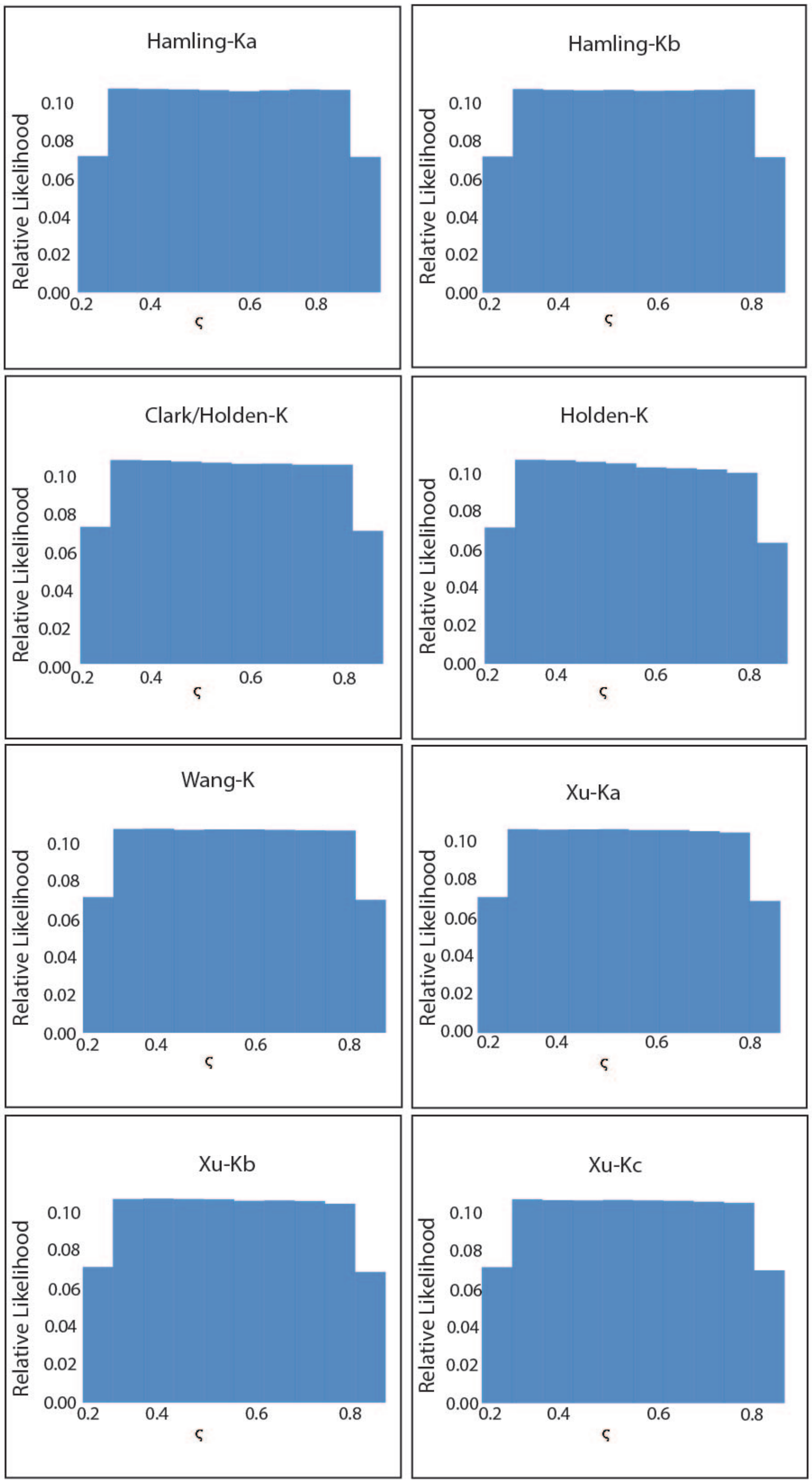

Figure 2.S11: Histograms of ς (*i.e.*, the marginals of ς) for each of the coseismic slip models considered.

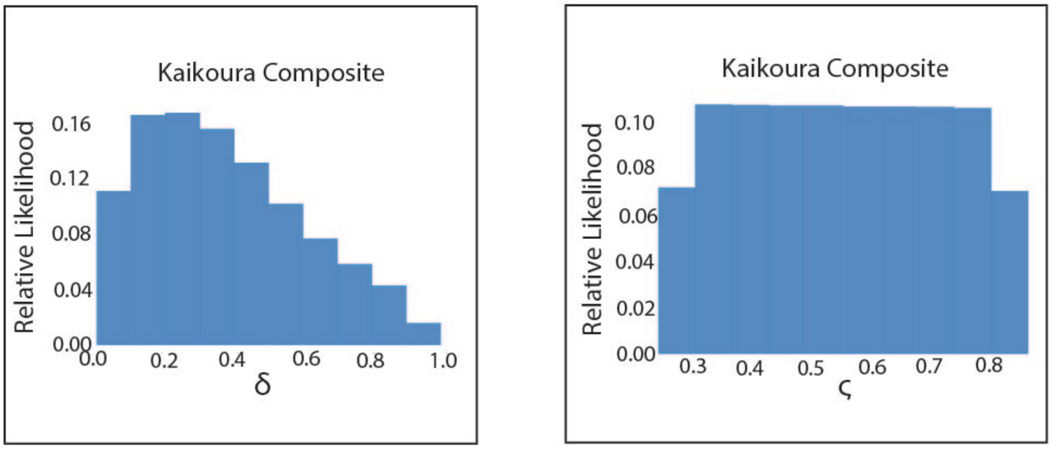

Figure 2.S12: Histograms of δ and ς (*i.e.*, the marginals of δ and ς) for the Kaikoura composite posterior.

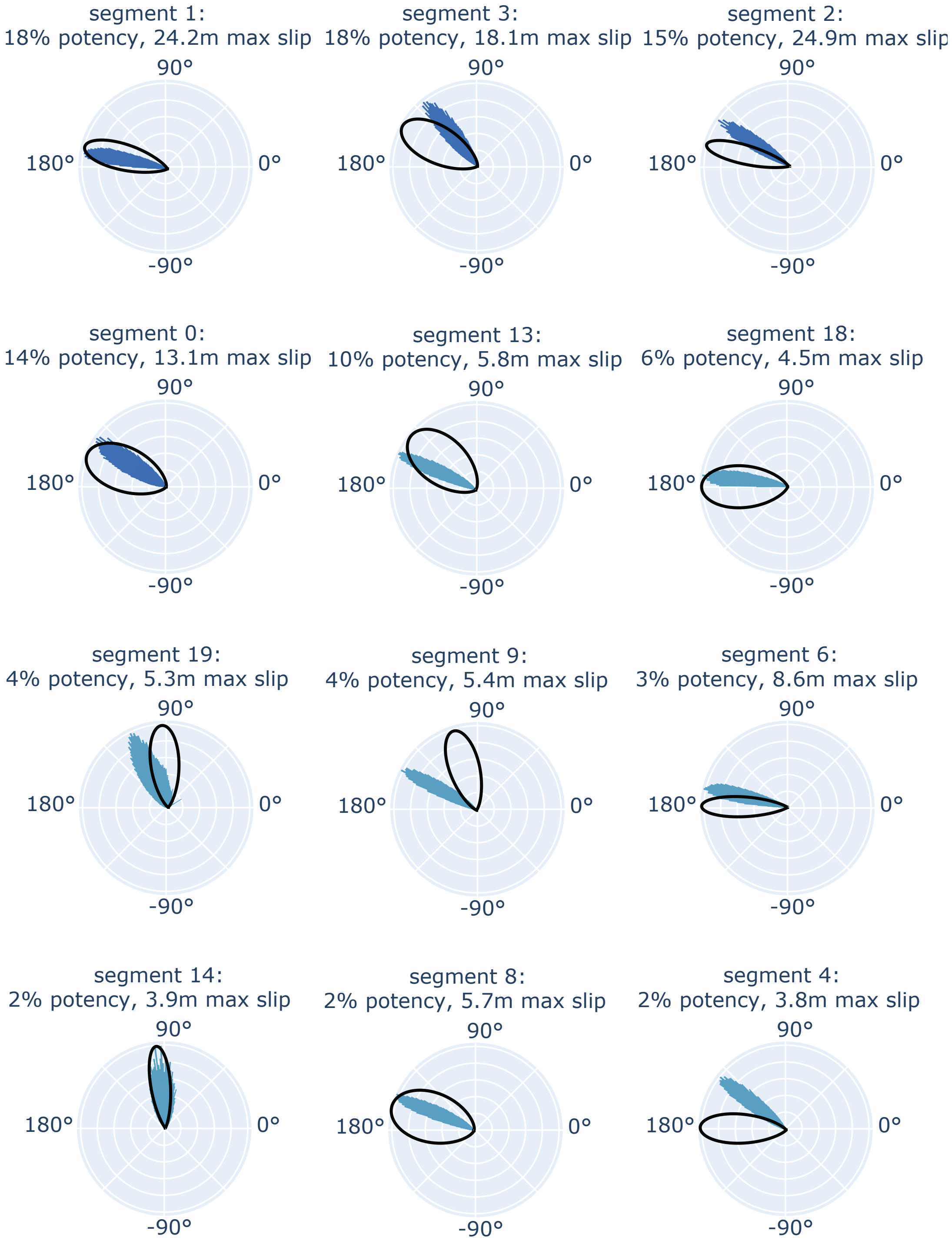

Figure 2.S13: Rose plots of predicted (bars) *vs.* observed (black line) rake for the segments of the Hamling-Ka coseismic slip model (Hamling et al., 2017). The percent potency and maximum slip observed for the segment is given in each rose plot's subtitle. Continues to next page.

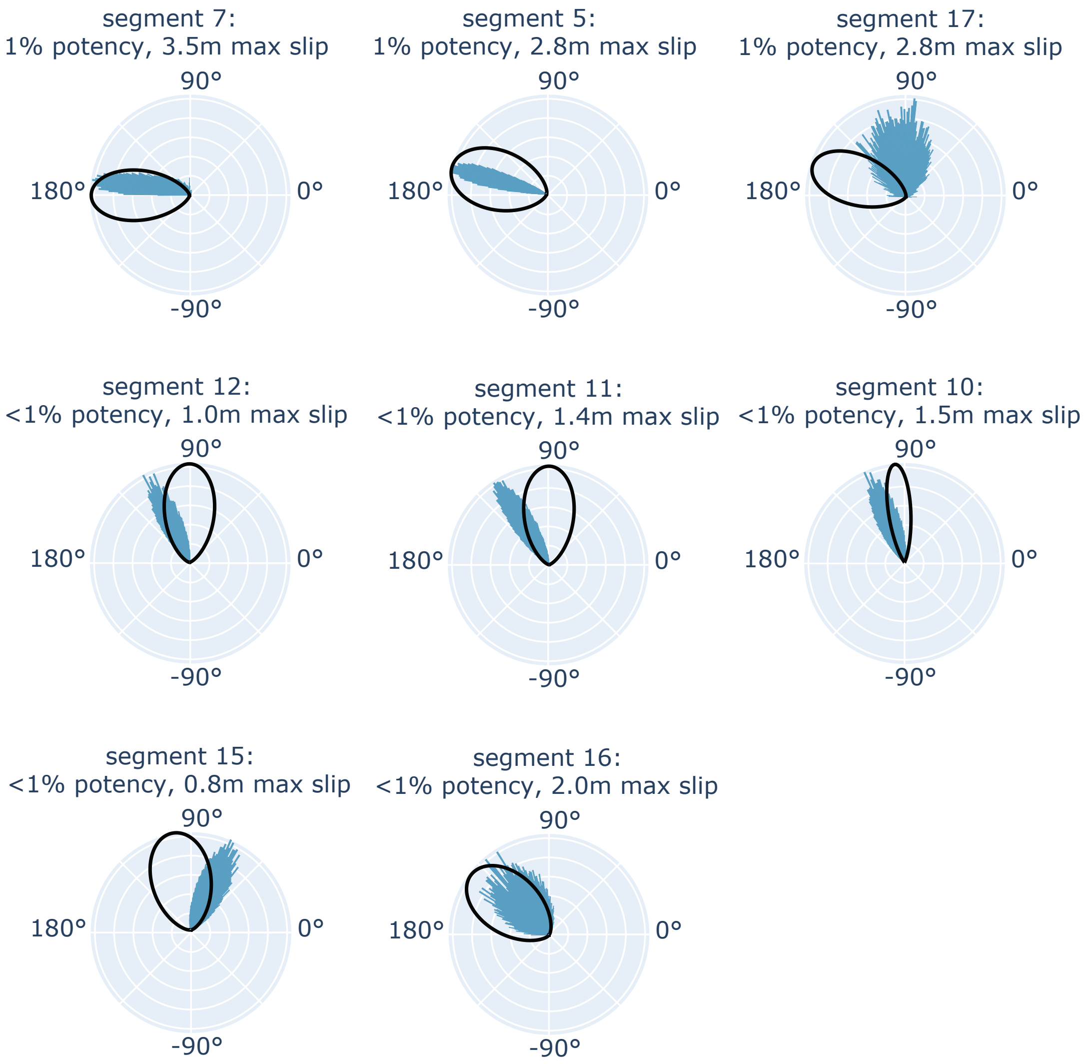

segment 7:
1% potency, 3.5m max slip

segment 5:
1% potency, 2.8m max slip

segment 17:
1% potency, 2.8m max slip

segment 12:
<1% potency, 1.0m max slip

segment 11:
<1% potency, 1.4m max slip

segment 10:
<1% potency, 1.5m max slip

segment 15:
<1% potency, 0.8m max slip

segment 16:
<1% potency, 2.0m max slip

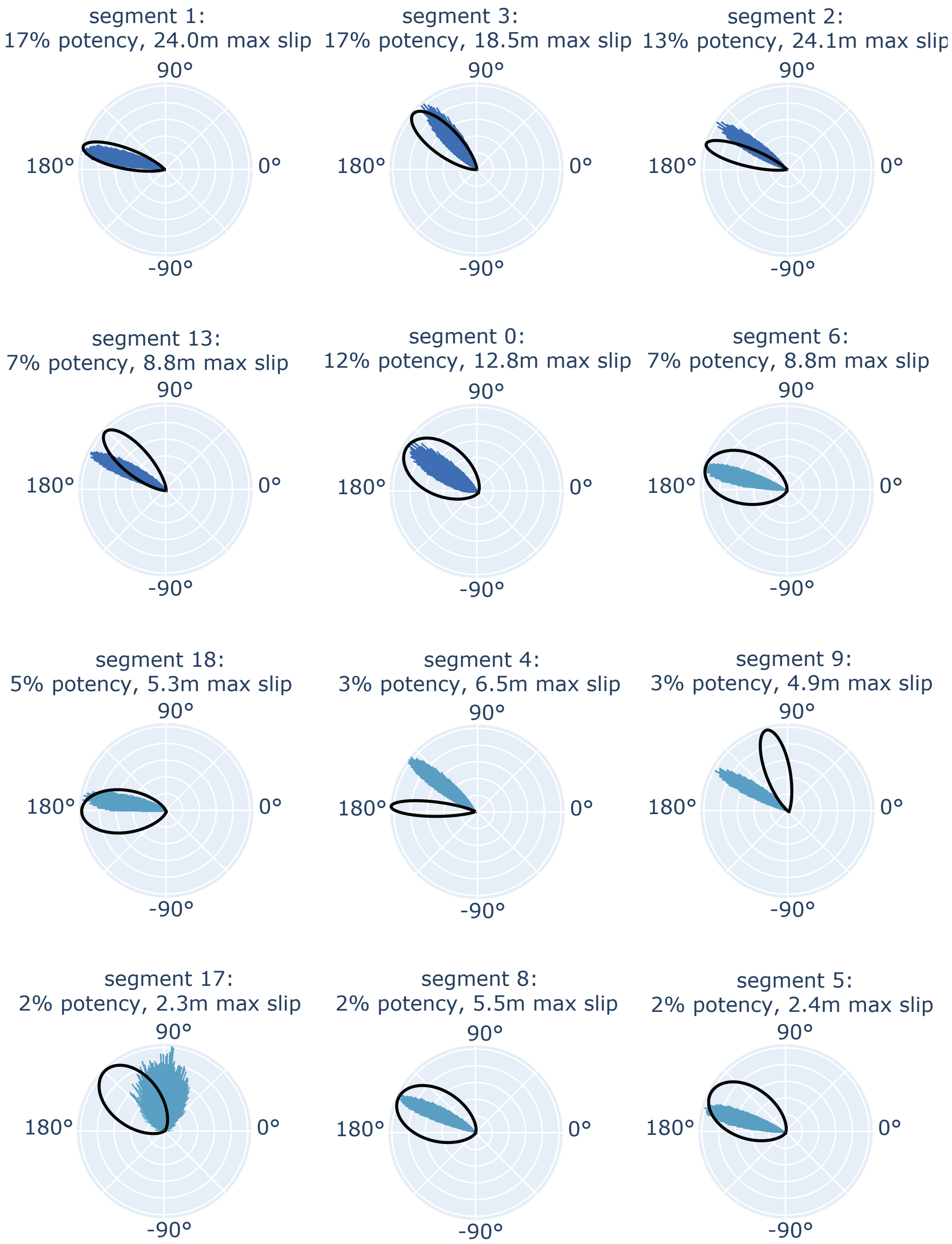

Figure 2.S14: Rose plots of predicted (bars) *vs.* observed (black line) rake for the segments of the Hamling-Kb coseismic slip model (Hamling et al., 2017). The percent potency and maximum slip observed for the segment is given in each rose plot's subtitle. Continues to next page.

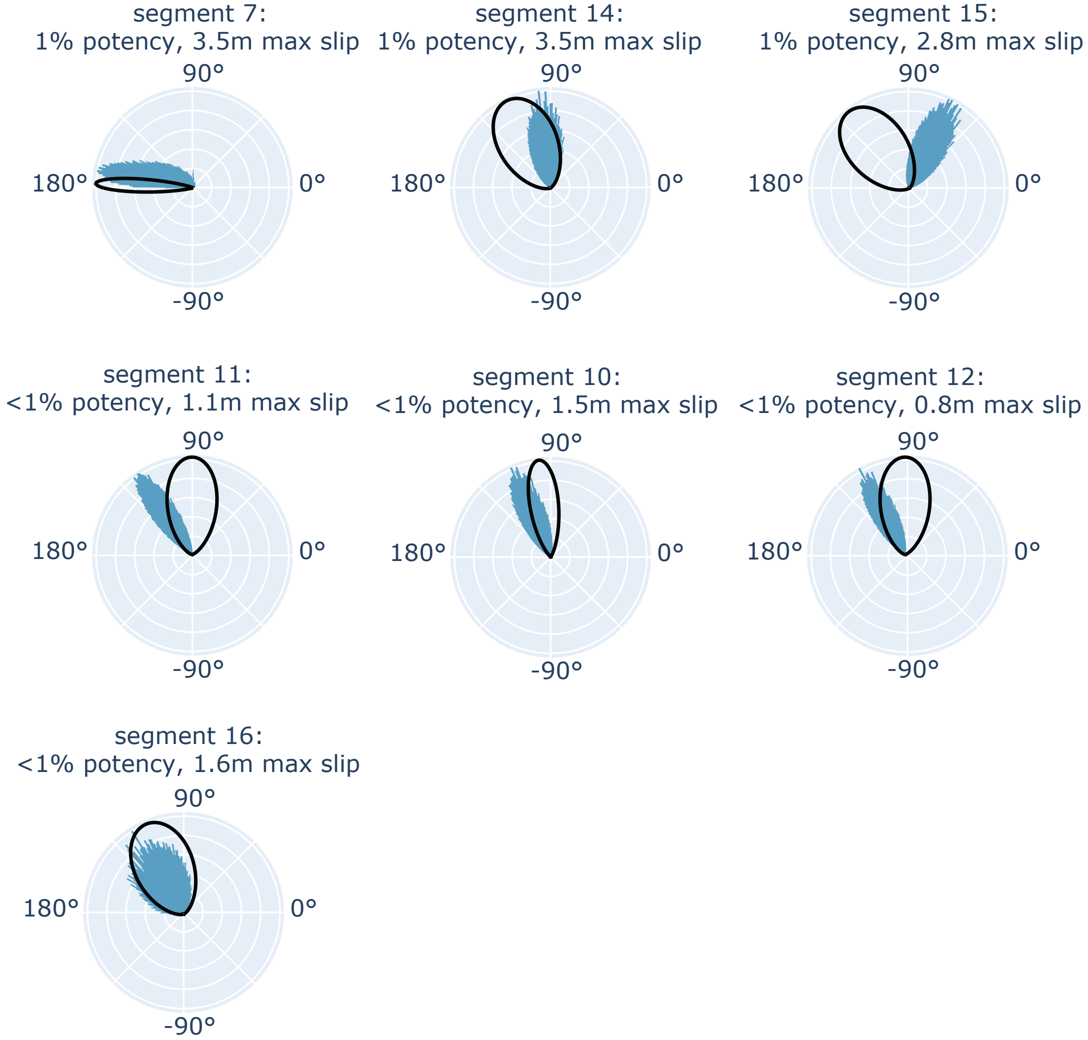
segment 7:
1% potency, 3.5m max slip
segment 14:
1% potency, 3.5m max slip
segment 15:
1% potency, 2.8m max slip
segment 11:
<1% potency, 1.1m max slip
segment 10:
<1% potency, 1.5m max slip
segment 12:
<1% potency, 0.8m max slip
segment 16:
<1% potency, 1.6m max slip
90°
180°
0°
-90°

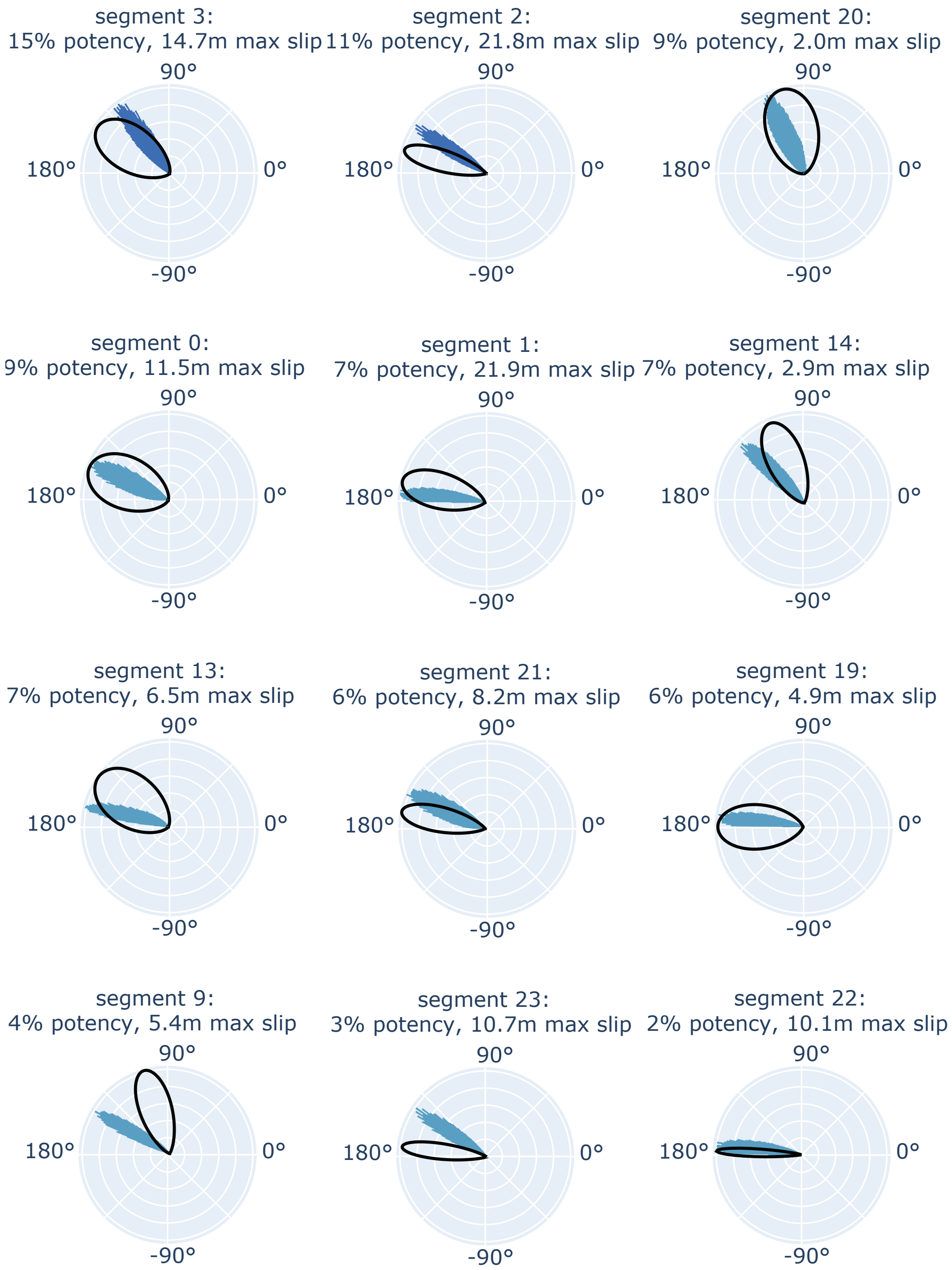

Figure 2.S15: Rose plots of predicted (bars) *vs.* observed (black line) rake for the segments of the Clark/Holden-K coseismic slip model (Clark et al., 2017; Holden et al., 2017). The percent potency and maximum slip observed for the segment is given in each rose plot's subtitle. Continues to next two pages.

segment 4:
2% potency, 2.9m max slip

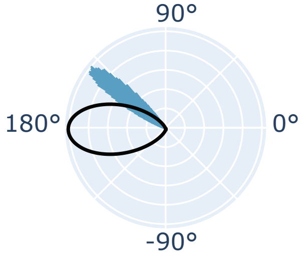

segment 6:
2% potency, 7.1m max slip

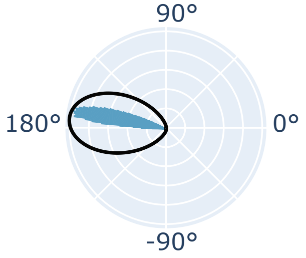

segment 8:
2% potency, 5.8m max slip

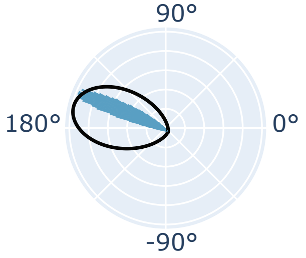

segment 7:
1% potency, 3.5m max slip

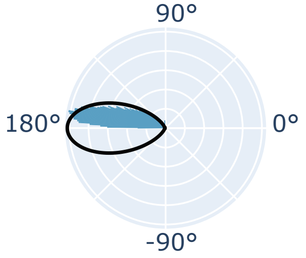

segment 5:
1% potency, 3.1m max slip

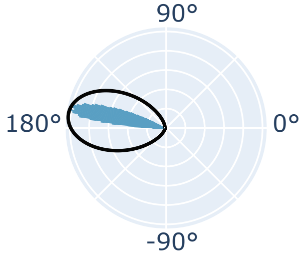

segment 24:
1% potency, 9.1m max slip

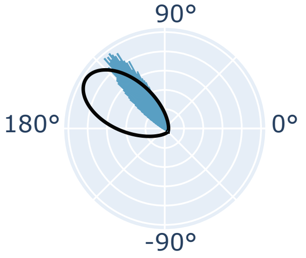

segment 15:
1% potency, 3.6m max slip

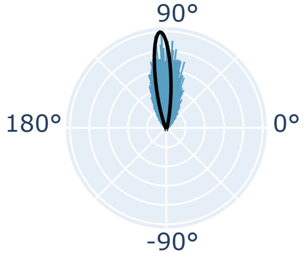

segment 16:
1% potency, 1.4m max slip

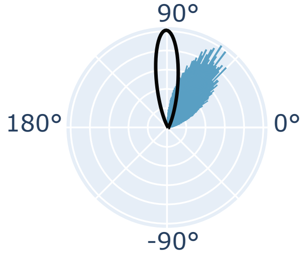

segment 10:
<1% potency, 1.6m max slip

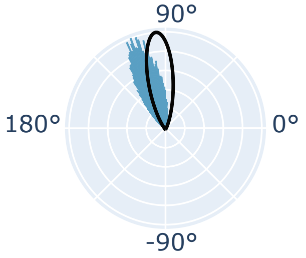

segment 11:
<1% potency, 1.3m max slip

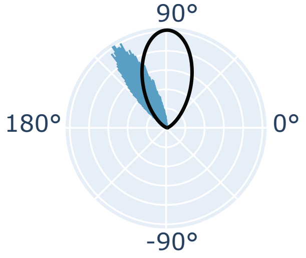

segment 17:
<1% potency, 1.6m max slip

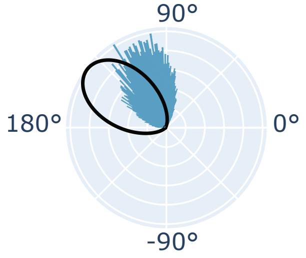

segment 18:
<1% potency, 2.1m max slip

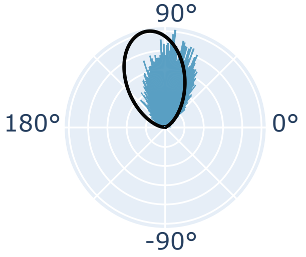

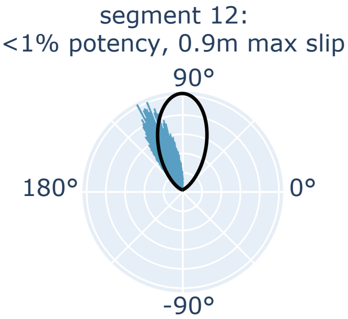
segment 12:
<1% potency, 0.9m max slip
90°
180°
0°
-90°

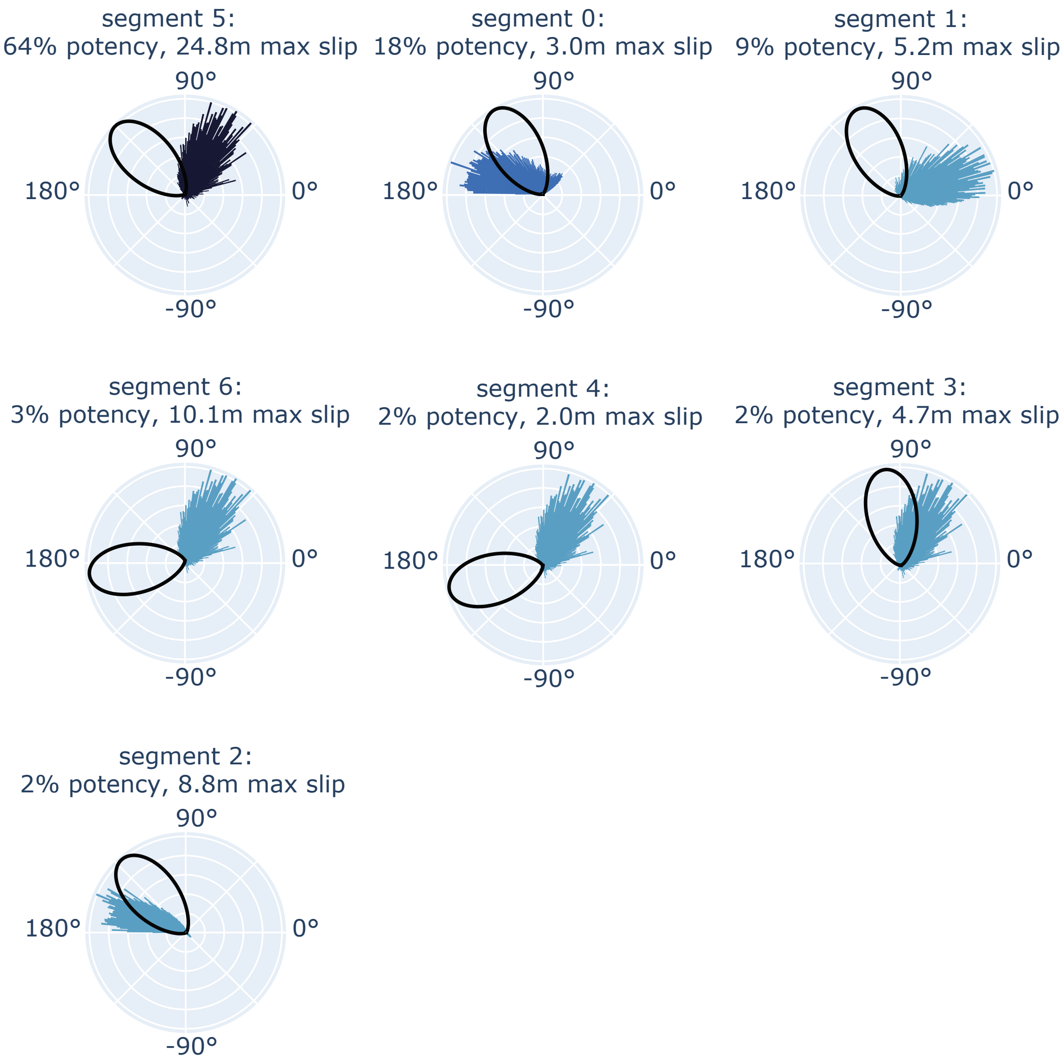

Figure 2.S16: Rose plots of predicted (bars) *vs.* observed (black line) rake for the segments of the Holden-K coseismic slip model (Holden et al., 2017). The percent potency and maximum slip observed for the segment is given in each rose plot's subtitle.

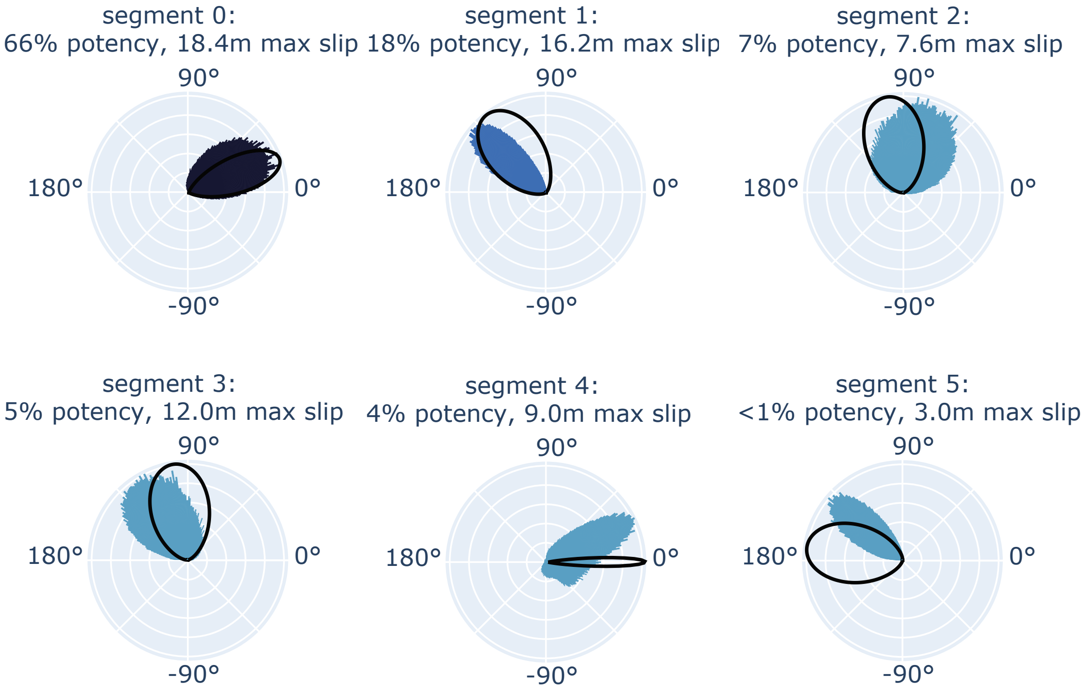

segment 0:
66% potency, 18.4m max slip

segment 1:
18% potency, 16.2m max slip

segment 2:
7% potency, 7.6m max slip

segment 3:
5% potency, 12.0m max slip

segment 4:
4% potency, 9.0m max slip

segment 5:
<1% potency, 3.0m max slip

Figure 2.S17: Rose plots of predicted (bars) *vs.* observed (black line) rake for the segments of the Xu-Ka coseismic slip model (Xu et al., 2018). The percent potency and maximum slip observed for the segment is given in each rose plot's subtitle.

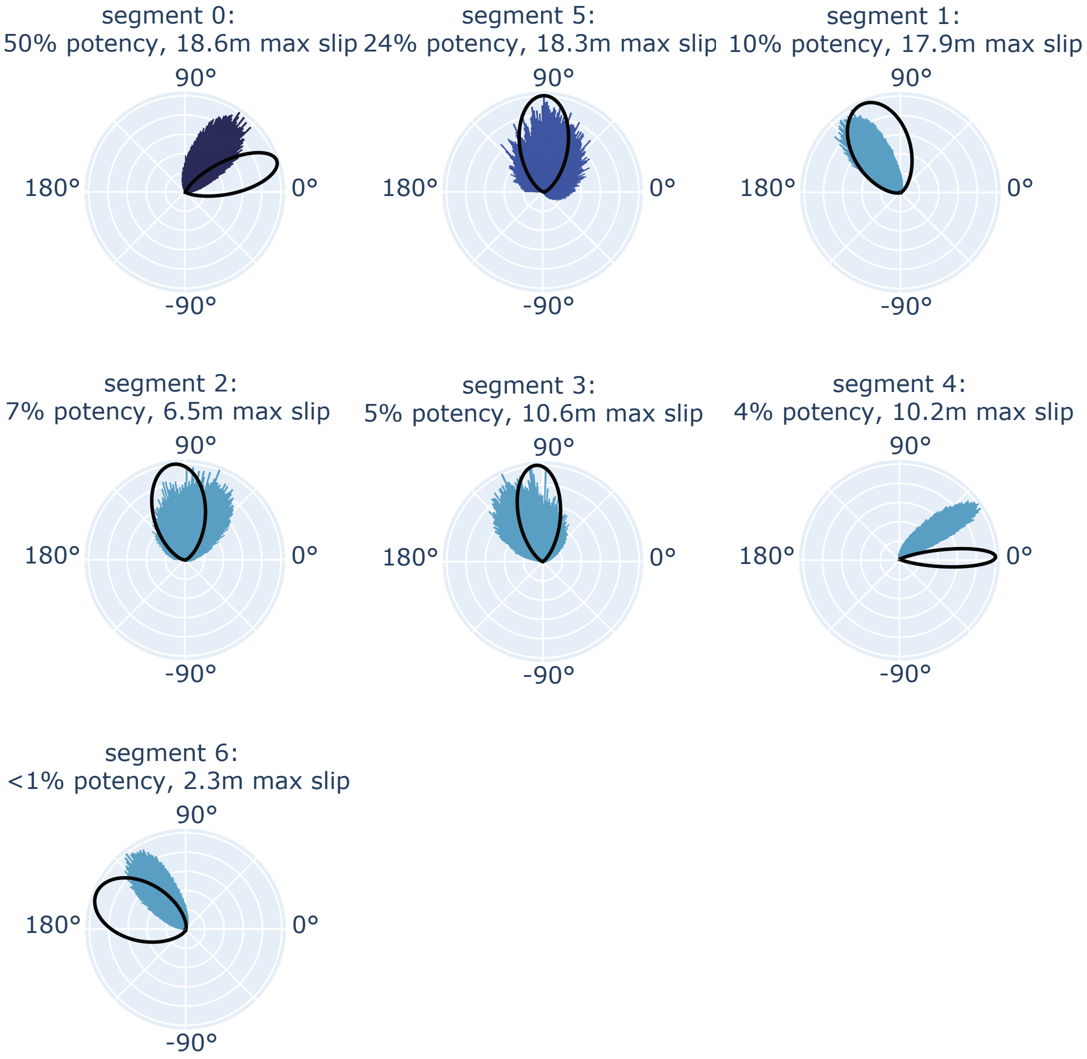

Figure 2.S18: Rose plots of predicted (bars) *vs.* observed (black line) rake for the segments of the Xu-Kb coseismic slip model (Xu et al., 2018). The percent potency and maximum slip observed for the segment is given in each rose plot's subtitle.

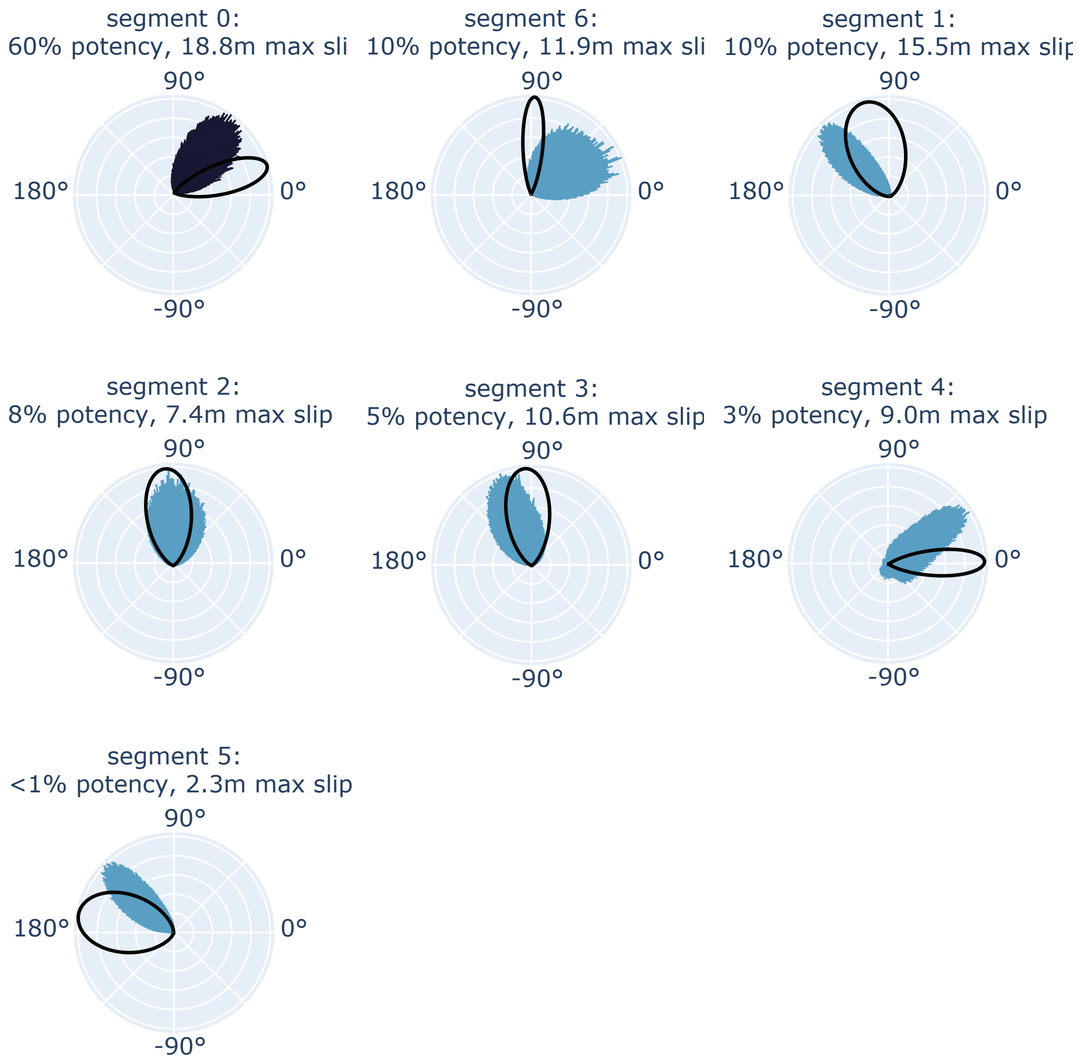

Figure 2.S19: Rose plots of predicted (bars) *vs.* observed (black line) rake for the segments of the Xu-Kc coseismic slip model (Xu et al., 2018). The percent potency and maximum slip observed for the segment is given in each rose plot's subtitle.

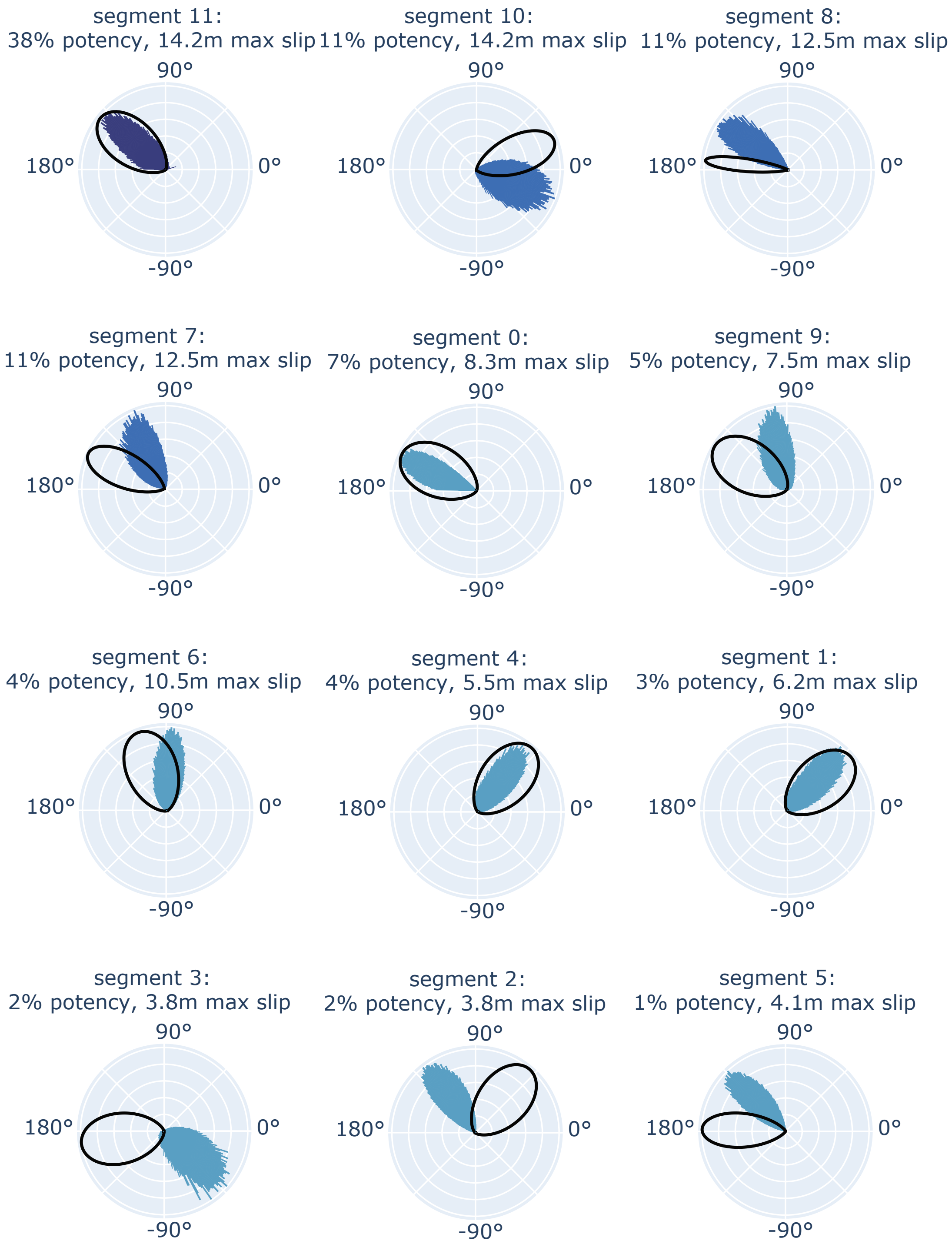

Figure 2.S20: Rose plots of predicted (bars) *vs.* observed (black line) rake for the segments of the Wang-K coseismic slip model (Wang et al., 2018). The percent potency and maximum slip observed for the segment is given in each rose plot's subtitle.

CHAPTER 3

Inferences of Seismogenic Stress for Northeastern South Island, New Zealand [*]

Abstract

The seismogenic tensorial stresses in the crust beneath northern South Island, New Zealand that are responsible for the 2010 $M_w 7.2$ Darfield and 22 February 2011 $M_w 6.2$ Christchurch earthquakes of the Canterbury Plains, South Island, New Zealand are compatible with an Andersonian strike-slip regime with a NW-SE trending most compressive stress. The stresses we infer from coseismic slip models of these two earthquakes are consistent with previous estimates of stress from earthquake focal mechanisms near the Alpine Fault. While the Alpine Fault has been quiescent through the modern seismic record, if the fault were to slip under the modern crustal loading conditions, this stress regime predicts a strong thrust component to the direction of slip. The strike-slip stress regime of the Canterbury Plains differs from the thrust stress regime that we previously estimated from coseismic models of the 2016 $M_w 7.8$ Kaikōura earthquake. We posit a mechanical model and demonstrate that loading due to thick sediment deposits overlying the crust of the Canterbury Plains is a sufficient mechanism for the rotation of the principal stresses between these two regions. Our mechanical model allows for the absolute tectonic stress in the northeast of South Island to constrain a most likely estimate of $\sim$26 MPa.

3.1 Introduction

The tectonics of northeastern South Island, New Zealand are characterized by the convergence of the Pacific and Australian plates, with westward subduction of the Pacific plate

---

[*] Chapter 3 will be submitted to *Journal of Geophysical Research: Solid Earth* as Walbert, O.L. and E. A. Hetland (2023). "Inferences of seismogenic stress for northeastern South Island, New Zealand", J. Geophys. Res.

along the Hikurangi trench in the north and onshore accommodation primarily along the Alpine Fault transpressional plate boundary and the Marlborough Fault System (Fig. 3.1; *e.g.*, *Stirling et al.*, 2012). The majority of significant earthquakes across the South Island in recent history have occurred off of the Alpine Fault, with most seismicity dispersed throughout the northeast and the south of the island. The 2010 $M_w 7.2$ Darfield earthquake occurred to the south of the Marlborough Fault System along previously unmapped faults in the Canterbury Plains (Fig. 3.2; *Quigley et al.*, 2010; *Elliott et al.*, 2012). The Darfield earthquake had four aftershocks over $M_w 5.7$, with the largest being the 22 February 2011 $M_w 6.2$ Christchurch earthquake (Fig. 3.2; *e.g.*, *Kaiser et al.*, 2012; *Quigley et al.*, 2016), hereafter referred to as the Christchurch earthquake. Collectively, the Darfield and the Christchurch earthquakes are commonly referred to as the Canterbury sequence. Both the Darfield and the Christchurch earthquake involved a mixture of reverse and strike-slip fault motion across multiple faults. Field surveys of the surface rupture along the Greendale Fault involved in the Darfield earthquake indicate predominantly right-lateral strike-slip displacements with vertical displacements at major fault bends (*Quigley et al.*, 2010), consistent with geodetic modelling (*Beavan et al.*, 2012; *Elliott et al.*, 2012). Seismic imaging of the Canterbury Plains subsurface suggests that the faults involved in the Darfield earthquake are reactivated normal faults (*e.g.*, *Dorn et al.*, 2010; *Browne et al.*, 2012). No surface ruptures were observed for the Christchurch earthquake (*Sibson et al.*, 2012), and geodetic studies disagree over the fault geometries and the amount of strike-slip motion (*Atzori et al.*, 2012; *Beavan et al.*, 2012; *Elliott et al.*, 2012).

The 2016 $M_w 7.8$ Kaikōura earthquake occurred within the Marlborough Fault System with possible slip along the Hikurangi subduction interface and included surface ruptures with offsets of a half meter or greater along at least twenty faults (*Litchfield et al.*, 2018). Several geodetic studies modeled the earthquake's coseismic slip with varying inferences of slip distributions, faulting mechanisms, slip magnitudes, and fault segment geometries (*e.g.*, *Xu et al.*, 2018). *Walbert and Hetland* (2022), hereafter referred to as WH22, inverted eight coseismic slip models (CSMs) of the Kaikōura earthquake for relative tensorial seismogenic stress. To account for discrepancies between the CSMs, WH22 allowed each CSM to have an equally likely representation of an earthquake's slip by computing a composite stress posterior as the non-mutually exclusive union of each of the CSM posteriors (Fig. 3.1). From long-term observations of kinematics of the Marlborough Fault System, WH22 determined a most likely estimate of a horizontal most compressive stress trending $100°$. WH22 resolved that the stress posterior for the Kaikoura earthquake is consistent with a thrust regime, with little difference in solution inferred from CSMs that included slip along the Hikurangi trench or not.

Several studies have inferred crustal stress in the South Island from earthquake focal mechanism inversions (Fig. 3.1; *Leitner et al.*, 2001; *Balfour et al.*, 2005; *Boese et al.*, 2012; *Townend et al.*, 2012; *Michailos et al.*, 2020). *Townend et al.* (2012) and *Balfour et al.* (2005) determined a strike-slip regime through most of the Marlborough Fault System, with a transition to a thrust regime to the east of the Marlborough Fault System in the Nelson region (*Townend et al.*, 2012), as well as to the north of the Marlborough Fault System in the Wellington region (*Balfour et al.*, 2005). Trends of maximum horizontal stress, S_{Hmax}, estimated by *Townend et al.* (2012) range from N84°E to N121°E for two clusters closest to the Kaikōura centroid location. *Balfour et al.* (2005) found an average S_{Hmax} of N115°E $\pm 16°$ for the Marlborough and Wellington regions. The most compressive stress estimated by WH22 for the Kaikōura earthquake is well within these ranges. *Leitner et al.* (2001), *Boese et al.* (2012), *Townend et al.* (2012), and *Michailos et al.* (2020) resolved near uniform orientations of S_{Hmax} in the central and northern Alpine Fault region (Fig. 3.1), consistent with estimates from *Townend et al.* (2012) for the Canterbury Plains.

In light of these past observations of crustal stress for the South Island, we constrain the tensorial crustal stress responsible for the Canterbury sequence from coseismic slip models of the Darfield and Christchurch earthquakes. We principal components of stress consistent with past studies. Together with the inferences of stress from WH22, our results indicate a transition in seismogenic stress from a thrust regime in the area of the Kaikōura earthquake region to a strike-slip regime in the Canterbury Plains. We demonstrate that this transition can be explained by the sedimentary load overlying the Canterbury Plains, which further allows us to constrain an absolute magnitude of tectonic stress for northern South Island.

3.2 Stress inversions of Canterbury CSMs

We use four CSMs of the Darfield and Christchurch earthquakes sourced from two published studies (Fig. 3.2; *Beavan et al.*, 2012; *Elliott et al.*, 2012) to estimate seismogenic tensorial stress. While additional CSMs were published for these earthquakes (*e.g.*, *Atzori et al.*, 2012), not all publications include complete model data necessary for our inversions. We refer to the CSMs of the Darfield earthquake from *Beavan et al.* (2012) and *Elliott et al.* (2012) as Beavan-D and Elliott-D, respectively. Both studies also included CSMs of the 2011 February 22 Christchurch earthquake, which we refer to as Beavan-C and Elliott-C. While the CSMs of each earthquake share common features, there are dissimilarities in the fault geometries and slip distributions along these faults (Fig. 3.2), likely due to differences in data and choices in regularization methods in imaging of the coseismic slip. For instance, while both studies used InSAR data, *Beavan et al.* (2012) supplemented the

InSAR observations with GPS data, while *Elliott et al.* (2012) used SAR pixel offsets and teleseismic data. We refer readers to these publications for further details on the authors' methodologies.

We use a Bayesian MCMC technique, fully described in WH22, to estimate stress. Our methodology fundamentally follows a long line of methods to estimate stress from earthquake slip data (*e.g.*, *Angelier*, 1979; *Hardebeck and Michael*, 2006; *Arnold and Townend*, 2007; *Medina Luna and Hetland*, 2013; *Styron and Hetland*, 2015). We summarize the salient aspects of WH22 here. Our estimation strategy relies on the Wallace-Bott assumption, after *Wallace* (1951) and *Bott* (1959), that the direction of slip along a fault plane is the direction of maximum shear stress along the fault plane. We describe the tensorial stress by the most compressive stress (MCS), the intermediate compressive stress (ICS), and the least compressive stress (LCS), and denote their magnitudes as σ_1, σ_2, and σ_3 ($\sigma_i < 0 \; \forall \; i$). The maximum shear stress along a fault plane only depends upon the relative magnitudes of stress (*McKenzie*, 1969), and we encapsulate the relative magnitudes as

$$\delta = (\sigma_2 - \sigma_3)/(\sigma_1 - \sigma_3) \tag{3.1}$$

and

$$\varsigma = \sigma_3/\sigma_1. \tag{3.2}$$

The orientations of the principal stresses are captured by three basis-spanning Euler angles, ϕ, θ, and ρ, describing the trend of MCS, dip of MCS, and dip of LCS, respectively (see for example Fig. 2.2). The model state m is comprised of these three Euler angles and δ and ς, and is related to the CSMs via Bayes theorem as

$$f_{\text{post}}\left(m|\lambda\right) = w L_{\text{obs}}\left(\hat{\lambda}|m,\lambda\right) f_{\text{prior}}\left(m\right), \tag{3.3}$$

where f_{post} is the posterior probability density function (PDF) that we seek to estimate, $\hat{\lambda}$ is the predicted rake (*i.e.*, the direction of maximum shear stress projected into the coseismic slip model fault segments from m according to the Wallace-Bott assumption), λ is the observed rake from the CSM, w is a normalization factor, L_{obs} is a likelihood function, and f_{prior} is the prior PDF. The prior PDF can be considered as knowledge of m independent from λ. We are interested in considering all physical possibilities of m, so we define a nearly non-informative prior as a 3-sphere of the Euler angles and the Cartesian plane of $0 \leq \delta \leq 1$ and $0.21 \leq \varsigma \leq 0.89$ (the lower and upper bounds of ς correspond to coefficients of friction of 0.85 and 0.06, respectively). L_{obs} compares the angular distance between λ to $\hat{\lambda}$ in an L2-sense with uncertainties quantified for λ and for uncertain fault segment geometries that propagate errors through the calculation of $\hat{\lambda}$.

We first determine posterior PDFs from each of the CSMs. Second, we compute a non-mutually exclusive composite posterior (hereafter referred to simply as the composite posterior) of each earthquake as

$$f_C\left(\sigma \,|\, CS_A \text{ or } CS_B\right) = f_A\left(\sigma \,|\, CS_A\right) + f_B\left(\sigma \,|\, CS_B\right) - f_J\left(\sigma \,|\, CS_A \,\&\, CS_B\right), \quad (3.4)$$

where f_A and f_B are the posteriors of CSMs CS_A and CS_B, respectively, and f_J is the joint of f_A and f_B,

$$f_J\left(\sigma \,|\, CS_A \,\&\, CS_B\right) = f\left(\sigma \,|CS_A\right) \cdot f\left(\sigma \,|CS_B\right). \quad (3.5)$$

The composite posterior allows for the earthquake's preceding state of stress to be represented by any or both of the individual stress posteriors determined from the CSMs proposed for each of the earthquakes (*i.e.*, we consider each of the CSMs as being equally likely representations of slip involved during an earthquake). Lastly, we compute a composite PDF of stress consistent with both of the Canterbury earthquakes given by the joint of the composite posteriors of the two Canterbury earthquakes.

3.3 Composite posteriors for the Canterbury Plains

We summarize our results for the composite posteriors of the Darfield and Christchurch earthquakes in Table 3.1 and in Figures 3.3 and 3.4, while the individual posteriors resulting from each of the four CSMs can be found in the Supplemental Material (Fig. 3.S1–3.S4). The marginal PDFs of the trends and plunges of the three principal components of stress are displayed in lower hemisphere Lambert projections. The composite posterior for the Darfield earthquake reveals a near-horizontal, SE-NW trending MCS with a MLE with azimuth 326° and westward plunge of 8° (Table 3.1, Fig. 3.3). LCS trends NE-SW with a MLE azimuth of 53° and plunge of 4°, while ICS is near-vertical with a MLE plunge of 78° (Table 3.1, Fig. 3.3). The marginal for δ favors smaller values with a most likely estimate of 0.1 (Fig. 3.5a), indicating that σ_2 and σ_3 are of similar magnitudes in contrast to a relatively larger MCS (Eq. 3.1). The two posteriors that form the Darfield composite have a high degree of similarity in the principal components of stress orientations (see Figs. 3.S1 and 3.S2 in the Supplemental Material). The Beavan-D posterior favors slightly lower δ values compared to Elliott-D (Fig. 3.S5 in the Supplemental Material).

The Christchurch composite posterior is less well resolved in comparison to the Darfield composite, with broad regions of models with relatively high likelihood (Fig. 3.4, 3.5; Table 3.1). The composite posterior for the Christchurch earthquake possesses a near-horizontal SE-NW trending MCS with MLE azimuth of $343°$ with a shallow plunge of $8°$ (Table 3.1, Fig. 3.4). The Christchurch composite reveals high likelihoods for both ICS and LCS as sub-vertical principal components of stress, with MLE of $292°$ azimuth and $22°$ plunge for ICS and $62°$ azimuth and $60°$ plunge for LCS. Similar to the Darfield composite, the Christchurch composite's δ marginal shows a preference for small values, with a most likely estimate of 0.2 (Fig. 3.5). The individual posteriors that contribute to this composite share similarities that are captured by the composite, such as a near horizontal MCS, moderate-to-steeply plunging ICS, and shallow-to-moderately plunging LCS (*c.f.*, Fig. 3.4, 3.S3, 3.S4). There is a rotation in the MLE between the Beavan-C and Elliott-C posteriors, with Beavan-C preferring a stronger E-W component in the trend to MCS, and a stronger N-S component in the trend of ICS. The LCS of Beavan-C possesses two high likelihood regions, one that provides a near-horizontal, NNE-SSW trend and a second that is an arcuate feature with a moderate, southern plunge (Fig. 3.S3). The Elliott-C posterior possesses strong similarity to the Darfield composite and individual CSM posteriors, with a near-horizontal, NW-SE trending MCS, moderate-to-steeply plunging ICS, and near-horizontal, NE-SW trending LCS (Fig. 3.S4).

As in WH22, we assess the fit of the posterior predicted rake distributions to Gaussian distributions, parameterized by average rake on each fault segment and its uncertainty, using the Jensen-Shannon (JS) divergence. The JS divergence is a symmetric distance between two PDFs, and as a point of reference, a Gaussian PDF that closely approximates a von Mises PDF of an angular variate has a JS divergence of about 0.2 or less (see the Appendix of WH22). For the four Darfield and Christchurch posteriors, we find that fourteen of the twenty fault segments have JS$\leq$0.18, and none have JS$>$0.4 (Table 3.S1). While the measure of misfit shows a divergence of the distribution of rakes predicted by the retained stress models and the observed rake of the CSMs, there are models retained within the stress posterior that are compatible with the CSM observed rake for every fault segment (Fig. 3.S7–3.S10 in the Supplemental Material).

The posterior predictions of rake are consistent with the average rakes on the fifteen fault segments of the two Darfield CSMs (Table 3.S1, Figs. 3.S7–3.S8 in the Supplemental Material). The largest misfit in the Beavan-D model is in the east of the model (segment 6), where the stress models predict a strong thrust component on the segment while the CSM of *Beavan et al.* (2012) estimated right-lateral strike-slip motion (Fig. 3.S7 in the Supplemental Material). The largest misfits in the Elliott-D model are on two segments toward the west of the CSM and one near the center.

The posterior predictions of rake for the five fault segments of the two Christchurch CSMs are compatible with the observed rake as well (Table 3.S1, Figs. 3.S9–3.S10 in the Supplemental Material). The distributions of predicted rakes for all of the segments are broader than the observed rake distributions (Figs. 3.S9–3.S10); increasing the uncertainty on the observed rake in these cases would likely lead to a reduction in the JS divergences for these segments (Table 3.S1). In the Beavan-C posterior, the posterior predicted rakes for segments 2 and 0 are very similar, despite differences in the observed model geometries for these segments.

3.4 Constraints on magnitude of tectonic stress

The composite posterior of the Darfield earthquake is consistent with an Andersonian strike-slip regime (*i.e.*, a stress regime with a vertical ICS and horizontal MCS and LCS). The stress inferred from the Christchurch earthquake is less well constrained. The Elliott-C posterior is more consistent with a strike-slip regime than the Beavan-C posterior, with an MCS close to that of the Darfield composite posterior (*cf.*, Fig. 3.3, 3.S4 in the Supplemental Material). To quantify the similarity between the stress constrained by both of the Canterbury Plains earthquakes, we compute the joint of the Darfield and Christchurch composite posteriors, which we refer to as the Canterbury composite (Fig. 3.6; Table 3.1). The Canterbury composite only includes stresses that are shared by both the Darfield and Christchurch posteriors and assumes that the state of stress does not change substantially following the Darfield earthquake. The Canterbury composite is not substantially different than the Darfield composite, and is consistent with a strike-slip stress regime with a near-horizontal, NW-SE trending MCS with a MLE azimuth of N147° (Table 3.1; *cf.* Figs. 3.3, 3.6). Our motivation to consider a single Canterbury composite follows from *Sibson et al.* (2012), *Holt et al.* (2013), and *Herman et al.* (2014), who found uniform stress orientations across the Canterbury sequence. They inferred S_{Hmax} to be $115^\circ \pm 5^\circ$ (*Sibson et al.*, 2012), $116^\circ \pm 18^\circ$ (*Holt et al.*, 2013), and N120°E (*Herman et al.*, 2014), consistent with the MCS trends we find (Fig. 3.6). Additionally, *Holt et al.* (2013) concluded that stress within the Canterbury Plains was consistent with a strike-slip regime, and *Sibson et al.* (2012) argued for an Andersonian wrench-faulting stress regime (*i.e.*, a vertical ICS and a horizontal LCS of similar magnitude). Not only are the trends of MCS in our Canterbury composite well within the uncertainty ranges from the past inferences of S_{Hmax}, but they are also consistent with S_{Hmax} inferred in the Alpine Fault region — a point we will come back to in subsection 3.5.3 (Fig. 3.6).

In contrast to the strike-slip nature of the Canterbury composite, the composite posterior determined by WH22 for the 2016 $M_w7.8$ Kaikōura earthquake is consistent with an Andersonian thrust regime (*i.e.*, a stress regime with a vertical LCS and horizontal MCS and ICS; Table 3.1). Our Kaikōura stress estimate was based on eight CSMs and is characteristic of the Marlborough Fault System region in the vicinity of the Hikurangi trench, just to the north of the Canterbury Plains (Fig. 3.1). The demarcation between a strike-slip and thrust stress regime depends on whether ICS or LCS is vertical, as both regimes are characterized by a horizontal MCS. Starting from the case of a vertical LCS in the region of the Kaikōura earthquake, either an increase in the vertical load and/or a decrease in loading of the horizontal plane in the crust beneath the Canterbury Plains could result in a vertical ICS, and thus a strike-slip stress regime. Here we show that sedimentary deposits overlying the bedrock of the Canterbury Plains are a sufficient load to result in a vertical ICS in an otherwise thrust regime (Fig. 3.7a). Under the Canterbury Plains, the Permian-Triassic Torlesse Terrane Greywacke bedrock that spans the northeastern South Island is overlain by as much as 2 km of sediments (*e.g.*, *Browne et al.*, 2012). We will demonstrate that the sediment overburden not only load the bedrock vertically, but they also unload in the horizontal plane under the assumption that the bedrock is elastic and laterally confined (Fig. 7a, B. Hager, *pers. communication*).

The vertical stress in the bedrock imparted by the sediment load, $\sigma^{(zz)}_{\text{burial}}$, is given by

$$\sigma^{(zz)}_{\text{burial}} = -\rho_s g h_s, \tag{3.6}$$

where ρ_s is the density of the overlying sediment, g is the gravitational acceleration, and h_s is the thickness of the sediment. We assume that the strain in the bedrock resulting from the sediment overburden, $\varepsilon_{\text{burial}}$, is only non-zero in the vertical component, $\varepsilon^{(zz)}_{\text{burial}} \neq 0$, and that the bedrock is purely elastic, so that

$$\sigma_{ij} = \lambda\delta_{ij}\varepsilon_{kk} + 2\mu\varepsilon_{ij}, \tag{3.7}$$

where λ and μ are the Lamé parameters and δ_{ij} is the Kronecker delta. From Eq. (3.7),

$$\sigma^{(zz)}_{\text{burial}} = (\lambda + 2\mu)\varepsilon^{(zz)}_{\text{burial}}, \tag{3.8}$$

and Eq. (3.6),

$$\varepsilon^{(zz)}_{\text{burial}} = -\frac{1}{(\lambda + 2\mu)}\rho_s g h_s. \tag{3.9}$$

If the sediment overburden does not result in a horizontal expansion of the bedrock, from

Eq. (3.7) we find the horizontal components of σ_{burial} are

$$\sigma^{(xx)}_{\text{burial}} = \sigma^{(yy)}_{\text{burial}} = -\frac{\lambda}{\lambda + 2\mu}\rho_s g h_s = -\frac{\nu}{1-\nu}\rho_s g h_s, \tag{3.10}$$

where $\nu = \lambda/(2\lambda + \mu)$ is the Poisson ratio. The stress tensor in the bedrock due to the sedimentary overburden is then

$$\sigma_{\text{burial}} = -\begin{pmatrix} \frac{\nu}{1-\nu} & 0 & 0 \\ 0 & \frac{\nu}{1-\nu} & 0 \\ 0 & 0 & 1 \end{pmatrix} \rho_s g h_s. \tag{3.11}$$

We next assume that the total stress, σ_{total}, is due to σ_{burial} along with a lithostatic, $\sigma_{\text{lithostatic}}$, and a tectonic, σ_{tectonic}, stress:

$$\sigma_{\text{total}} = \sigma_{\text{burial}} + \sigma_{\text{lithostatic}} + \sigma_{\text{tectonic}}. \tag{3.12}$$

The lithostatic stress at a depth $z_0 > h_s$ and with a bedrock density of ρ_0 is

$$\sigma_{\text{lithostatic}} = -g(\rho_s h_s + (z_0 - h_s)\rho_0)\mathcal{I}, \tag{3.13}$$

where $\mathcal{I}$ is the identity matrix. Using the Kaikōura posterior to motivate our choice of σ_{tectonic}, and ignoring the slight plunges of MCS and ICS in that posterior, we take the tectonic stress to be of the form

$$\sigma_{\text{tectonic}} = -\begin{pmatrix} \phi\tau & 0 & 0 \\ 0 & \tau & 0 \\ 0 & 0 & 0 \end{pmatrix}, \tag{3.14}$$

where $\tau > 0$ is the absolute magnitude of MCS and $\phi\tau$ is the magnitude of ICS ($0 < \phi < 1$). For simplicity in this derivation, we are assuming that the x and y directions correspond to MCS and ICS, respectively. ϕ can be related to the parameters δ (Eq. 4.2) and ς (Eq. 4.3) as

$$\phi = \delta(1 - \varsigma) + \varsigma. \tag{3.15}$$

σ_{tectonic} describes a thrust stress regime, and only adding an isotropic lithostatic stress would not change that — a scenario consistent with the Kaikōura earthquake area. Eqs. (3.11 – 3.14) result in the following non-zero components for σ_{total}:

$$\sigma^{(xx)}_{\text{total}} = -g\left(\rho_s h_s + (z_0 - h_s)\,\rho_0\right) - \phi\tau - \frac{\nu}{1-\nu}\rho_s g h_s, \tag{3.16}$$

$$\sigma_{\text{total}}^{(yy)} = -g\left(\rho_s h_s + (z_0 - h_s)\,\rho_0\right) - \tau - \frac{\nu}{1-\nu}\rho_s g h_s, \tag{3.17}$$

$$\sigma_{\text{total}}^{(zz)} = -g\left(\rho_s h_s + (z_0 - h_s)\,\rho_0\right) - \rho_s g h_s. \tag{3.18}$$

For the stresses in Eqs. (3.16 – 3.18) to describe a strike-slip regime, the components need to satisfy the following constraint:

$$\sigma_{\text{total}}^{(xx)} < \sigma_{\text{total}}^{(zz)} < \sigma_{\text{total}}^{(yy)}, \tag{3.19}$$

corresponding to MCS, ICS, and LCS, respectively. In satisfying Eq. (3.19), we find that the tectonic stress is bounded by

$$(1 - \frac{\nu}{1-\nu})\rho_s g h_s < \tau < \frac{1}{\phi}(1 - \frac{\nu}{1-\nu})\rho_s g h_s. \tag{3.20}$$

For our calculations, we assume a range of sediment densities, ρ_s, between $1750kg/m^3$ and $2500kg/m^3$ based on estimates for sands and gravels with 25-50% porosity. We consider two possible Poisson ratios, $\nu = 0.25$ or $\nu = 0.17$, for a Poisson solid and an empirical value for the Torlesse Terrane Greywacke basement rock (*McNamara et al.*, 2014). We take a range of values for the depth of the sediment overburden from $h_s = 0.5$ km to $h_s = 2$ km (*Browne et al.*, 2012). Using the distribution of δ and ς from the Canterbury composite posterior (Fig. 3.6), we solve for the limits of τ given by Eq. (3.20) (Fig. 3.7a). For $\rho_s = 2200kg/m^3$, and $h_s = 1.5km$, we find that the lower limits of the absolute magnitude of tectonic stress is about 22 MPa for $\nu = 0.25$ and about 26 MPa for $\nu = 0.17$ (Fig. 3.7c). The upper limit on tectonic stress, dependent upon our estimate of ϕ for the Canterbury composite, ranges from 22 – 81 MPa with a MLE of 22 MPa for $\nu = 0.25$ and about 26 – 97 MPa with a MLE of 26 MPa for $\nu = 0.17$ (Fig. 3.7c). We provide additional calculations for additional parameter values in the Supplemental Material (Fig. 3.S12).

3.5 Discussion

In the following subsections, we explore inconsistencies between CSMs by investigating whether including stress inversions from additional CSMs in our composite posteriors would influence the likelihood of our results. We then compare the results of our stress calculations from section 3.4 to previous geophysical studies of the South Island to support our interpretation of regional loading and our constraint on absolute tectonic stress. Finally, we explore the implications of regional stress estimates on the mechanism of slip inferred for the Alpine Fault plate boundary.

3.5.1 Validation of the composite stress posterior

To validate our composite posteriors, we compare forward predictions of rake on the fault segments in the CSMs of *Atzori et al.* (2012). The fault traces of the Darfield CSM in *Atzori et al.* (2012), hereafter referred to as Atzori-D, are similar to both Beavan-D and Elliott-D in the western half of the earthquake, while Atzori-D has similarities only with Elliott-D in the east. We find that the predictions of rake computed from the Darfield composite stress posterior for all eight fault segments of Atzori-D are consistent with the observed slip rakes on those segments. Assuming an uncertainty of 20° on the imaged rake on all the fault segments in Atzori-D (insufficient details are provided by the authors to estimate rake uncertainties as we did for the *Beavan et al.* (2012) and *Elliott et al.* (2012) models). The JS divergence for the eight segments ranges from 0.12 to 0.29 with a median of 0.17, with the largest divergence corresponding to the easternmost segment.

The 2-segment *Atzori et al.* (2012) slip model for the 22 February 2011 Christchurch earthquake, Atzori-C, is most similar in its fault traces to Elliott-C. The rakes on the Atzori-C segments predicted by the Christchurch composite posterior have JS divergences for the two segments of 0.32 and 0.33, again assuming 20° uncertainties of the estimated rakes in Atzori-C. While the divergences for Atzori-C are larger than in the Atzori-D case, they still indicate a general consistency of the predicted rakes with Atzori-C.

There are two ways to view the consistency of our composite posteriors and the Atzori models. If one assumes the Atzori models as independent information, the consistency provides a validation of our composite posteriors — note that owing to shared data, the Atzori models are not entirely independent from the Beavan or Elliott models. Alternatively, the consistency indicates that fully assimilating the Atzori CSMs in our MCMC estimation scheme would not yield additional information on the stress consistent with the earthquakes. Both of these views reflect a compatibility between the Atzori models and the two CSMs of each of the earthquakes that we consider here.

3.5.2 Assessment of the mechanical constraint on tectonic stress

In Section 3.4 we used the transition in inferred stress regimes from the Kaikōura earthquake area to the Canterbury Plains to bound the absolute magnitude of a tectonic stress. While admittedly the argument is simple, the bounds of ~25 MPa to ~65 MPa we infer are consistent with the global model of *Ghosh et al.* (2013), which argued for an average deviatoric stress of 30–70 MPa in the lithosphere. Stresses estimated by *Styron and Hetland* (2015) from coseismic slip models of the 2008 $M_w7.9$ Wenchuan, China earthquake, using topography of the Longmenshan to bound the magnitude of tectonic stress, are notably larger than we infer. They estimated a lower bound of ∼13 MPa/km, which would imply an average stress of ∼130 MPa over a ∼20 km thick crust, although the tectonic setting of the Wenchuan earthquake is different than South Island, New Zealand. More relevant to our study, *Coblentz et al.* (1998) calculated average stresses of ∼20–40 MPa over the plate boundaries of the Indo-Australian Plate. Finally, our inferred stresses are compatible with estimated stress drops of the Darfield (∼6 MPa; *Elliott et al.*, 2012), Christchurch (∼15 MPa; *Elliott et al.*, 2012), and Kaikōura (∼34 MPa; *Xu et al.*, 2018) earthquakes.

Our argument in Section 4 demonstrates that the sedimentary load at the surface is sufficient to cause a strike-slip regime in the Canterbury Plains compared to the thrust regime in the Kaikōura earthquake area. There may be other mechanisms that vertically load the Canterbury Plains relative to the Kaikōura earthquake area, or alternatively vertically unload the Kaikōura earthquake area relative to the Canterbury Plains, potentially providing an explanation for the variation in stress regimes (Fig. 3.S11). For instance, vertical loading south of the Marlborough Fault System might be due to either crustal thickening or underplating. Crustal thickening of central South Island is well documented (*e.g.*, *Kleffmann et al.*, 1998), and potential isostatic adjustment of the thickened crust could result in a vertical loading. Inferences of a strike-slip regime within the Southern Alps (Fig. 3.1; *Leitner et al.*, 2001; *Boese et al.*, 2012; *Townend et al.*, 2012; *Michailos et al.*, 2020), a region where a thick sedimentary load as in our argument cannot be appealed to, might indicate vertical loading resulting from the thickened crust (*e.g.*, *Eberhart-Phillips and Bannister*, 2010). The crustal thickening observed for the Southern Alps winnows towards the Canterbury Plains, lending support for the importance of sedimentary overburden to the observed crustal loading that we model in section 3.4. *Spasojević and Clayton* (2008) argued that oceanic crust has underplated South Island, based on a seismic horizon they identified in the upper mantle. *Spasojević and Clayton* (2008) determined that the horizon was 45.6 ± 2.2 km under the Canterbury Plains, shallower than the 68.7 ± 3.2 km depth near the area of the Kaikōura earthquake, which might indicate a variation of the dynamics of the underplating. The variation in underplating could result in a vertical loading of the crust south of the Marlborough Fault System. *Spasojević and Clayton* (2008) found similar Moho depths in both regions, so if variations in underplating are contributing to crustal stresses, they are not impacting crustal thickening. Alternatively, a de-coupling of the Hikurangi megathrust below the region of the Kaikōura earthquake might lead to vertical unloading of the overriding crust, resulting in a thrust regime for the region of the Kaikōura earthquake in a regional strike-slip regime. However, *Reyners* (1998) argued that the Hikurangi megathrust under the Marlborough Fault System was permanently locked, and hence not accumulating strain, which is consistent with the block models of *Wallace et al.* (2012) where all of the plate motion was accommodated by the Marlborough Fault System.

There are several instances where surficial or near-surface processes have been linked to variations in seismicity. Seismic activity has been correlated with typhoons, or their effects, in Taiwan (*e.g.*, *Zhai et al.*, 2021), for instance through reduction in atmospheric pressure triggering slow earthquakes (*Liu et al.*, 2009) or variations in earthquake statistics due to typhoon-driven erosion (*e.g.*, *Steer et al.*, 2020). *Chang et al.* (2018) determined that aftershocks of the 1999 Mw 7.6 Chi-Chi, Taiwan, earthquake were impacted by the temporary damming of the Chin-shui river. They argued that a point source load at the surface, approximating the weight of the impounded water, was consistent with focal mechanisms of normal and strike-slip aftershocks following the thrust mainshock. While the notion that surface loads can change the stress regime locally is similar to what we propose here, *Chang et al.* (2018) only considered whether a single point load in isolation was favorable to slip on one or both of the resolved nodal planes, via Coulomb stress transfer. As a result, they did not explicitly determine whether the load would change the stress regime from thrust to strke-slip or normal, and hence provided no constraints on tectonic stress.

3.5.3 Implications for slip along the Alpine Fault

We investigate the mechanical compatibility of the principal stresses we infer for our Canterbury composite with the potential mechanism of slip on the modernly quiescent Alpine Fault, particularly given the expectation that the Alpine Fault will likely fail with a large strike-slip component (*e.g.*, *Stirling et al.*, 2012; *Bradley et al.*, 2017). The NW-SE trend of MCS in our Canterbury composite posterior is consistent with estimates of S_{Hmax} on, and proximal to, the Alpine Fault (Fig. 3.6; *Leitner et al.*, 2001; *Boese et al.*, 2012; *Townend et al.*, 2012; *Michailos et al.*, 2020). Both *Boese et al.* (2012) and *Michailos et al.* (2020) concluded that the Alpine Fault is unfavorably oriented for slip in an Andersonian sense due to the high angle between S_{Hmax} and the strike of the fault. The most recent large earthquake on the Alpine Fault was estimated to have occurred in 1748±10 (*Bull*, 1996) and 7–9 m horizontal and 1–2 m vertical offsets were measured from geomorphic markers (*Berryman et al.*, 2012; *De Pascale et al.*, 2014). The large ratio between horizontal and vertical offsets from this historic earthquake motivates the inference that the Alpine Fault is purely strike-slip in the National Seismic Hazard Model (*Stirling et al.*, 2012) and a predominately strike-slip with only minor reverse slip fault motion considered in the Alpine Fault Magnitude 8 Hazard Scenario (average rake of 15° *Bradley et al.*, 2017).

The average strike of the Alpine Fault is N55°E with a dip of 60° to the east (*e.g.*, *Stirling et al.*, 2012). Assuming Mohr-Coulomb fault failure of the Alpine Fault, with coefficients of friction 0.06–0.85, the optimal MCS trend for right lateral strike-slip is between $80°$–$98°$ (Fig. 3.8). A vanishingly small coefficient of friction would be required for the Alpine Fault to slip in a pure strike-slip fashion within the stress field evidenced by estimates from our work and that of others (Fig. 3.6; *Leitner et al.*, 2001; *Boese et al.*, 2012; *Townend et al.*, 2012; *Michailos et al.*, 2020). Inferences of S_{Hmax} are largely consistent across the Canterbury Plain to the Alpine Fault (Fig. 3.8). Thus, arguments appealing to a rotation of stress at the Alpine Fault are unlikely to be applicable here, as have been posited to explain the incompatibility between the orientations of stress away from the San Andreas fault and strike-slip motion on that fault by *Zoback et al.* (1987).

In contrast, the optimal MCS trend for a pure thrust dip-slip faulting mechanism would be normal to the Alpine Fault with an azimuth of $145°$ (Fig. 3.8) and plunge of $17°$ – $36°$ to the east for coefficients of friction between 0.06 and 0.85. The MLE azimuth of MCS is N146°E, only $1°$ off of the normal to the Alpine fault and predicted optimal MCS trend for thrust failure (Fig. 3.8). The most likely plunge of the MCS we resolve, $8°E$, is shallower than the range of plunges expected for pure thrust, however, there are solutions within the MCS of our posterior that possess high likelihoods for plunges as steep as $30°$, well within the range of an optimal thrust MCS (Fig. 3.6, 3.8). Additionally, as the listric nature of the Alpine Fault at depth includes a shallowing of the fault at depth, Mohr-Coulomb failure of the Alpine Fault with a thrust component may be possible under the current stress regime. It would be prudent to consider future mechanisms of slip along the Alpine Fault based on current regional stresses to possess a greater thrust component.

3.6 Conclusions

We infer stress from coseismic slip models of the Darfield earthquake and its largest Christchurch aftershock, and find that the stress preceding these earthquakes is consistent with an Andersonian strike-slip stress regime within the Canterbury Plains. We find that MCS and LCS are near- to sub-horizontal, trending NW-SE and NE-SW, respectively. This strike-slip regime is in contrast to the Andersonian thrust regime we inferred from coseismic slip models of the Kaikōura earthquake in the Marlborough Fault System (WH22). The transition in crustal stress regimes can be explained by a vertical loading of the crust below the Canterbury Plains relative to the Kaikōura earthquake area. We demonstrate that thick sedimentary layers in the Canterbury Plains are mechanically sufficient to rotate a horizontal ICS to vertical, resulting in a strike-slip regime in the Canterbury Plains. In this model, we constrain a most likely estimate on the magnitude of tectonic stress of ∼26 MPa. Finally, the stress we determine from the Canterbury earthquakes is broadly consistent with previous estimates of S_{Hmax} on, and proximal to, the Alpine Fault. Stress estimates from our work and that of previous studies are not consistent with strike-slip motion along the Alpine Fault, and support a stronger thrust component than is often assumed.

3.7 Data and resources

Stress inversion code is available from GitHub and Zenodo (doi: 10.5281/zenodo.6385669). The Supplemental Material includes a table of details of all segments in the coseismic slip models considered, along with figures of the orientations of principal stresses for the posteriors obtained for each of the coseismic slip models, the marginals of δ and ς, and comparisons of the predicted and observed rakes on each segment. Data used in this paper are from published sources listed in the references. Active fault traces in Fig. 3.1 are from *Langridge et al.* (2016). Historical earthquakes in Figs. 3.1–3.2 are for M6+ events queried from the GeoNet catalog (https://quakesearch.geonet.org.nz; last accessed January 2023). Focal mechanisms in Fig. 3.1 are best-fit double couple solutions from the Global Centroid Moment Tensor Project database (last accessed on June 2021). Figs. 3.1–3.4 were made using the Generic Mapping Tools version 6.1.1 (www.generic-mapping-tools.org; *Wessel et al.*, 2019).

3.8 Acknowledgments

This research was funded by NSF grant EAR 1722994 to EAH. Additional funding to OLW to conduct this research was provided by generous alumni donations to the Department of Earth and Environmental Science, University of Michigan. The mechanical stress model we develop here is modified from a demonstration problem in Brad Hager's graduate continuum mechanics course at MIT, EAH is grateful for the opportunity to have studied under his insightful guidance.

3.9 Tables - Chapter 3

Table 3.1: Most likely estimates (MLE) for the trend and plunge of the principal stress directions in the composite posteriors of the Darfield and Christchurch earthquake, the Canterbury composite, and the 2016 $M_w 7.8$ Kaikōura earthquake (WH22).

	Trend/Plunge MLE		
Stress Posterior	MCS	ICS	LCS
Darfield	$326°/8°$W	$14°/78°$W	$53°/4°$W
Christchurch	$343°/8°$W	$292°/22°$W	$62°/60°$W
Canterbury	$147°/8°$E	$5°/78°$W	$54°/10°$W
Kaikōura	$100°/0°$	$184°/12°$S	$350°/72°$N

3.10 Figures - Chapter 3

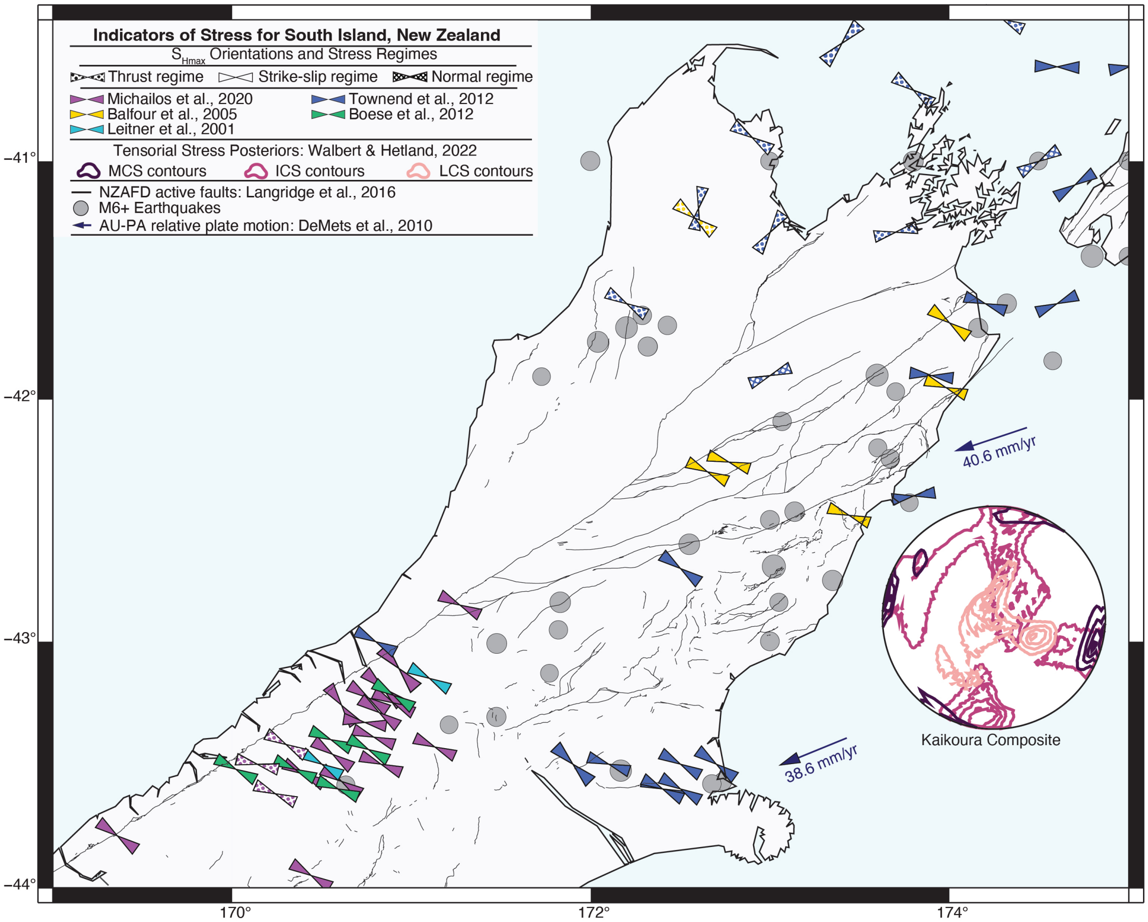

Figure 3.1: Map of northern South Island, New Zealand and previous stress estimates. The orientation of the MLE of S_{Hmax} are indicated by orientation of bow-ties, with inferred stress regimes indicated by the pattern filling the bow-ties (*i.e.,* strike-slip regime refers to a vertical ICS, thrust features a vertical LCS, and normal features a vertical MCS). See legend for color key of study estimates (Leitner *et al.*, 2001; Balfour *et al.*, 2005; Boese *et al.*, 2012; Townend *et al.*, 2012; Michailos *et al.*, 2020). Blue offshore vectors represent orientation and magnitude of Au-Pa relative plate motion at the centroid locations for the 2016 M_w7.8 Kaikōura earthquake and 2010 M_w7.2 Darfield earthquake (DeMets *et al.*, 2010). Magnitude 6+ earthquakes (gray circles; GeoNet catalog) and active faults (thin black lines; Langridge *et al.*, 2016).

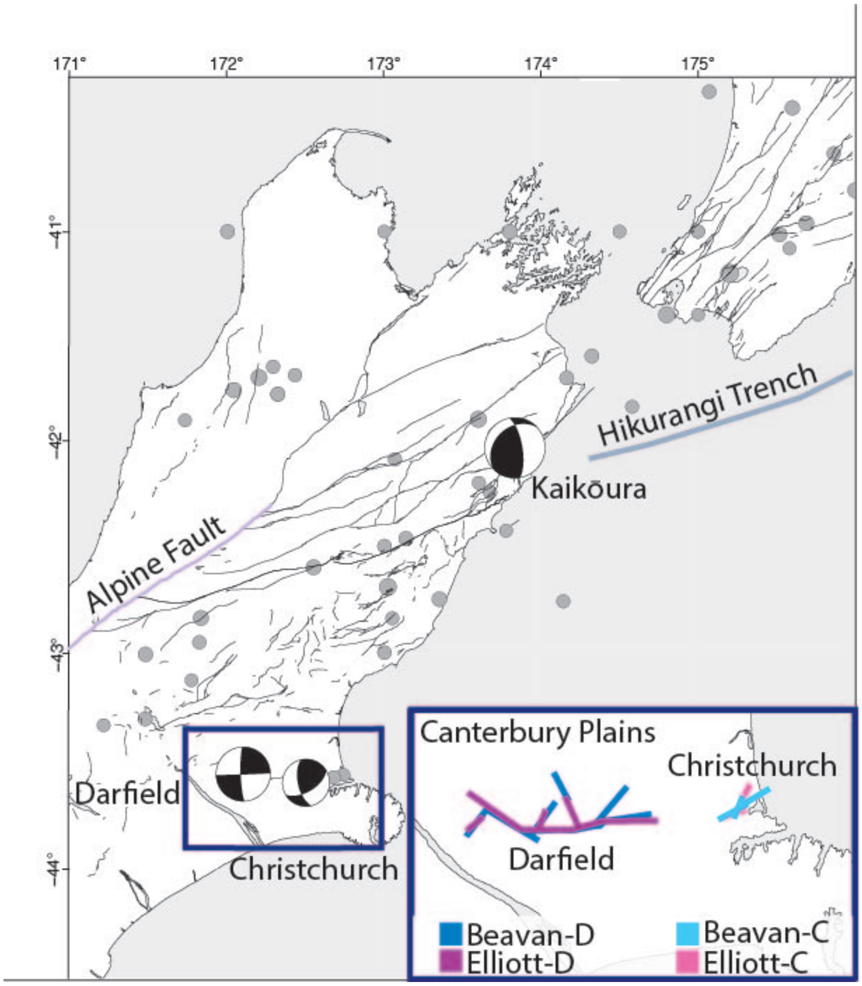

Figure 3.2: Global Centroid Moment Tensor double-couple focal mechanisms of the Darfield, Christchurch, and Kaikōura earthquakes plotted at their centroid location. Insets show the surface traces of the fault segments in the coseismic slip models of Beavan *et al.* (2012; Beavan-D and Beavan-C) and Elliott *et al.* (2012; Beavan-C and Elliott-C). Only segment 2 of Beavan-C is labeled as it is discussed specifically in Sections 3.3 and 3.5.1. Also shown are magnitude 6+ earthquakes (gray circles; GeoNet catalog) and active faults (thin black lines; Langridge *et al.*, 2016).

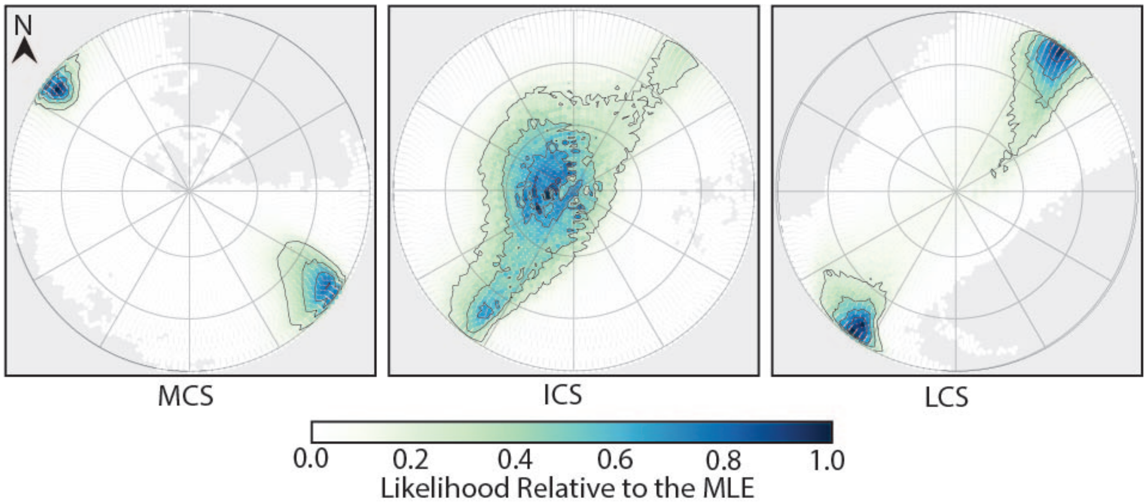

Figure 3.3: Lambert projections of the lower hemisphere piercing points for the non-mutually exclusive union composite posterior determined from the Darfield coseismic slip models. Contours are the regions of highest relative likelihood with intervals of 0.2. Colors are normalized by the maximum likelihood for each component. Top of the page is oriented towards North and grid-lines indicate $30°$ intervals of trend and plunge, where the outermost circle represents a horizontal plunge of $0°$ and the center of the circle a vertical plunge of $90°$.

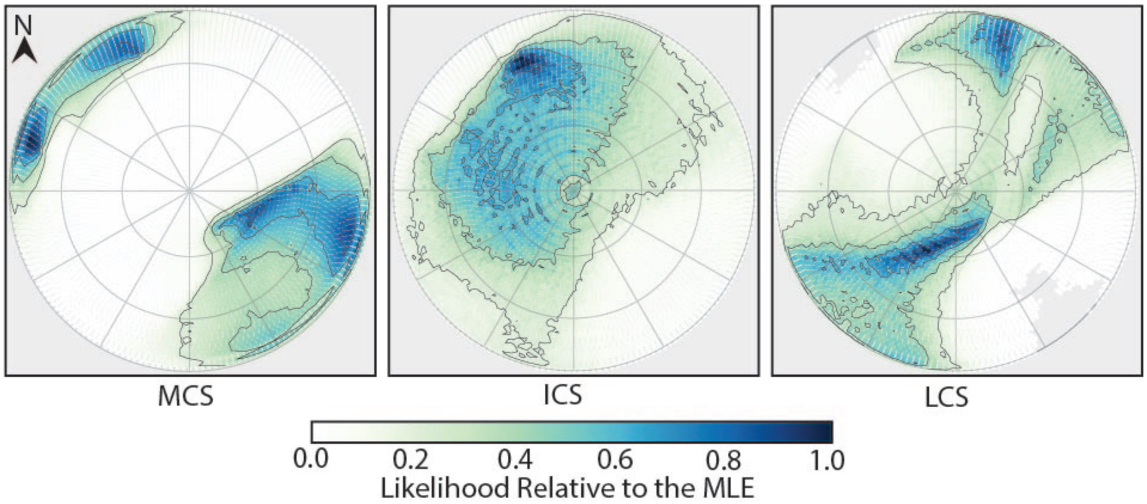

Figure 3.4: Lambert projections of the lower hemisphere piercing points for the non-mutually exclusive union composite posterior determined from the Christchurch coseismic slip models. See caption of Fig. 3.3 for details of the projections.

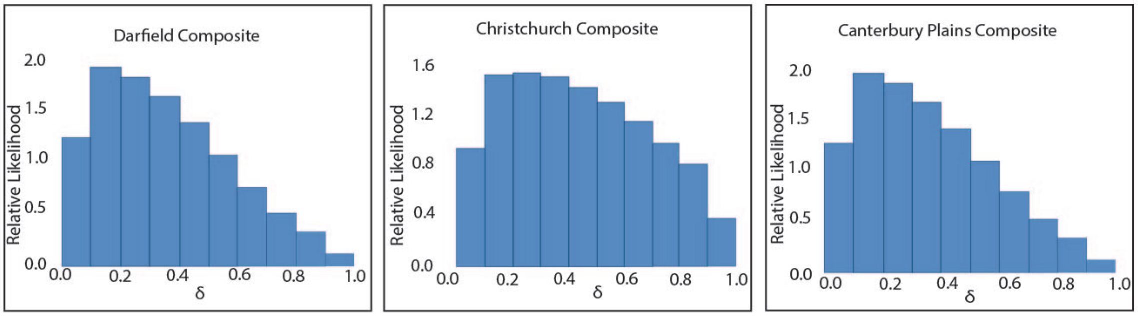

Figure 3.5: Histograms of δ (*i.e.*, the marginals of δ) from the Darfield, Christchurch, and Canterbury composite posteriors.

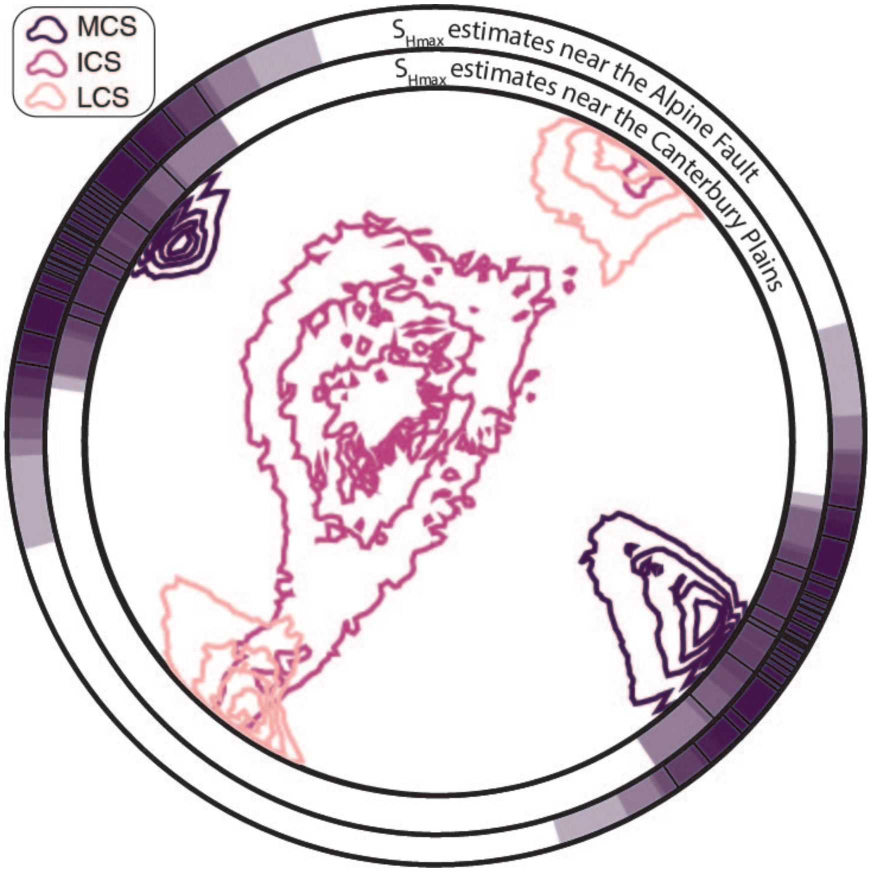

Figure 3.6: The orientations of the principal components of stress for the Canterbury composite posterior displayed in a Lambert projection as contours for the regions of highest relative likelihood with intervals of 0.2 (MCS, ICS, and LCS are shown as dark purple, magenta, and light pink contours, respectively). Two concentric rings bordering the posterior indicate the orientations of S_{Hmax} estimated from previous studies, with the inner ring displaying estimates near the Canterbury Plains (*c.f.*, Fig. 3.1; Townend *et al.*, 2012) and the outer ring with estimates near the Alpine Fault (*c.f.*, Fig. 3.1; Leitner *et al.*, 2001; Boese *et al.*, 2012; Townend *et al.*, 2012; Michailos *et al.*, 2020). The MLE of S_{Hmax} of each estimate is marked as a black tick line, with its uncertainty range depicted by shading.

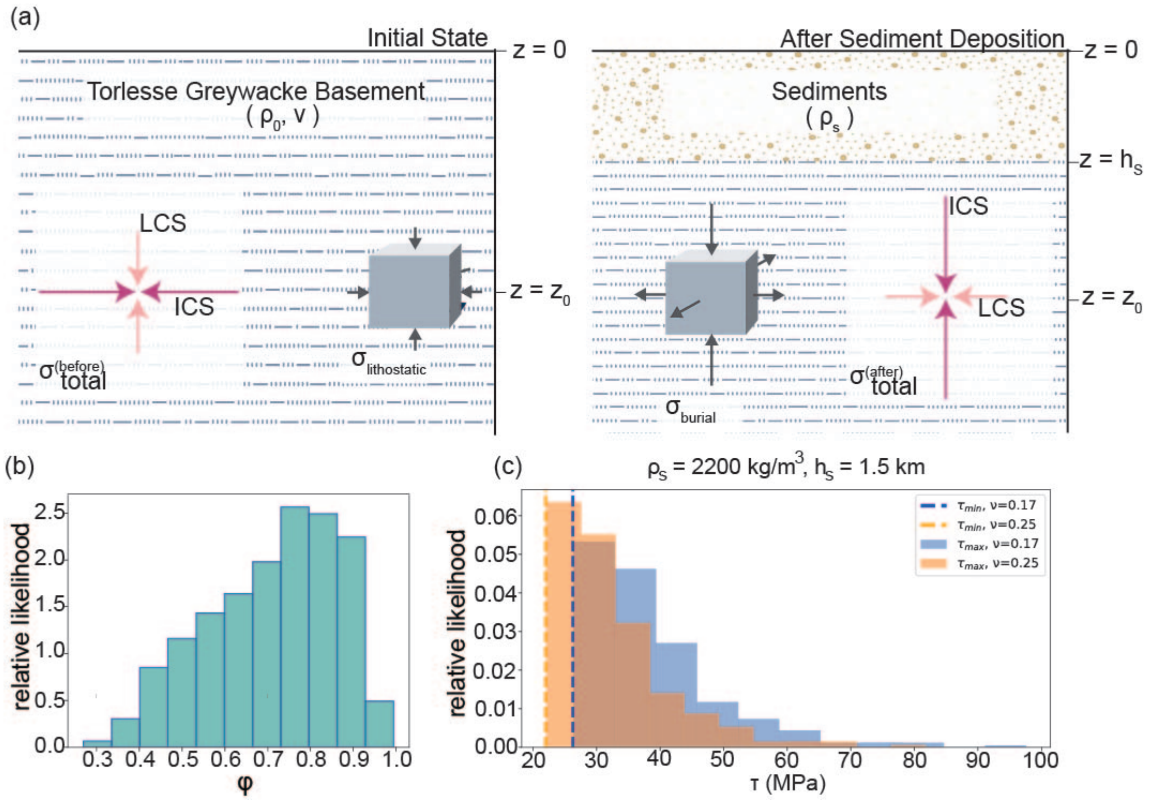

Figure 3.7: (a) Cartoons depicting the sediment loading model in Section 3.4, showing the total stresses either with no sedimentary cover (left panel) or with a sedimentary cover (right panel). A background lithospheric stress is only depicted in left panel but is present in both panels, while the stress due to sediment load is shown in right panel. (b) Histogram of ϕ, Eq. (3.15), indicating the relative magnitudes of ICS to MCS in tectonic stress. (c) Histograms of the maximum tectonic stress and vertical lines for the minimum tectonic stress for two Poisson ratios ($\nu = 0.17$ blue, $\nu = 0.25$ orange), sediment density of $2200 kg/m^3$, and sediment thickness of $1.5 km$.

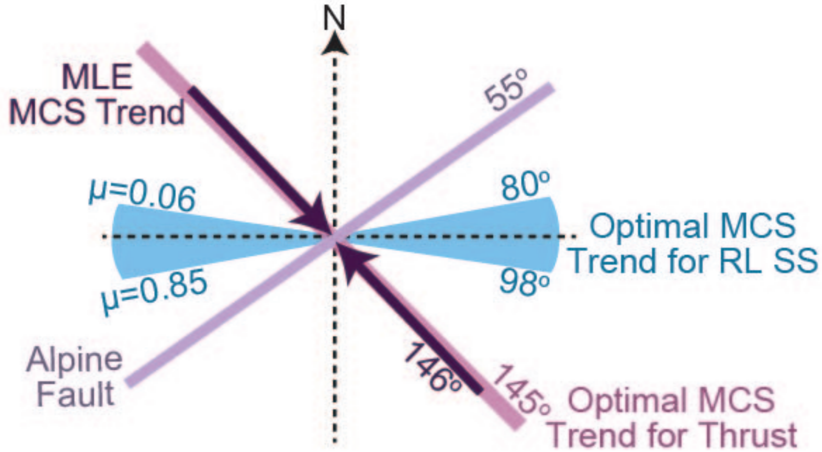

Figure 3.8: Illustration depicting the optimal orientation of MCS in a Mohr-Coulomb sense for pure right-lateral strike-slip motion for coefficients of friction between 0.06 to 0.85 (cyan) and for pure thrust motion (mauve) along a fault striking N55°E (*i.e.*, the Alpine Fault). The MLE of the trend of the MCS for the Canterbury composite posterior is shown as purple double-arrows.

3.11 Supplemental material - Chapter 3

3.11.S1 Description of the supplemental material

In this supplement, we include one table and twelve figures. Table 3.S1 details information from our study for each segment of the four coseismic slip models (*Beavan et al.*, 2012; *Elliott et al.*, 2012), including each segment's relative percent potency, maximum slip, and the Jensen-Shannon (JS) divergence between predicted and observed rake. We refer readers to *Walbert and Hetland* (2022) for a description of these quantities. Figures 3.S1–3.S4 are the stress posteriors for each coseismic slip model, displayed as Lambert projections of the lower hemisphere piercing points for each principal component with contours from the composite posteriors (Figs. 3.3–3.4). Figures 3.S5–3.S6 are marginals of δ and ς displayed as histograms for each coseismic slip model. Figures 3.S7–3.S10 are rose plots for the rake predicted by the stress posterior on each segment of the coseismic slip models. Figure 3.S11 depicts the tensorial seismogenic stress posteriors for the Canterbury Plains as the Canterbury composite posterior (*i.e.*, the joint posterior of the Darfield and Christchurch earthquake composites), and the Marlborough Fault System as the composite posterior of the 2016 $M_w7.8$ Kaikōura earthquake (*Walbert and Hetland*, 2022). Cross-sectional sketches within the inset illustrate the crustal features that may contribute to the loading of the crust beneath the Canterbury Plains relative to the Marlborough Fault System. Finally, Figure 3.S12 demonstrates how changes in the sediment density, depth of sediment, and Poisson ratio impact the magnitude of tectonic stress.

3.11.S2 Data and resources specific to the supplemental material

Data used in this paper came from published sources listed in the references below. Figs. S1–S4 and S11 were made using the Generic Mapping Tools version 6.1.1 (www.generic-mapping-tools.org; *Wessel et al.*, 2019).

3.11.S3 Tables

Table 3.S1: The percent relative potency, maximum slip, and the Jensen-Shannon (JS) divergence between predicted and observed rake for the segments of each coseismic slip model (Beavan *et al.*, 2012; Elliott *et al.*, 2012).

slip model	segment number	potency (%)	max. slip (m)	JS divergence
Beavan-D	0	34	7.6	0.03
	1	18	4.6	0.26
	2	15	5.6	0.07
	6	12	3.3	0.27
	3	9	5.6	0.05
	5	7	2.5	0.02
	4	6	4.0	0.05
Elliott-D	1	22	7.3	0.02
	0	22	3.7	0.18
	2	17	8.3	0.02
	3	11	6.6	0.01
	6	9	5.0	0.38
	7	7	3.4	0.02
	5	7	1.2	0.36
	4	6	2.9	0.27
Beavan-C	2	46	2.5	0.17
	0	31	1.4	0.22
	1	23	1.6	0.17
Elliott-C	0	67	2.6	0.16
	1	33	0.8	0.07

3.11.S4 Figures

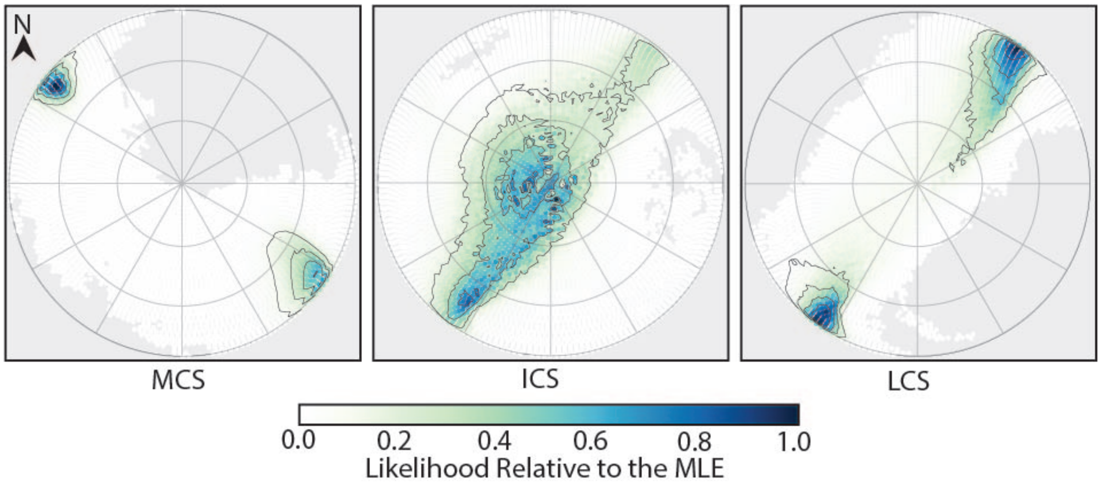

Figure 3.S1: Lambert projection of the lower hemisphere piercing points for the principal components of stress for the Beavan-D posterior (Beavan et al., 2012), with overlaid contours from the Darfield composite posterior (Fig. 3.3 in the main text). Contours are the regions of highest likelihood with intervals of 0.2. Colors are normalized by the maximum likelihood for each component. Top of the page is oriented towards North and grid-lines indicate 30° intervals of trend and plunge, where the outermost circle represents a plunge of 0° and the center of the circle a plunge of 90°.

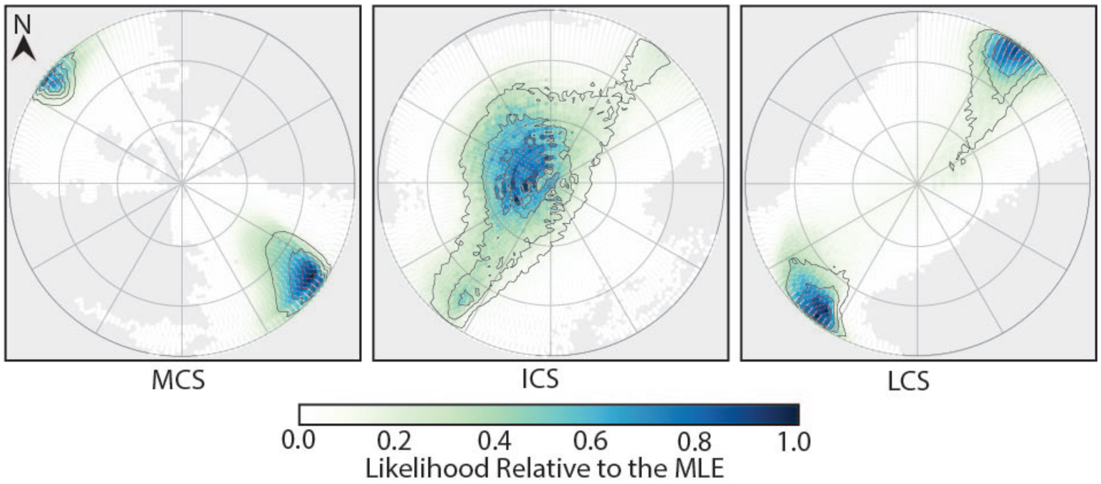

Figure 3.S2: Lambert projection of the lower hemisphere piercing points for the principal components of stress for the Elliott-D posterior (Elliott et al., 2012), with overlaid contours from the Darfield composite posterior (Fig. 3.3 in the main text). See caption of Fig. 3.S1 for details of the display.

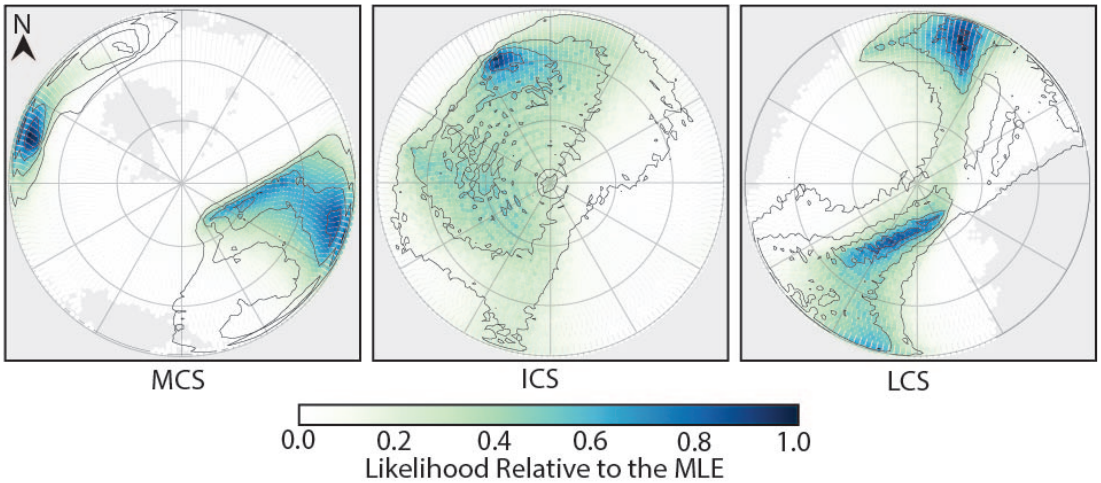

Figure 3.S3: Lambert projection of the lower hemisphere piercing points for the principal components of stress for the Beavan-C posterior (Beavan et al., 2012), with overlaid contours from the Christchurch composite posterior (Fig. 3.4 in the main text). See caption of Fig. 3.S1 for details of the display.

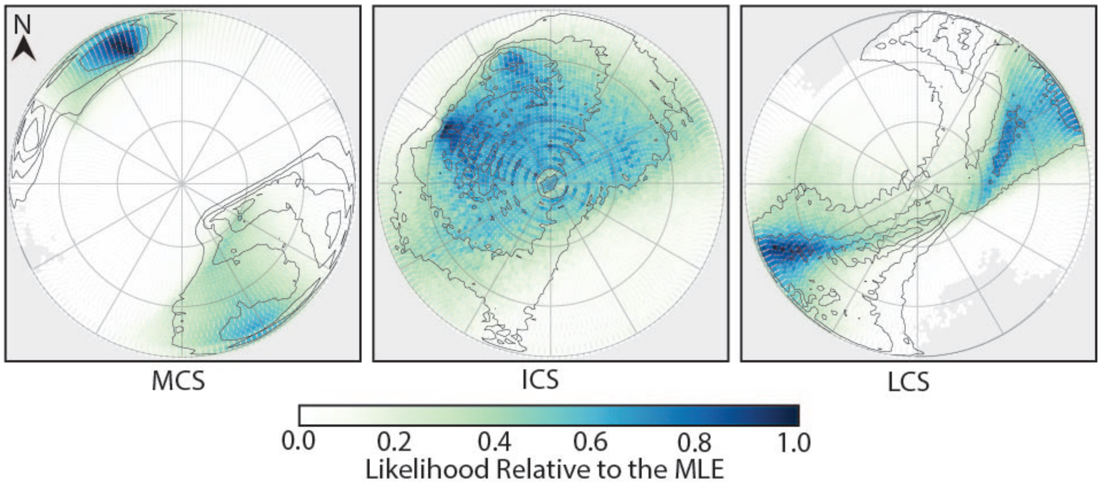

Figure 3.S4: Lambert projection of the lower hemisphere piercing points for the principal components of stress for the Elliott-C posterior (Elliott et al., 2012), with overlaid contours from the Christchurch composite posterior (Fig. 3.4 in the main text). See caption of Fig. 3.S1 for details of the display.

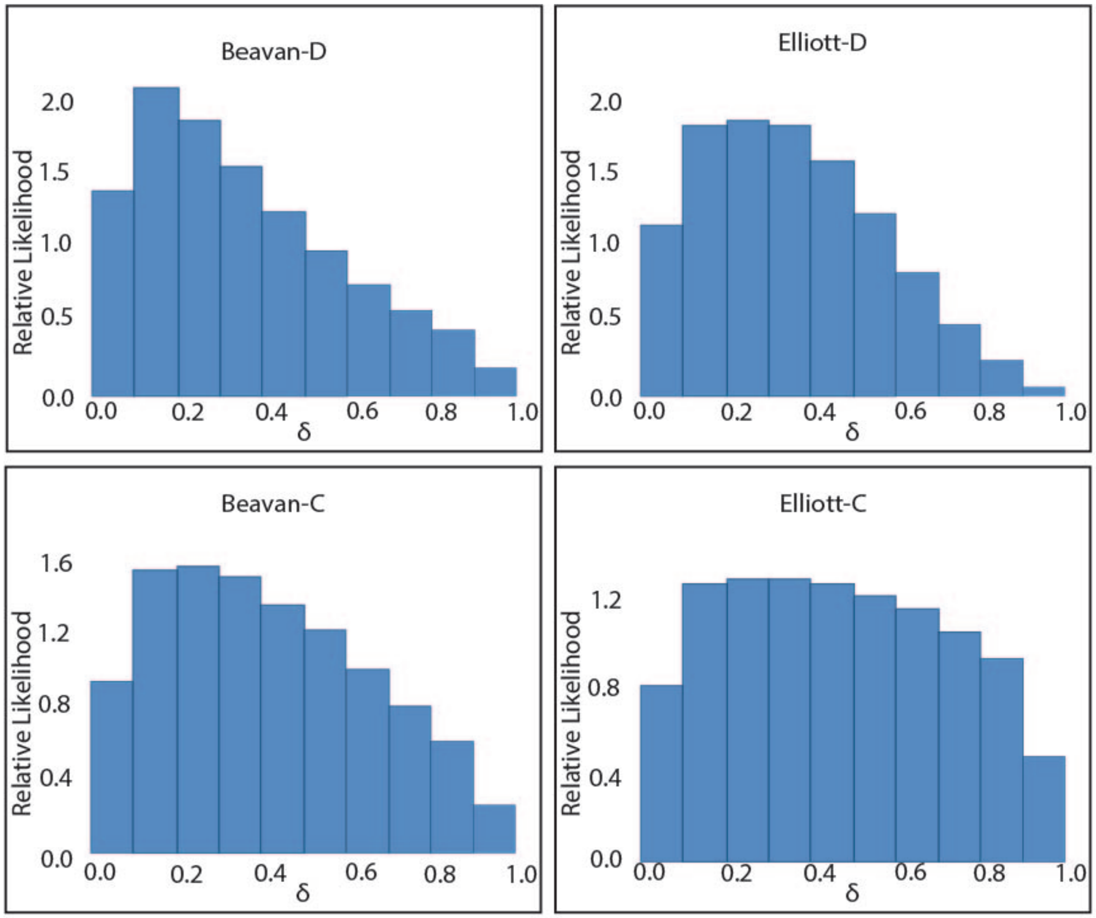

Figure 3.S5: The marginals of δ displayed as histograms for the posterior of each coseismic slip model (Beavan et al., 2012, Elliott et al., 2012).

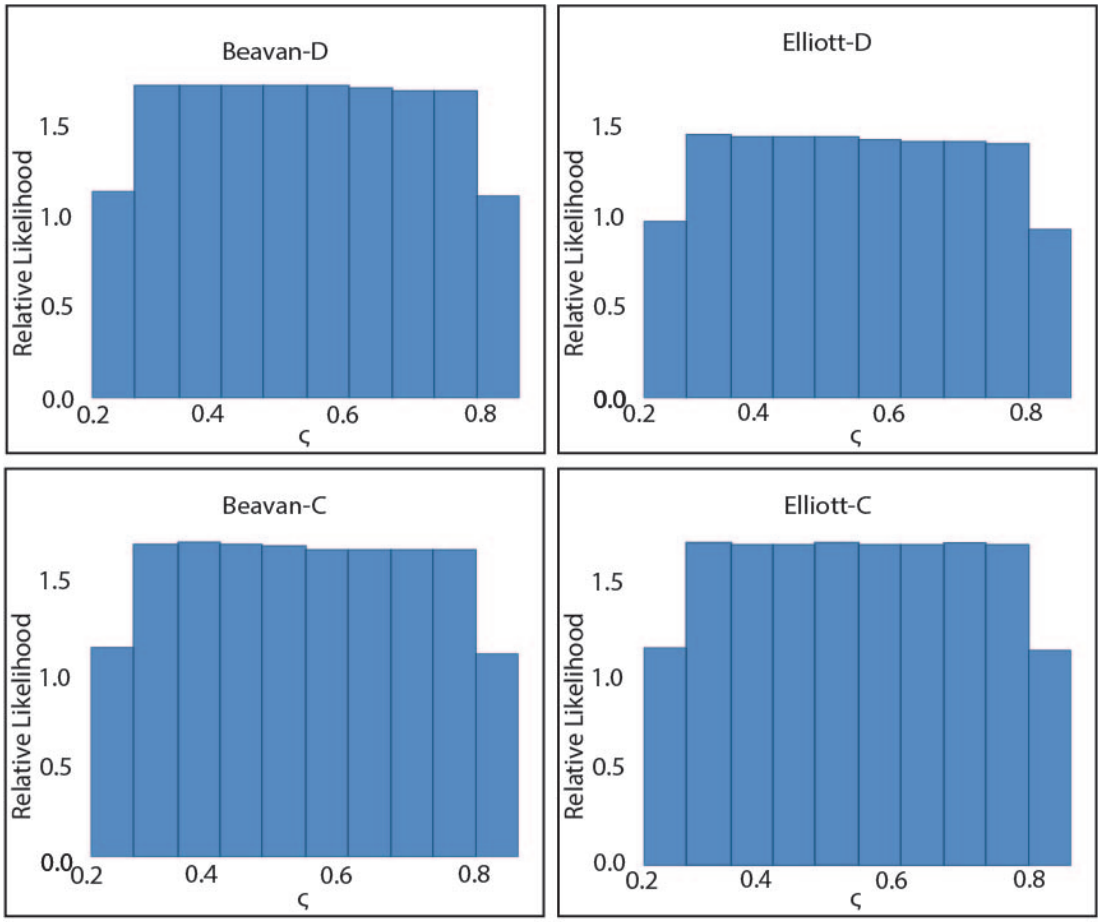

Figure 3.S6: The marginals of ς displayed as histograms for the posterior of each coseismic slip model (Beavan et al., 2012, Elliott et al., 2012).

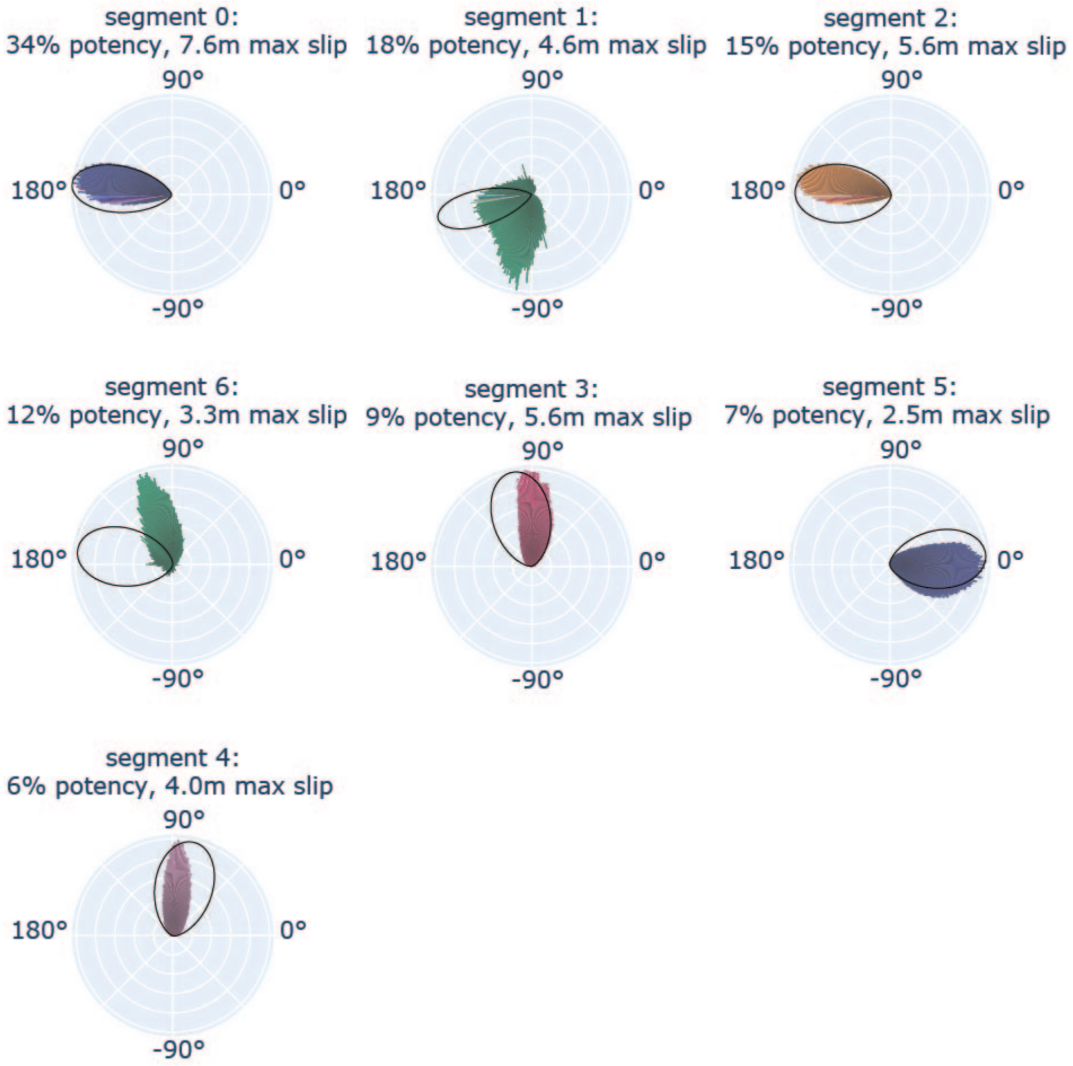

segment 0:
34% potency, 7.6m max slip

segment 1:
18% potency, 4.6m max slip

segment 2:
15% potency, 5.6m max slip

segment 6:
12% potency, 3.3m max slip

segment 3:
9% potency, 5.6m max slip

segment 5:
7% potency, 2.5m max slip

segment 4:
6% potency, 4.0m max slip

Figure 3.S7: Rose plots of rake predicted (bars) by the Beavan-D stress posterior compared to rake observed (line) by the Beavan-D coseismic slip model (Beavan et al., 2012).

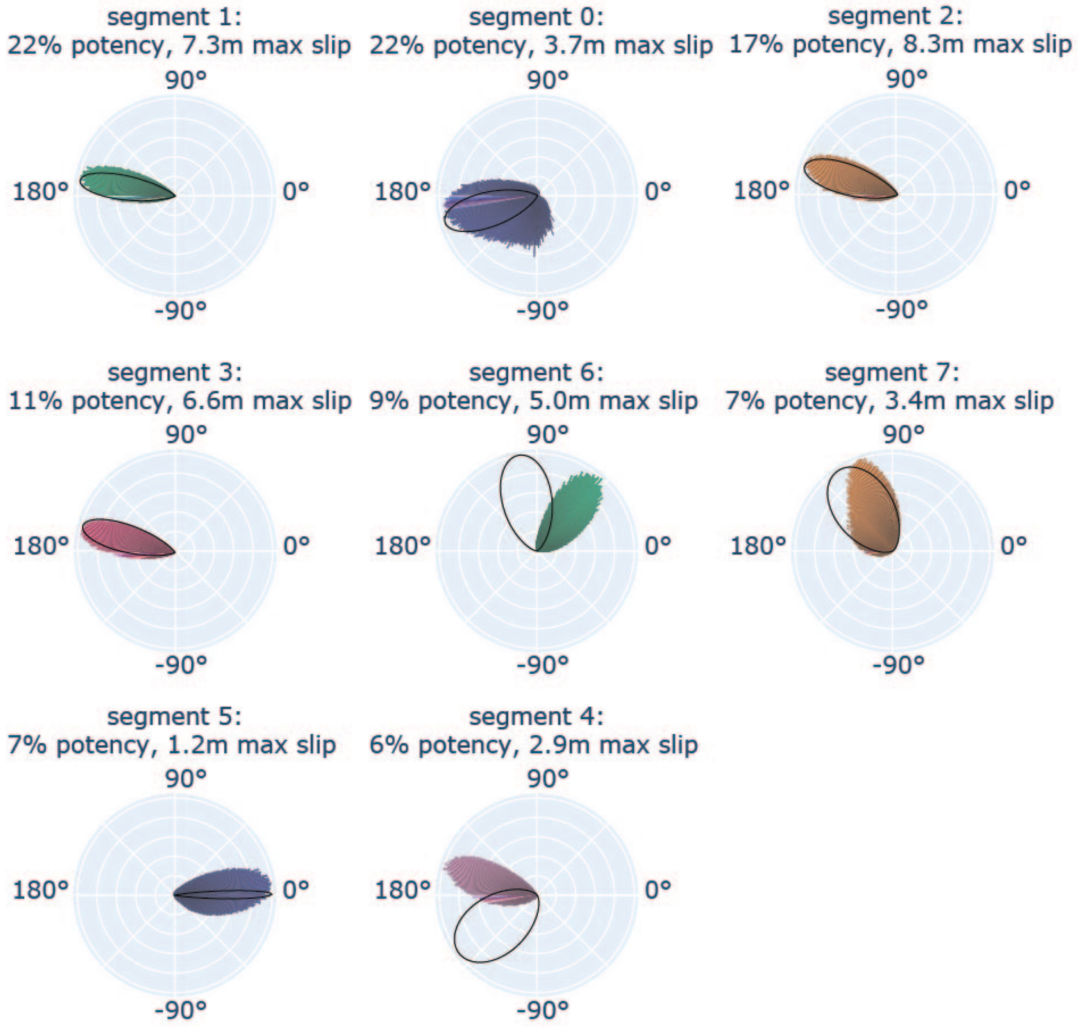

Figure 3.S8: Rose plots of rake predicted (bars) by the Elliott-D stress posterior compared to rake observed (line) by the Elliott-D coseismic slip model (Elliott et al., 2012).

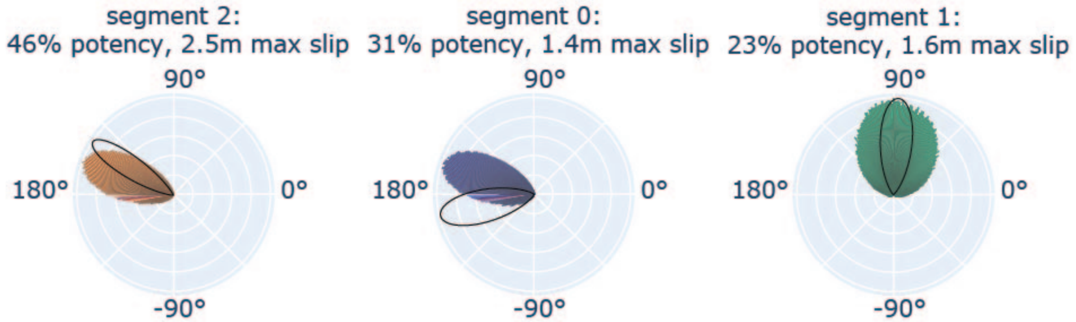

Figure 3.S9: Rose plots of rake predicted (bars) by the Beavan-C stress posterior compared to rake observed (line) by the Beavan-C coseismic slip model (Beavan et al., 2012).

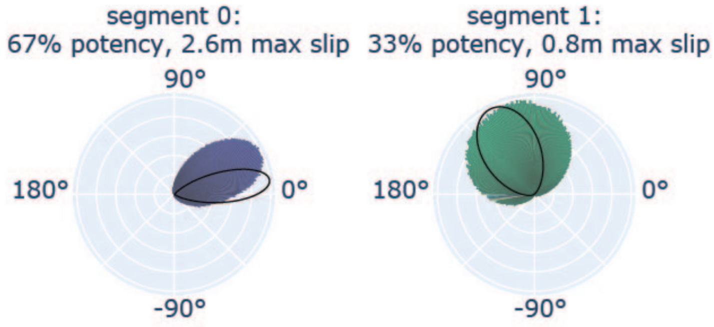

Figure 3.S10: Rose plots of rake predicted (bars) by the Elliott-C stress posterior compared to rake observed (line) by the Elliott-C coseismic slip model (Elliott et al., 2012).

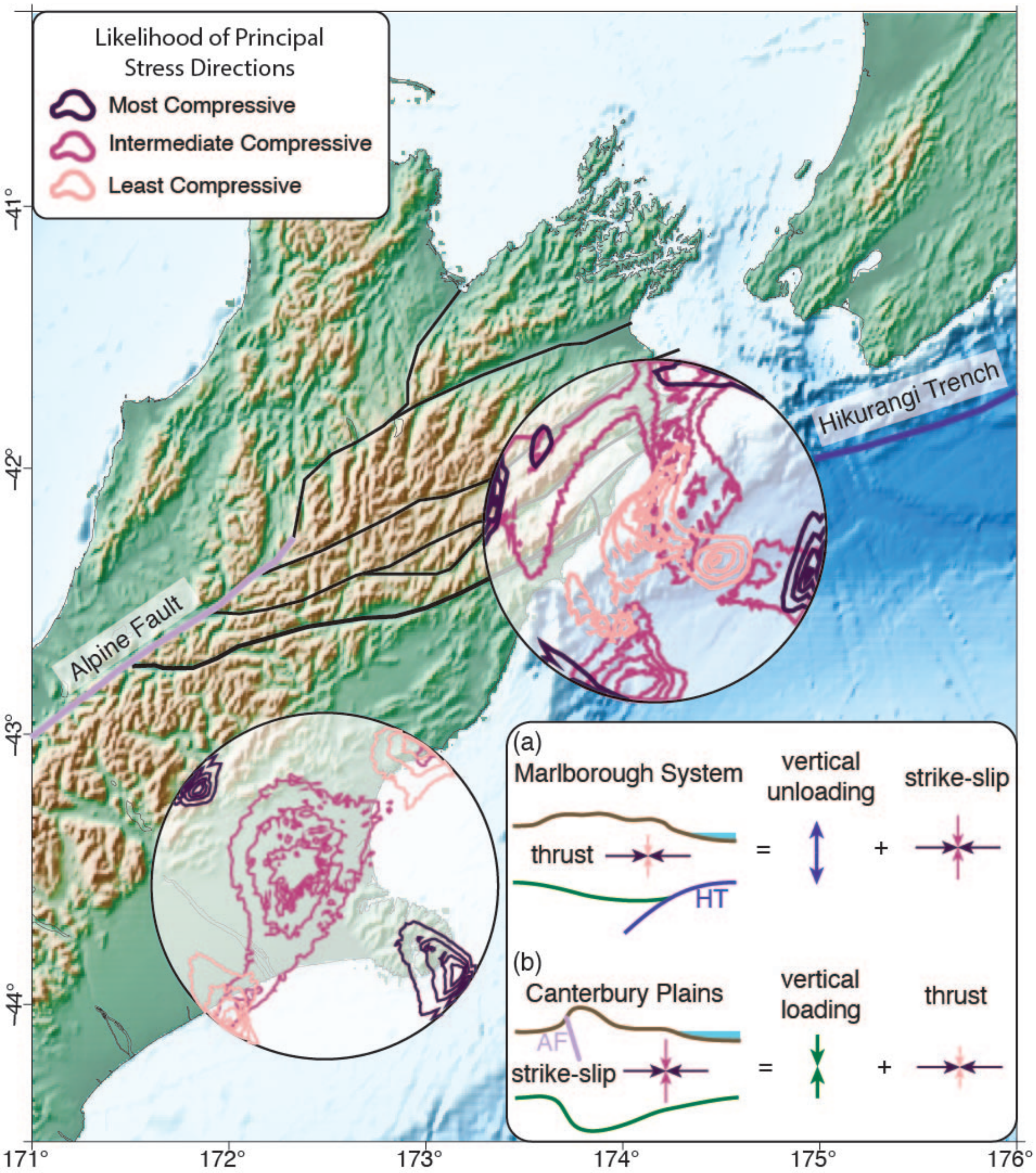

Figure 3.S11: Stress posteriors of the joint posterior of the Darfield and Christchurch earthquakes determined in this study (Fig. 3.6) and the composite posterior of the 2016 $M_w7.8$ Kaikōura earthquake we previously developed (Walbert & Hetland, 2022) plotted near the hypocenters of the Darfield and Kaikōura earthquakes, respectively. Inset depicts sketches illustrating alternative mechanisms that may reconcile the strike-slip and thrust regimes inferred from the Canterbury Plains and Marlborough Fault System, respectively (see Section 3.5.2 for further discussion). (a) Vertical unloading of the Marlborough Fault System due to floundering of the Hikurangi Trench, resulting in a transition of a strike-slip stress regime to a thrust regime. (b) Vertical loading of the Canterbury Plains due to crustal thickening to result in the inferred strike-slip stress regime, resulting in a transition of a thrust stress regime to a strike-slip regime. Arrows in inset denote the principal stresses (arrow color is as in the main figure legend), or the vertical unloading (a) or loading (b). AF and HT in inset figures are faults representative of the Alpine Fault or Hikurangi Trench, respectively.

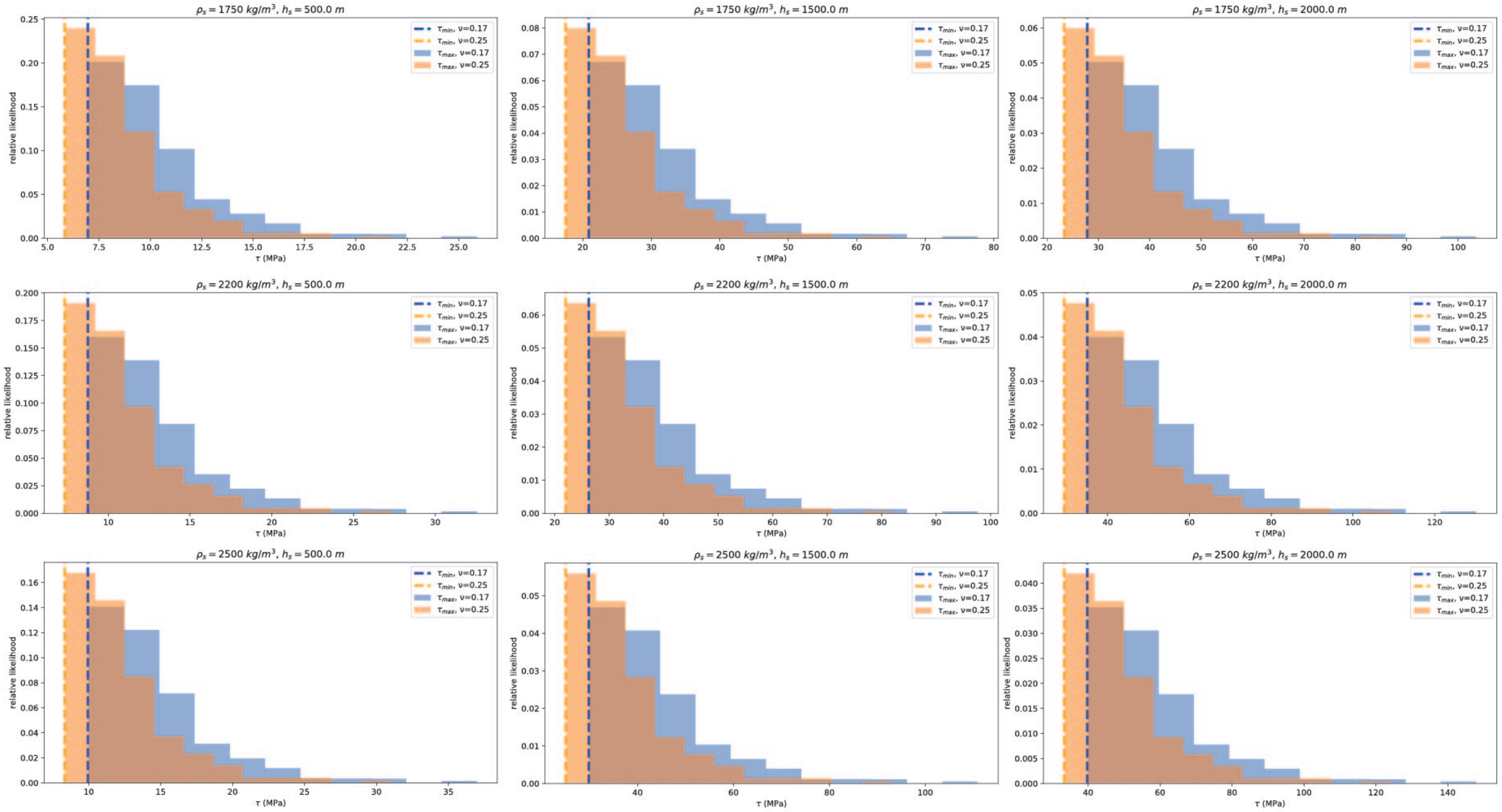

Figure 3.S12: Magnitude of tectonic stress dependent upon Poisson ratios, ν, of 0.17 and 0.25, sediment densities, ρ_s, of $1750kg/m^3$, $220kg/m^3$, and $2500kg/m^3$, and sediment overburden thickeness, h_s, of $0.5km$, $1km$, and $2km$. See Fig. 3.7 for context.

CHAPTER 4

Stress-Informed Clustering of Earthquake Focal Mechanisms in the Afar Triple Junction *

Abstract

We propose an objective approach to agglomerative hierarchical clustering of earthquake focal mechanisms that accounts for the distance between earthquake locations and the seismogenic stresses estimated from the focal mechanisms of those earthquakes. We apply this methodology to 316 earthquakes between 1967–2017 in the Afar Depression and along the western Gulf of Aden, the Main Ethiopian Rift, and the southern Red Sea. We infer the seismogenic tensorial stresses from the focal mechanisms of these earthquakes using a Bayesian Markov Chain Monte Carlo estimation technique. We determine distance metrics based on the inter-event geodesic distance and the Jensen-Shannon distance between the stress posterior probability density functions. Our best-fit model has a cluster localized to the Gulf of Aden in the east, and one spanning from the Main Ethiopian Rift northward through the Red Sea. Both clusters resolve a normal stress regime, with a 47° counter-clockwise rotation of the horizontal principal components of stress from the west to the east. The clustered events have a spatially diffuse boundary coincident with the Danakil Block, a structure that has been geodetically imaged to be rotating counter-clockwise relative to the Arabian and Nubian Plates.

4.1 Introduction

In order to characterize the regional crustal stresses within the Afar Depression and surrounding divergent boundaries, we propose a novel, unsupervised clustering approach that

---

[*] Chapter 4 is in preparation for submission as Walbert, O.L. and E.A. Hetland "Stress-Informed Clustering of Earthquake Focal Mechanisms in the Afar Triple Junction."

considers both distances between earthquakes and the tensorial seismogenic stresses. Prior studies that sought to determine clusters of earthquakes have focused on either similarity in their spatial relationships, their focal mechanisms (*e.g.*, *Michailos et al.*, 2020), or on the mechanism of the earthquakes (*e.g.*, *Otsubo et al.*, 2008). The inherent assumption behind these clustering methods is that neighboring earthquakes or earthquakes with similar focal mechanisms are a response to the same crustal loading conditions. A complication for interpretation that arises in the latter clustering methods is that clusters can be spatially overlapping owing to the fact that multiple types of earthquakes could occur in the same spatial region (*e.g.*, *Cesca et al.*, 2016). *Medina Luna* (2015) demonstrated that earthquakes with different mechanisms might be consistent with the same causative stress. Clustering earthquakes based on location is usually performed by geologic knowledge and the style of faulting indicated by the focal mechanism. However, this approach is subjective and places *a priori* constraints on the inferred regional stresses.

We aim to assimilate both inter-event distances between earthquakes and the similarity of their seismogenic stresses, taking into account that earthquakes of different mechanisms may have resulted from the same seismogenic stress. We use five decades (1967–2017) of focal mechanisms from *Hofstetter and Beyth* (2003) and *Ruch et al.* (2021). We find two clusters consistent with a normal stress regime for our best-fit model. This model indicates a horizontal WSW-ENE trending least compressive stress in the west for the Main Ethiopian Rift, west Afar Depression, and southern Red Sea, and a horizontal NNE-SSW trending least compressive stress in the east for the eastern Afar Depression and the Gulf of Aden. The horizontal principal components of stress reveal a $47°$ counter-clockwise rotation from the tectonic structures in the west to the east.

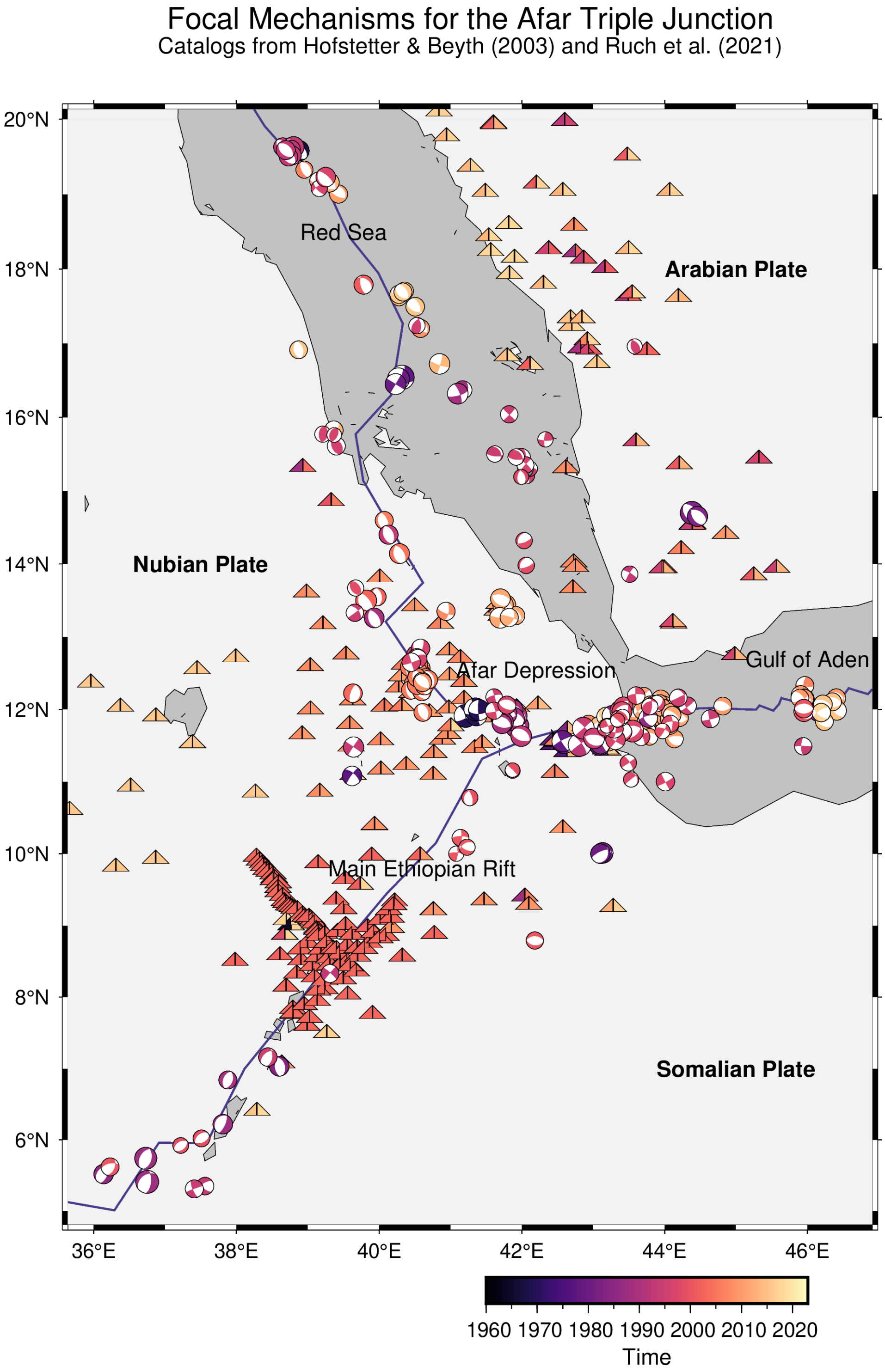

Figure 4.1: Map of the study region for the Afar Depression. Focal mechanisms from the Hofstetter and Beyth (2003) and Ruch et al. (2021) catalogs are shown with compressional quadrants color-mapped to the event's origin time. Seismic station locations are marked as triangles and color-mapped such that the left-side of the triangle marks the beginning and the right-side of the triangle marks the end of the station's recording period. Blue plate boundaries from Bird (2003).

4.2 Methodology

4.2.1 Focal mechanism catalogs

We study 316 earthquakes that occurred between 1967 and 2017 in the Afar Depression and along the southern Red Sea, the western Gulf of Aden, and the Main Ethiopian Rift (Fig. 4.1), using the catalogs published by *Hofstetter and Beyth* (2003) and *Ruch et al.* (2021). The catalog of *Hofstetter and Beyth* (2003) includes 125 focal mechanisms for earthquakes with magnitude $m_B \geq 4.0$ for the region between 1968–2000. The sparse regional broadband station coverage within this period (Fig. 4.1) results in a catalog magnitude of completeness of $m_B \geq 5.0$ prior to 1980 and $m_B \geq 4.3$ after 1980. The *Hofstetter and Beyth* (2003) catalog includes source parameters for several events determined by Harvard CMT and previous catalogs (*Ayele*, 1998; *Kebede et al.*; *Ayele and Arvidsson*, 1998). *Ruch et al.* (2021) published a seismic catalog for the region of 15,200 earthquakes, with focal mechanisms determined for 290 of the events — 191 being unique from that published by the *Hofstetter and Beyth* (2003) catalog. The *Ruch et al.* (2021) catalog includes focal mechanisms for events that occurred between 1967–2017 from several providers, including the Bulletin of the International Seismological Centre and several publications (*Ebinger et al.*, 2008; *Keir et al.*, 2009; *Belachew et al.*, 2011). The focal mechanisms included in the catalogs include strike-slip, normal, and reverse faulting mechanisms. We refer readers to both source publications for further details of their data sources and methodologies (*Hofstetter and Beyth*, 2003; *Ruch et al.*, 2021).

4.2.2 Estimation of tensorial stress from focal mechanism data

We invert the focal mechanisms using a Bayesian Markov Chain Monte Carlo (MCMC) technique to estimate tensorial stress models consistent with the focal mechanism's nodal plane geometries as posterior probability density functions, f_{post} (PDFs).

$$f_{post}\left(m \mid \lambda\right) = wL_{obs}\left(\lambda \mid m\right) f_{prior}\left(m\right) \tag{4.1}$$

This estimation strategy follows our methodology described by *Walbert and Hetland* (2022), with an extension to focal mechanism data. Our inversion technique samples a non-informative prior PDF, f_{prior}, defined by discretized models, m, of the orientation and relative magnitudes of the principal components of stress as the most compressive stress (MCS), intermediate compressive stress (ICS), and least compressive stress (LCS). The stress model is given by $m = \{\phi, \theta, \rho, \delta, \varsigma\}$, where the Euler angles ϕ, θ, and ρ uniquely represent the orientation of the model stress tensor, and δ and ς are the relative magnitudes of the principal components of stress, defined as

$$\delta = \frac{\sigma_2 - \sigma_3}{\sigma_1 - \sigma_3} \tag{4.2}$$

and

$$\varsigma = \frac{\sigma_3}{\sigma_1}. \tag{4.3}$$

$\sigma_1, \sigma_2,$ and σ_3 are the absolute magnitudes of stress associated with the MCS, ICS, and LCS, respectively. We form our prior PDF as a lattice by discretizing the model space with minor modifications to *Walbert and Hetland* (2022). Here, we define our spherical model space for ϕ and θ as the vertices of a triangularized icosahedron as an approximation of a discretized sphere to decrease potential variability in the distance between models, thus improving equilibration to model probabilities (*e.g.*, *Baumgardner and Frederickson*, 1985). In addition, we ensure an equal probability of sampling models that include bounding values of our non-wrapping lattice of the relative magnitude parameters.

At each step of the MCMC, we select a trial model from the collection of lattice nodes neighboring the most recently retained model including the most recently retained model itself, all with equal likelihood. This trial model is retained as a sample of the posterior PDF if the Gaussian likelihood, L_{obs}, between the difference of the focal mechanism rake on a given nodal plane, λ, to the predicted rake (i.e., the orientation of maximum shear stress on one of the nodal plane's geometry, according to the Wallace-Bott assumption; *Wallace*, 1951; *Bott*, 1959), is greater than the Gaussian likelihood determined for the most recently retained model. This strategy follows a Metropolis algorithm (*Metropolis et al.*, 1953) where the trial model is accepted if the ratio of the likelihoods of the trial model versus the most recently retained model is greater than a randomly sampled value from the Uniform distribution parameterized between 0 and 1. If the trial model is rejected, then the current model is replicated in the Markov Chain.

The Gaussian likelihood function considers the intrinsic uncertainty on the rake, as well as the uncertainties from the strike and dip propagated into rake prediction (*e.g.*, *Tarantola*, 2005). Including sources of errors in our likelihood function is essential due to the uncertainty in focal mechanism solutions, which may arise due to errors in velocity models or source locations and can be compounded by trade-offs in source parameter estimation (*e.g.*, *Tan et al.*, 2018). While recent studies have quantified source parameter uncertainties (*e.g.*, *Alvizuri et al.*, 2018), the focal mechanism catalogs we take as data do not include uncertainty estimates on nodal plane geometries or event location. We assume a uniform standard deviation of $15°$ on nodal plane strike, dip, and rake. This is sufficient for our purposes, as a $15°$ standard deviation on the rake at 99.7% confidence allows for discrimination between faulting mechanisms (*e.g.*, distinguishing a reverse mechanism from a strike-slip mechanisms).

We first determine a stress posterior for each nodal plane separately, and then combine them to determine a stress posterior for a given focal mechanism following *Arnold and Townend* (2007) and *Medina Luna and Hetland* (2013). *Walbert and Hetland* (2022) utilized finite coseismic slip models to infer seismogenic stress, which allowed for sub-fault resolution of the slip surfaces involved in an earthquake. In this work, we assume that the slip surface is one of the nodal planes. It is not possible to identify the fault plane from point-source solutions alone. We allow for either of the nodal planes to represent the slip surface by estimating the posterior PDF for each of the nodal plane geometries through our Bayesian MCMC strategy. Subsequently, we calculate the mutually exclusive union from the resulting PDFs, f_{NP_1} and f_{NP_2}, to achieve the full posterior PDF of the focal mechanism, f_{FM}

$$f_{\mathrm{FM}}\left(\sigma \,|\, \mathrm{NP}_1 \,\&\, \mathrm{NP}_2\,\right) = f_{post}\left(\sigma \,|\, \mathrm{NP}_1\right) \cap f_{post}\left(\sigma \,|\, \mathrm{NP}_2\right). \tag{4.4}$$

4.2.3 Objective agglomerative hierarchical clustering of seismicity

We employ an agglomerative hierarchical clustering algorithm with Ward's linkage (*Ward*, 1963) to group our focal mechanism dataset according to specified distance metrics. Agglomerative hierarchical clustering allows us to consider the structure formed by these groupings as the nearest clusters are merged from the base of a dendrogram, where each datum represents an individual cluster, upward. Ward's linkage method merges these clusters so that each cluster's variance is minimized (*Ward*, 1963). We determine the number of clusters from the clustering model's dendrogram by truncating the dendrogram at the mid-point of the maximum dendrogram height.

We calculate clustering models for three distance metrics: a stress-based distance metric, an inter-event distance metric, and hybrids of these two, for which we explore different weightings of the inter-event component. We assign the inter-event distance metric as the geodesic distance between epicenters of seismic events. We calculate the pairwise geodesic distances to form a symmetric distance matrix, $\mathcal{D}_{\mathcal{G}}$.

The stress-based distance is the pairwise Jensen-Shannon (JS) distance between our estimates of the stress posterior PDFs. The JS distance, $\mathcal{D}_{\mathcal{JS}}$, is determined from the square root of the JS divergence, a symmetric and finite measure of the overlap of PDFs bounded between 0 and 1. For two PDFs, P and Q, $\mathcal{D_{JS}}$ is defined as

$$\mathcal{D_{JS}} = \left(\frac{1}{2}\mathcal{D_{KL}}\left(P\,||\,M\right) + \frac{1}{2}\mathcal{D_{KL}}\left(Q\,||\,M\right)\right)^{\frac{1}{2}}, \tag{4.5}$$

such that

$$M = \frac{1}{2}\left(P + Q\right), \tag{4.6}$$

and $\mathcal{D}_{KL}$ is the Kullbach-Liebler divergence, defined as

$$\mathcal{D_{KL}}\left(P\,||\,Q\right) = \sum_{x \varepsilon X} P\left(x\right) \log\left(\frac{P(x)}{Q(x)}\right). \tag{4.7}$$

We form a distance matrix with each ij element comprised of the JS distance between the i^{th} and j^{th} stress posteriors.

Finally, we calculate the hybrid distance from the inter-event and stress-based distances as a combined distance matrix, $\mathcal{D_C}$, given by

$$\mathcal{D_C} = \mathcal{D_{JS}} + w\frac{\mathcal{D_G}}{max(\mathcal{D_G})}, \tag{4.8}$$

where w is a weighting parameter that we select in 0.1 intervals between 0.1 and 1. We normalize $\mathcal{D_G}$ by the maximum pairwise geodesic distance to enforce bounds between 0 and 1, consistent with bounds on $\mathcal{D_{JS}}$.

Following the calculation of the agglomerative hierarchical clustering models, we determine the stress consistent with all of the earthquakes in each cluster. We calculate this stress as the joint posterior PDF, f_J, from the N stress posterior PDFs included in each cluster as

$$f_J\left(\sigma\,|\,\mathrm{FM}_1\,\&\,\mathrm{FM}_2\,\&\,\cdots\,\&\,\mathrm{FM}_N\right) = \prod^{N} f_{\mathrm{FM}}. \tag{4.9}$$

4.3 Results

Using our Bayesian MCMC technique, we estimate 316 stress posteriors from the focal mechanisms considered (Fig. 4.1; *Hofstetter and Beyth*, 2003; *Ruch et al.*, 2021). The distance matrix composed of the pairwise JS distance between each of the stress posteriors is displayed in Fig. 4.2. Fig. 4.2 also includes the agglomerative hierarchical clustering dendrogram associated with $\mathcal{D_{JS}}$. Truncating the dendrogram at the mid-point of the maximum height yields two clusters, JS_0 and JS_1, with 170 events and 146 events, respectively. The focal mechanisms belonging to each of these two dendrogram branches are plotted in

Fig. 4.3. Most earthquakes in JS_0 are located in the Gulf of Aden, while those in JS_1 are located beneath the Red Sea, the Afar Depression, and the Main Ethiopian Rift. There are several events in one cluster that are located in the spatial regions dominated by earthquakes in the other cluster, a result of measuring the distance using only $\mathcal{D}_{JS}$. Both of the joint posteriors calculated from events in JS_0 and JS_1 are approximately normal stress regimes, with an MCS 10–20° from vertical and LCS nearly horizontally oriented (Table 4.1, Fig. 4.4). The MCS for cluster JS_1 is slightly steeper than for JS_0; however, the largest difference between the two clusters is in the trend of the principal stresses (Table 4.1, Fig. 4.4). LCS in JS_0 trends SSW-NNE, while LCS trends SW-NE (Table 4.1, Fig. 4.4).

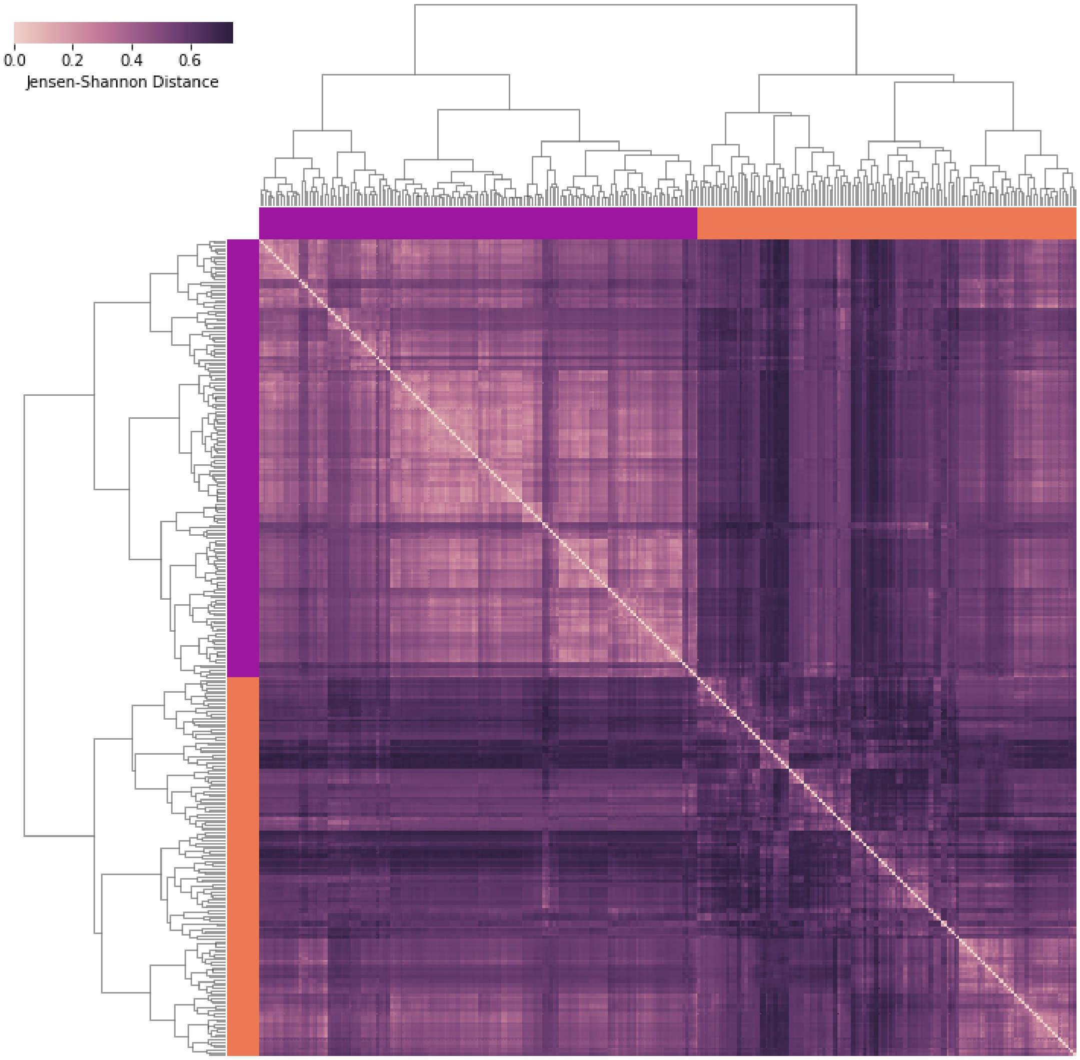

Figure 4.2: JS distance matrix, $\mathcal{D}_{JS}$, displayed as a heat map. The dendrogram formed through agglomerative hierarchical clustering of $\mathcal{D}_{JS}$ with Ward linkage is shown at the top and left of the distance matrix, with the purple or orange solid bars indicating the elements in each of the two clusters formed by breaking the top-level of the dendrogram.

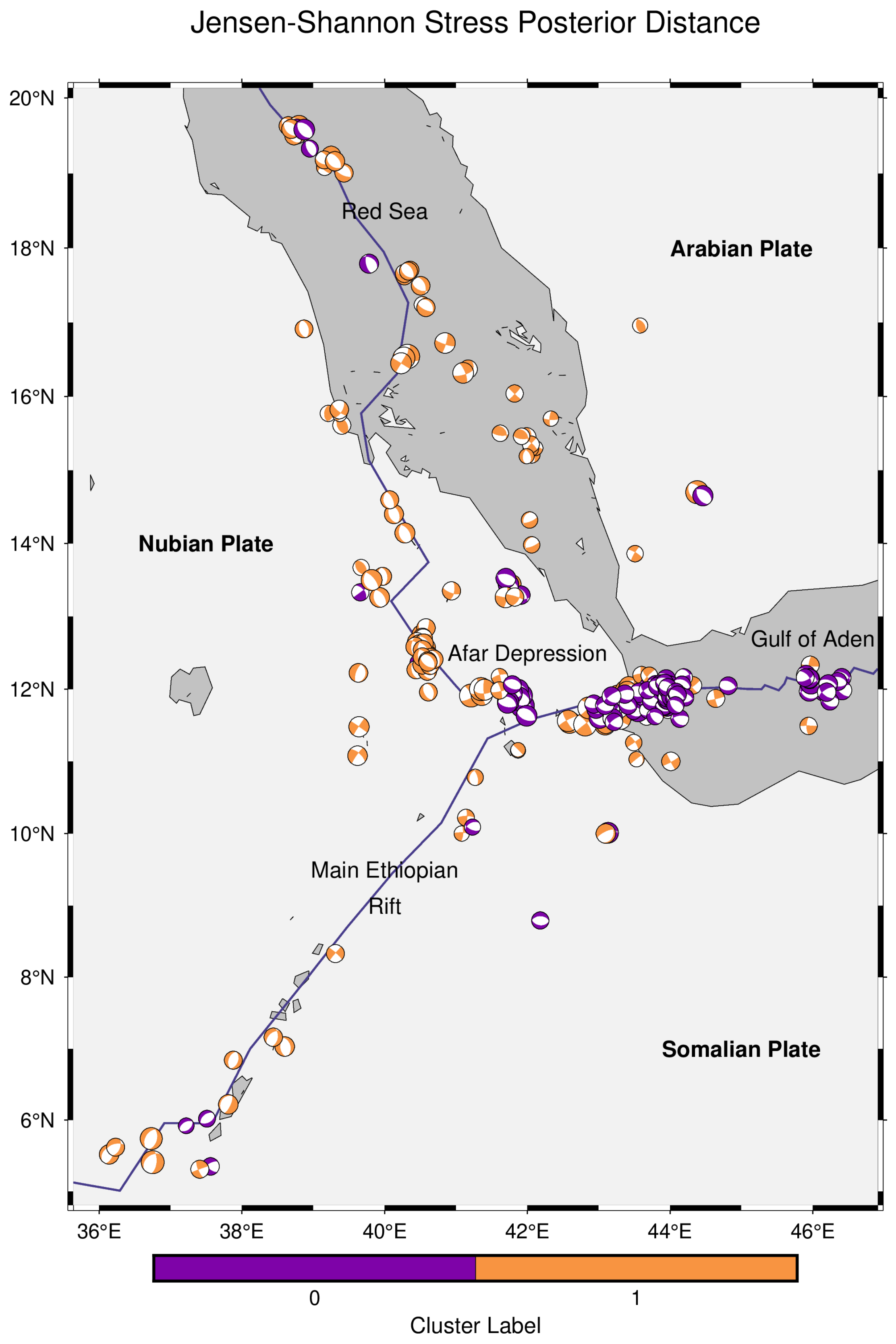

Figure 4.3: Focal mechanisms with T-quadrant colored according to which of the JS clusters defined in Fig. 4.2 it belongs to.

Clusters	Events	MCS	ICS	LCS	δ	ς	RSS
All Events	316	-	-	-	-	-	-
JS_0	170	$302^\circ \pm 6^\circ/71^\circ \pm 7^\circ$	$105^\circ \pm 2^\circ/18^\circ \pm 7^\circ$	$197^\circ \pm 2^\circ/5^\circ \pm 2^\circ$	0.9	0.822	30.12
JS_1	146	$122^\circ \pm 0^\circ/78^\circ \pm 0^\circ$	$334^\circ \pm 0^\circ/10^\circ \pm 0^\circ$	$243^\circ \pm 0^\circ/6^\circ \pm 0^\circ$	0.9	0.822	47.93
G_0	182	$258^\circ \pm 41^\circ/78^\circ \pm 0^\circ$	$106^\circ \pm 0^\circ/10^\circ \pm 2^\circ$	$13^\circ \pm 3^\circ/5^\circ \pm 3^\circ$	0.9	0.822	43.72
G_1	13	$198^\circ \pm 33^\circ/76^\circ \pm 8^\circ$	$10^\circ \pm 58^\circ/10^\circ \pm 8^\circ$	$10^\circ \pm 43^\circ/7^\circ \pm 6^\circ$	0.1	0.822	11.5
G_2	34	$129^\circ \pm 9^\circ/7^\circ \pm 13^\circ$	$230^\circ \pm 21^\circ/63^\circ \pm 10^\circ$	$40^\circ \pm 3^\circ/22^\circ \pm 4^\circ$	0.9	0.822	20.38
G_3	87	$58^\circ \pm 1^\circ/78^\circ \pm 0^\circ$	$310^\circ \pm 4^\circ/4^\circ \pm 1^\circ$	$219^\circ \pm 4^\circ/11^\circ \pm 0^\circ$	0.4	0.822	50.05
$C01_0$	163	$316^\circ \pm 25^\circ/81^\circ \pm 5^\circ$	$139^\circ \pm 6^\circ/9^\circ \pm 5^\circ$	$39^\circ \pm 13^\circ/3^\circ \pm 2^\circ$	0.9	0.278	131.99
$C01_1$	153	$303^\circ \pm 9^\circ/74^\circ \pm 10^\circ$	$105^\circ \pm 4^\circ/15^\circ \pm 10^\circ$	$197^\circ \pm 1^\circ/4^\circ \pm 3^\circ$	0.7	0.55	15.68
$C02_0$	155	$122^\circ \pm 0^\circ/78^\circ \pm 0^\circ$	$334^\circ \pm 0^\circ/10^\circ \pm 0^\circ$	$243^\circ \pm 0^\circ/6^\circ \pm 0^\circ$	0.9	0.822	66.38
$C02_1$	161	$117^\circ \pm 8^\circ/56^\circ \pm 15^\circ$	$282^\circ \pm 5^\circ/33^\circ \pm 15^\circ$	$16^\circ \pm 1^\circ/6^\circ \pm 2^\circ$	0.9	0.822	23.24
$C03_0$	115	$158^\circ \pm 11^\circ/61^\circ \pm 6^\circ$	$359^\circ \pm 6^\circ/28^\circ \pm 7^\circ$	$264^\circ \pm 5^\circ/8^\circ \pm 1^\circ$	0.5	0.822	80.8
$C03_1$	201	$110^\circ \pm 1^\circ/30^\circ \pm 9^\circ$	$272^\circ \pm 7^\circ/59^\circ \pm 9^\circ$	$16^\circ \pm 2^\circ/6^\circ \pm 1^\circ$	0.9	0.822	33.31
$C04_0$	158	$122^\circ \pm 0^\circ/78^\circ \pm 0^\circ$	$334^\circ \pm 0^\circ/10^\circ \pm 0^\circ$	$243^\circ \pm 0^\circ/6^\circ \pm 0^\circ$	0.9	0.822	72.62
$C04_1$	158	$114^\circ \pm 7^\circ/49^\circ \pm 16^\circ$	$280^\circ \pm 5^\circ/40^\circ \pm 16^\circ$	$16^\circ \pm 1^\circ/6^\circ \pm 2^\circ$	0.9	0.822	22.78
$C05_0$	154	$122^\circ \pm 0^\circ/78^\circ \pm 0^\circ$	$334^\circ \pm 0^\circ/10^\circ \pm 0^\circ$	$243^\circ \pm 0^\circ/6^\circ \pm 0^\circ$	0.9	0.822	61.94
$C05_1$	162	$109^\circ \pm 5^\circ/42^\circ \pm 13^\circ$	$277^\circ \pm 5^\circ/48^\circ \pm 13^\circ$	$15^\circ \pm 1^\circ/6^\circ \pm 2^\circ$	0.9	0.822	23.87
$C06_0$	94	$73^\circ \pm 65^\circ/74^\circ \pm 15^\circ$	$30^\circ \pm 54^\circ/14^\circ \pm 14^\circ$	$253^\circ \pm 8^\circ/6^\circ \pm 4^\circ$	0.6	0.822	50.71
$C06_1$	222	$302^\circ \pm 7^\circ/78^\circ \pm 2^\circ$	$106^\circ \pm 1^\circ/11^\circ \pm 1^\circ$	$196^\circ \pm 0^\circ/3^\circ \pm 1^\circ$	0.9	0.618	56.86
$C07_0$	109	$119^\circ \pm 11^\circ/78^\circ \pm 2^\circ$	$334^\circ \pm 2^\circ/10^\circ \pm 3^\circ$	$243^\circ \pm 1^\circ/6^\circ \pm 2^\circ$	0.9	0.822	24.57
$C07_1$	207	$302^\circ \pm 2^\circ/78^\circ \pm 0^\circ$	$106^\circ \pm 0^\circ/11^\circ \pm 0^\circ$	$196^\circ \pm 0^\circ/3^\circ \pm 0^\circ$	0.9	0.618	45.16
$C08_0$	132	$238^\circ \pm 2^\circ/78^\circ \pm 0^\circ$	$137^\circ \pm 1^\circ/2^\circ \pm 0^\circ$	$46^\circ \pm 1^\circ/12^\circ \pm 0^\circ$	0.1	0.822	77.2
$C08_1$	184	$131^\circ \pm 23^\circ/78^\circ \pm 1^\circ$	$286^\circ \pm 0^\circ/11^\circ \pm 1^\circ$	$16^\circ \pm 1^\circ/4^\circ \pm 2^\circ$	0.9	0.822	27.48
$C09_0$	137	$120^\circ \pm 11^\circ/78^\circ \pm 0^\circ$	$317^\circ \pm 2^\circ/11^\circ \pm 2^\circ$	$227^\circ \pm 2^\circ/4^\circ \pm 2^\circ$	0.5	0.822	81.25
$C09_1$	179	$125^\circ \pm 13^\circ/78^\circ \pm 1^\circ$	$286^\circ \pm 0^\circ/11^\circ \pm 1^\circ$	$16^\circ \pm 1^\circ/4^\circ \pm 2^\circ$	0.9	0.618	26.12
$C10_0$	97	$238^\circ \pm 0^\circ/66^\circ \pm 0^\circ$	$75^\circ \pm 4^\circ/23^\circ \pm 1^\circ$	$342^\circ \pm 3^\circ/6^\circ \pm 1^\circ$	0.1	0.278	63.02
$C10_1$	219	$122^\circ \pm 2^\circ/78^\circ \pm 1^\circ$	$286^\circ \pm 0^\circ/11^\circ \pm 1^\circ$	$16^\circ \pm 0^\circ/3^\circ \pm 0^\circ$	0.9	0.822	55.24

Table 4.1: Clustering results for 316 earthquakes included in the focal mechanism catalogs of Hofstetter & Beyth (2003) and Ruch et al. (2021). For each clustering model, we list the number of events included, the average and standard deviation of the joint posterior PDF principal components as trend/plunge, the most likely estimate of the joint posterior PDF relative magnitude marginals, and the rake residual sum of squares (RSS) for the joint posterior PDFs.

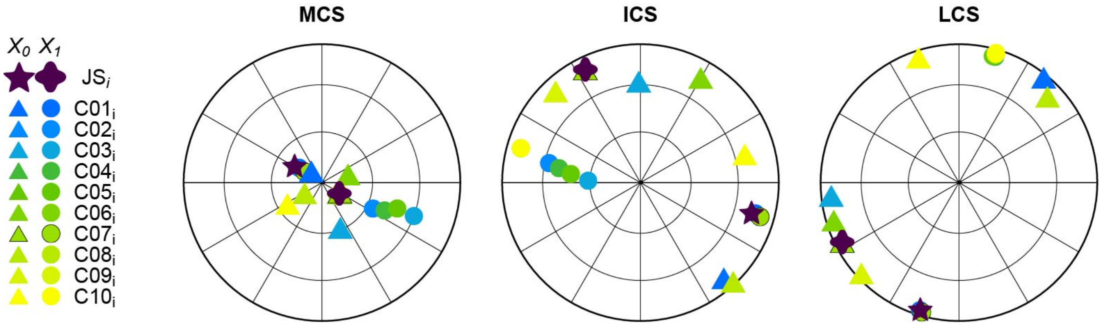

Figure 4.4: Orientations of the principal stresses for each cluster in the JS and CO1–C10 cluster models. Lower hemisphere shown in a Lambert projection, with circles indicating dips in 30° increments and radial lines indicating trends in 30° increments.

Clustering based on the distance metric $\mathcal{D}_G$ results in four clusters, G_0, G_1, G_2, and G_3, where we again segment the population at the mid-point of the dendrogram. The distance matrix corresponding to $\mathcal{D}_G$ is shown in Fig. 4.5, along with the dendrogram. As this clustering model reduces the variance within each cluster according to their inter-event distance, the clusters are geographically concentrated, with clusters localized to the Gulf of Aden (G_0), Main Ethiopian Rift (G_1), Red Sea (G_2), and the Afar Depression (G_3; Fig. 4.6). The principal components of stress of the posteriors of the four clusters reveal three normal stress regimes for G_0, G_1, and G_3, and one strike-slip regime corresponding to G_2 (Table 4.1). Note that while the MCS for G_2 is resolved to plunge approximately horizontal, if the trend of MCS for G_2 is parallel to the strike of the fault planes involved in this cluster's earthquakes, the expected faulting mechanism is normal slip rather than strike-slip.

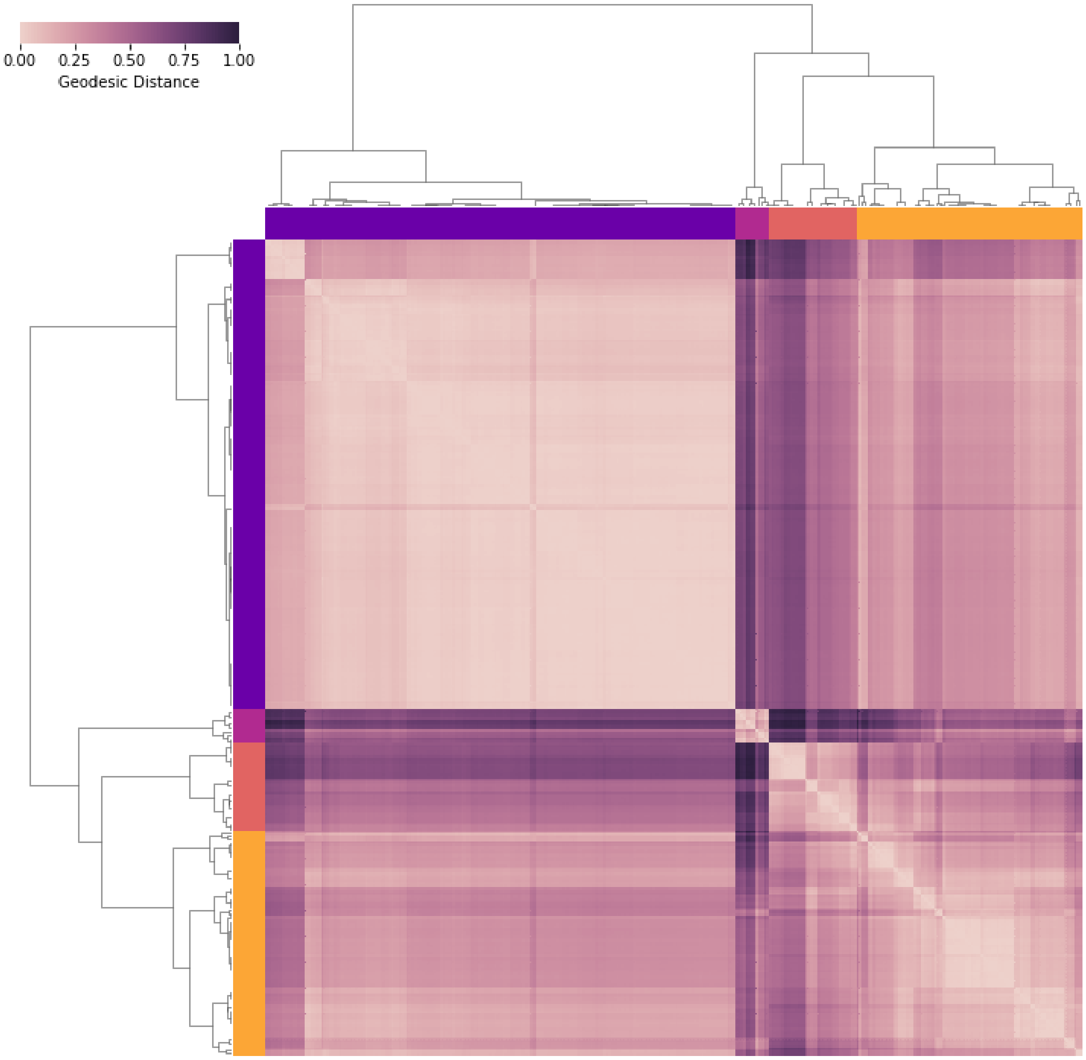

Figure 4.5: Geodesic distance matrix, $\mathcal{D}_G$, displayed as a heat map. Caption is as in Fig. 4.2.

Geodesic Distance

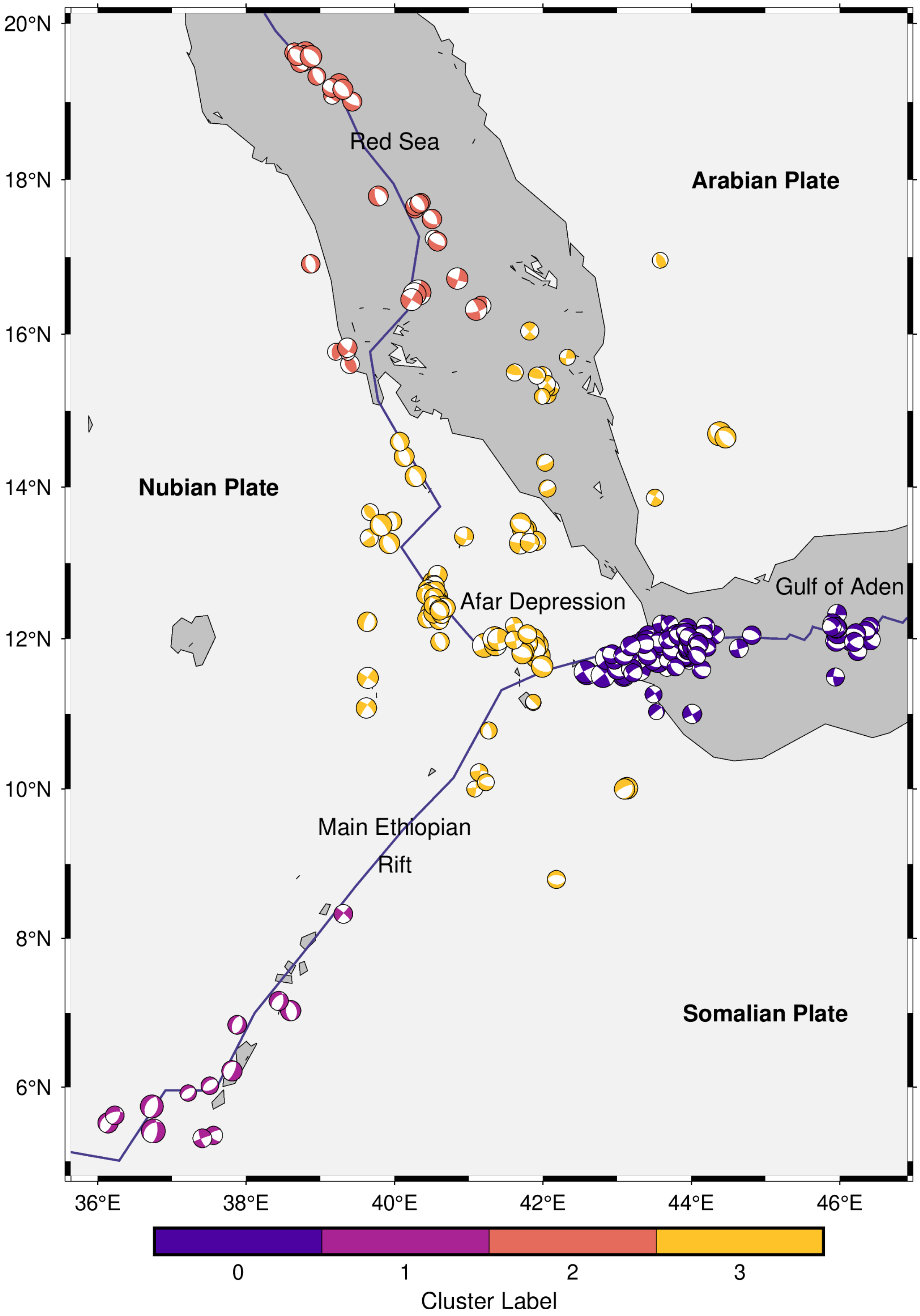

Figure 4.6: Focal mechanisms with T-quadrant colored according to which of the G clusters defined in Fig. 4.5 it belongs to.

In order to explore clusters that are informed by both similarity of stress posteriors and spatial proximity, we calculate ten additional clustering models that combine $\mathcal{D}_{JS}$ and $\mathcal{D}_G$ with varying weights on the contribution of the normalized $\mathcal{D}_G$. We refer to these clustering models as $C01$ through $C10$, where the numeric value denotes the weighting between 0.1 through 1.0. As above, we truncate each of the model's dendrograms at the mid-point of the linkage distances, which for all cases results in two clusters (*e.g.*, Fig. 4.7). At least one of the clusters in each model approximates a normal stress regime (Fig. 4.4; Table 4.1). A few clusters, with smaller weights on the geodesic distance, are characterized by oblique stress regimes, with moderately plunging MCS and ICS ($C02_1$, $C03_0$, $C03_1$, $C04_1$; Table 4.1); however, all clusters in each model are characterized be a nearly horizontal LCS (Fig. 4.4).

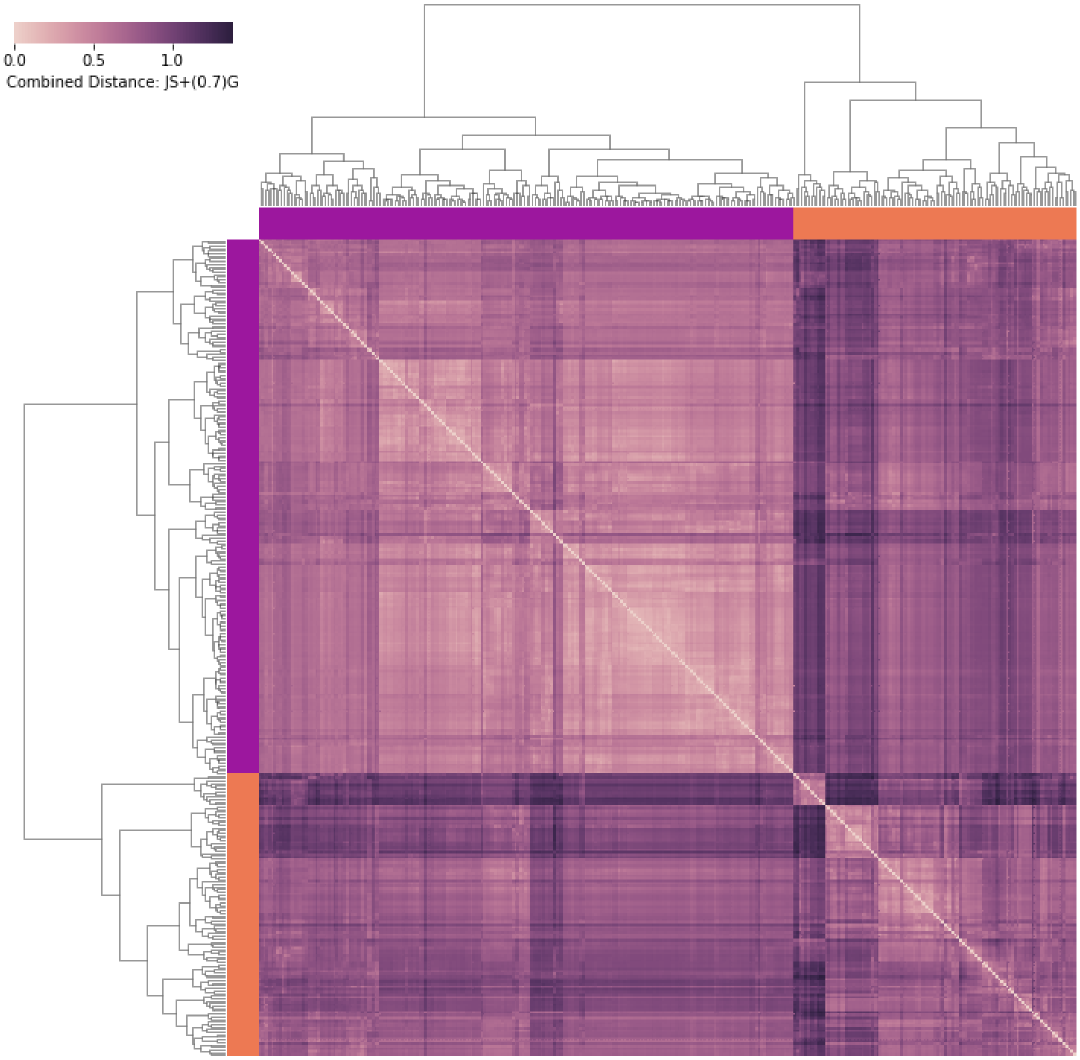

Figure 4.7: The symmetric distance matrix corresponding to the combined distance matrix $\mathcal{D}_{C07} = \mathcal{D}_{JS} + 0.7\frac{\mathcal{D}_{\mathcal{G}}}{max(\mathcal{D}_{\mathcal{G}})}$ displayed as a heat map. Caption is as in Fig. 4.2.

We find that all of the combined distance metric approaches resolve one spatially concentrated cluster in the Gulf of Aden, and a second cluster that spans the Main Ethiopian Rift, Afar Depression, and the Red Sea (*e.g.*, Fig. 4.8; the distance matrix heat-maps, dendrograms, and maps of clustered focal mechanisms for all combined models, $C01$– $C10$, can be found in the Supplemental Material). The geographic distribution of the clusters in the $C01$–$C10$ models is similar to the JS clusters where we only considered similarity in the stress posteriors (*c.g.*, Fig. 4.3, Fig. 4.8). The largest variation between the combined metric models occurs in the clustering of events beneath the Afar Depression where labeled events strongly overlap (*e.g.*, Fig. 4.8, and figures in the Supplemental Material).

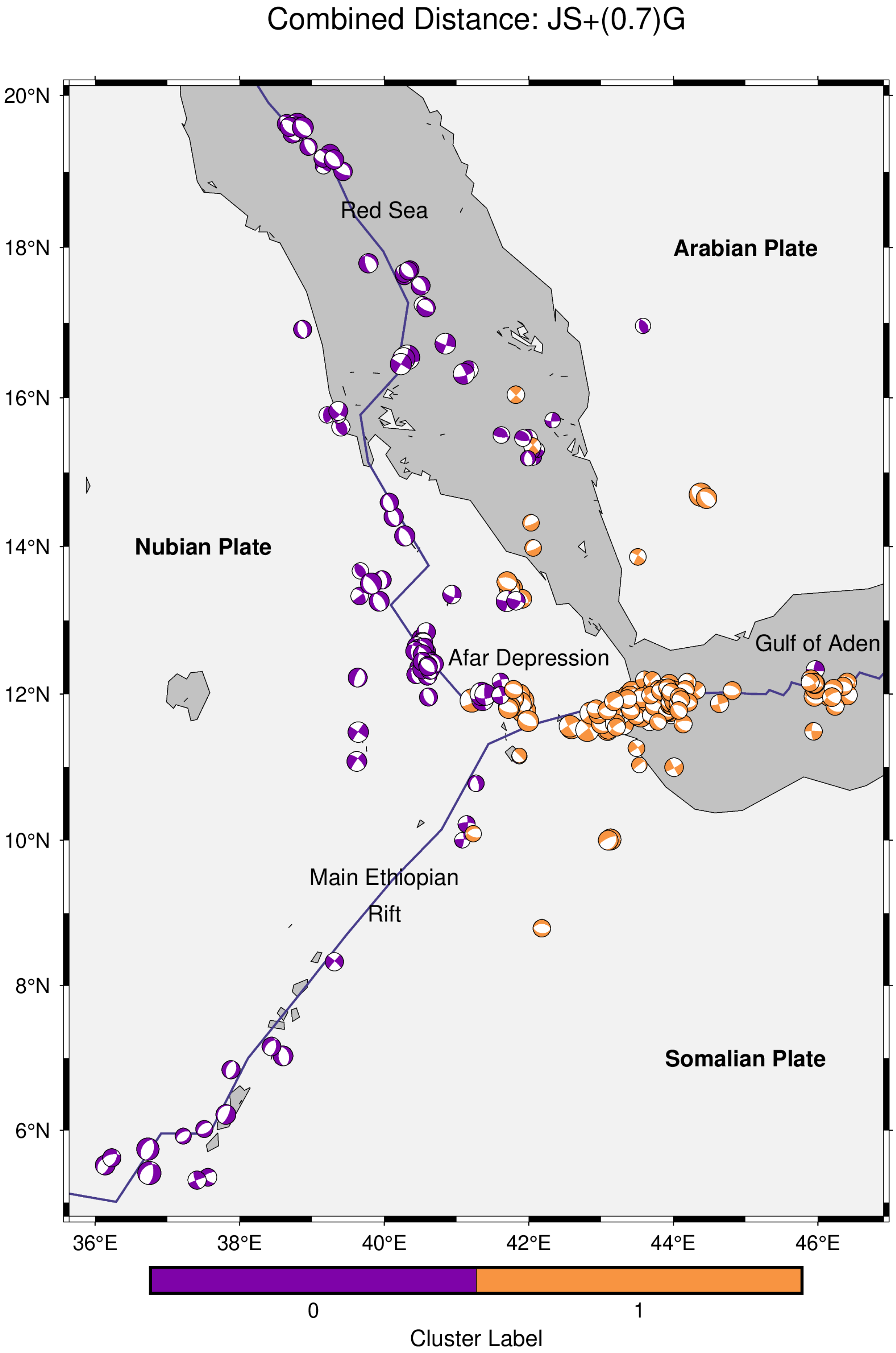

Figure 4.8: Focal mechanisms with T-quadrant colored according to which of the $C07$ clusters defined in Fig. 4.7 it belongs to.

We can gauge the fit of the clusters through the rake residual sum of squares (RSS), a metric that indicates the total variance within the calculated residuals for each of the clusters, which is described in more detail in the Discussion section. The two clusters in the JS cluster model have RSS of about 30 and 49, while the individual clusters in the $C01 - C10$ models varies from 16 to 144 (Table 4.1). The cluster model $C07$ has the lowest total RSS of the two clusters of all of the cluster models created, with RSS values of 25 and 45 of clusters $C07_0$ and $C07_1$, respectively (Table 4.1). The two clusters in $C07$ have a spatial distribution similar to the clusters in the JS model, but with less overlap far from the Afar Depression (*cf.*, Figs. 4.3 and 4.8). The largest geographical overlap between the clusters is in the southern Red Sea, off the coast of Yemen (Fig. 4.8). The orientation of stress determined from the focal mechanisms in the two $C07$ clusters are virtually the same as those from the earthquakes in the two JS clusters (Fig. 4.4). The geographic attribution of the clusters, with clusters dominated by either Gulf of Aden or Red Sea to Ethopian rift system earthquakes, largely persists for all of the combined distance clustering models considered. The orientations of the principal stresses do vary between the cluster models, with most variation in the orientation of ICS (Fig. 4.4). Nevertheless, in all of the models MCS in both clusters is near vertical, and except for cluster model $C10$, each model has one cluster characterized by a sub-SSW-NNE trending LCS, and one with a SW-NE trending LCS (Table 4.1 and Fig. 4.4). That all of the cluster models converge supports a similarity in the background stress extending from the Red Sea south through the Main Ethiopian rift, which is a similar orientation to, but with an approximately 45° counter-clockwise rotation in the trend of the LCS, as the background stress in the Gulf of Aden (Fig. 4.8).

4.4 Discussion

4.4.1 Clustering model validation

To determine the best representation of the background seismogenic stress from the focal mechanisms, we must examine how well our resulting clustering models fit the focal mechanism observations. We calculate joint posterior PDFs from the stress posterior PDFs for the focal mechanisms included in each cluster, as described above. From these joint posteriors, we calculate the direction of the maximum shear stress on each of the nodal planes, assumed to be the rake during an earthquake — in other words, we assume that when a fault slips, it does so, on average, in the direction in which the shear stress on that fault is the largest, the so-called Wallace-Bott assumption. Finally, we compute the clustering model misfit as the residual sum of squares (RSS) for the predicted rake versus the observed rake from each nodal plane (Table 4.1). We find that all of the joint posterior PDFs calculated for the clustering models result in a rake RSS that is less than if we were to calculate joint posterior PDFs from randomized clusters. The clustering model with the smallest misfit, $C07$, has a total rake RSS of 69 over its two clusters (Table 4.1), which is less than the next smallest rake RSS of 78 for clustering model JS (Table 4.1). All other clustering models possess an increased total rake RSS, including clustering model G, despite G possessing two additional clusters compared to the other models. One might expect that the increased number of clusters in model G would allow for an improved fit for localized seismicity. However, the variance of the clusters in G was only minimized with respect to inter-event distance.

Our regional representations of stress through the joint posteriors associated with each of the clusters may not be the true background seismogenic stress for all of the events in that cluster. For instance, it is possible that a localized stress that diverges from the regional stress may be responsible for an isolated group of earthquakes within one of the clusters. Case in point is the Afar Depression, which is not only a seismically active region but volcanic as well, and many studies have argued for a relationship between seismic swarms and volcanic activity (*e.g.*, *Ruch et al.*, 2021). Volcanic activity within the Afar might perturb the stress field from that of the Red Sea and Main Ethiopian Rift, and the slip in an isolated earthquake, or few earthquakes, would be reflective of those perturbed stresses and not of the regional stress field. However, we do not find a distinct cluster associated with the Afar, and we do not observe temporal patterns in the clustering of seismicity. It may simply be that there are not enough earthquakes in the Afar, relative to the larger region, that would allow the disambiguation of an Afar cluster from the Red Sea-to-Main Ethiopian Rift cluster. In regards to the second note, if the stresses driving the Afar earthquakes were distinct from the regional stress, we expect to see a temporal variation. Our results do not identify temporal patterns in stress, however, this may be due to a lack of focal mechanism data for the small-magnitude earthquakes involved in the seismic swarms. Finally, the uncertainty in the focal mechanisms may be underestimated, either in total or for some subset of them. Only a limited number of seismic stations were installed during the period covering the early earthquakes in the focal mechanism catalog we consider, and those stations had poor azimuthal coverage of the Afar (Fig. 4.1); as a result, the source parameters we take as data may have higher errors than we assume.

We return to the point that a subset of isolated earthquakes within a given cluster might actually be due to localized seismogenic stresses perturbed from the more regional average. A related issue is that some of the focal mechanisms we consider might be erroneous representations of the true slip in that earthquake. To address these issues collectively, we can consider focal mechanisms that do not represent the regional background stress effectively as noise or outliers, and by repeating the clustering allowing for the removal of these outlier events, we can assess the degree to which potentially divergent focal mechanisms might be affecting our clustering model. We identify outliers if events exceeded a maximum dendrogram height threshold from the JS model dendrogram's base to the nearest cluster. We iterated over varying thresholds, but for brevity, only report the outcome of a maximum height threshold of 0.4 in the Supplemental Material (Table 4.S1). This maximum distance threshold results in a removal of 39 outliers of the 316 events (Table 4.S1). We find that clustering the remaining 277 events reduces the rake RSS for most clustering models. The clustering model from the dataset following the removal of outlier events with the minimum rake RSS is $C01D$ (Table 4.S1). $C01D$ is formed by clustering the combined distance matrix with a weight of 0.1 of the normalized geodesic distance between event locations, compared to the weight of 0.7 for the best-fit model of all events, $C07$. Notably, however, the marginals of the joint posterior PDFs determined for both of these models are nearly identical. For both models, the first cluster results in a nearly vertical MCS, WNW-ESE horizontal ICS, ENE-WSW horizontal LCS, and large relative magnitudes of stress for events that spatially extend through the southern Red Sea and the Main Ethiopian Rift. The second cluster for both models results in near- to sub-vertical MCS, near- to sub-horizontal E-W ICS, horizontal N-S LCS, and large relative magnitudes of stress with spatial concentration of events in the east of the Afar Depression and the Gulf of Aden. As the stress tensors estimated from the best-fit models of both the original and outlier removed approaches indicate the same states of regional stress, we feel that our estimated stress tensors are robust given the earthquakes considered. Finally, we take $C07$ as our preferred model for regional stress for the Afar Depression as it makes fewer presumptions of the data.

4.4.2 Previous stress estimates and tectonic implications

There are abundant measurements of near-surface stresses from borehole breakouts and induced fractures within exploration wells to the west and north of our study area. *Bosworth* (2008) interpreted observations from borehole breakouts, drilling-induced fractures, volcanic vents and earthquake stress inversions to delineate stress fields for the central and northern Nubian Plate. The Central Africa Intra-Plate stress field interpreted by *Bosworth* (2008) lies to the west of our study region and is characterized by a generally E-W maximum horizontal stress, which transitions in a 90° degree rotation into the Mediterranean Convergence Zone stress field to the north and west has a N-S maximum horizontal stress.

Smaller scale stress rotations have been noted for the Gulf of Suez in the northern Red Sea, where induced fractures and borehole breakout measurements have revealed a maximum horizontal stress from the Central Sub-Basin of 141° from borehole breakouts and 134° from fractures (*Bosworth and Durocher*, 2017), Southern Sub-Basin of $100^\circ \pm 18^\circ$ (*Bosworth and Taviani*, 1996), and to the south in the Hilal oil field of 150° (*Radwan et al.*, 2021).

Previous studies of regional stresses for the regions surrounding the Afar Depression consider focal mechanism and paleo-slip data. These studies are in general agreement that a normal stress regime (*i.e.*, a vertical MCS) characterizes this triple junction setting, however, a broad range of horizontal stress estimates have been determined. For example, *Delvaux and Barth* (2010) grouped 332 focal mechanisms from the East African Rift System into 24 groupings based on geographic locality, the similarity of faulting mechanism, and presumed tectonic setting, with five of their groupings overlapping with our study area. *Delvaux and Barth* (2010) inverted 16 focal mechanisms for the Red Sea, resulting in a near-vertical MCS, and horizontal ICS and LCS, trending to the NW-SE and NE-SW, respectively. In contrast, a study by *Abdelfattah et al.* (2020) of the eastern flank of the Red Sea within the Arabian plate inferred a moderately-plunging MCS trending to the southwest, a moderately-plunging ICS trending to the northeast, and a horizontal LCS trending to the northwest-southeast from the inversion of focal mechanisms for a strike-slip $M_w 4.0$ earthquake and 9 $M_w 2.0 - 2.8$ strike-slip aftershocks. For the Main Ethiopian Rift, *Delvaux and Barth* (2010) inverted seven focal mechanisms and determined a near-vertical MCS and near-horizontal ICS and LCS trending WNW-ESE and NNE-SSW, respectively. *Muluneh et al.* (2018) performed a stress inversion study from 44 focal mechanisms localized to the Main Ethiopian Rift, finding near-vertical MCS, near-horizontal ICS and LCS trending nearly north-south and east-west respectively, with a 20° rotation from that inferred by *Delvaux and Barth* (2010) for the same locality. Our best-fit clustering model indicates that seismicity extending from the Main Ethiopian Rift, through the western Afar Depression, and along the southern Red Sea is consistent with a normal stress regime with a horizontal, NW-SE trending ICS, and NE-SW trending LCS ($C07_0$; Fig. 4.8, Table 4.1).

For the eastern Afar, *Delvaux and Barth* (2010) inverted 31 focal mechanisms and found a near-vertical MCS and horizontal ICS and LCS, trending nearly N-S and E-W, respectively; however, for 33 events that they divided into the Afar Depression, they argued for a substantial rotation in the principal components of stress, with a near-vertical ICS, and horizontal MCS and LCS trending to the WNW-ESE and SSW-NNE, respectively. A paleo-stress study by *Sue et al.* (2014) investigated the Ali Sabieh range in the southeast of the Afar Depression. They concluded from a population of strike-slip and dip-slip paleo-slip data that the location experienced extension characterized by a sub-vertical plunging MCS and horizontal LCS trending between ENE-WSW to WNW-ESE, followed by a transition to a strike-slip stress regime, which was characterized by a vertical ICS and horizontal MCS and LCS trending N-S to NNW-SSE and E-W to ENE-WSW, respectively (*Sue et al.*, 2014). While their study did not measure the timing of the historic slip records, *Sue et al.* (2014) suggest that the rotation of MCS and ICS may have occurred coincident with transitions in regional tectonics in the Oligo-Miocene, circa the advent of the Afar Triple Junction. Continuing to the east, *Delvaux and Barth* (2010) additionally found a strike-slip stress regime for the Gulf of Aden from the inversion of 15 focal mechanisms that resulted in a near-vertical ICS, and horizontal MCS and LCS trending nearly E-W and N-S, respectively.

The cluster from our best fitting model that encompasses seismicity in the east of the Afar Depression and the Gulf of Aden reveals a normal stress regime with a horizontal, ESE-WNW trending ICS, and horizontal, NNE-SSW trending LCS ($C07_1$; Fig. 4.8, Table 4.1). The maximum and minimum horizontal stress for the spatial groupings for the Afar Depression and Gulf of Aden from *Delvaux and Barth* (2010) are within 6° of our results, however, *Delvaux and Barth* (2010) vertical ICS indicates a strike-slip regime for the region rather than the normal stress regime we find from our work. Possible explanations for this discrepancy are (1) that the magnitudes of MCS and ICS are similar, which is supported by our estimate of a large relative magnitude of stress for our joint marginal of δ, or (2) one of the principal stresses is oriented close to the average fault planes of the earthquakes included in this cluster, which is supported by the work of *Medina Luna* (2015), which demonstrated the inherent inability to distinguish an MCS distinct from ICS for focal mechanisms under this condition. The observations of two populations of slip regimes (*i.e.*, strike-slip and normal) from the *Sue et al.* (2014) paleo-stress study might also lend support to ICS and MCS of similar magnitudes in the southeastern Afar.

The joint posterior PDFs we determine from the two clusters of our best fit model for regional crustal stress reveal a 47° counter-clockwise rotation of the horizontal principal components of stress from West to East across the east African coastal region. There is a diffuse geographic boundary between the events labeled for the two clusters that aligns with the eastern border of the Afar Depression where it is bounded by the Danakil Block. A possible mechanism accommodating this rotation of stress is the counter-clockwise rotation of the Danakil Block relative to the Nubian Plate at a rate of $1.9^\circ Myr^{-1}$ and the Arabian Plate at a rate of $1.5^\circ Myr^{-1}$ (*McClusky et al.*, 2010).

4.4.3 Motivation for further investigation of the impact of data selectivity on stress inferences

While the discrepancies in the focal mechanism stress inversion studies of the same localities may be sensitive to fine scale rotations in stress as the exploration well data is proposed to be, we suggest that these estimates for the same localities are at least in part sensitive to data selectivity and that the degree to which these discrepancies reflect physical transitions in stress should be further investigated. Major differences in how data is processed in stress inversion studies include authors' selectivity for focal mechanisms that are arbitrarily deemed similar, choice of boundaries in which to group focal mechanisms, and the designation of a slip surface from seismically ambiguous nodal planes to produce a preferred model fit. In contrast, our methodology seeks to remove potential biases through probabilistic inference from non-informative prior PDFs and data with quantified uncertainties, albeit loosely, for estimating tensorial crustal stress from individual observations of earthquake slip. Furthermore, we use a clustering techniques that reduces bias due to manually deciding cluster boundaries within which it is assumed that the seismogenic stress is the same, or at least is the same within model resolution. While our methodology stands to be improved, such as by determining the sensitivity of regional stress inferences from incomplete datasets or the spatial and temporal breadth of data that should be incorporated for a robust estimate, we believe that our work provides direction for determining regional patterns in seismicity based in data, avoiding subjective treatment of that data. In future work, we intend to investigate the sensitivity of our methodology to incomplete or partial datasets. Additionally, we will incorporate a more sophisticated uncertainty quantification strategy for the focal mechanism and earthquake location data.

4.5 Conclusions

We present a novel means of clustering earthquake focal mechanisms based on stress posterior PDF estimates and the inter-event geodesic distances between earthquakes. We propose this clustering algorithm to group earthquakes and objectively infer regional seismogenic stresses. We estimate stress posterior PDFs from the focal mechanisms of 316 earthquakes in the Afar Depression and surrounding rift axes, the southern Red Sea, the Main Ethiopian Rift, and the western Gulf of Aden. Our best-fit model results in two clusters; one is concentrated in the Gulf of Aden, while the second spans the Main Ethiopian Rift, Afar Depression, and the Red Sea. We calculate the joint posterior PDF to infer regional stresses consistent with all these clusters' earthquakes. We find that a normal stress regime characterizes both clusters and infer a counter-clockwise rotation of the horizontal principal components of stress (*i.e.*, the ICS and LCS) from the regional stress inferred for the Main Ethiopian Rift, western Afar Depression, and the Red Sea, compared to the Gulf of Aden. The transition between these two clusters occurs spatially near the Danakil Block. Our inferred regional stress models are robust to noise in the earthquake focal mechanism catalog, where noise might originate as focal mechanisms resulting from localized perturbations from the regional stress or as focal mechanisms that are erroneous representations of the true earthquake mechanics. Discrepancies noted by past stress studies for this region may likely be due to differences in data selectivity, as well as the possibility of mechanical differences along tectonic boundaries localized to the eastern Afar Depression. Future work should explore the sensitivity of stress inversion studies to data selectivity as a means of working towards objective stress estimation strategies.

Data and Resources

The Supplemental Material includes figures of each of the clustering models as maps and time-series, as well as a table and accompanying set of figures demonstrating the results of removing noisy focal mechanisms from the clustering experiments. Data used in this study are from *Hofstetter and Beyth* (2003) and *Ruch et al.* (2021), whose publications are listed in the references. All figures in this study were generated using the Generic Mapping Tools version 6.1.1 (www.generic-mapping-tools.org; *Wessel et al.*, 2019).

Acknowledgments

This research was funded in part by Department of Earth and Environmental Science, University of Michigan fellowships from generous alumni donations.

4.6 Supplemental Material - Chapter 4

4.6.S1 Tables

Grouping	Events	MCS	ICS	LCS	δ	ς	RSS
Noise	39	-	-	-	-	-	-
JSD 0	177	302° ± 1°/78° ± 3°	106° ± 0°/12° ± 3°	196° ± 0°/3° ± 1°	0.9	0.618	34.23
JSD 1	100	132° ± 19°/77° ± 3°	339° ± 8°/11° ± 4°	248° ± 8°/6° ± 1°	0.9	0.822	40.22
C01D 0	116	123° ± 7°/78° ± 0°	334° ± 3°/10° ± 1°	243° ± 3°/6° ± 1°	0.9	0.822	35.26
C01D 1	161	115° ± 7°/56° ± 17°	281° ± 5°/33° ± 17°	16° ± 1°/6° ± 2°	0.9	0.822	22.29
C03D 0	96	237° ± 8°/66° ± 2°	74° ± 10°/23° ± 2°	342° ± 10°/6° ± 1°	0.1	0.278	43.74
C03D 1	181	109° ± 1°/35° ± 5°	276° ± 4°/54° ± 5°	15° ± 1°/6° ± 1°	0.9	0.822	25.75
C04D 0	119	129° ± 22°/78° ± 0°	337° ± 9°/9° ± 2°	246° ± 8°/7° ± 2°	0.9	0.822	45.37
C04D 1	158	112° ± 7°/51° ± 18°	279° ± 5°/39° ± 18°	16° ± 1°/5° ± 2°	0.9	0.822	21.73
C06D 0	112	139° ± 30°/78° ± 2°	348° ± 21°/9° ± 3°	254° ± 17°/6° ± 2°	0.9	0.822	55.24
C06D 1	165	302° ± 1°/76° ± 6°	106° ± 1°/14° ± 6°	197° ± 0°/4° ± 1°	0.9	0.618	27.39
C07D 0	129	238° ± 1°/78° ± 0°	131° ± 4°/3° ± 1°	41° ± 5°/11° ± 0°	0.5	0.822	115.77
C07D 1	148	118° ± 6°/59° ± 15°	282° ± 4°/30° ± 15°	17° ± 1°/6° ± 2°	0.9	0.822	22.47
C08D 0	83	238° ± 0°/66° ± 1°	76° ± 7°/23° ± 1°	343° ± 6°/7° ± 2°	0.1	0.278	49.54
C08D 1	194	302° ± 1°/77° ± 3°	120° ± 14°/12° ± 3°	184° ± 13°/3° ± 1°	0.9	0.618	53.8
C10D 0	82	238° ± 0°/66° ± 0°	76° ± 6°/23° ± 1°	343° ± 5°/7° ± 2°	0.1	0.278	51.2
C10D 1	195	122° ± 0°/77° ± 3°	286° ± 0°/12° ± 3°	17° ± 0°/3° ± 1°	0.9	0.822	39.69

Table 4.S1: Supplemental clustering results allowing for removal of outlier events from the original 316 earthquakes included in the focal mechanism catalogs of Hofstetter & Beyth (2003) and Ruch et al. (2021). For each grouping, the number of events included is listed, followed by the average and standard deviation of the marginals of the joint posteriors, and the residual sum of squares (RSS) for rake predicted from the joint posteriors for the nodal planes of each of the focal mechanisms in the cluster versus nodal plane rake observed by the catalog. Note that the following clustering models were identical and only the first of these is shown: C01D and C02D; C04D and C05D; C08D and C09D.

4.6.S2 Figures

4.6.S2.1 Clustering Results of Models from Main Text

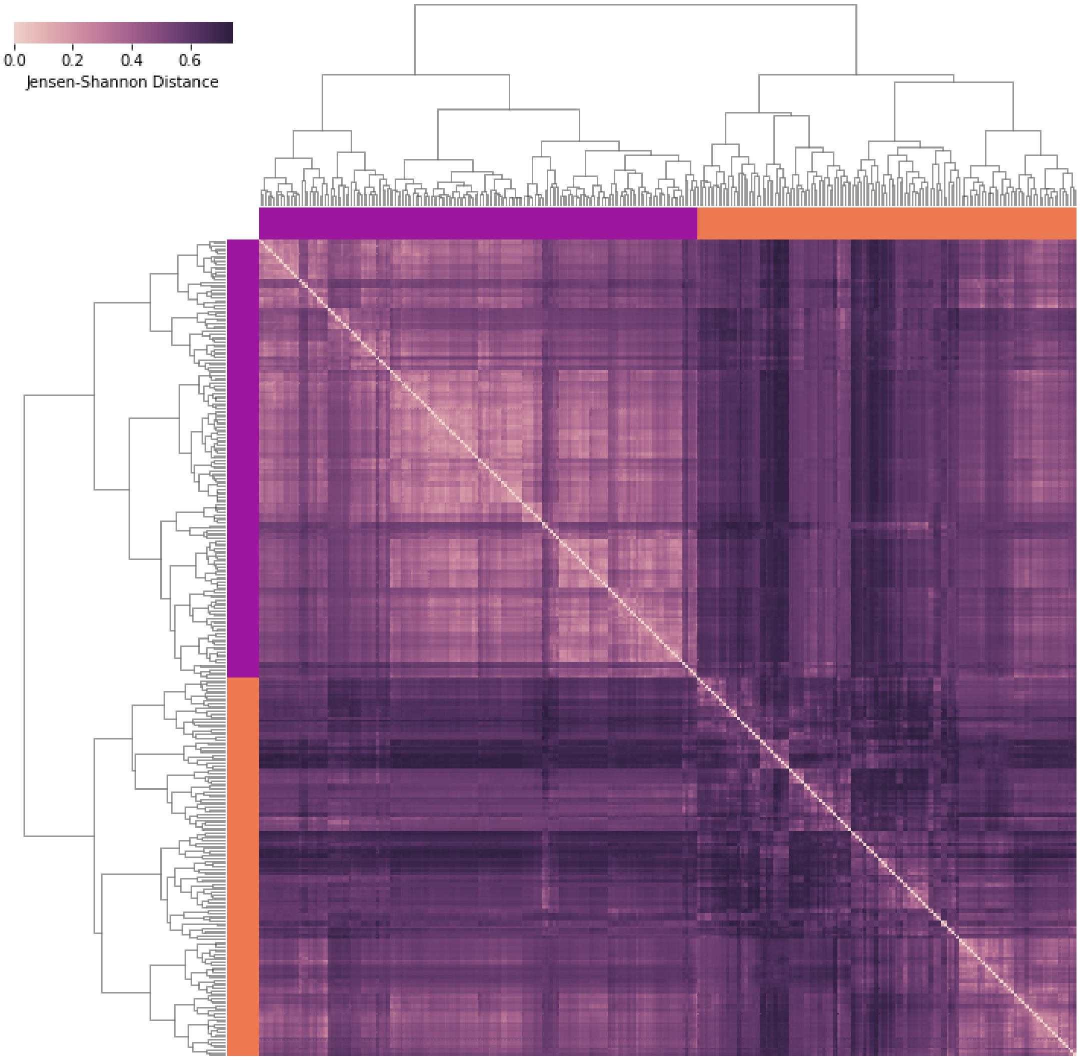

Figure 4.S1: The symmetric distance matrix corresponding to $\mathcal{D}_{JS}$ displayed as a heat map. The dendrogram formed through agglomerative hierarchical clustering of $\mathcal{D}_{JS}$ with Ward linkage is shown at the top and left of the distance matrix, with the purple or orange solid bars indicating the elements in each of the two clusters formed by breaking the top-level of the dendrogram. Appears as Fig. 4.2 in the text.

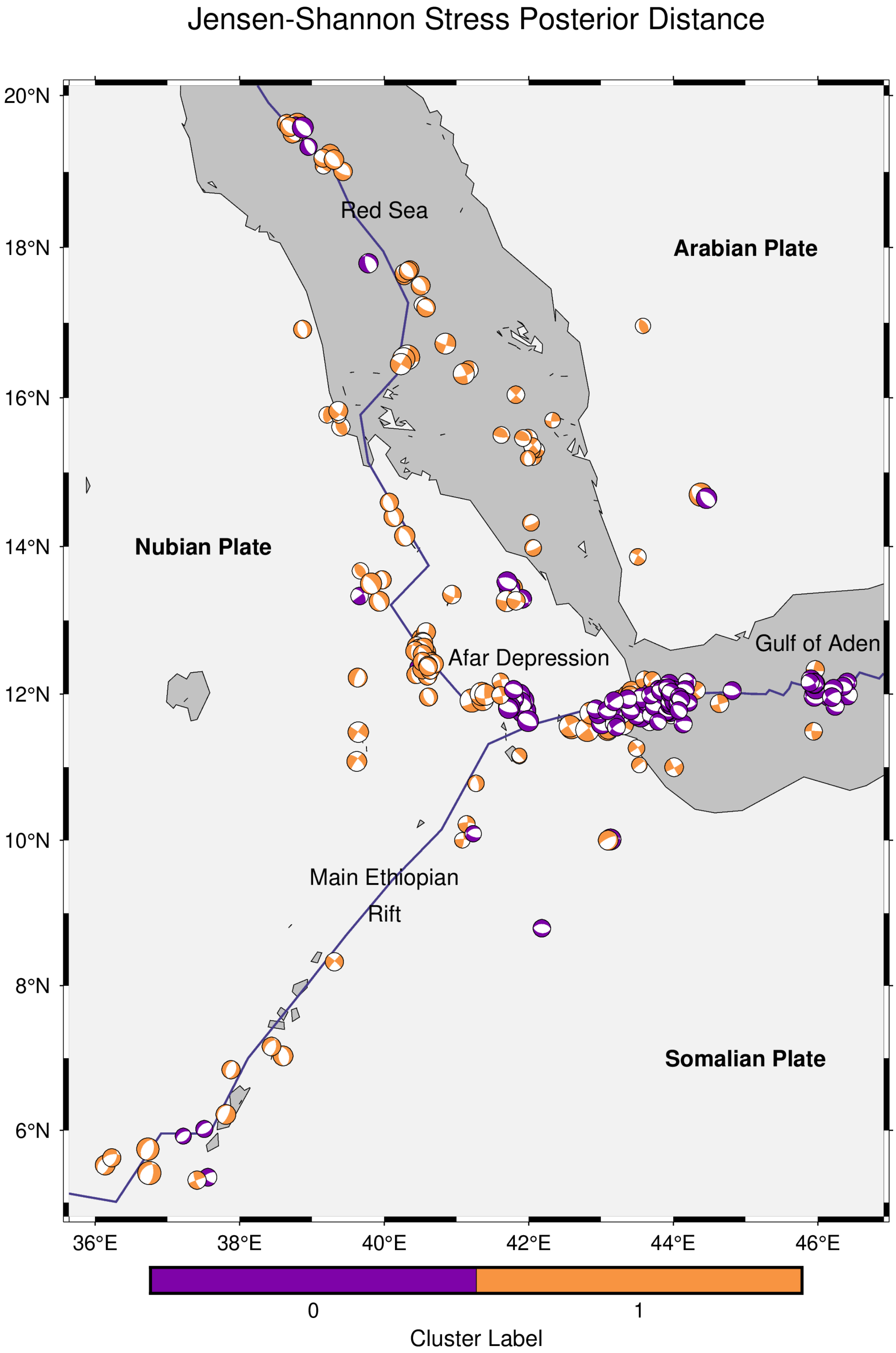

Figure 4.S2: Focal mechanisms with T-quadrant colored according to which of the JS clusters defined in Fig. 4.S1 it belongs to. Appears as Fig. 4.3 in the text.

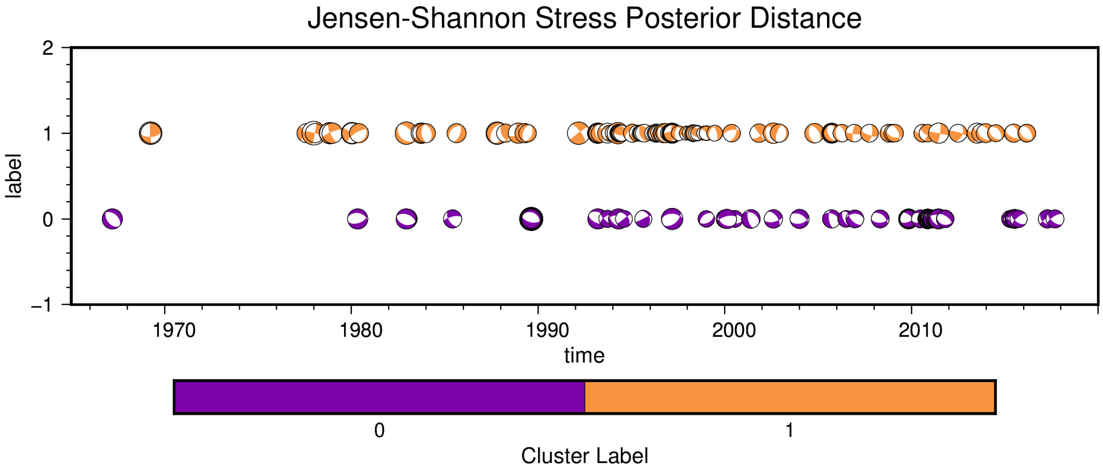

Figure 4.S3: Focal mechanisms with T-quadrant colored according to which of the JS clusters defined in Fig. 4.S1 it belongs to plotted through time.

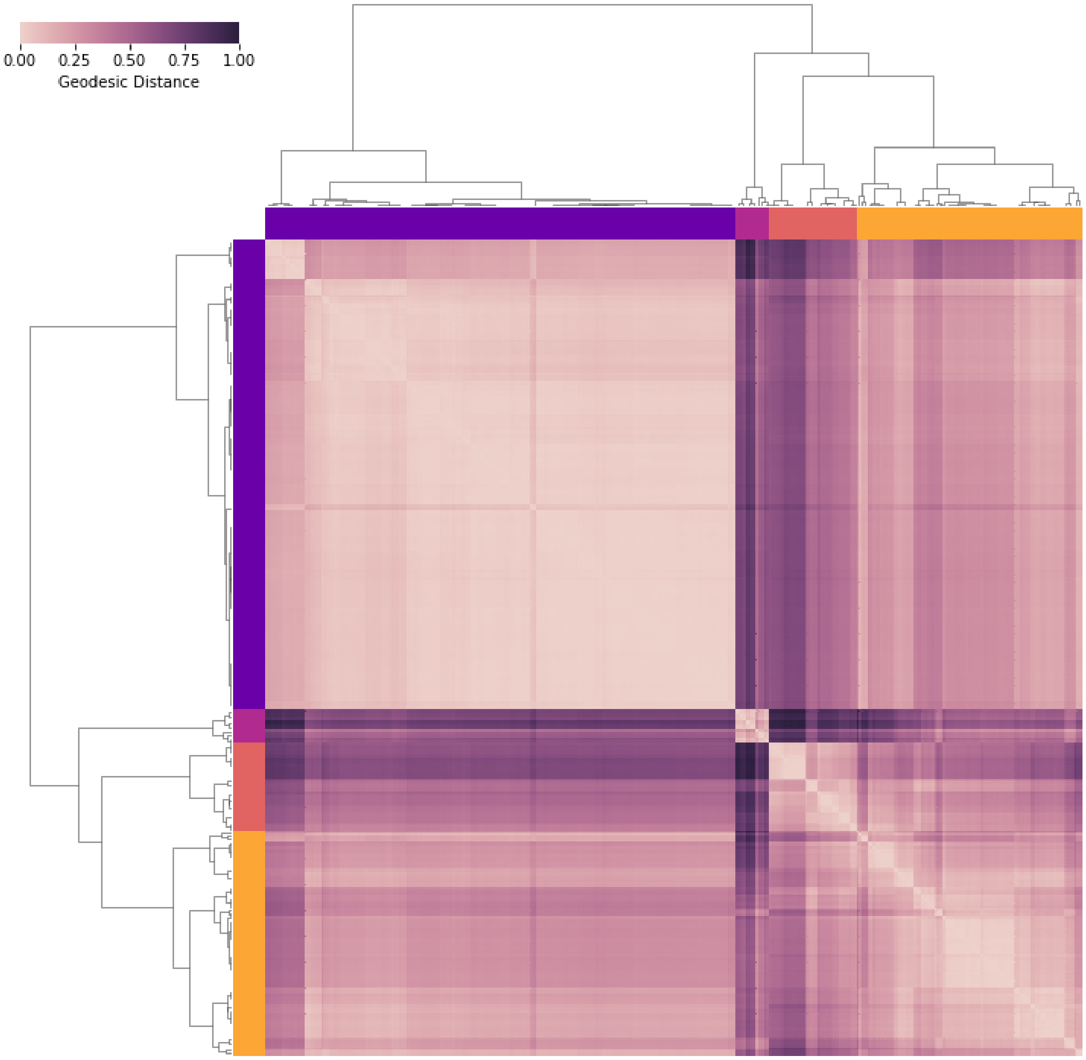

Figure 4.S4: The symmetric distance matrix corresponding to $\mathcal{D}_G$ as a heatmap. Caption is as in Fig. 4.S1. Appears as Fig. 4.5 in the text.

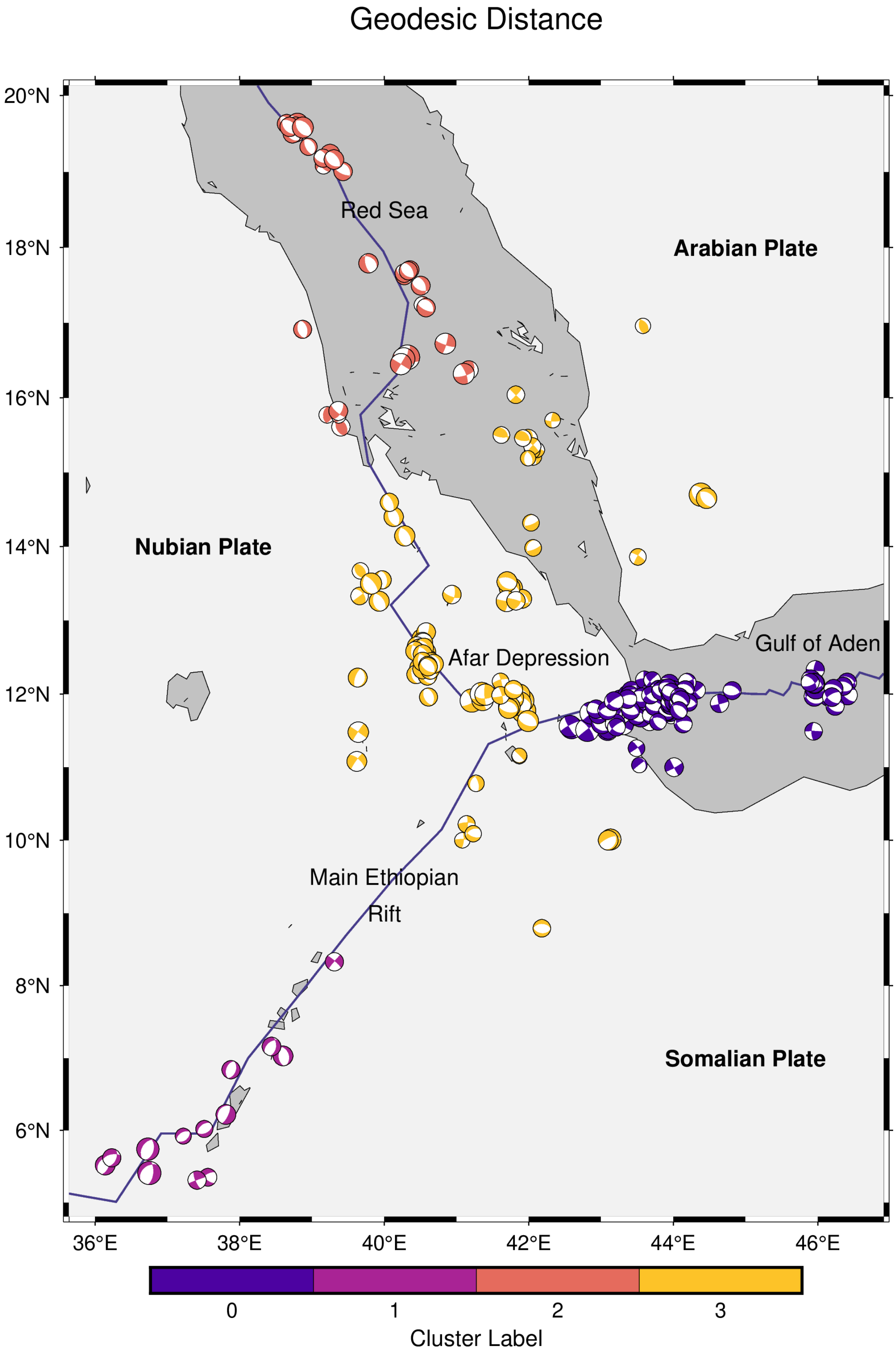

Figure 4.S5: Focal mechanisms with T-quadrant colored according to which of the G clusters defined in Fig. 4.S4 it belongs to. Appears as Fig. 4.6 in the text.

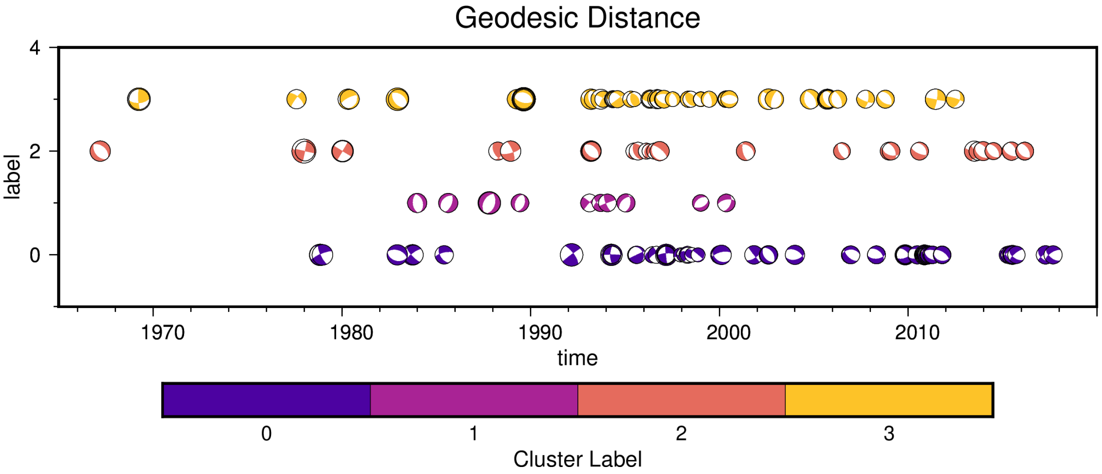

Figure 4.S6: Focal mechanisms with T-quadrant colored according to which of the G clusters defined in Fig. 4.S4 it belongs to plotted through time.

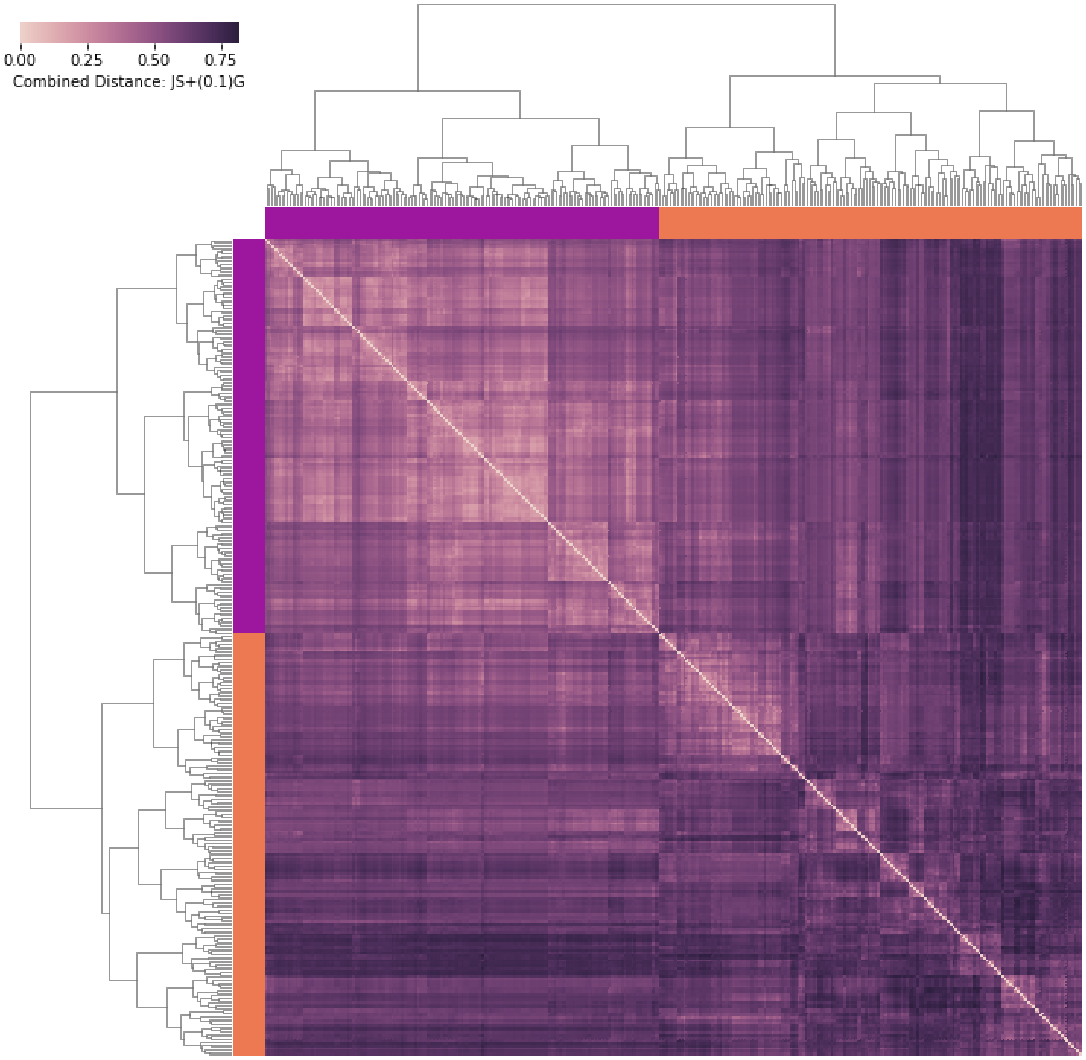

Figure 4.S7: The symmetric distance matrix corresponding to $\mathcal{D}_{C01} = \mathcal{D}_{JS} + 0.1\frac{\mathcal{D}_{\mathcal{G}}}{max(\mathcal{D}_{\mathcal{G}})}$ as a heatmap. Caption is as in Fig. 4.S1.

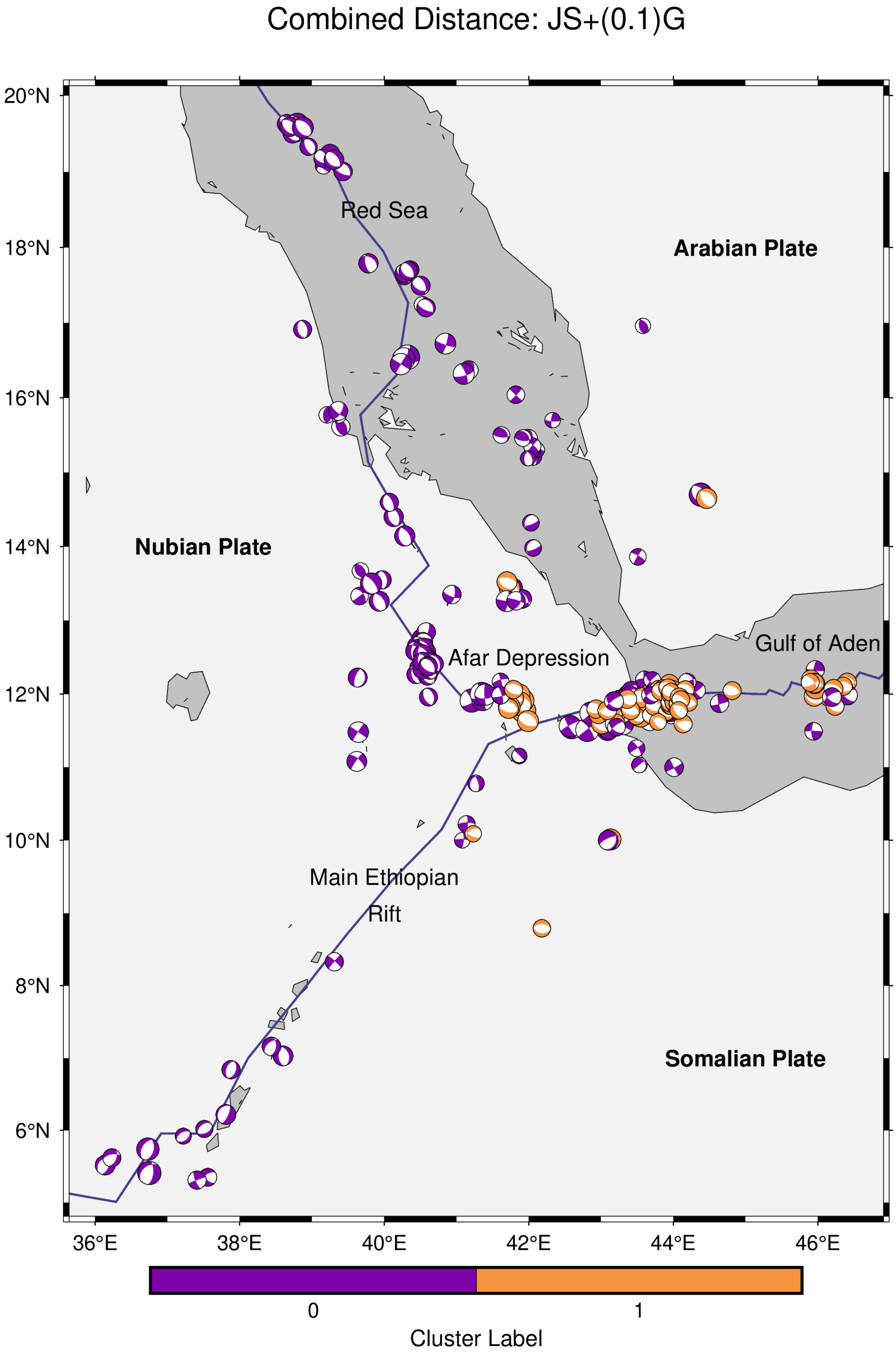

Figure 4.S8: Focal mechanisms with T-quadrant colored according to which of the $C01$ clusters defined in Fig. 4.S7 it belongs to.

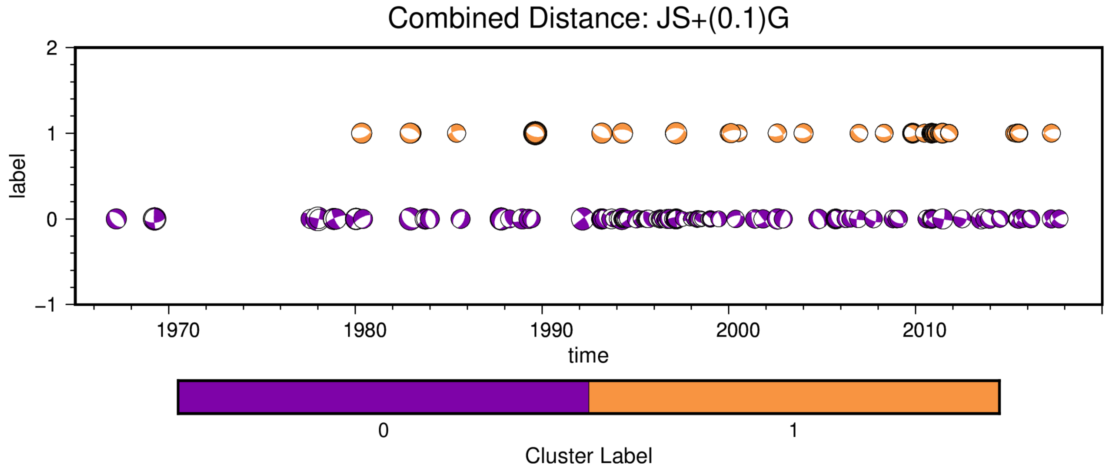

Figure 4.S9: Focal mechanisms with T-quadrant colored according to which of the $C01$ clusters defined in Fig. 4.S7 it belongs to plotted through time.

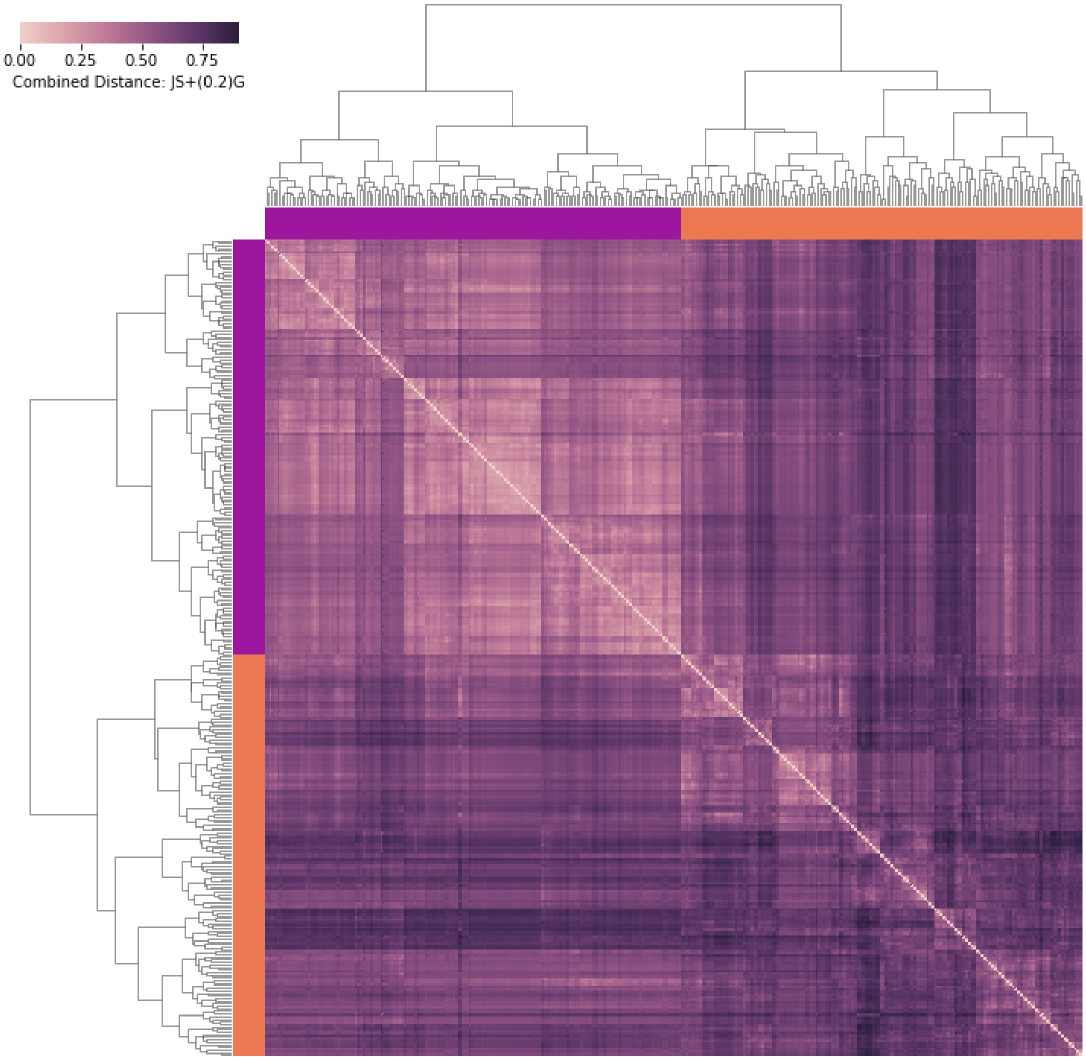

Figure 4.S10: The symmetric distance matrix corresponding to $\mathcal{D}_{C02} = \mathcal{D}_{JS} + 0.2\frac{\mathcal{D}_{\mathcal{G}}}{max(\mathcal{D}_{\mathcal{G}})}$ as a heatmap. Caption is as in Fig. 4.S1.

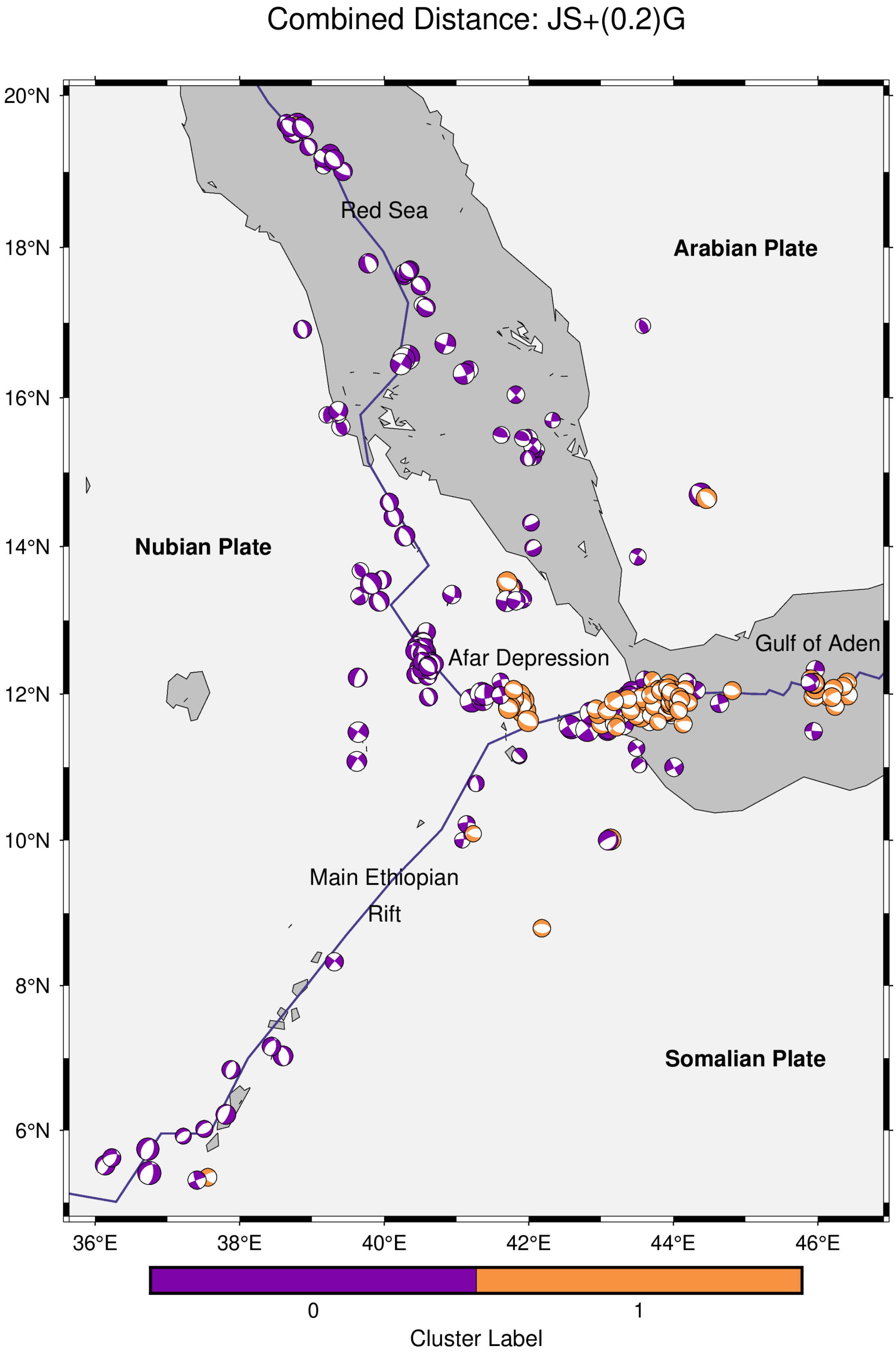

Figure 4.S11: Focal mechanisms with T-quadrant colored according to which of the $C02$ clusters defined in Fig. 4.S10 it belongs to.

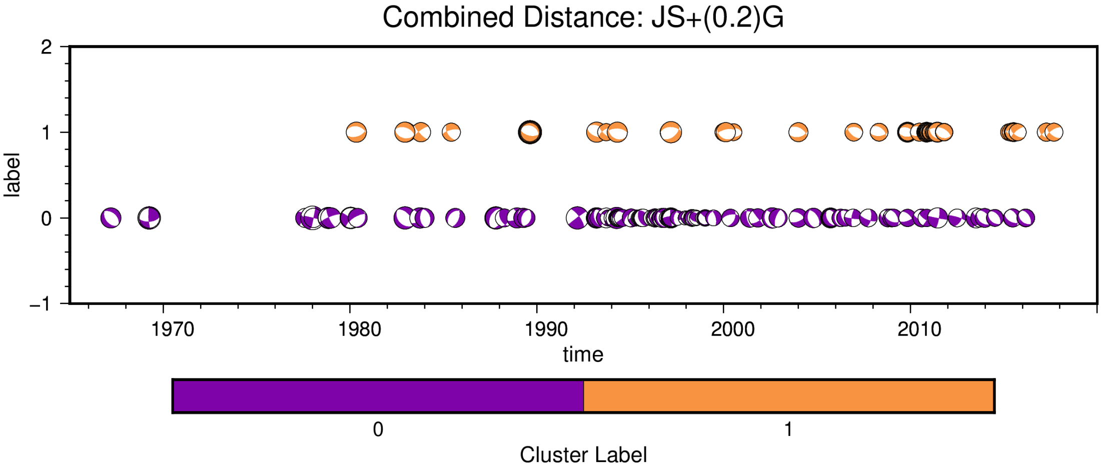

Figure 4.S12: Focal mechanisms with T-quadrant colored according to which of the $C02$ clusters defined in Fig. 4.S10 it belongs to plotted through time.

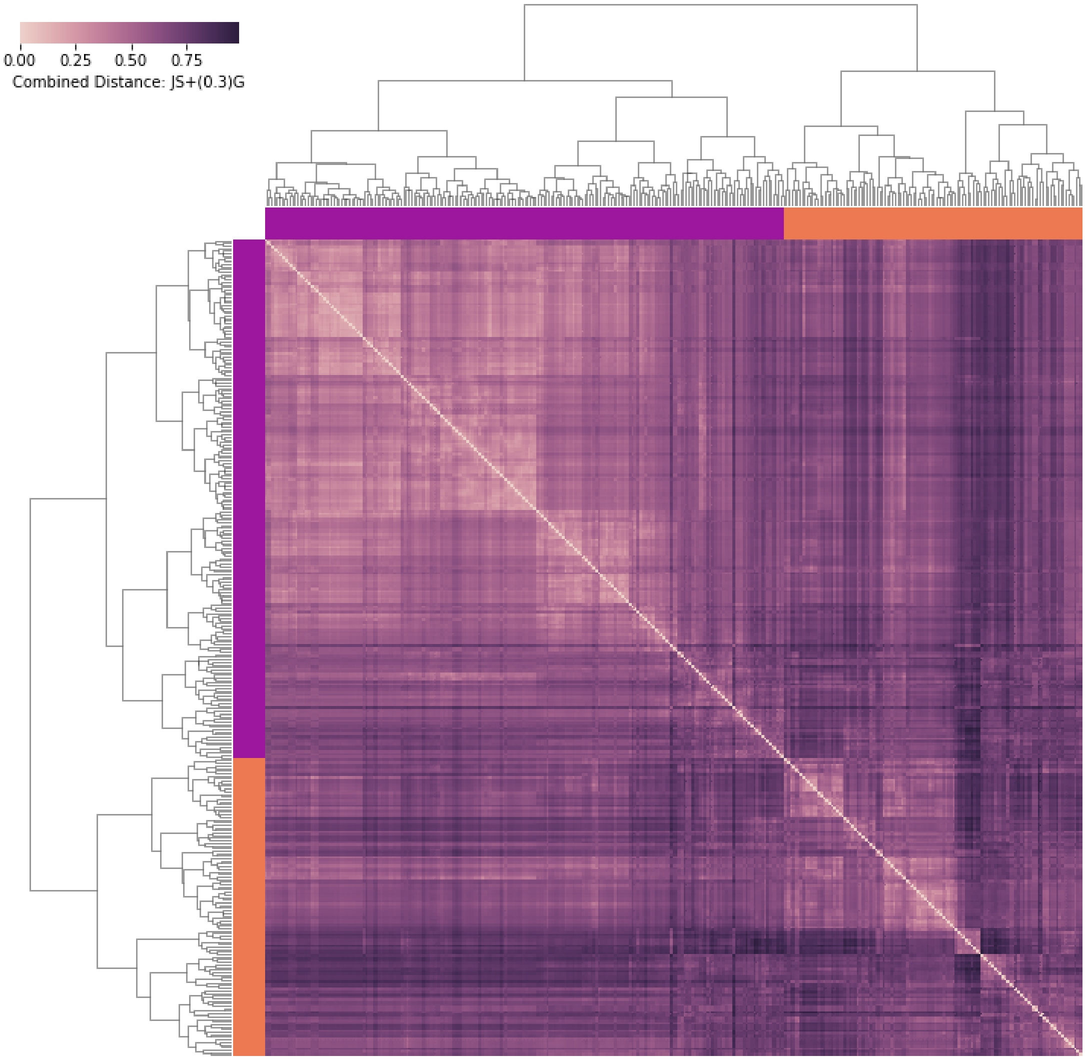

Figure 4.S13: The symmetric distance matrix corresponding to $\mathcal{D}_{C03} = \mathcal{D}_{JS} + 0.3\frac{\mathcal{D}_{\mathcal{G}}}{max(\mathcal{D}_{\mathcal{G}})}$ as a heatmap. Caption is as in Fig. 4.S1.

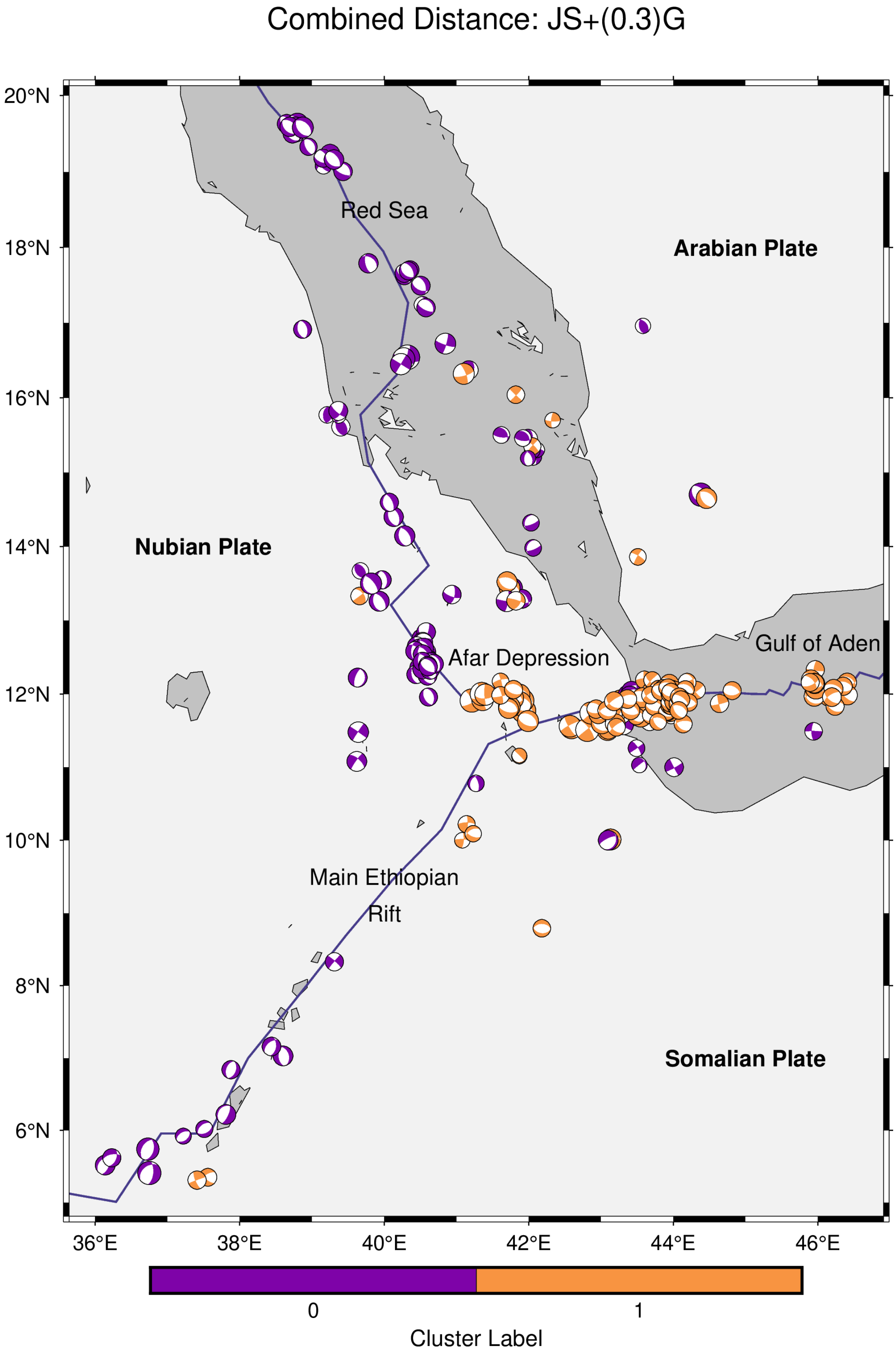

Figure 4.S14: Focal mechanisms with T-quadrant colored according to which of the $C02$ clusters defined in Fig. 4.S13 it belongs to.

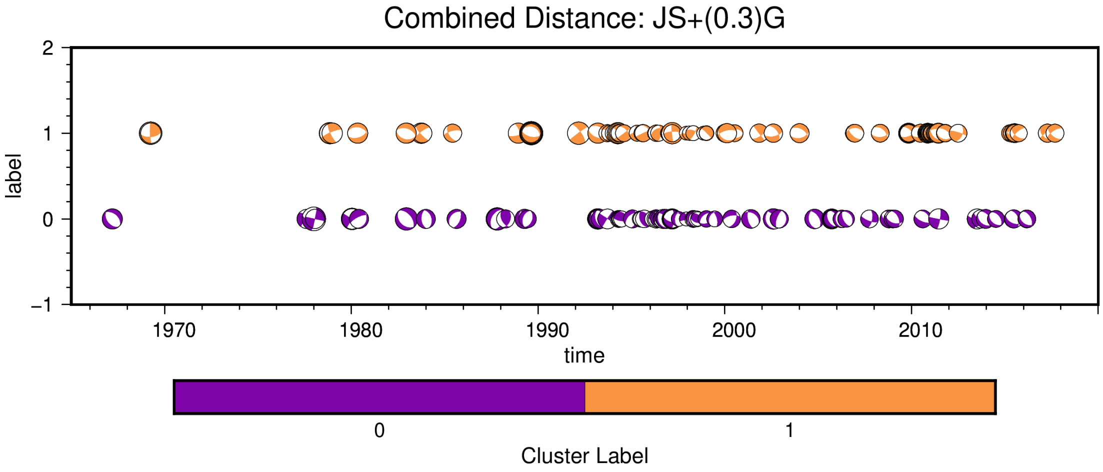

Figure 4.S15: Focal mechanisms with T-quadrant colored according to which of the $C03$ clusters defined in Fig. 4.S13 it belongs to plotted through time.

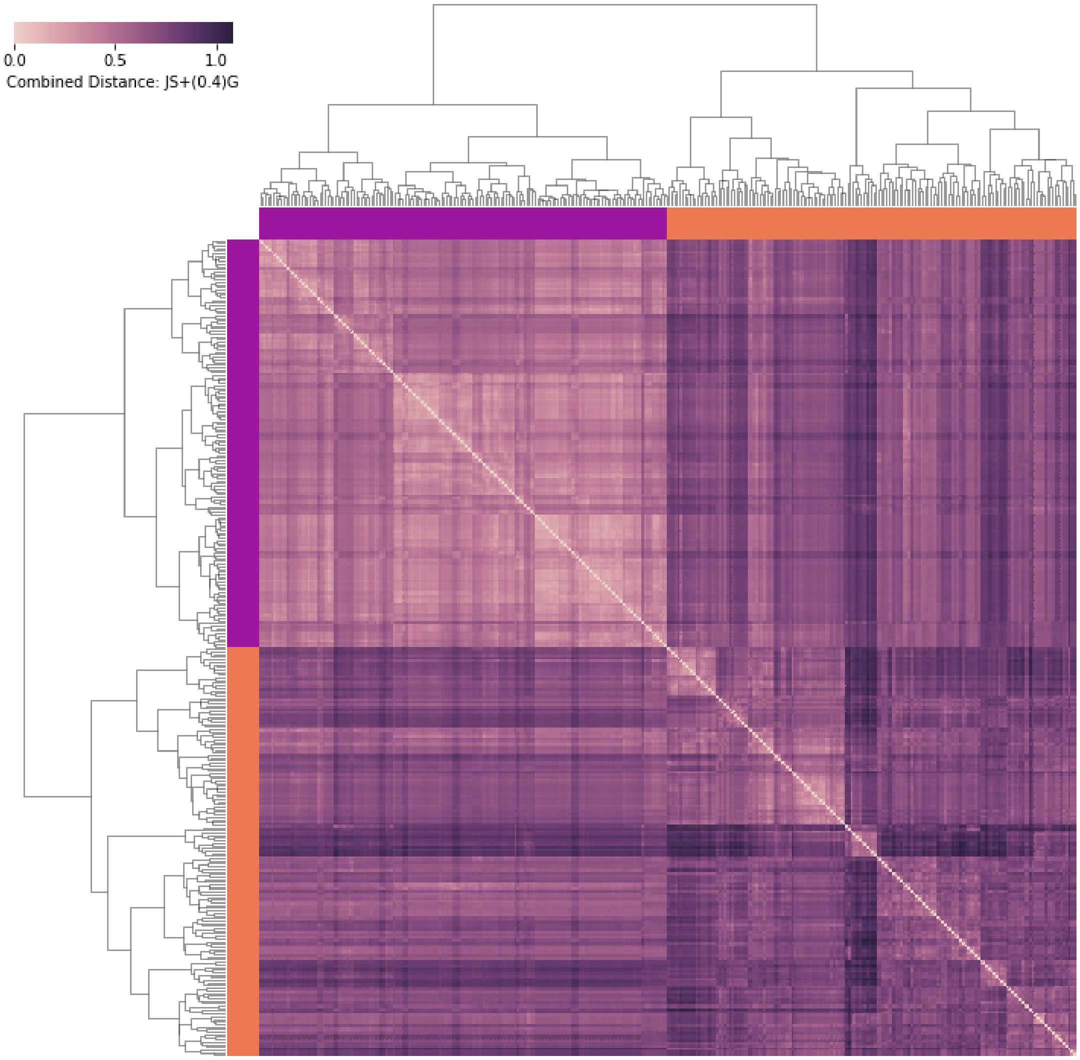

Figure 4.S16: The symmetric distance matrix corresponding to $\mathcal{D}_{C04} = \mathcal{D}_{JS} + 0.4\frac{\mathcal{D}_{\mathcal{G}}}{max(\mathcal{D}_{\mathcal{G}})}$ as a heatmap. Caption is as in Fig. 4.S1.

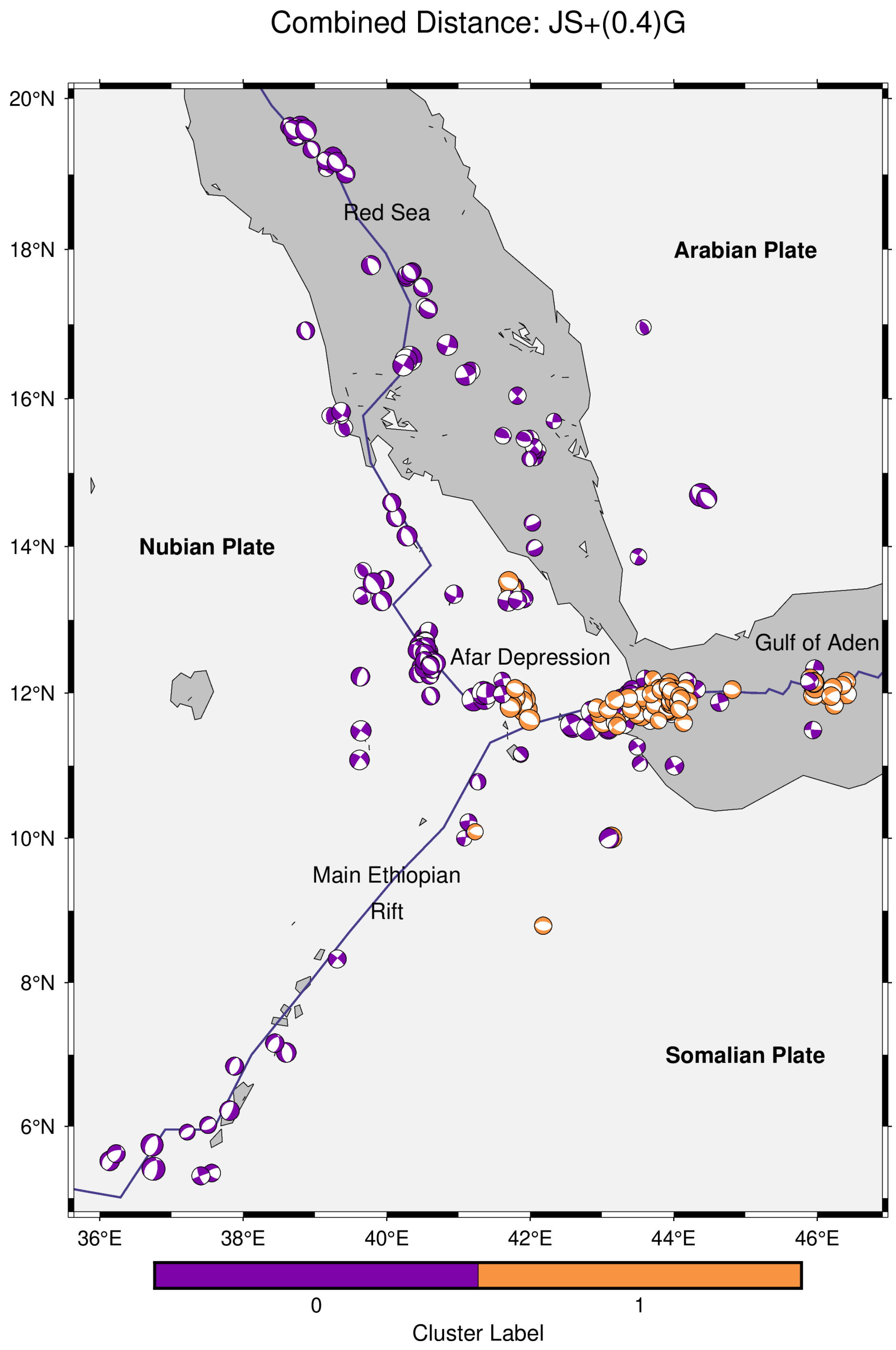

Figure 4.S17: Focal mechanisms with T-quadrant colored according to which of the $C04$ clusters defined in Fig. 4.S16 it belongs to.

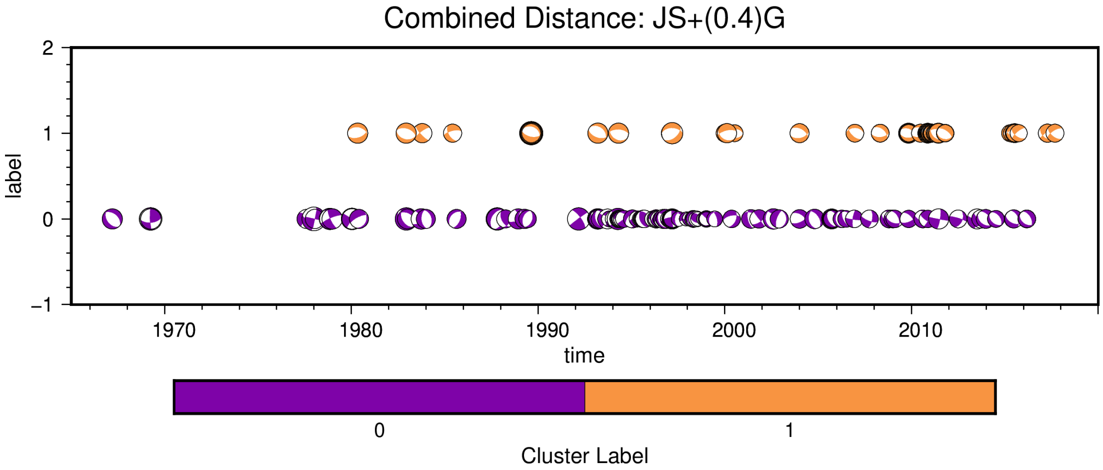

Figure 4.S18: Focal mechanisms with T-quadrant colored according to which of the $C04$ clusters defined in Fig. 4.S16 it belongs to plotted through time.

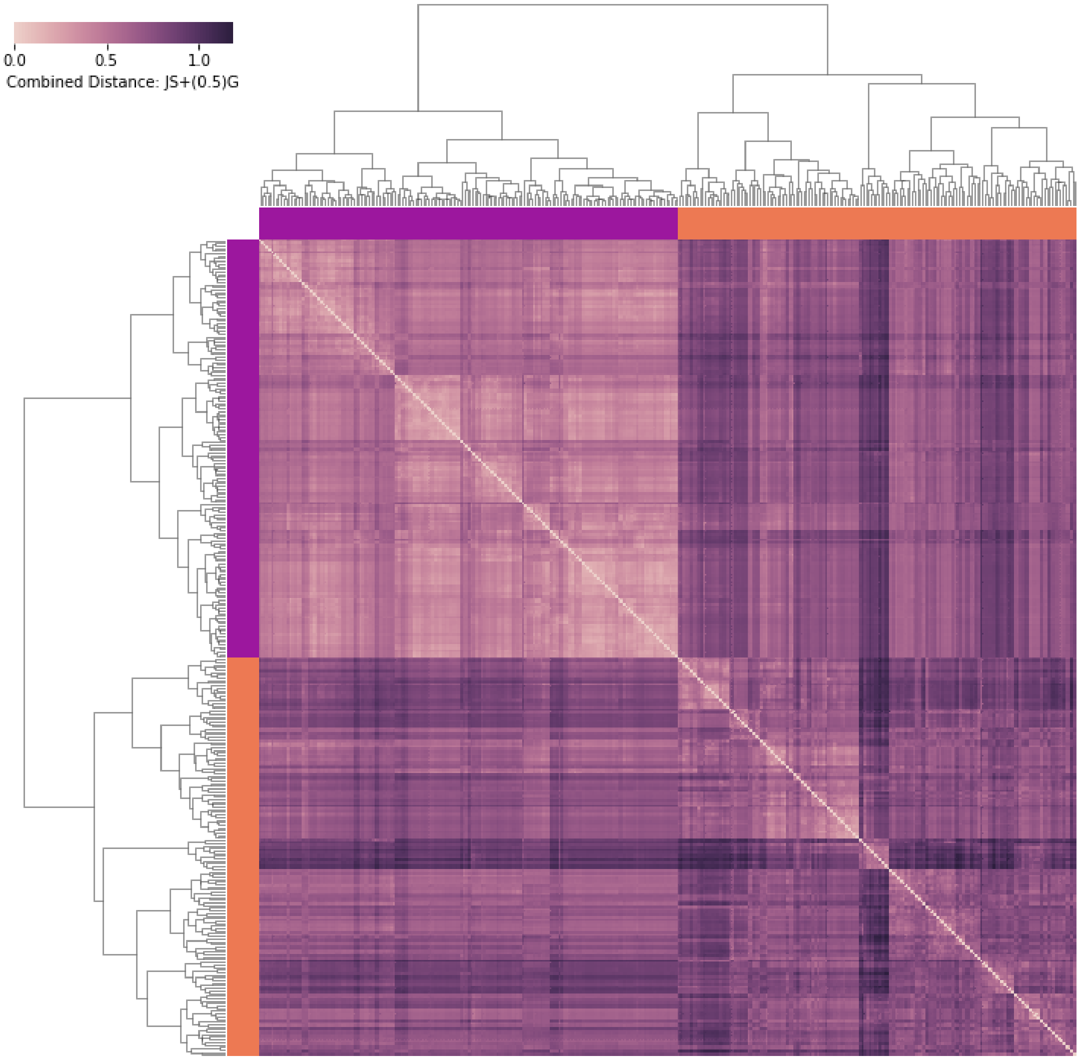

Figure 4.S19: The symmetric distance matrix corresponding to $\mathcal{D}_{C05} = \mathcal{D}_{JS} + 0.5\frac{\mathcal{D}_{\mathcal{G}}}{max(\mathcal{D}_{\mathcal{G}})}$ as a heatmap. Caption is as in Fig. 4.S1.

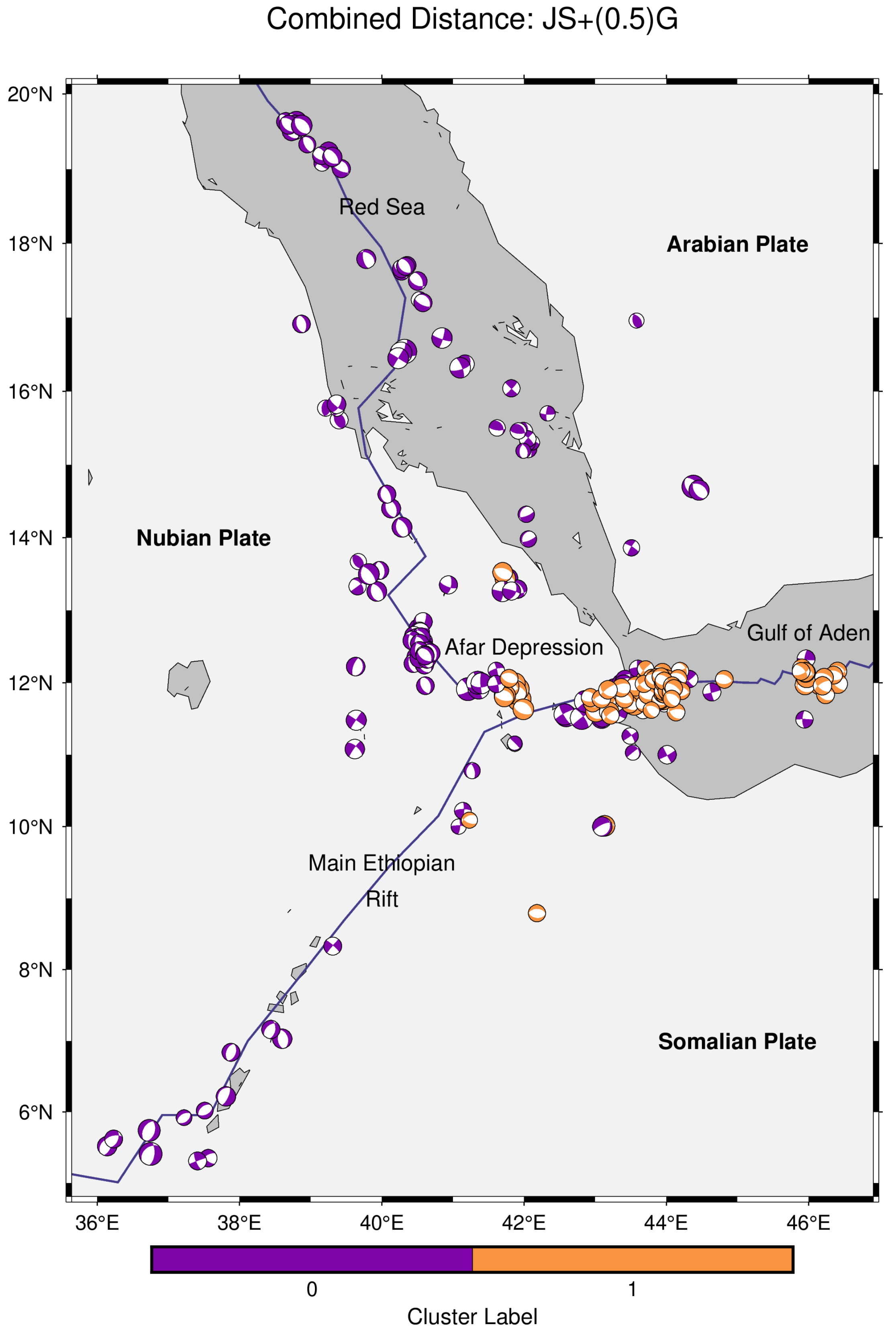

Figure 4.S20: Focal mechanisms with T-quadrant colored according to which of the $C05$ clusters defined in Fig. 4.S19 it belongs to.

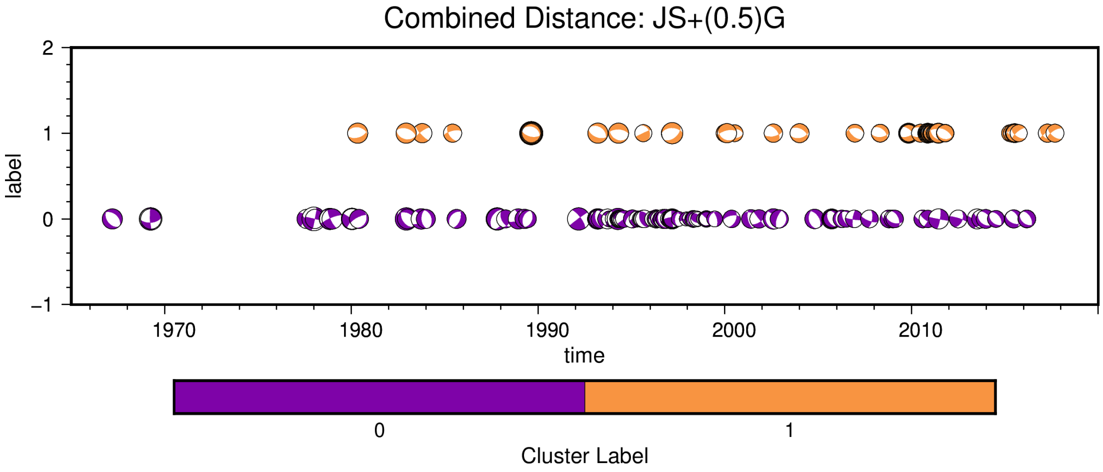

Figure 4.S21: Focal mechanisms with T-quadrant colored according to which of the $C05$ clusters defined in Fig. 4.S19 it belongs to plotted through time.

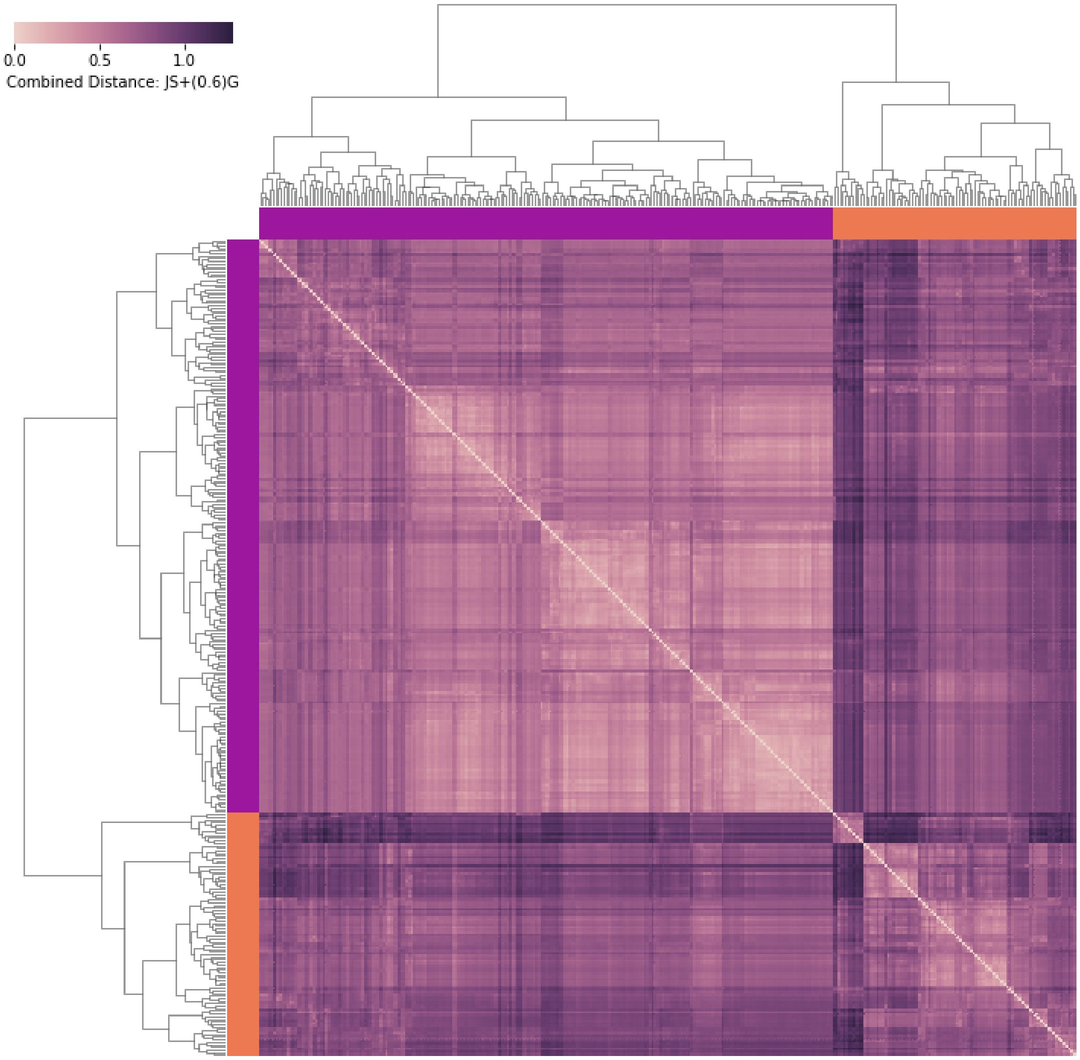

Figure 4.S22: The symmetric distance matrix corresponding to $\mathcal{D}_{C06} = \mathcal{D}_{JS} + 0.6\frac{\mathcal{D}_{\mathcal{G}}}{max(\mathcal{D}_{\mathcal{G}})}$ as a heatmap. Caption is as in Fig. 4.S1.

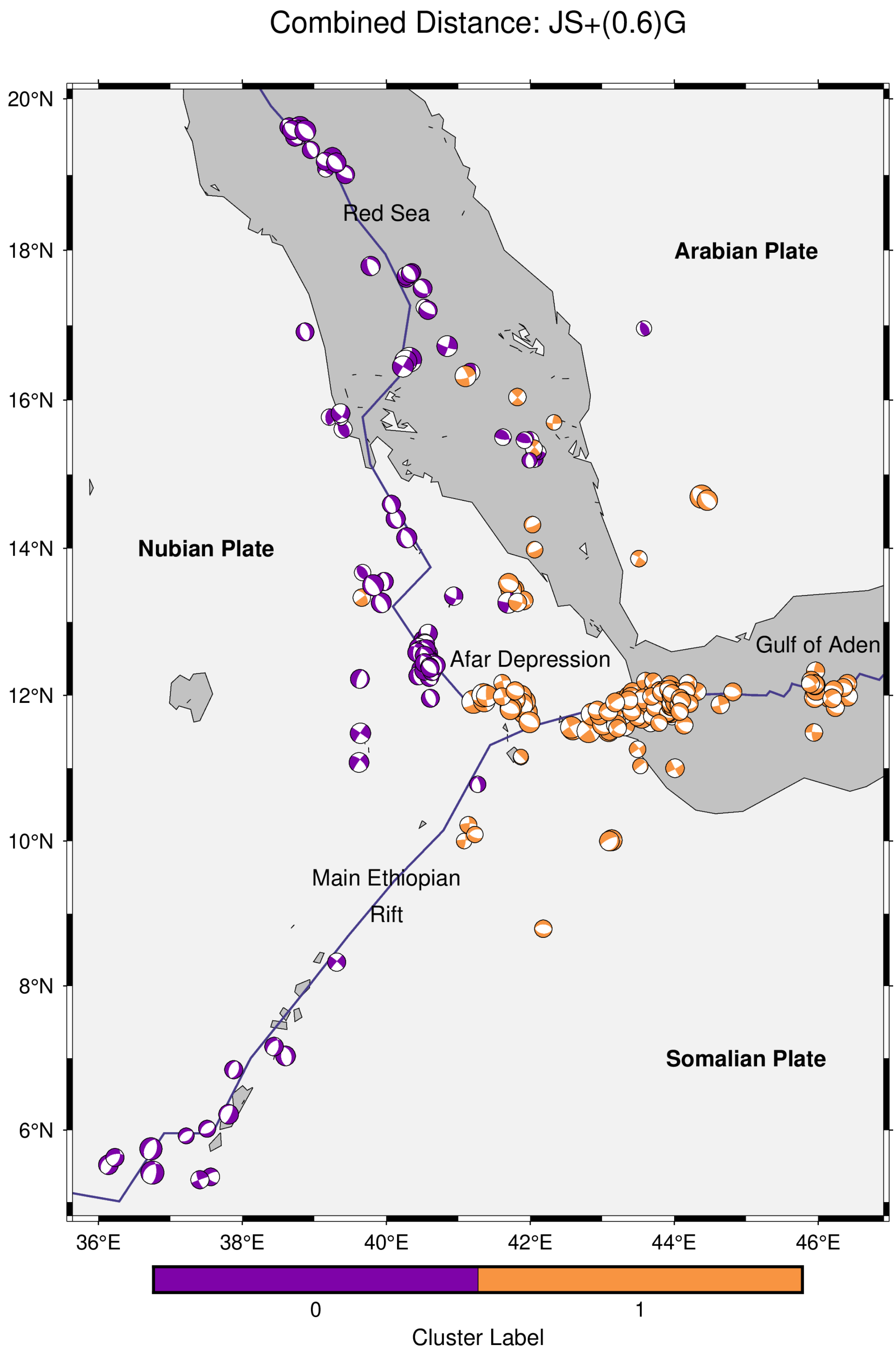

Figure 4.S23: Focal mechanisms with T-quadrant colored according to which of the $C06$ clusters defined in Fig. 4.S22 it belongs to.

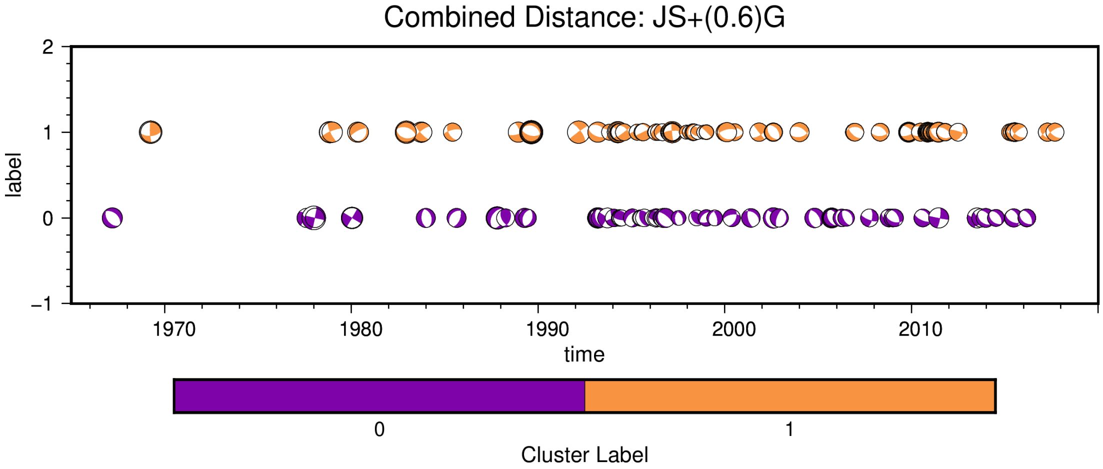

Figure 4.S24: Focal mechanisms with T-quadrant colored according to which of the $C06$ clusters defined in Fig. 4.S22 it belongs to plotted through time.

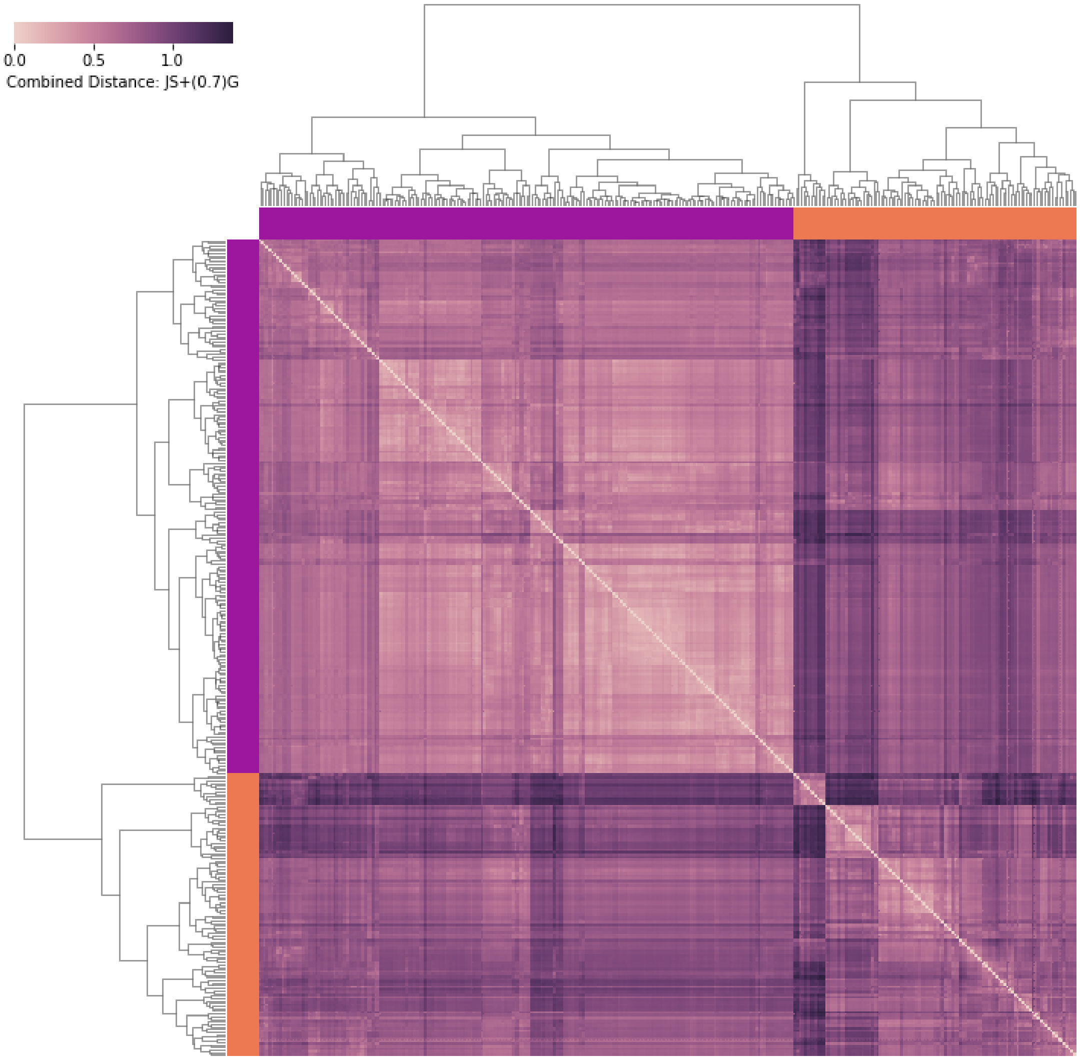

Figure 4.S25: The symmetric distance matrix corresponding to $\mathcal{D}_{C07} = \mathcal{D}_{JS} + 0.7\frac{\mathcal{D}_{\mathcal{G}}}{max(\mathcal{D}_{\mathcal{G}})}$ as a heatmap. Caption is as in Fig. 4.S1. Appears as Fig. 4.7 in the text.

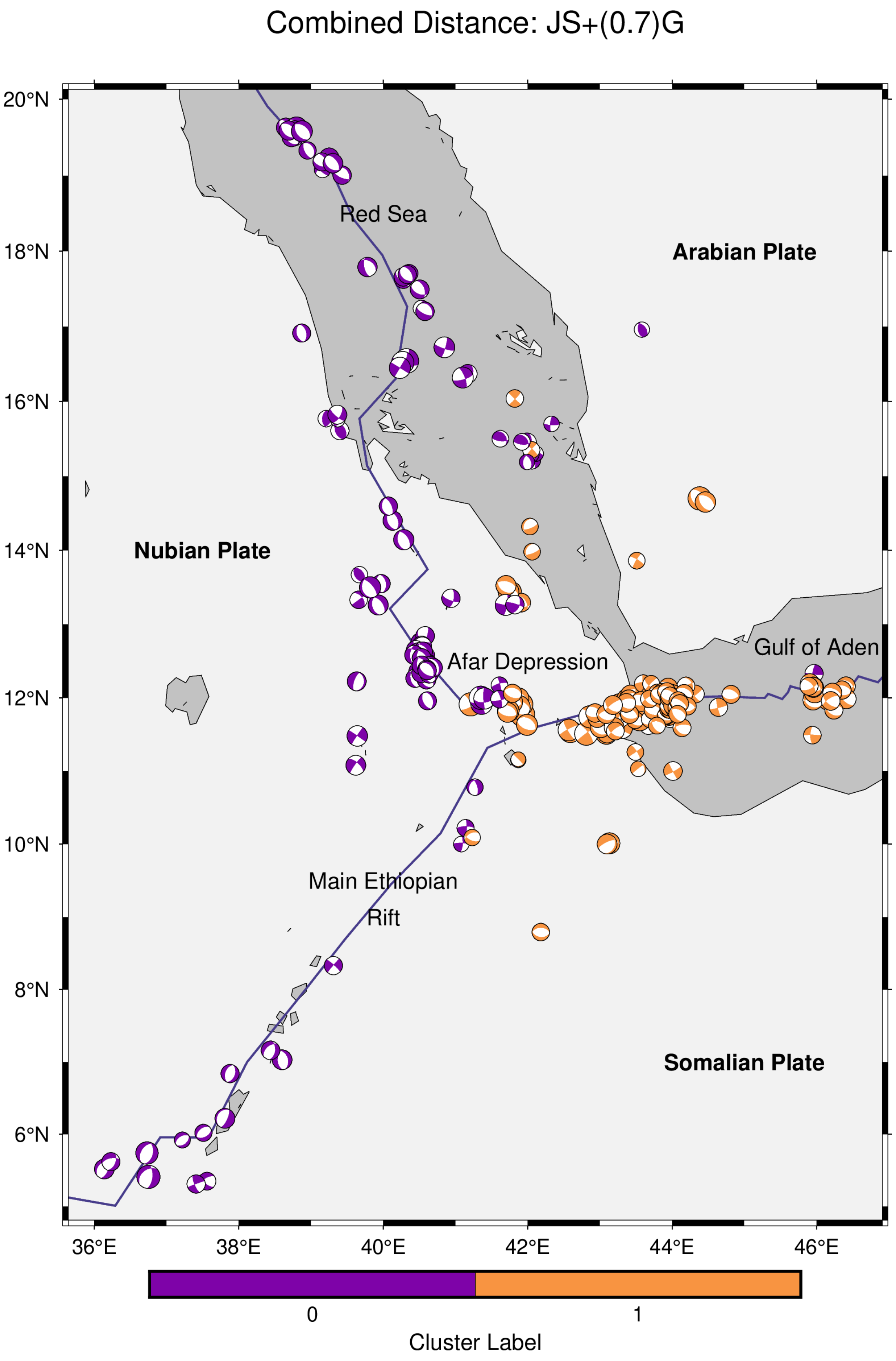

Figure 4.S26: Focal mechanisms with T-quadrant colored according to which of the $C07$ clusters defined in Fig. 4.S25 it belongs to. Appears as Fig. 4.8 in the text.

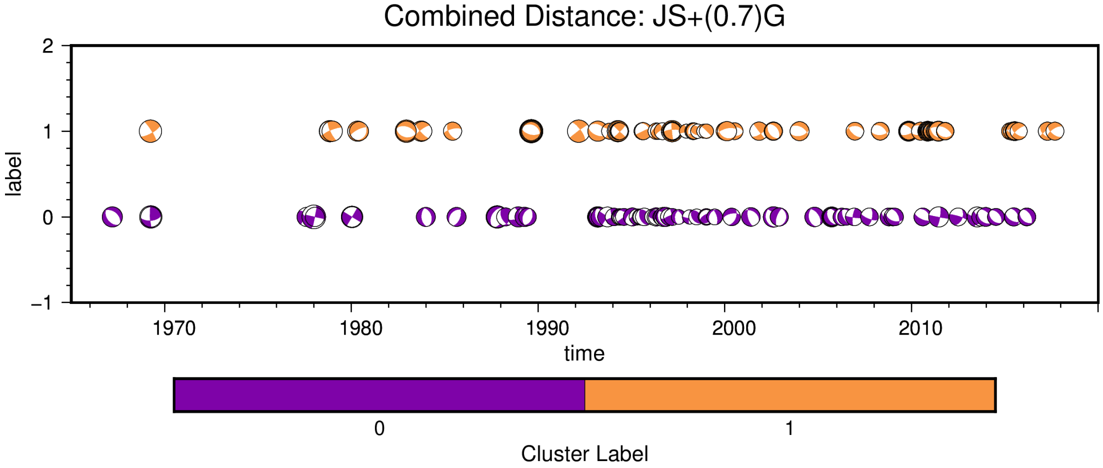

Figure 4.S27: Focal mechanisms with T-quadrant colored according to which of the $C07$ clusters defined in Fig. 4.S25 it belongs to plotted through time.

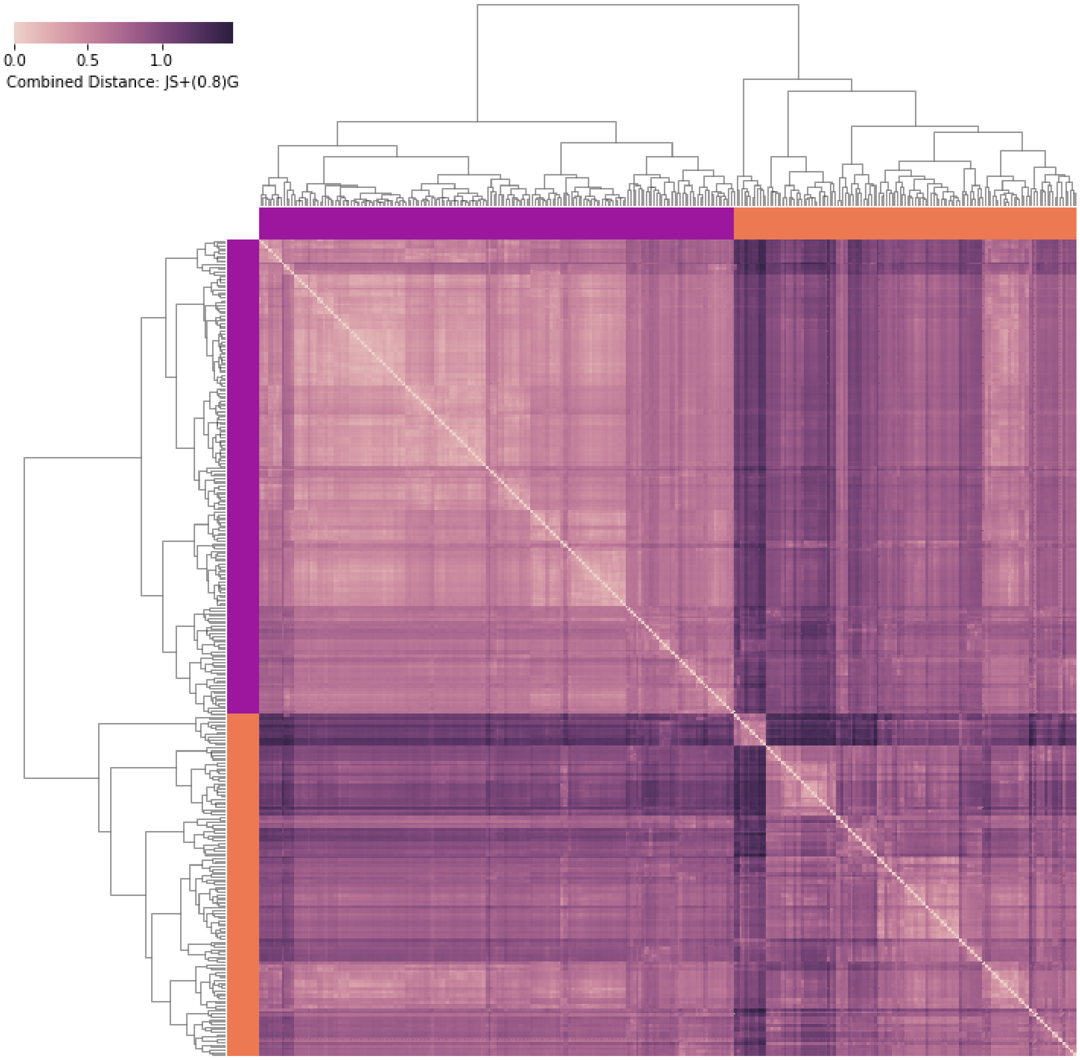

Figure 4.S28: The symmetric distance matrix corresponding to $\mathcal{D}_{C08} = \mathcal{D}_{JS} + 0.8\frac{\mathcal{D}_{\mathcal{G}}}{max(\mathcal{D}_{\mathcal{G}})}$ as a heatmap. Caption is as in Fig. 4.S1.

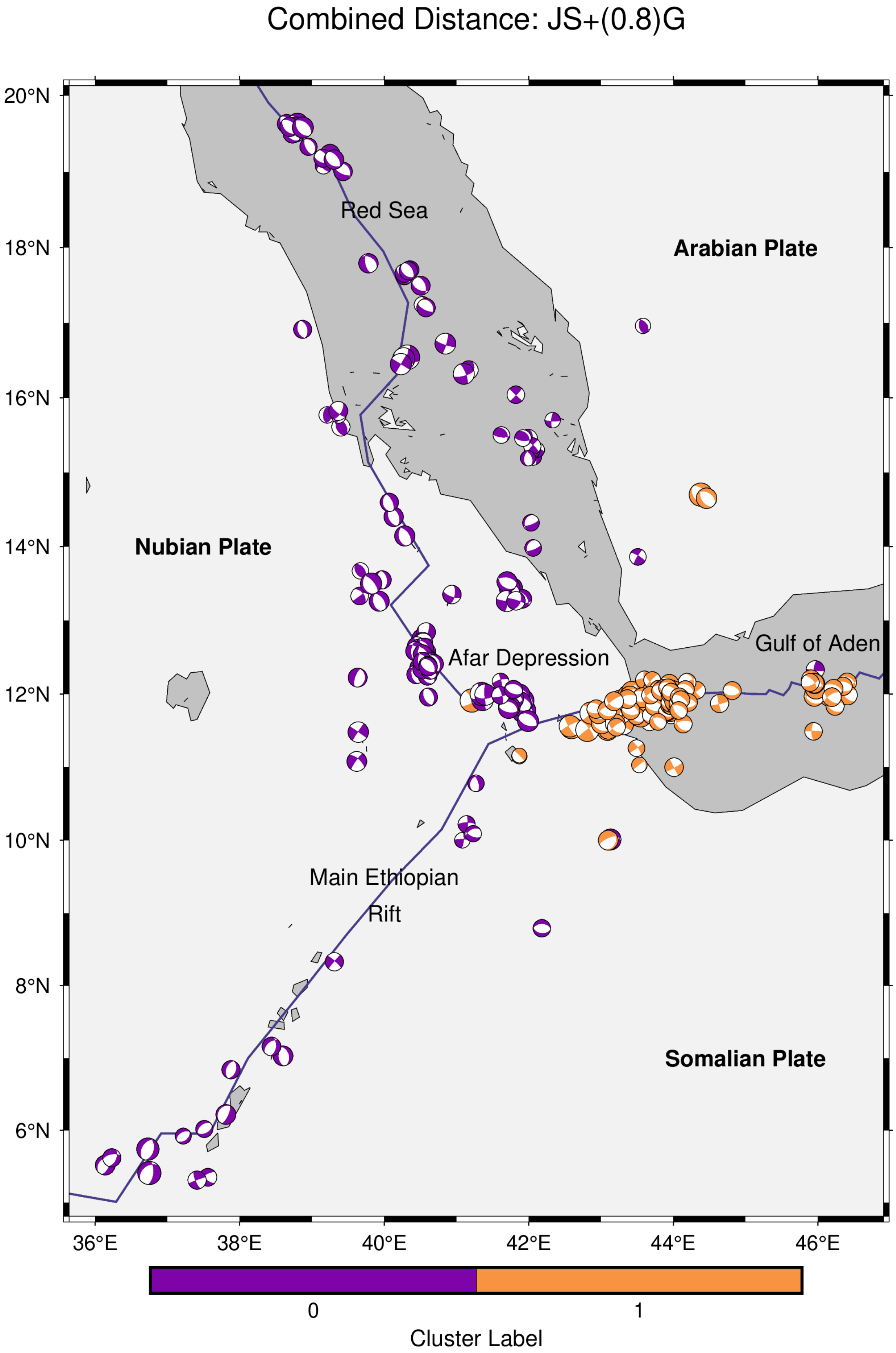

Figure 4.S29: Focal mechanisms with T-quadrant colored according to which of the $C08$ clusters defined in Fig. 4.S28 it belongs to.

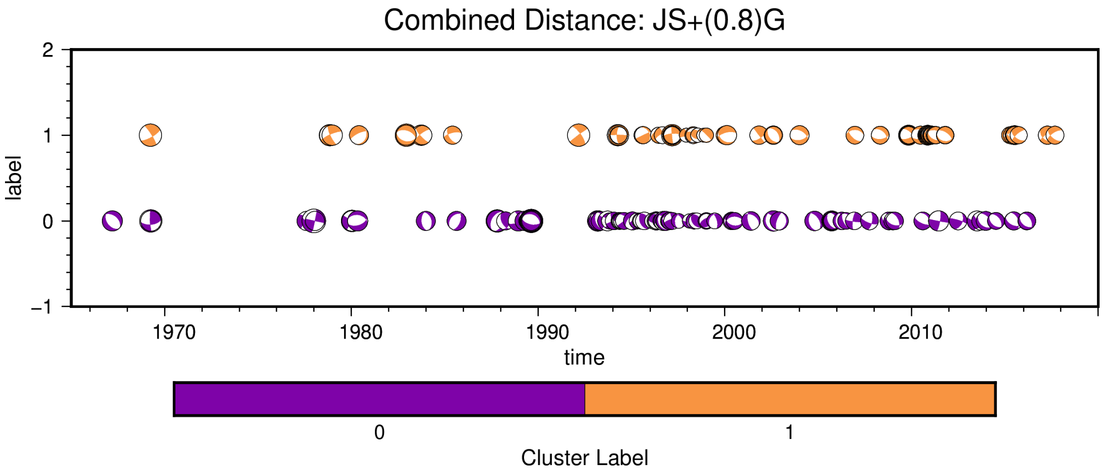

Figure 4.S30: Focal mechanisms with T-quadrant colored according to which of the $C08$ clusters defined in Fig. 4.S28 it belongs to plotted through time.

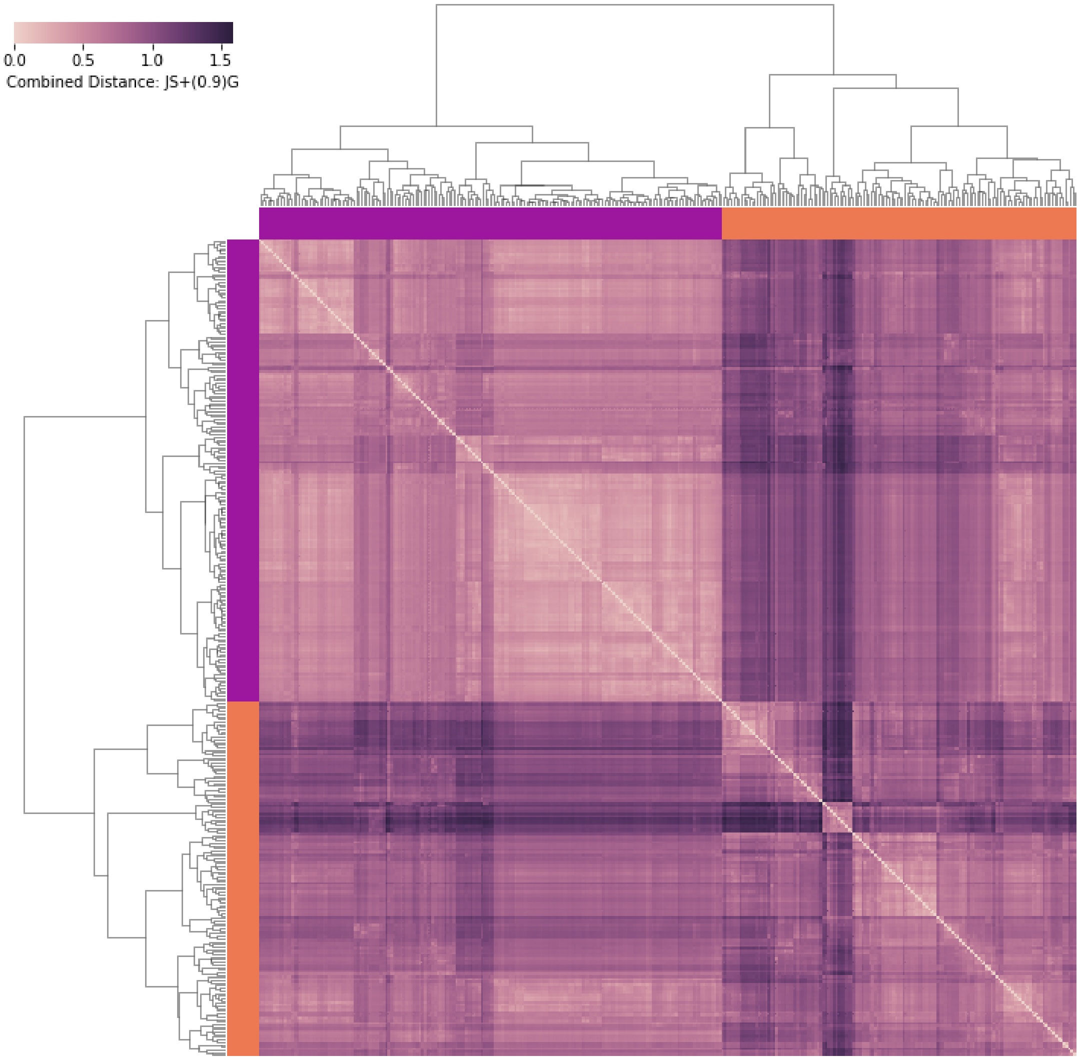

Figure 4.S31: The symmetric distance matrix corresponding to $\mathcal{D}_{C09} = \mathcal{D}_{JS} + 0.9\frac{\mathcal{D}_{\mathcal{G}}}{max(\mathcal{D}_{\mathcal{G}})}$ as a heatmap. Caption is as in Fig. 4.S1.

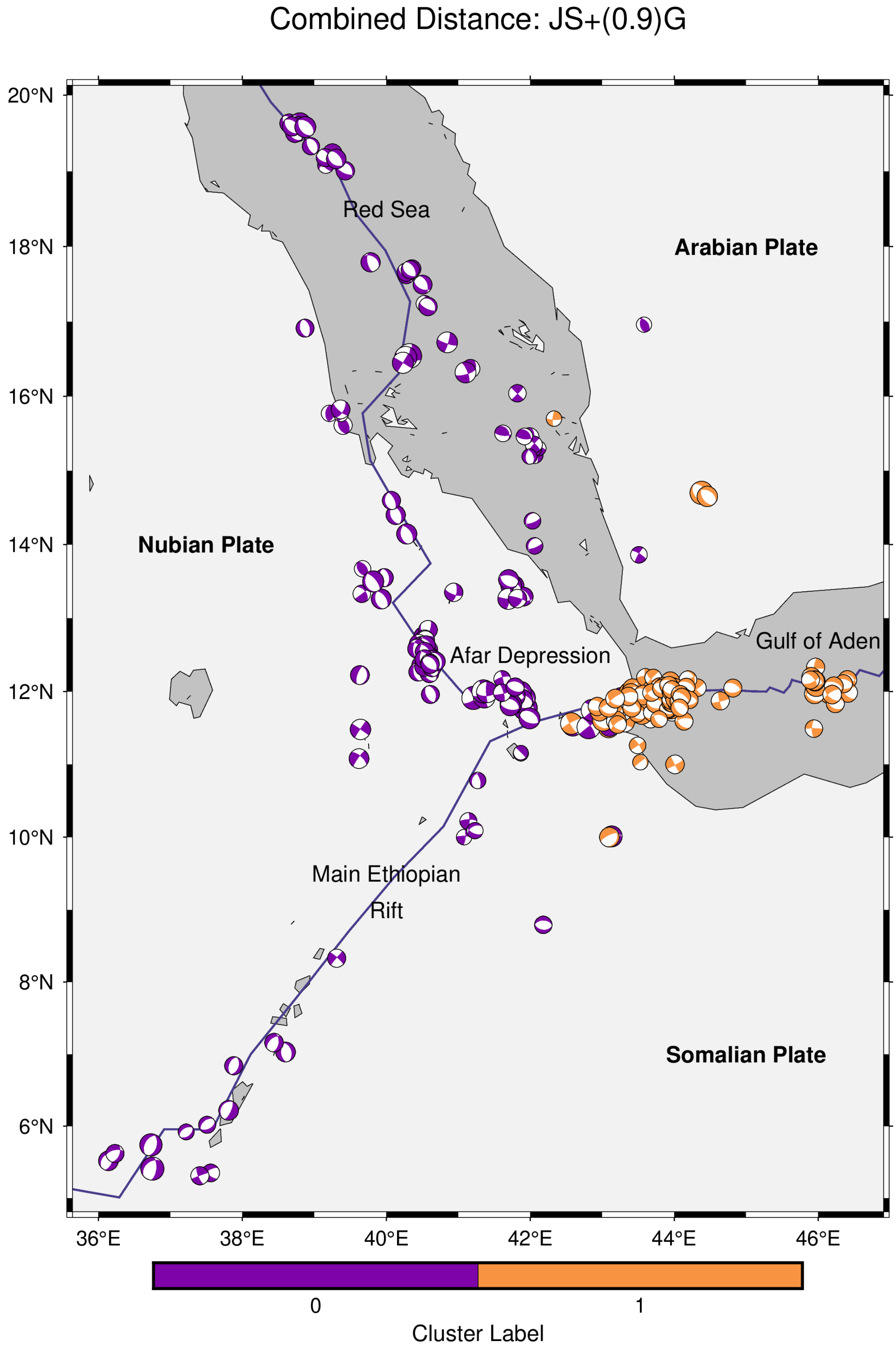

Figure 4.S32: Focal mechanisms with T-quadrant colored according to which of the $C09$ clusters defined in Fig. 4.S31 it belongs to.

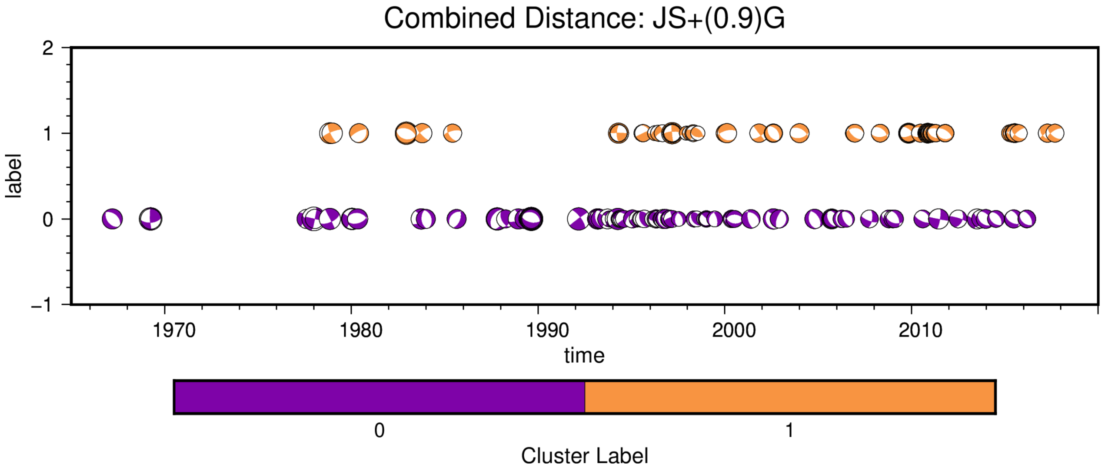

Figure 4.S33: Focal mechanisms with T-quadrant colored according to which of the $C09$ clusters defined in Fig. 4.S31 it belongs to plotted through time.

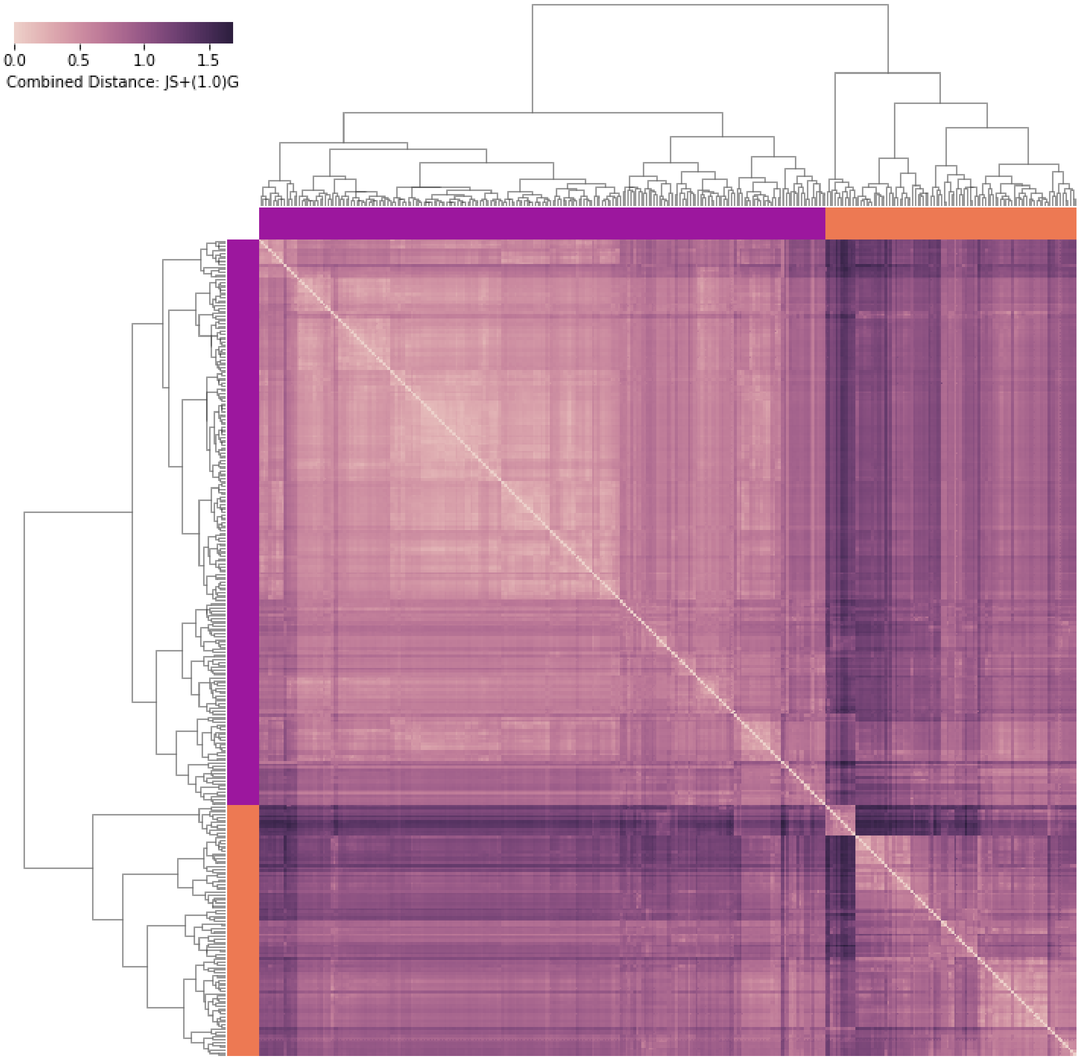

Figure 4.S34: The symmetric distance matrix corresponding to $\mathcal{D}_{C10} = \mathcal{D}_{JS} + 1.0\frac{\mathcal{D}_{\mathcal{G}}}{max(\mathcal{D}_{\mathcal{G}})}$ as a heatmap. Caption is as in Fig. 4.S1.

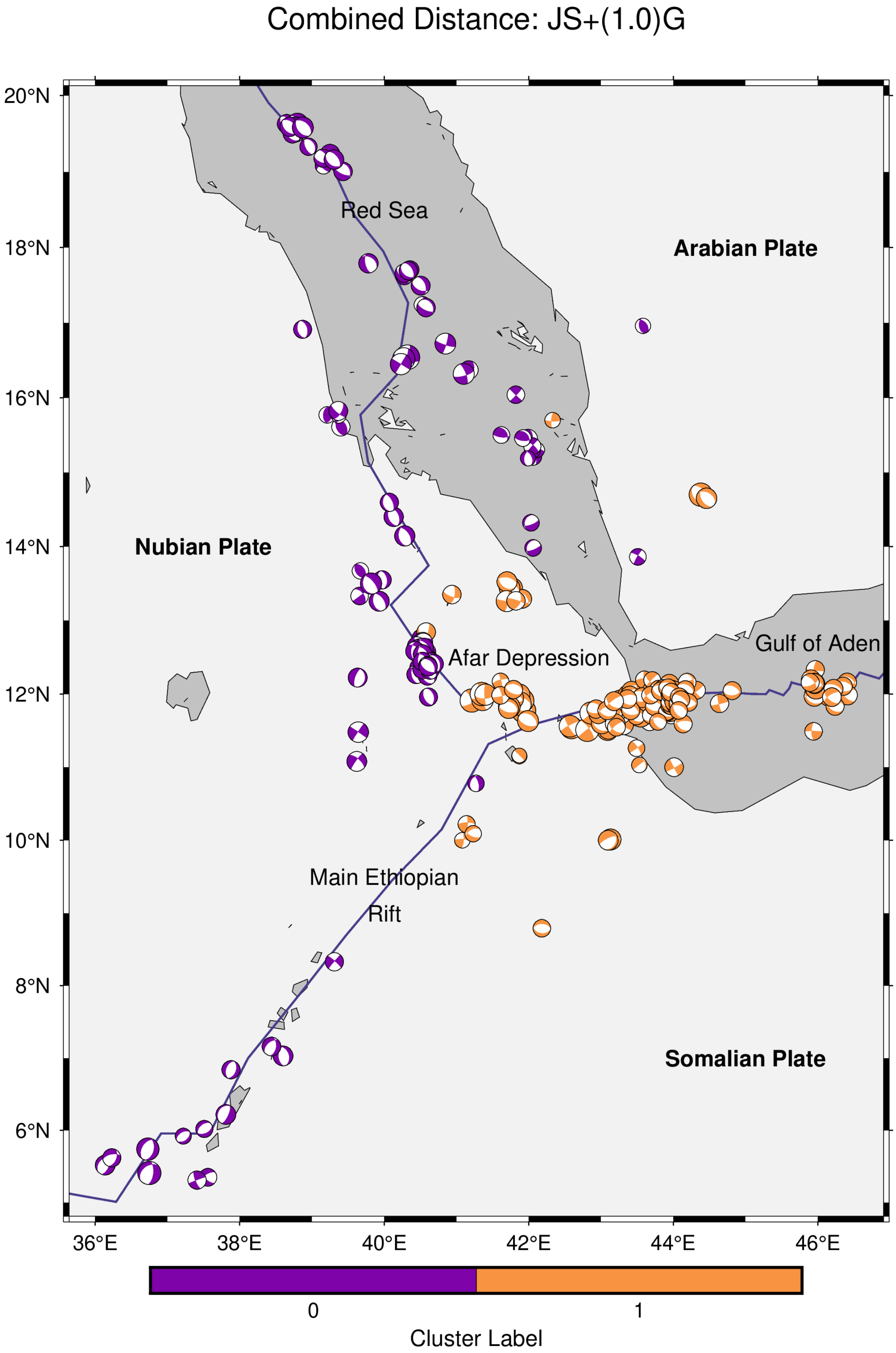

Figure 4.S35: Focal mechanisms with T-quadrant colored according to which of the $C10$ clusters defined in Fig. 4.S34 it belongs to.

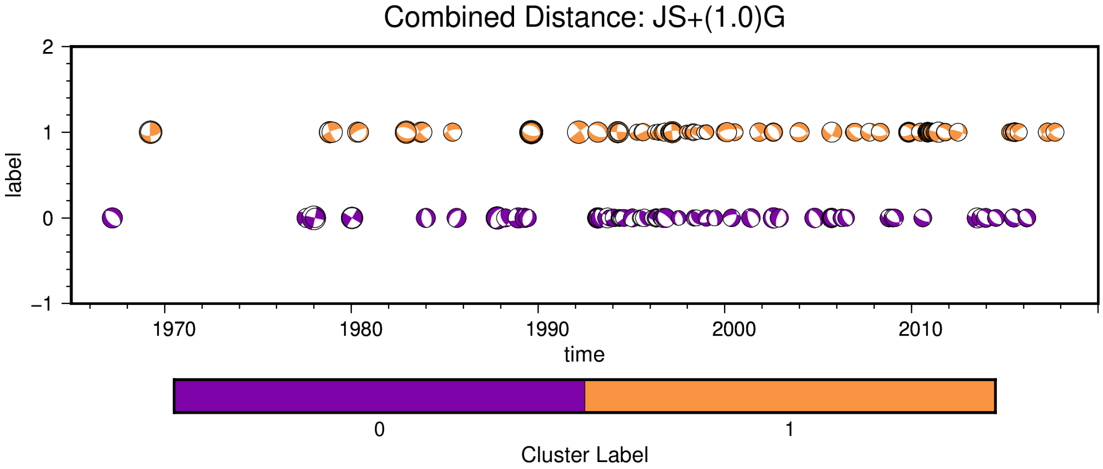

Figure 4.S36: Focal mechanisms with T-quadrant colored according to which of the $C10$ clusters defined in Fig. 4.S34 it belongs to plotted through time.

4.6.S2.2 Clustering Results from Noise Removal Models

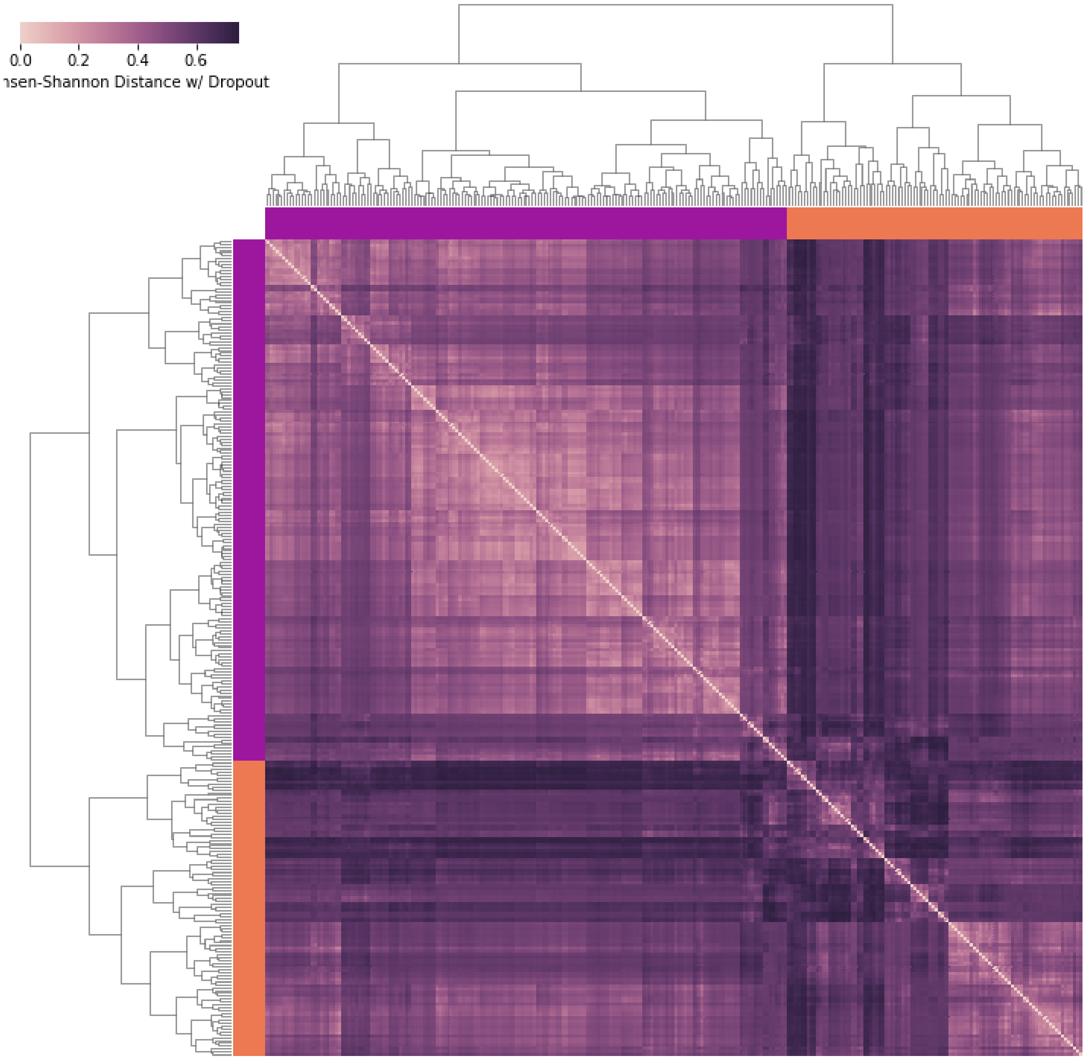

Figure 4.S37: The symmetric distance matrix corresponding to $\mathcal{D}_{JSD}$ as a heatmap. Caption is as in Fig. 4.S1.

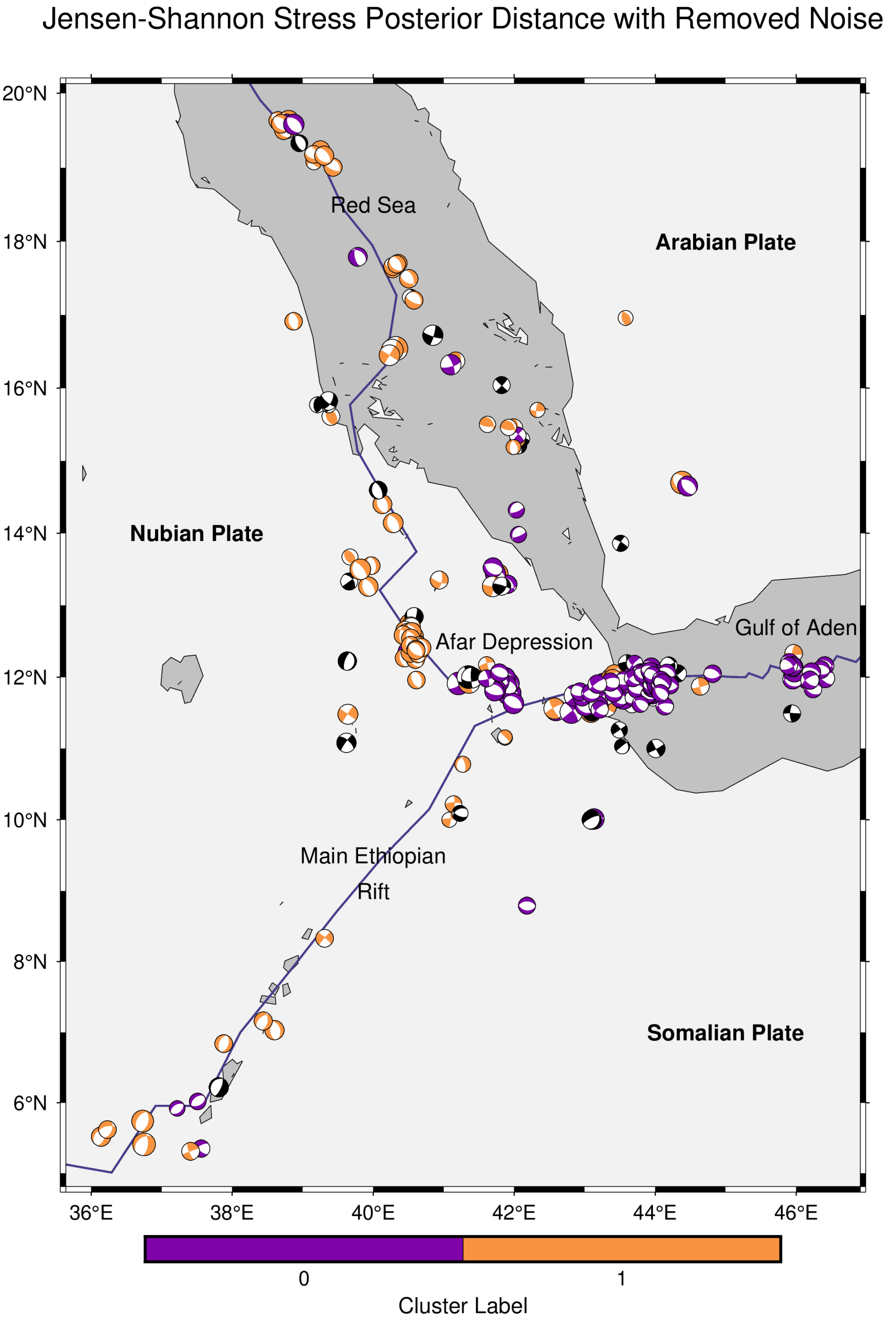

Figure 4.S38: Focal mechanisms with T-quadrant colored according to which of the JSD clusters defined in Fig. 4.S37 it belongs to.

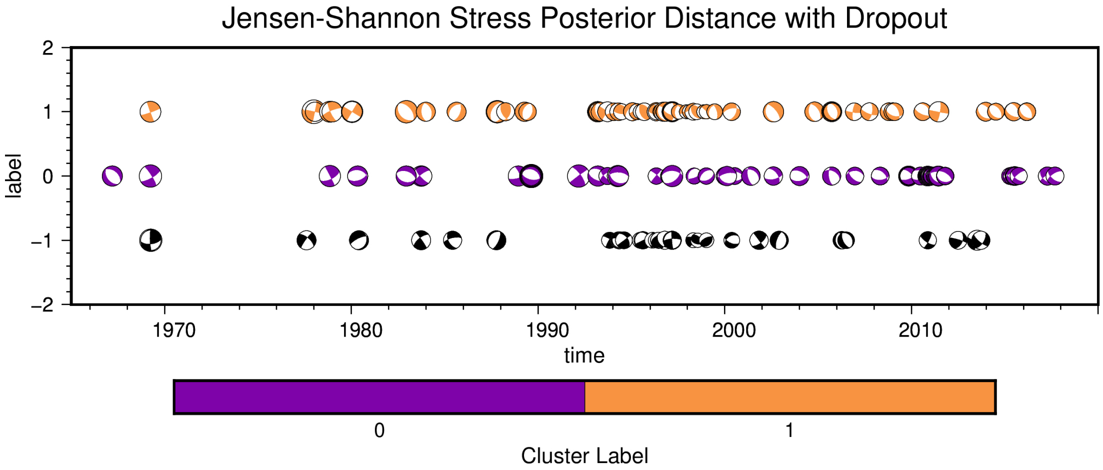

Figure 4.S39: Focal mechanisms with T-quadrant colored according to which of the JSD clusters defined in Fig. 4.S37 it belongs to plotted through time.

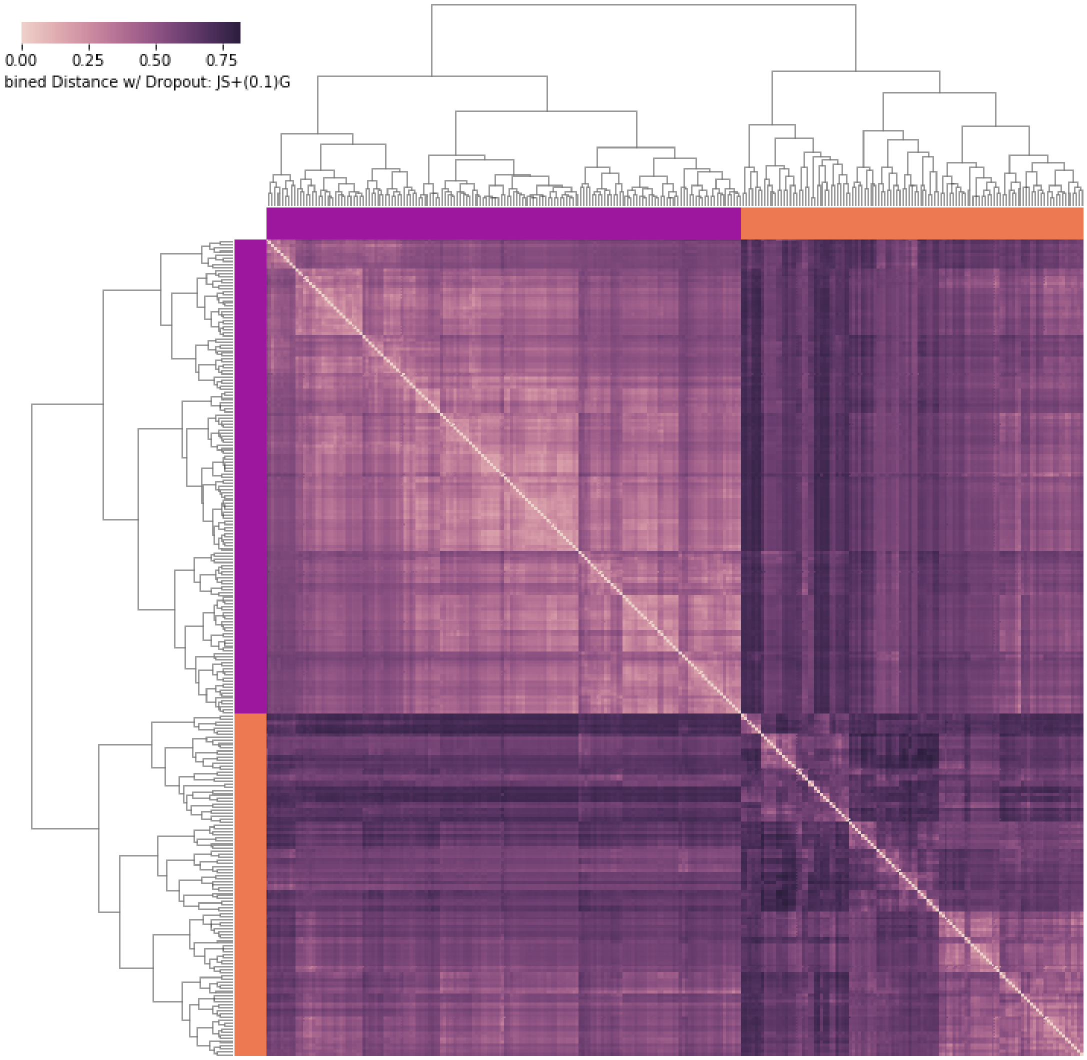

Figure 4.S40: The symmetric distance matrix corresponding to $\mathcal{D}_{C01D} = \mathcal{D}_{JSD} + 0.1\frac{\mathcal{D}_{\mathcal{GD}}}{max(\mathcal{D}_{\mathcal{GD}})}$ as a heatmap. Caption is as in Fig. 4.S1. Model $C02D$ provides identical results.

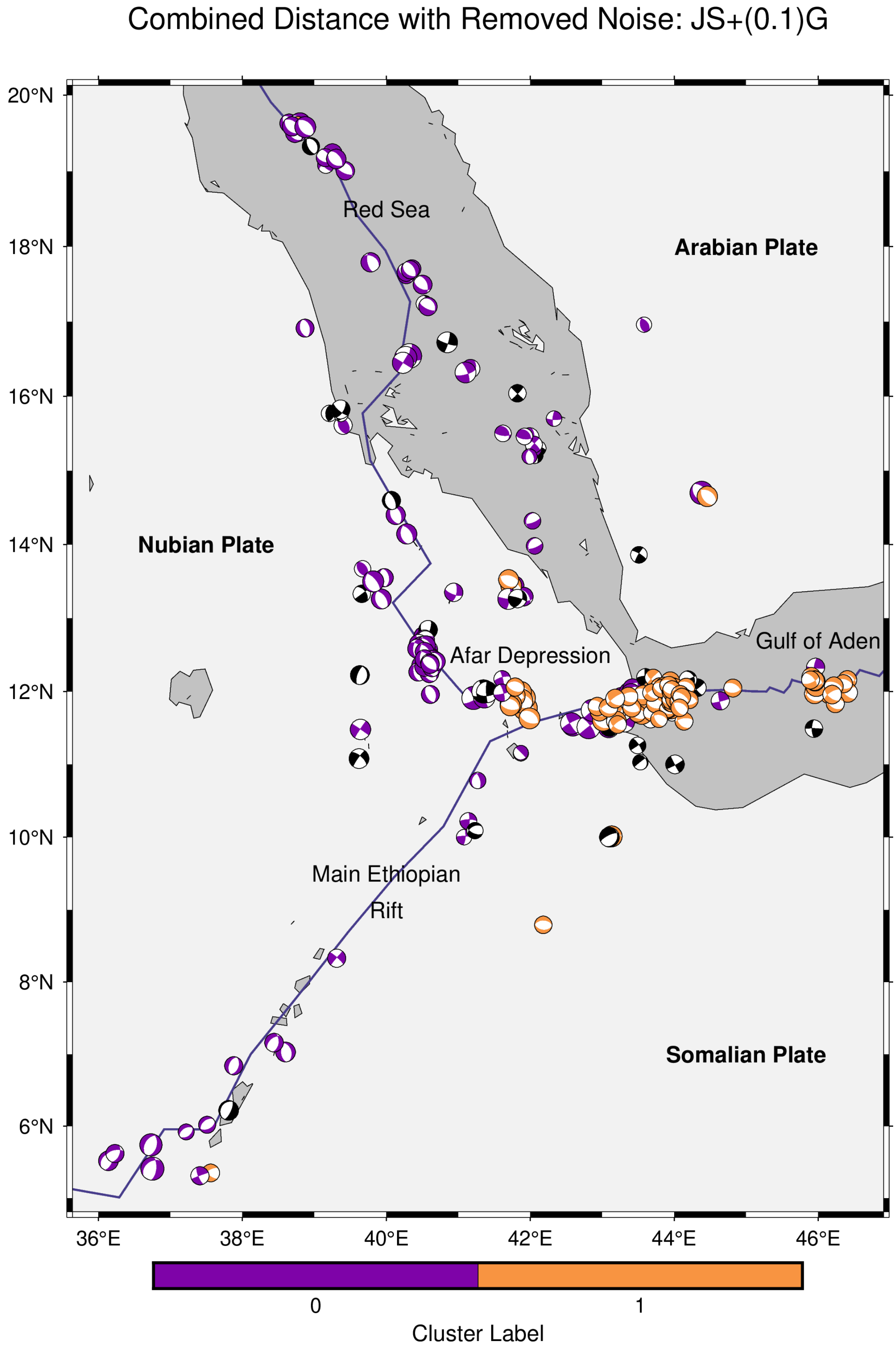

Figure 4.S41: Focal mechanisms with T-quadrant colored according to which of the $C01D$ clusters defined in Fig. 4.S40 it belongs to. Model $C02D$ provides identical results.

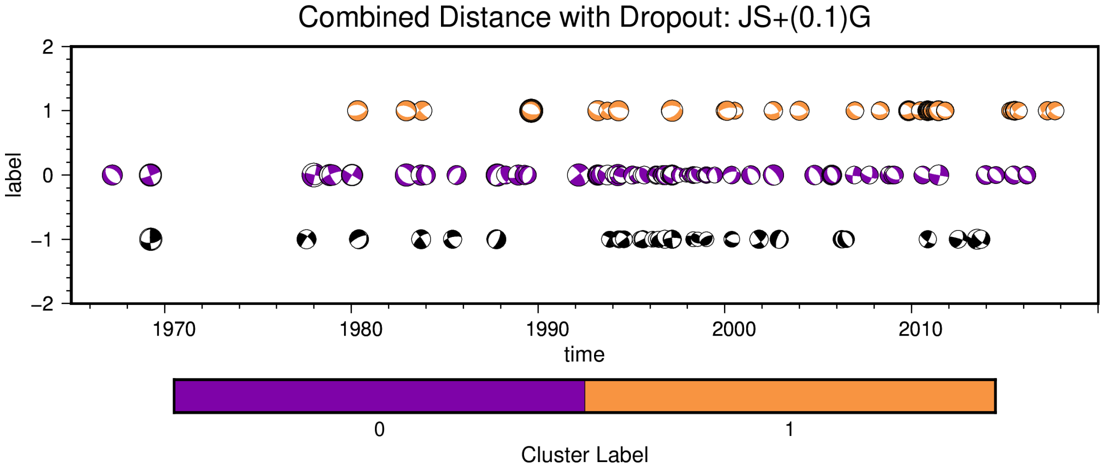

Figure 4.S42: Focal mechanisms with T-quadrant colored according to which of the $C01D$ clusters defined in Fig. 4.S40 it belongs to plotted through time. Model $C02D$ provides identical results.

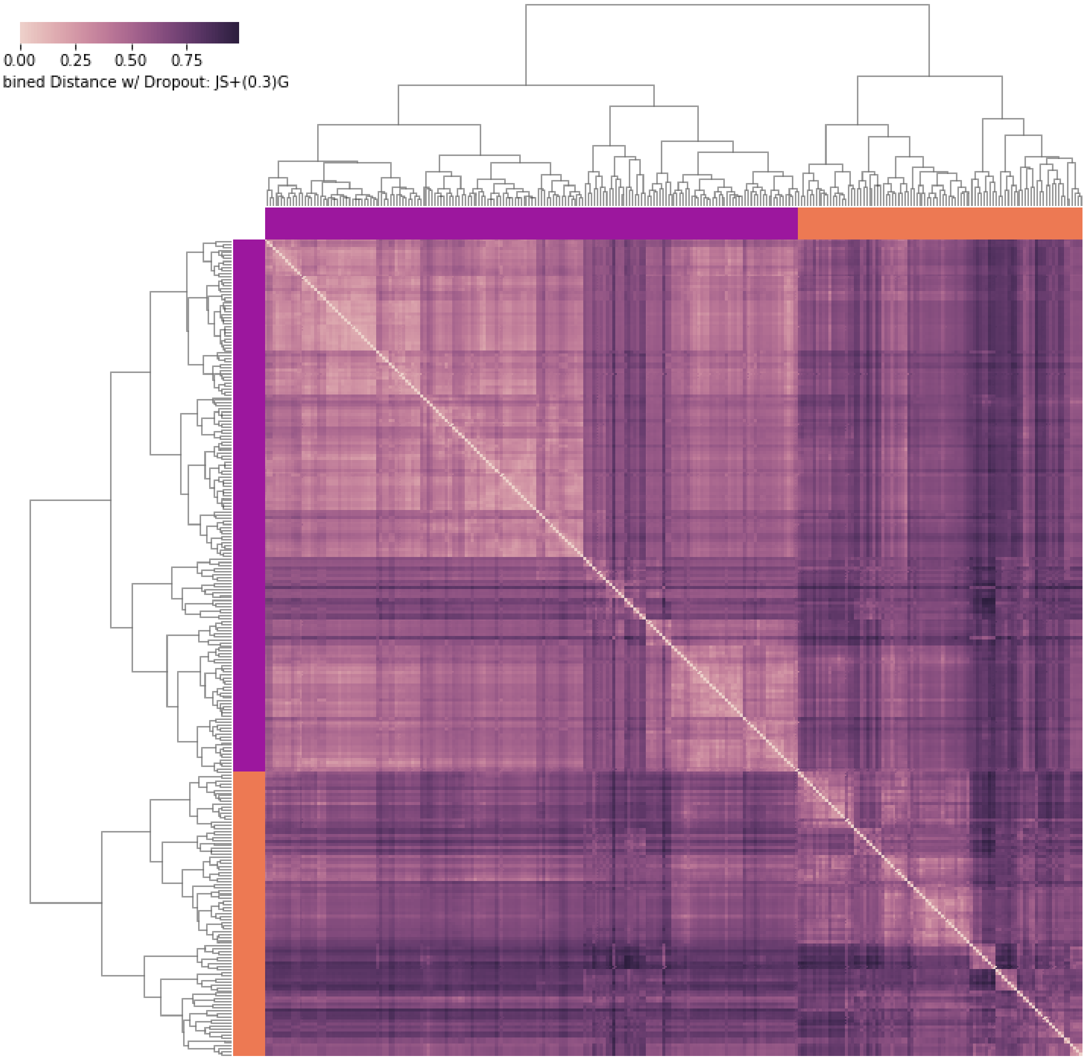

Figure 4.S43: The symmetric distance matrix corresponding to $\mathcal{D}_{C03D} = \mathcal{D}_{JSD} + 0.3\frac{\mathcal{D}_{\mathcal{GD}}}{max(\mathcal{D}_{\mathcal{GD}})}$ as a heatmap. Caption is as in Fig. 4.S1.

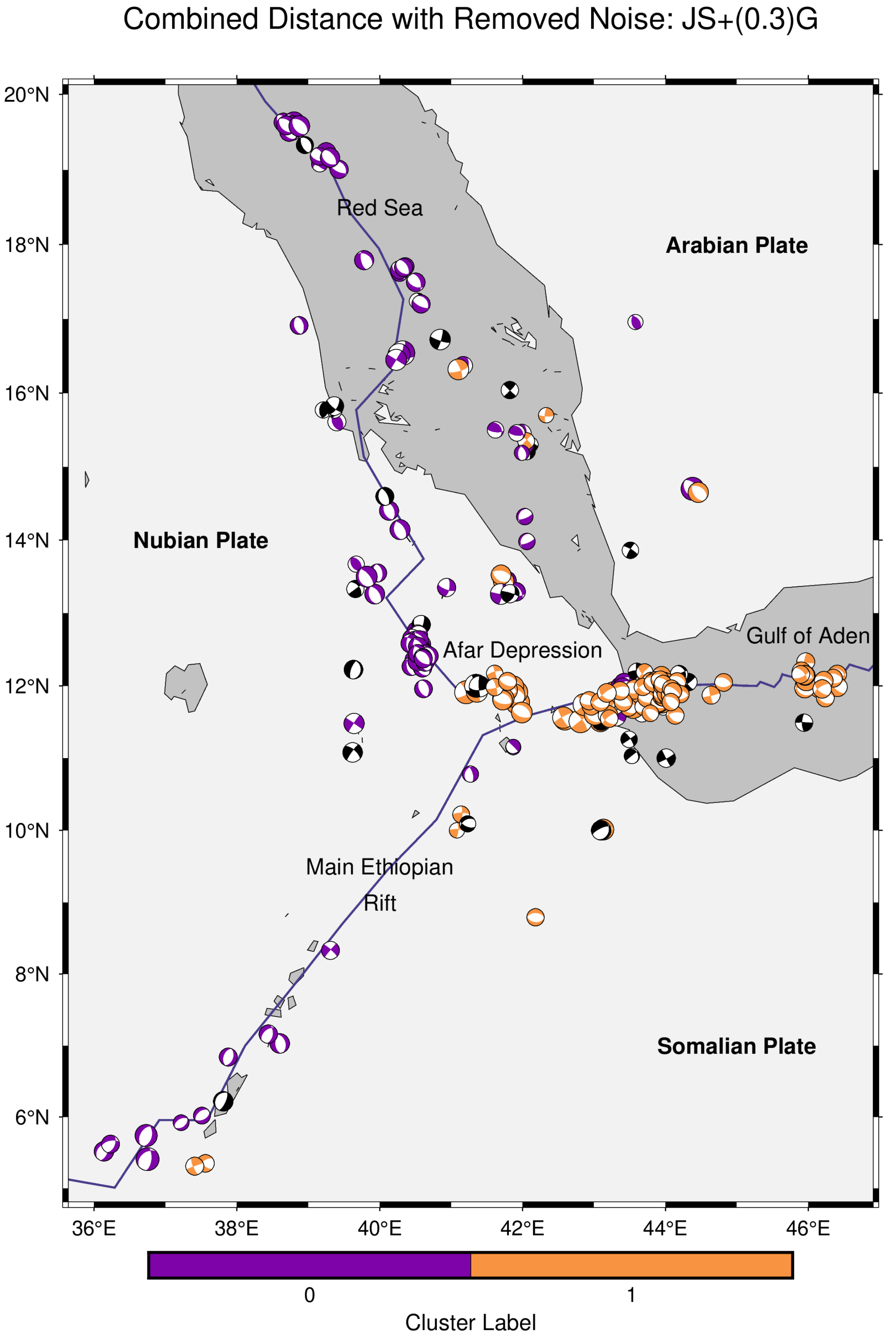

Figure 4.S44: Focal mechanisms with T-quadrant colored according to which of the $C03D$ clusters defined in Fig. 4.S43 it belongs to.

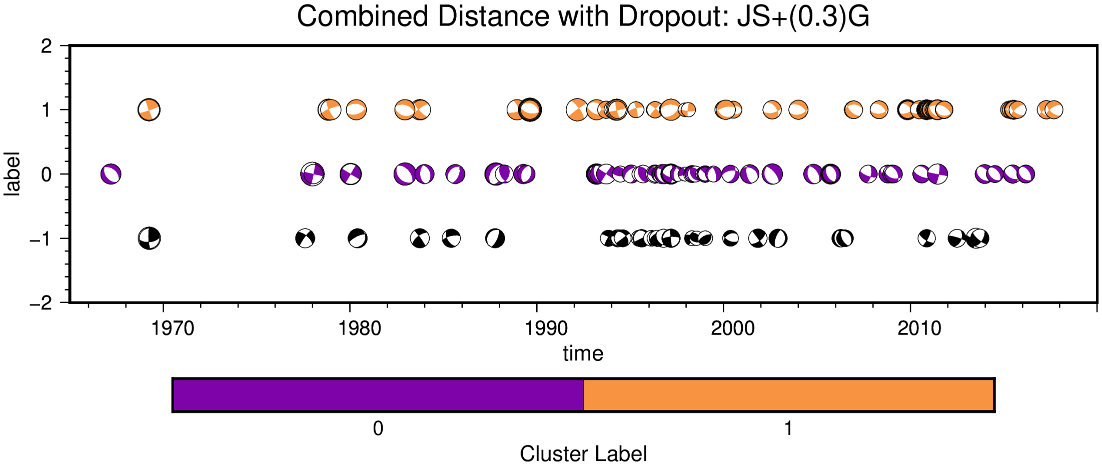

Figure 4.S45: Focal mechanisms with T-quadrant colored according to which of the $C03D$ clusters defined in Fig. 4.S43 it belongs to plotted through time.

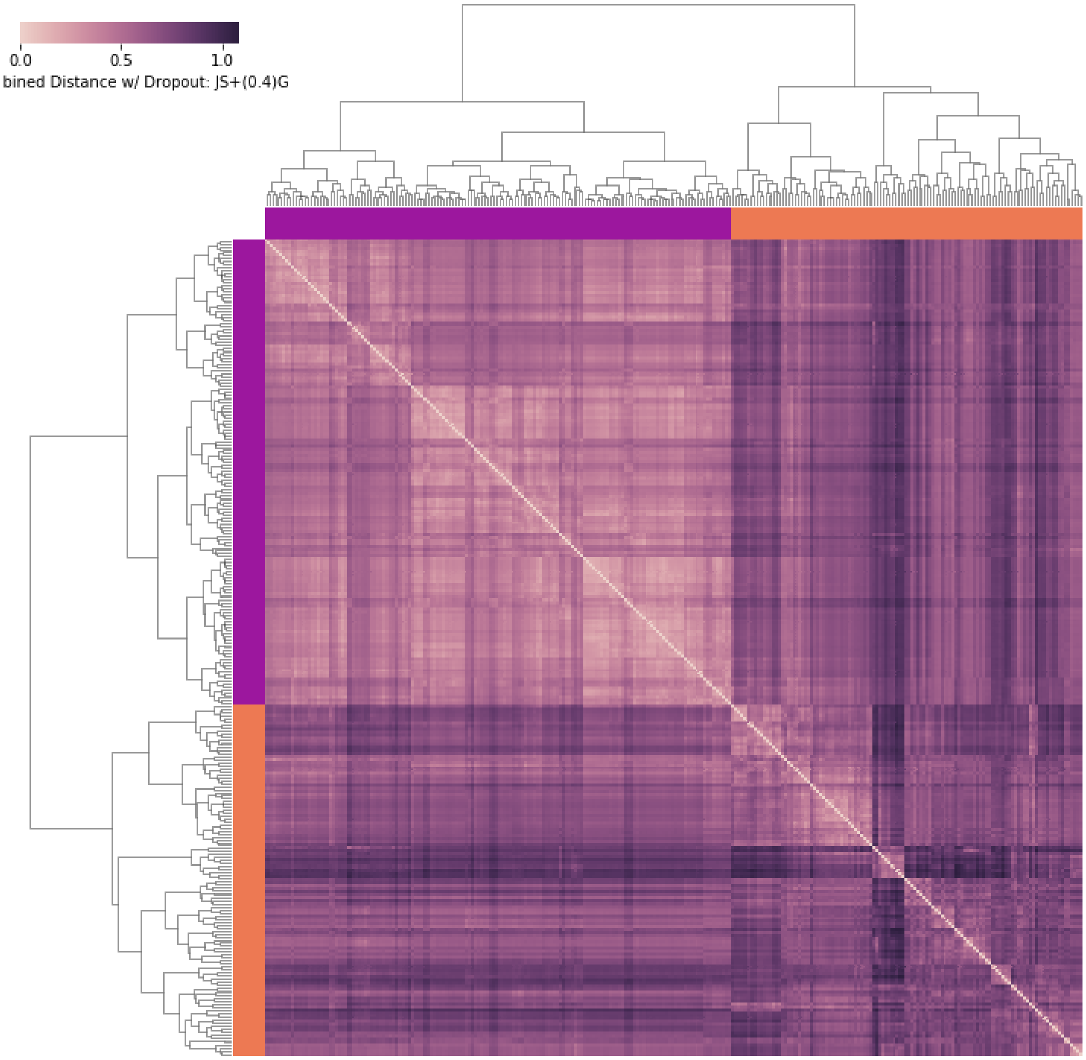

Figure 4.S46: The symmetric distance matrix corresponding to $\mathcal{D}_{C04D} = \mathcal{D}_{JSD} + 0.4\frac{\mathcal{D}_{\mathcal{GD}}}{max(\mathcal{D}_{\mathcal{GD}})}$ as a heatmap. Caption is as in Fig. 4.S1. Model $C05D$ provides identical results.

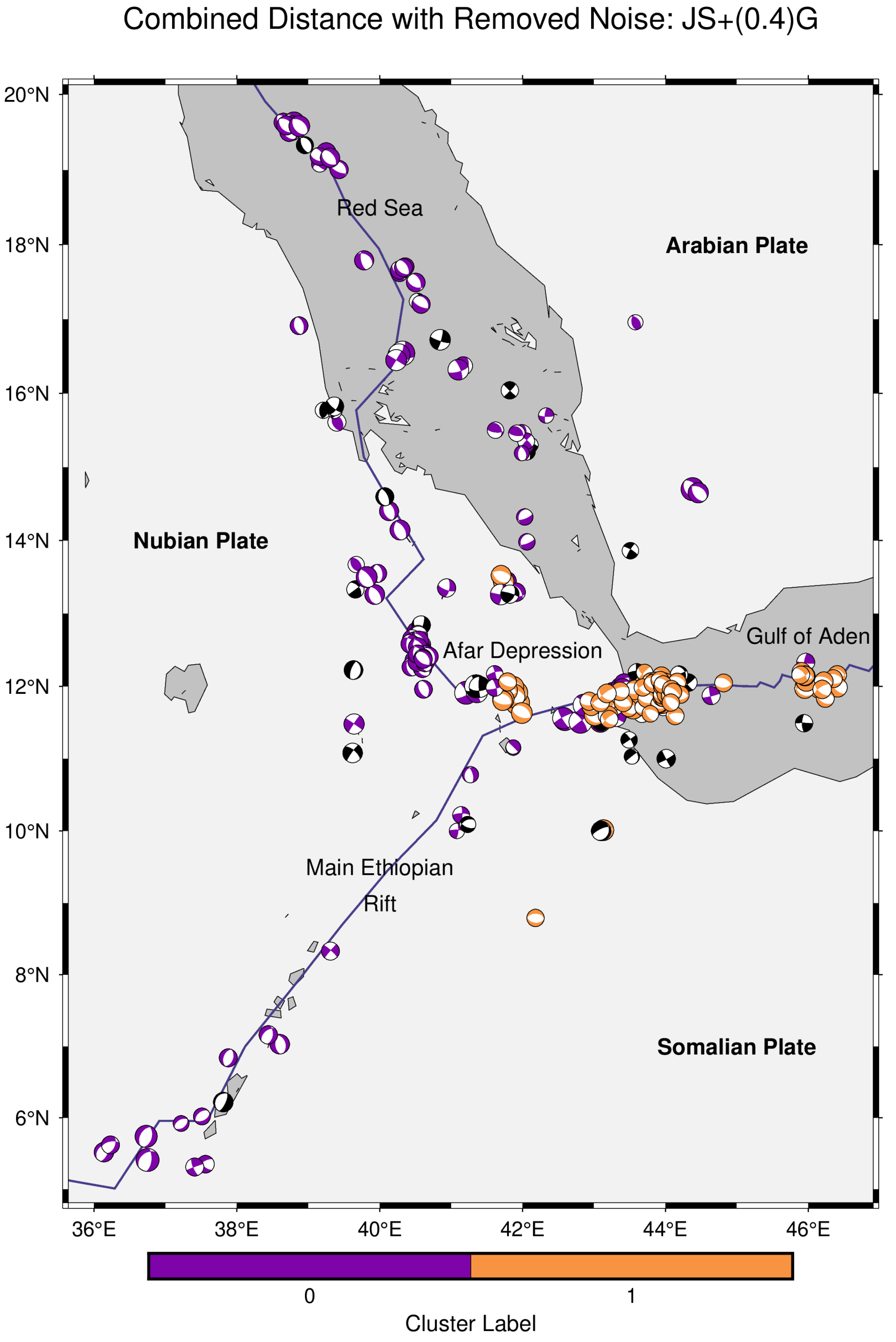

Figure 4.S47: Focal mechanisms with T-quadrant colored according to which of the $C04D$ clusters defined in Fig. 4.S46 it belongs to. Model $C05D$ provides identical results.

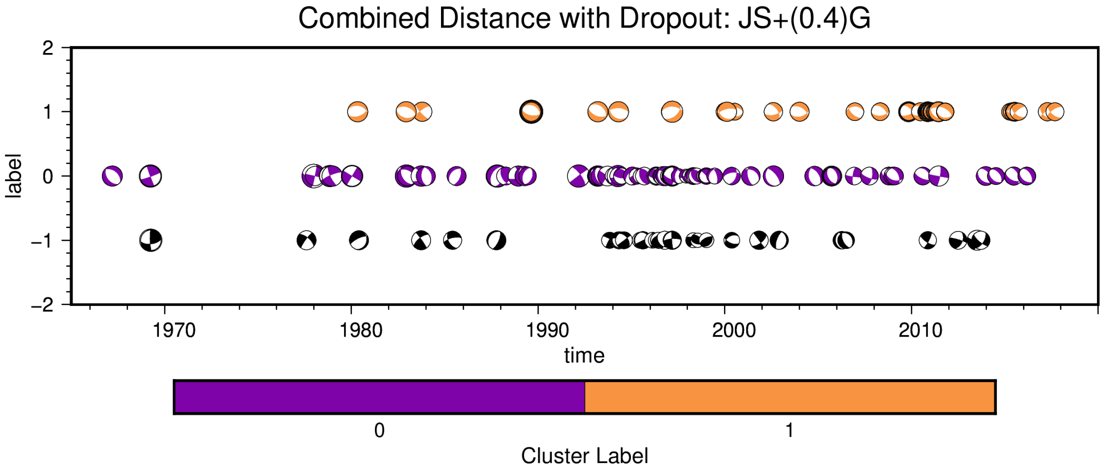

Figure 4.S48: Focal mechanisms with T-quadrant colored according to which of the $C04D$ clusters defined in Fig. 4.S46 it belongs to plotted through time. Model $C05D$ provides identical results.

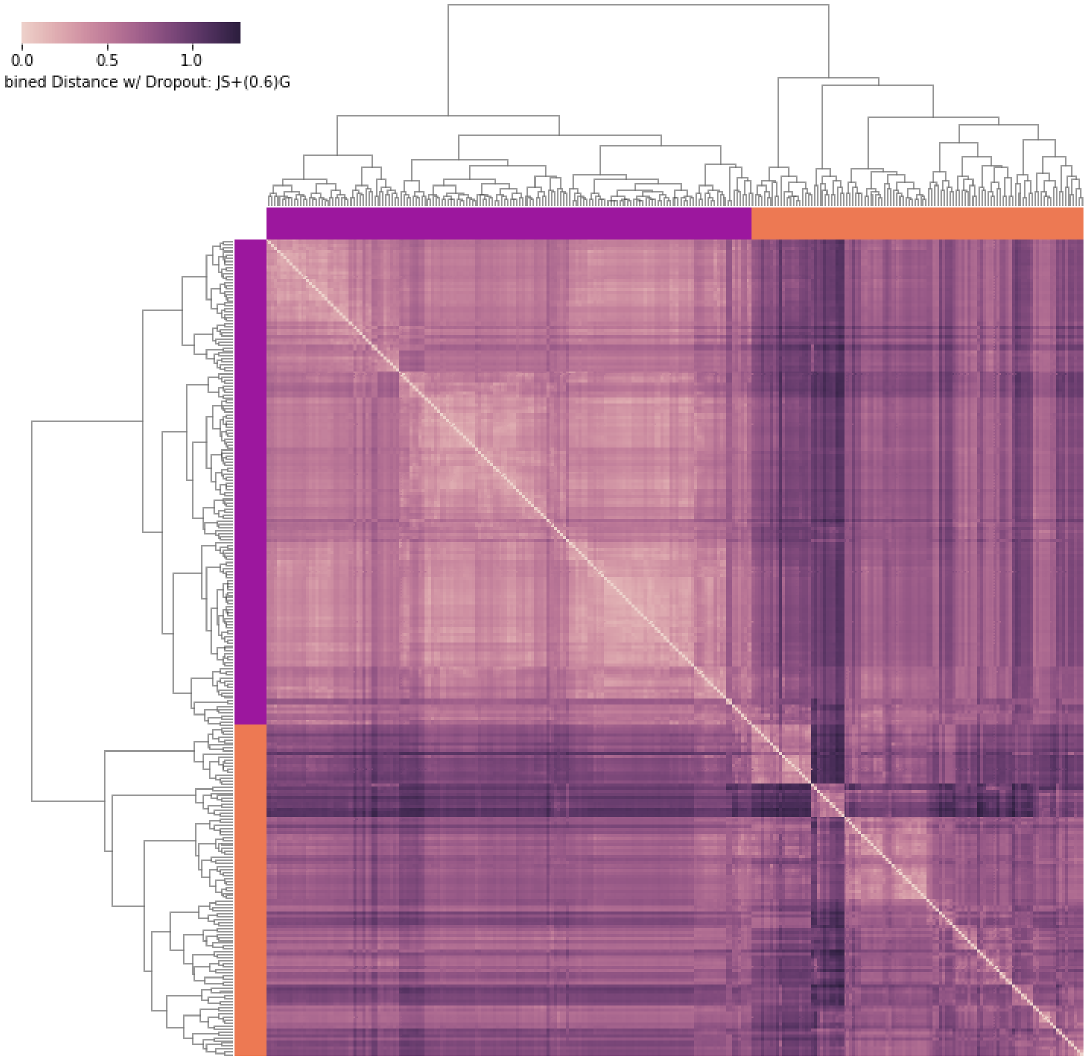

Figure 4.S49: The symmetric distance matrix corresponding to $\mathcal{D}_{C06D} = \mathcal{D}_{JSD} + 0.6\frac{\mathcal{D}_{\mathcal{GD}}}{max(\mathcal{D}_{\mathcal{GD}})}$ as a heatmap. Caption is as in Fig. 4.S1.

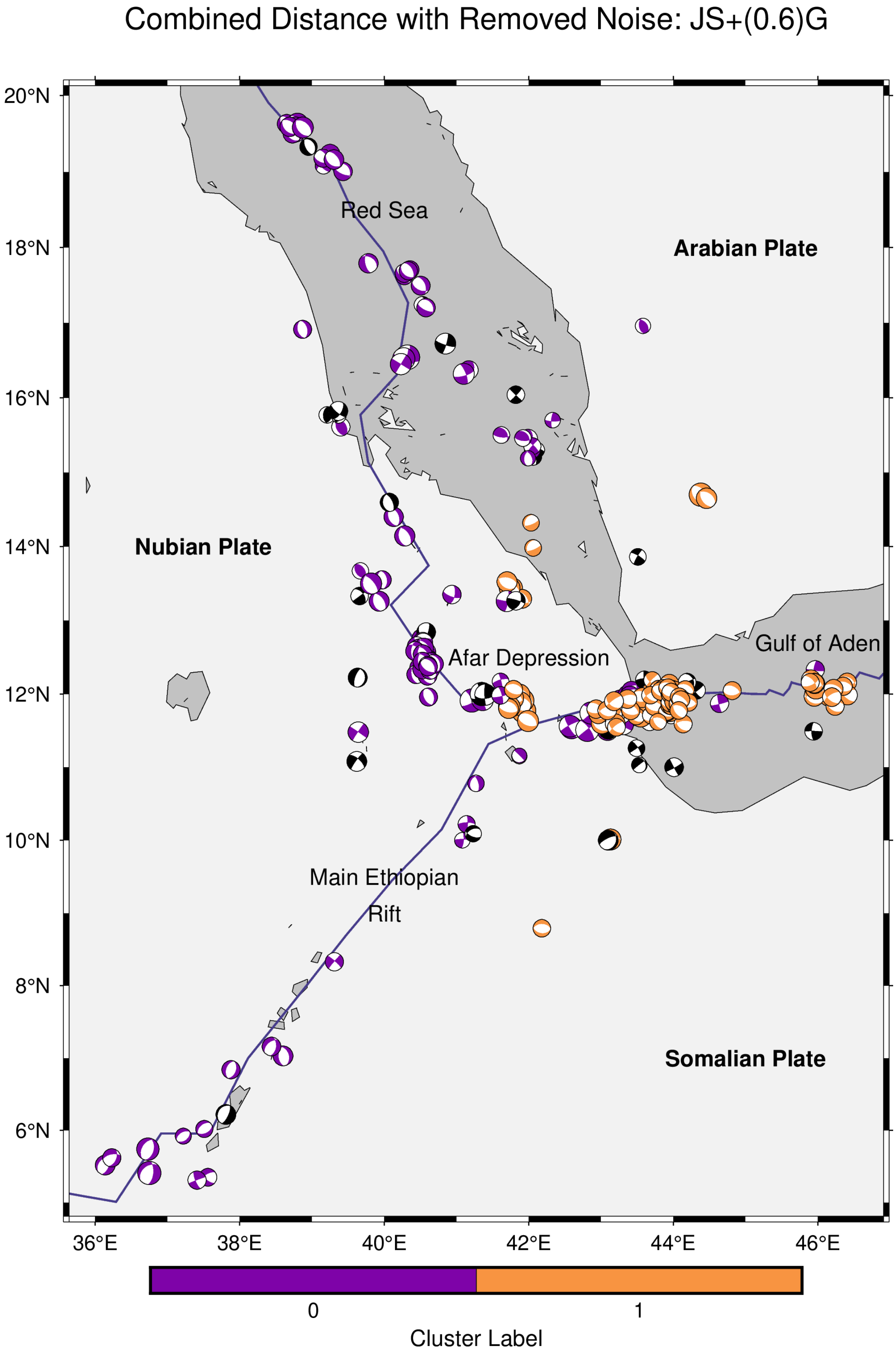

Figure 4.S50: Focal mechanisms with T-quadrant colored according to which of the $C06D$ clusters defined in Fig. 4.S49 it belongs to.

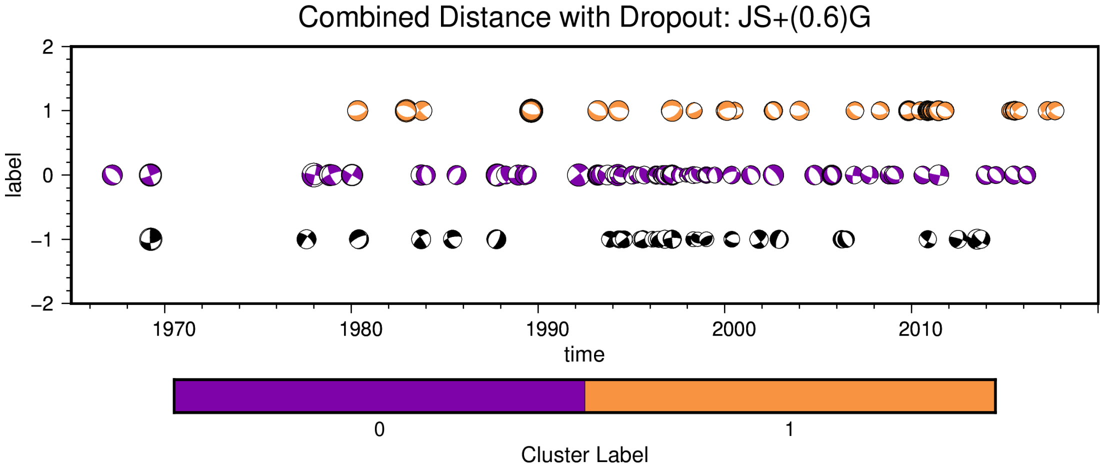

Figure 4.S51: Focal mechanisms with T-quadrant colored according to which of the $C06D$ clusters defined in Fig. 4.S49 it belongs to plotted through time.

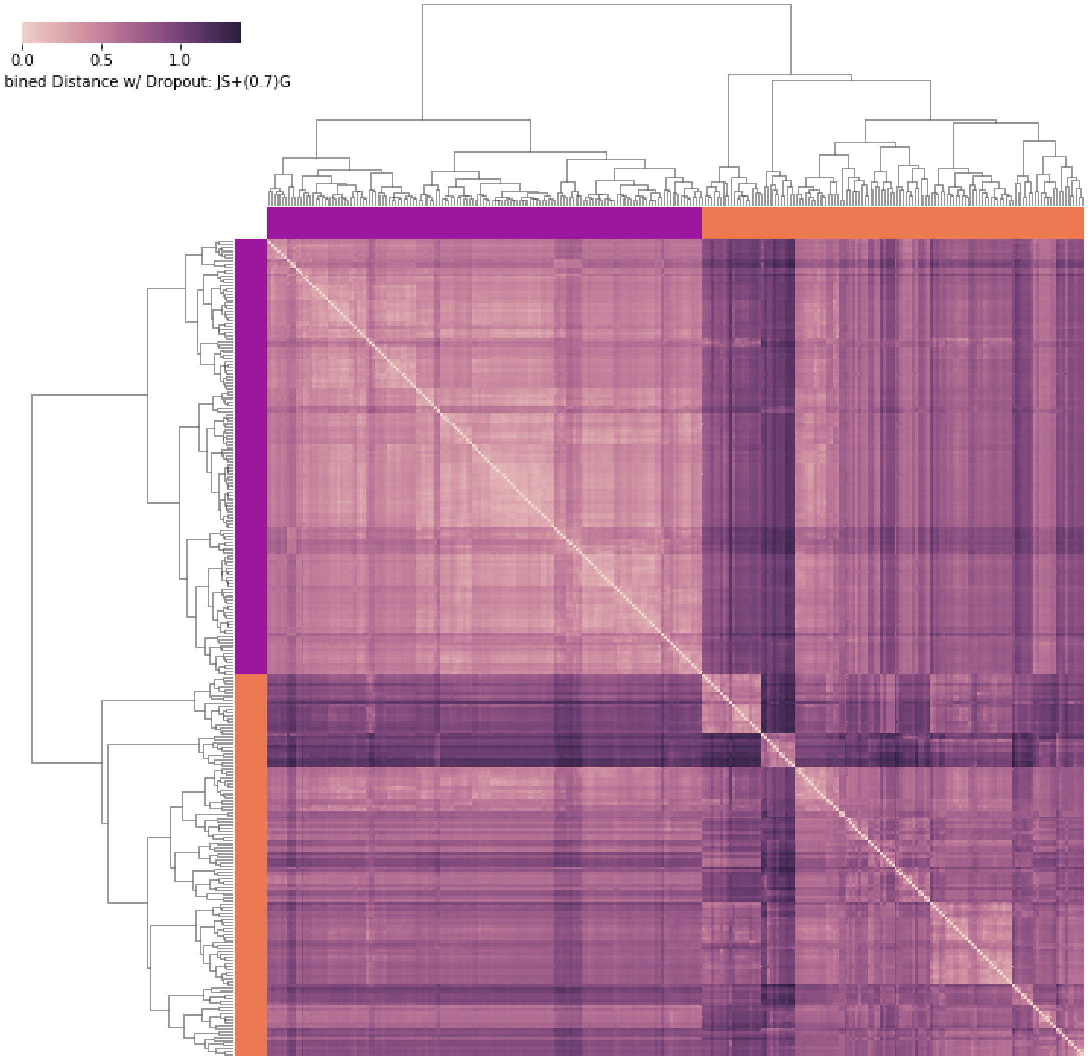

Figure 4.S52: The symmetric distance matrix corresponding to $\mathcal{D}_{C07D} = \mathcal{D}_{JSD} + 0.7\frac{\mathcal{D}_{\mathcal{GD}}}{max(\mathcal{D}_{\mathcal{GD}})}$ as a heatmap. Caption is as in Fig. 4.S1.

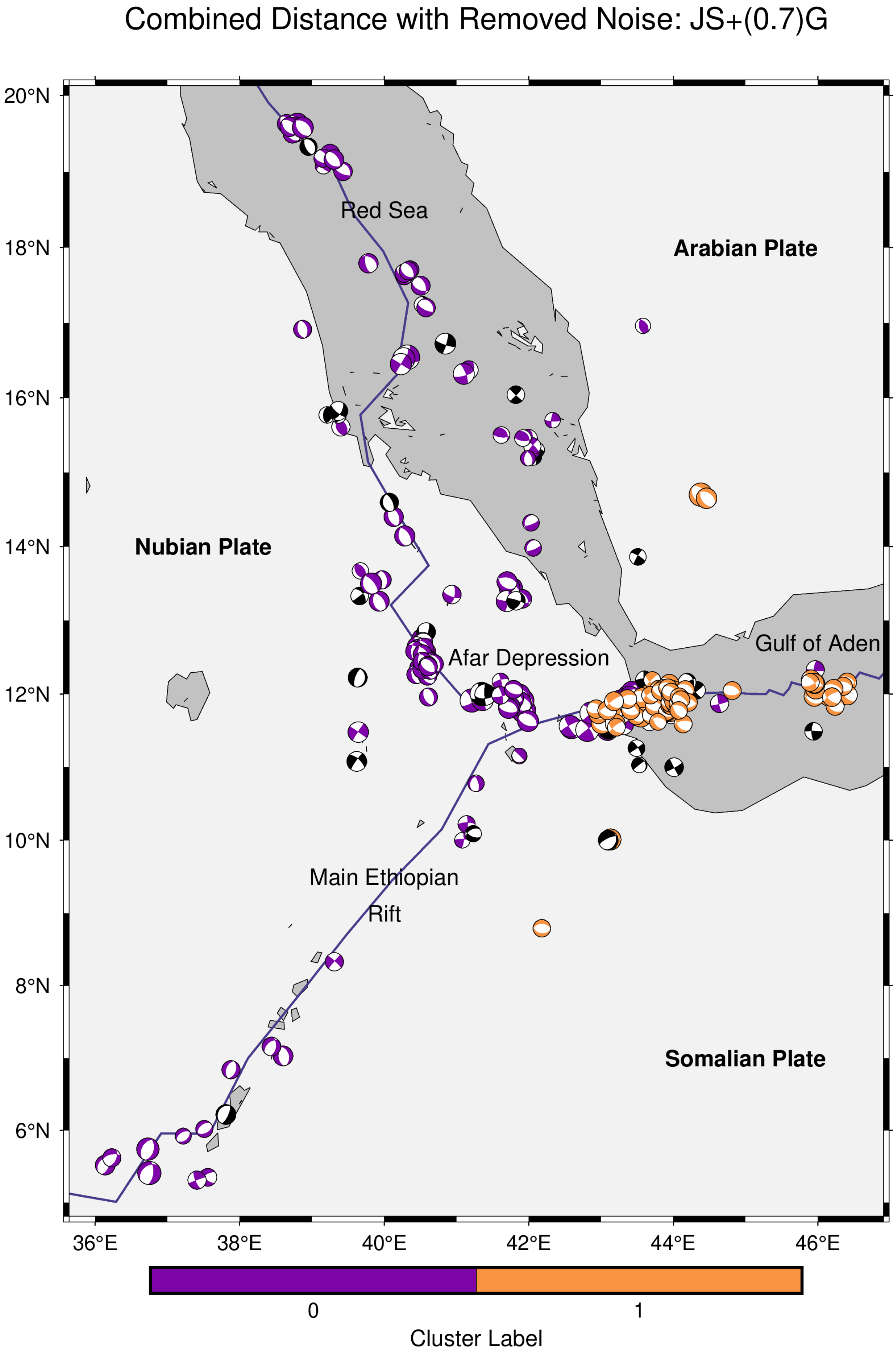

Figure 4.S53: Focal mechanisms with T-quadrant colored according to which of the $C07D$ clusters defined in Fig. 4.S52 it belongs to.

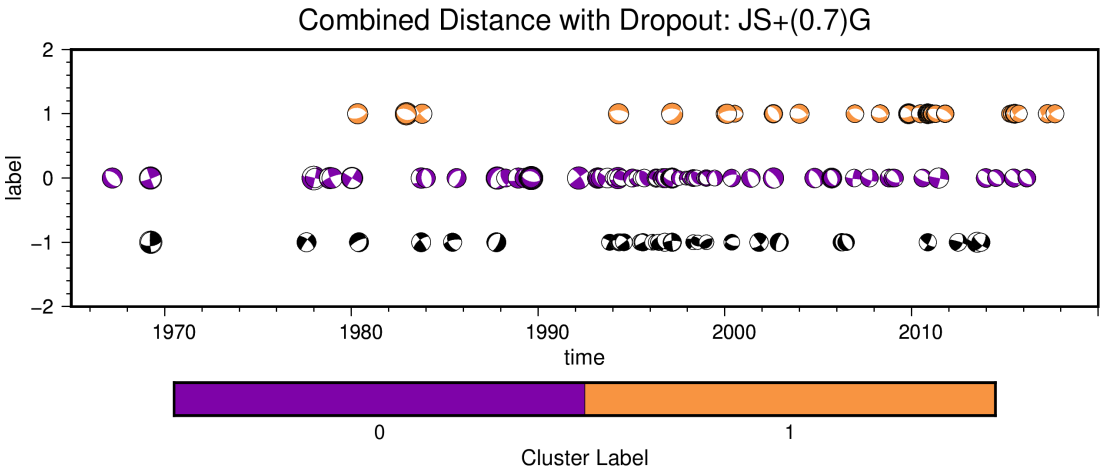

Figure 4.S54: Focal mechanisms with T-quadrant colored according to which of the $C07D$ clusters defined in Fig. 4.S52 it belongs to plotted through time.

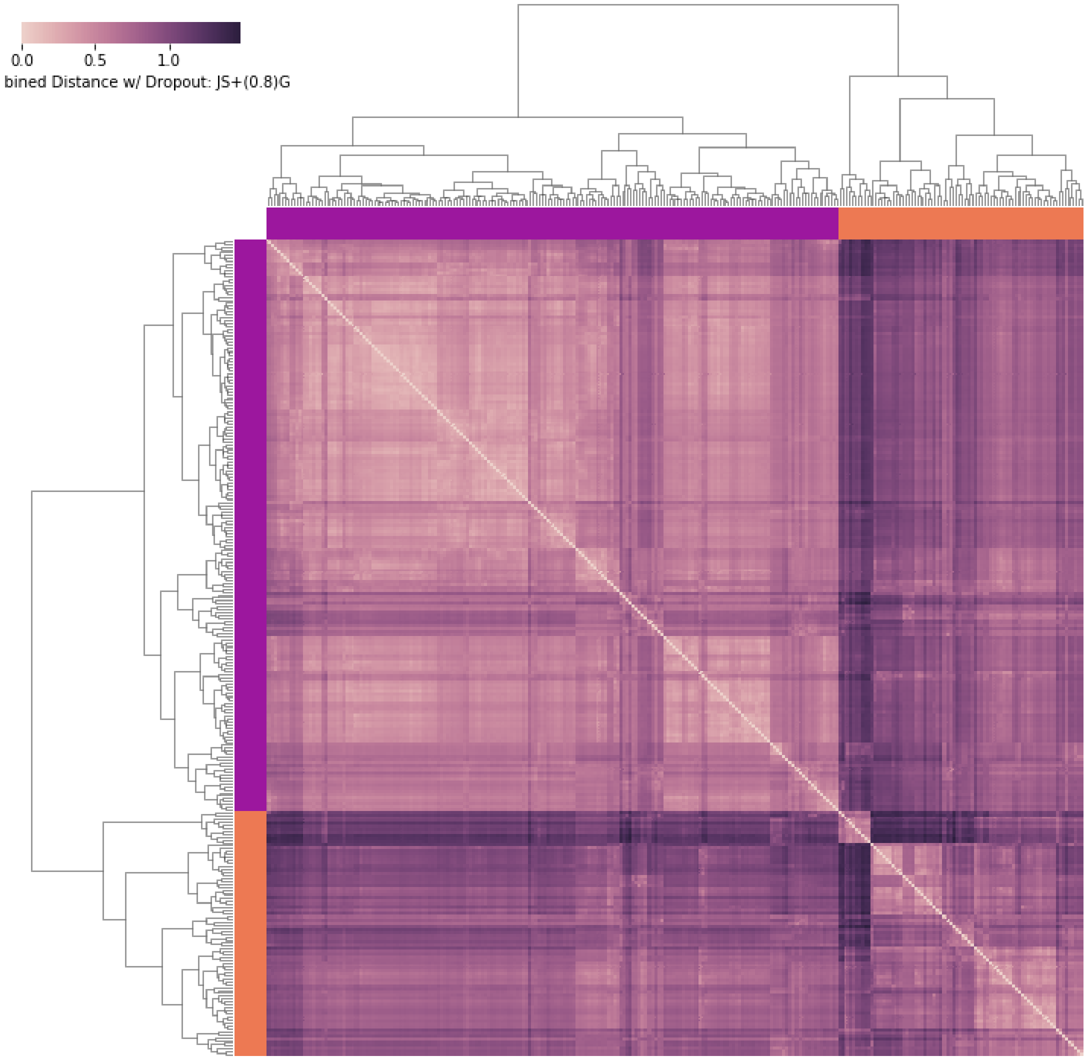

Figure 4.S55: The symmetric distance matrix corresponding to $\mathcal{D}_{C08D} = \mathcal{D}_{JSD} + 0.8\frac{\mathcal{D}_{\mathcal{GD}}}{max(\mathcal{D}_{\mathcal{GD}})}$ as a heatmap. Caption is as in Fig. 4.S1. Model $C09D$ provides identical results.

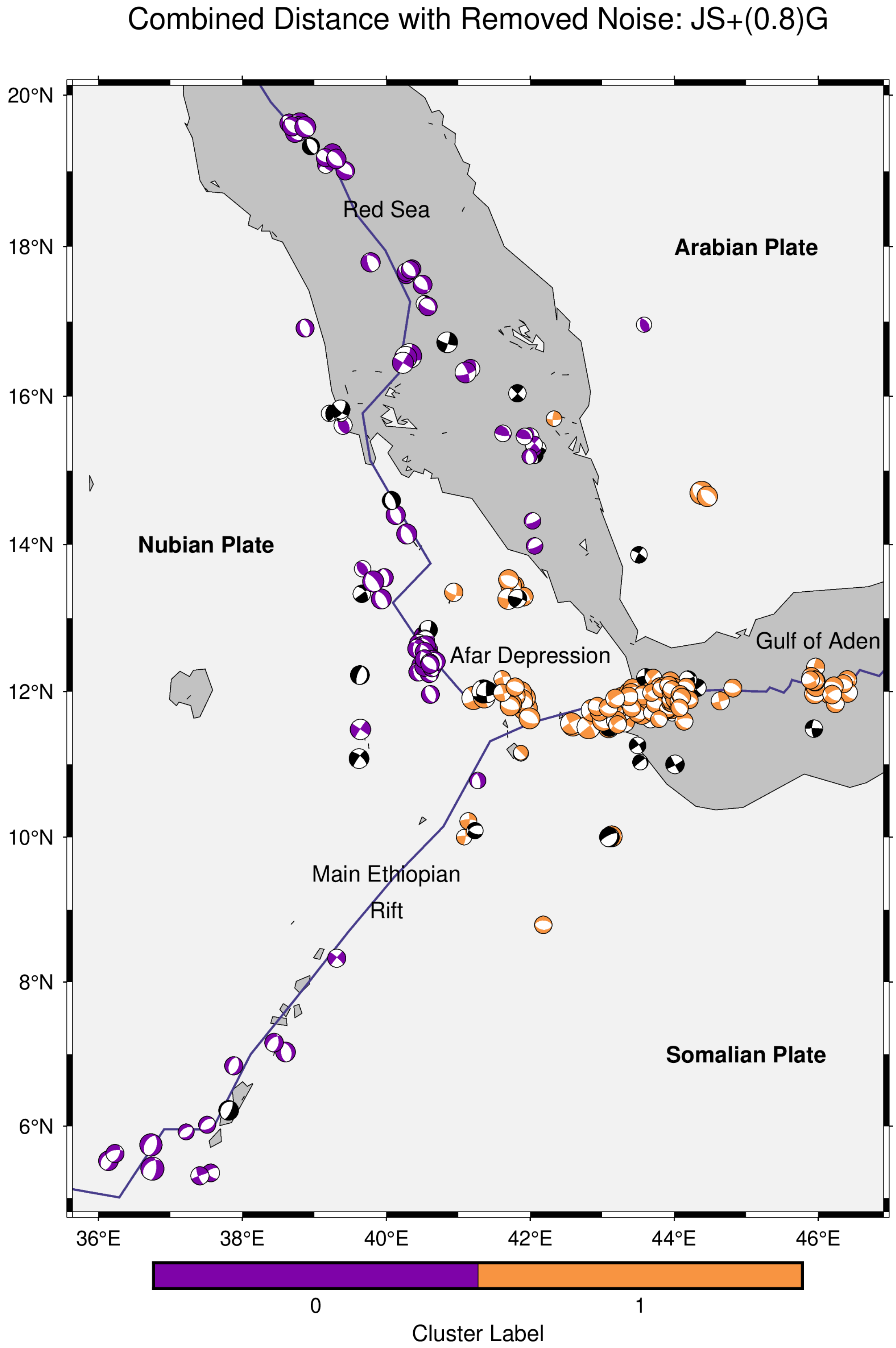

Figure 4.S56: Focal mechanisms with T-quadrant colored according to which of the $C08D$ clusters defined in Fig. 4.S55 it belongs to. Model $C09D$ provides identical results.

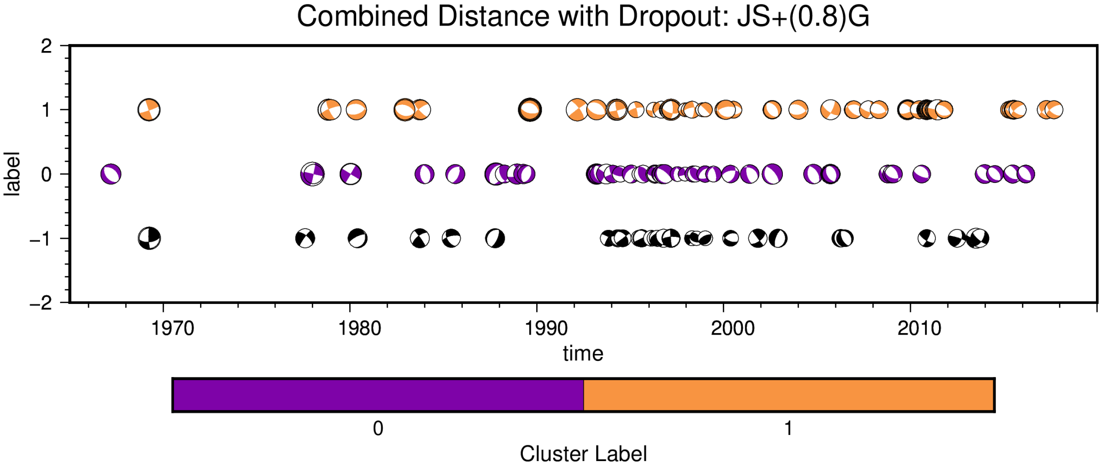

Figure 4.S57: Focal mechanisms with T-quadrant colored according to which of the $C08D$ clusters defined in Fig. 4.S55 it belongs to plotted through time. Model $C09D$ provides identical results.

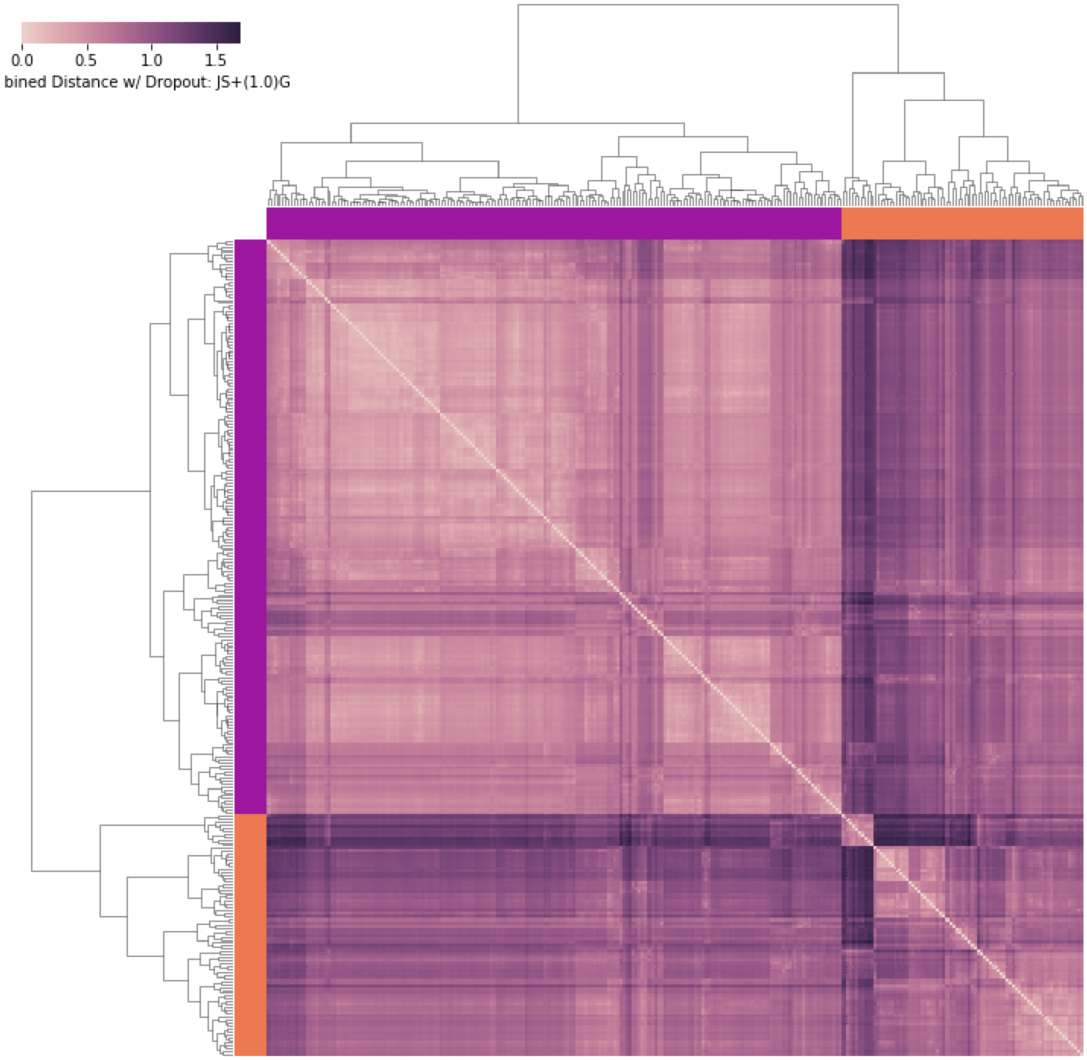

Figure 4.S58: The symmetric distance matrix corresponding to $\mathcal{D}_{C10D} = \mathcal{D}_{JSD} + 1.0\frac{\mathcal{D}_{\mathcal{GD}}}{max(\mathcal{D}_{\mathcal{GD}})}$ as a heatmap. Caption is as in Fig. 4.S1.

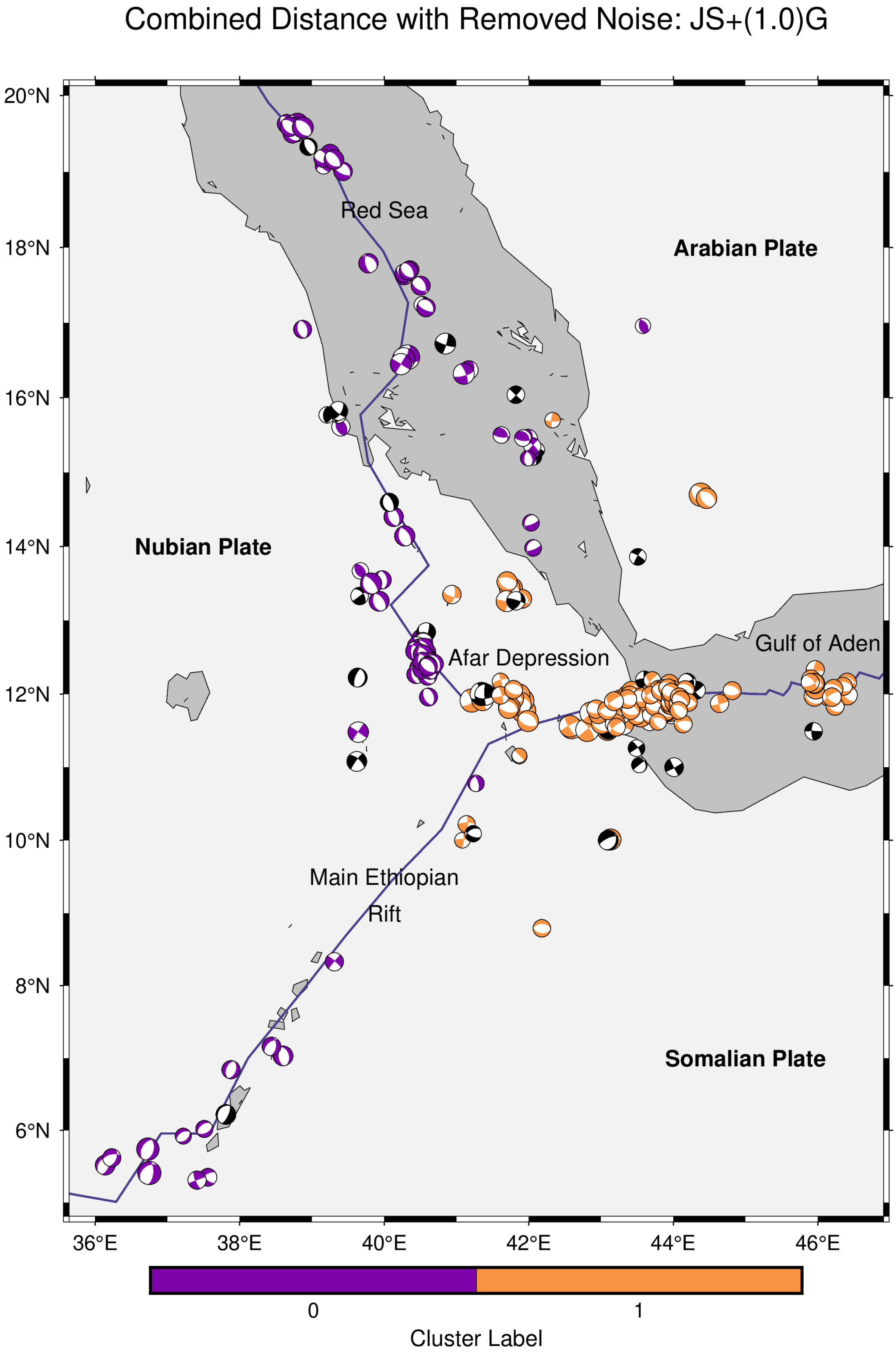

Figure 4.S59: Focal mechanisms with T-quadrant colored according to which of the $C10D$ clusters defined in Fig. 4.S58 it belongs to.

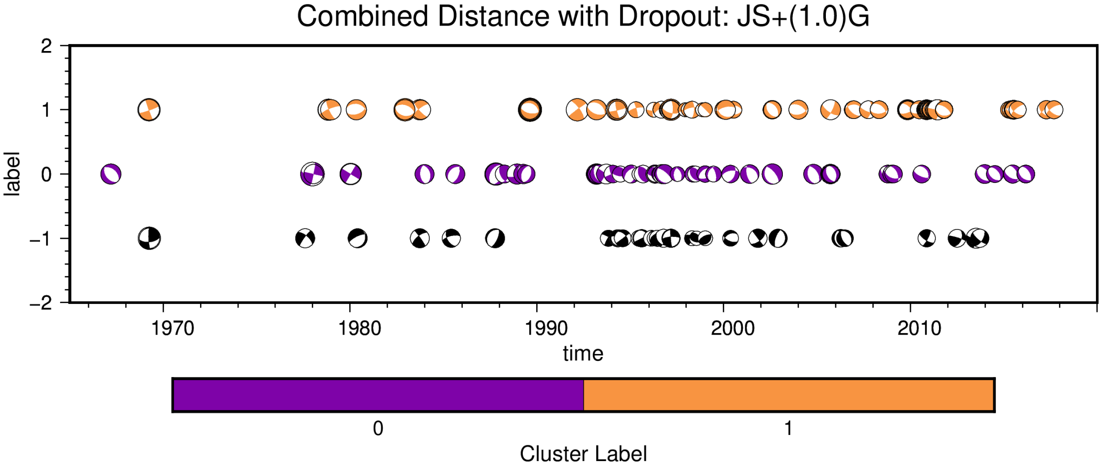

Figure 4.S60: Focal mechanisms with T-quadrant colored according to which of the $C10D$ clusters defined in Fig. 4.S58 it belongs to plotted through time.

CHAPTER 5

Conclusions

Stress in Earth's crust is a fundamental quantity that is of interest to many fields in the Earth sciences. As in situ measurements of stress within Earth's seismogenic crust remain challenging, observations of earthquakes as phenomena of this stress provide a means of making inferences of crustal stress averaged over the extent of an earthquake. The insights these inferences offer constrain orientations and relative magnitudes of crustal stress tensors and can be used to improve understanding of causative mechanisms for these stresses. In this dissertation, we take geodetically and seismically derived observations of slip from earthquakes to constrain tensorial crustal stress in a probabilistic framework with a concentration on exploring the spatial relationship of crustal stress in tectonic environments.

We proposed a Bayesian Markov Chain Monte Carlo estimation technique for constraining tensorial crustal stress in a probabilistic framework in Chapter 2. Our technique allows for the inference of the crustal stresses preceding an earthquake from earthquake slip data. This chapter concentrated on coseismic slip models as a source of earthquake slip data, for which we posited an uncertainty quantification for the errors inherent in this data source. Quantified data uncertainties are necessary for our Bayesian estimation approach. However, the uncertainties on fault geometry parameters estimated by coseismic slip models are typically not quantified or disseminated with models. As we inform our stress inversion of the observed fault strike, dip, and rake of each fault segment of a coseismic slip model, we developed a quantification strategy to determine estimates on how well the coseismic slip model constrains these parameters. We posited that a fault segment's sub-faults possessing a high potency (*i.e.*, the product of the area and the magnitude of slip resolved upon the sub-fault) are likely better resolved by the model than sub-faults with low potency, owing to the higher geodetic signal in high potency areas that are inverted to constrain a coseismic slip model. Following this assumption, we calculated the angular variance on fault segment strike, dip, and rake from the geometries discretized at the sub-fault level weighted by their potencies (Eq. (2.S3)). We then scaled the variance on fault segment rake by the potency of each segment relative to the full coseismic slip model

(Eq. (2.S4)) to account for variations in the ability to constrain signal along multiple fault segments. We quantified the final uncertainties on fault segment strike and dip through an arbitrary scaling dependent upon the relative segment potency to the total potency of the model (Eq. (2.S5)). We incorporated the uncertainties on fault segment strike and dip via the errors propagated through our rake prediction calculation (Eq. (2.S6)). Our strategy for quantifying uncertainties on fault segment geometries has the effect of allowing for higher confidence in the values constrained by a coseismic slip model in regions with high geodetic signal in contrast to regions with low signal where resolving these parameters may be more likely to be hindered by noise.

We demonstrated our technique to estimate stress posteriors from synthetic examples of multiple conflicting earthquake slip observations with multiple slip surfaces. We developed a composite posterior as the non-mutually exclusive union of each of the posteriors determined from each of the slip models considered. This composite stress posterior allows for each of the individual stress posteriors to be equally likely representations of the pre-earthquake state of stress, and by extension, allows for each of the slip models inverted for the stress posteriors to be an equally likely representation of the actual slip in the earthquake. It also assumes that the stress preceding the earthquake is included in one or more stress posteriors incorporated in the composite. This approach is in contrast to calculating the joint of multiple stress posteriors, which makes a more confined assumption that all stress posteriors resolve the stress preceding the earthquake.

We applied our estimation technique to several published coseismic slip models of the 2016 $M_w 7.8$ Kaikōura, South Island, New Zealand earthquake. This earthquake ruptured more than 20 fault segments with varied fault geometries and slip patterns, making it particularly apt for a highly constrained estimate of seismogenic stress using our method. Our results showed that the crustal stress preceding the Kaikōura earthquake was consistent with a thrust stress regime with a WNW-ESE trending most compressive stress. An additional benefit of the probabilistic framework of our proposed methodology allowed us to interrogate our stress posterior to determine the mechanical consistency of a coseismic slip model with respect to its fault segments and as a complete model.

We explored regional transitions in crustal stresses for New Zealand's South Island in Chapter 3. In this chapter, we estimated the stress preceding two earthquakes that occurred in the Canterbury Plains of South Island, New Zealand, the 2010 $M_w 7.2$ Darfield and 22 February 2011 $M_w 6.2$ Christchurch earthquakes. We resolved a strike-slip stress regime, with the most likely estimate of the most compressive stress trending to the NW-SE, from coseismic slip models of these earthquakes. Next, we posited a mechanical model of vertical loading in the Canterbury Plains that is consistent with the rotation in the principal components of stress we observe from our estimate of the Kaikōura earthquake, presented in the previous chapter, and our estimate for the Canterbury Plains earthquakes, presented in this chapter. This model demonstrated that loading from sediments that overly the Canterbury Plains is sufficient for the observed rotation in stress, from the thrust to strike-slip stress regimes inferred for the Kaikōura and Canterbury regions, respectively. From this mechanical model, we constrained the absolute magnitude of tectonic stress for northeastern South Island, New Zealand. Further, we suggested that evidence from multiple crustal stress studies predicts that a future earthquake for the South Island's Alpine Fault on-shore plate boundary will possess an oblique mechanism with a more substantial thrust component than is currently assumed.

In Chapter 4, we presented an unsupervised clustering approach of earthquakes informed by the geodesic distance between earthquake epicenters and the distance between stress posteriors estimated from focal mechanisms determined for the earthquakes. This work aimed to reduce bias in grouping earthquakes for regional stress inferences. Our stress estimation in this work took nodal plane geometries of focal mechanisms as earthquake slip data, and the clustering method we developed used distance metrics calculated from our stress posteriors and the earthquake locations. Similar to the coseismic slip model data used in Chapter 2, focal mechanisms and earthquake source data reported by catalogs typically lack reported uncertainties, despite these uncertainties being inherent with substantial trade-offs in determining earthquake source parameters from seismic data. In this chapter, we allow for a uniform 15° standard deviation on each of the source parameters (*i.e.*, the nodal plane strike, dip, and rake). As noted in Chapter 4, this level of uncertainty allows that, at 99.7% confidence, the focal mechanism determination can at least distinguish between faulting mechanisms. In future work, we expect to pose a more sophisticated uncertainty quantification strategy that will treat focal mechanisms and earthquake locations constrained for earthquakes with larger magnitudes recorded by seismic stations with full azimuthal coverage as possessing more certainty than those that are not.

In Chapter 4, we estimated tensorial stress from five decades of focal mechanisms for the Afar Depression and surrounding regions, including the Red Sea, Gulf of Aden, and Main Ethiopian Rift. We calculated clusters of these earthquakes based on our geodesic- and stress-based metrics and resolved two clusters for the region. Both clusters are consistent with a normal stress regime and reveal a rotation in the horizontal principal components of stress from west to east. Furthermore, the boundary between these clusters coincides with the Danakil Block, a tectonic structure undergoing a similar counter-clockwise rotation.

Future research directions should include a detailed study of the influence of incomplete observations of earthquake slip on the inferred regional crustal stresses. This technical direction is motivated by discrepancies between culminated stress estimates from past studies for earthquakes from the Afar Triple Junction that we discussed in Chapter 4. Without considering the sensitivity of stress inversions to incomplete observations of earthquake slip in a region, studies that cluster multiple observations to infer regional crustal stresses may potentially suffer bias in their solutions. Developing a procedure to ensure that inferred stresses are robust to limited observations of earthquake slip and ambiguities in the data and inferences (*e.g.*, *Medina Luna*, 2015) will improve the compatibility of estimates from future stress studies.

An additional future research direction for stress inversions following an improved understanding of data sensitivities includes incorporating multiple forms of earthquake slip data (*i.e.*, coseismic slip models, focal mechanisms, paleo-slip measurements of fault striae, and borehole breakouts). The benefit of fusing these data types is the ability to calculate constrained regional stress estimates that will be more robust to outliers. Such a procedure may also provide a means to better constrain absolute stress magnitudes in Earth's crust in various tectonic settings (*e.g.*, Chapter 3). As described in this work, stress inference work is often limited to regional studies that seek to constrain relative magnitudes of stress from observations of earthquake slip; additional geophysical data and modeling techniques are required to estimate the absolute magnitudes of these stress tensors. Finally, possessing highly resolved regional stress estimates may provide an opportunity to couple additional geophysical datasets to constrain absolute magnitudes of stress (*e.g.*, vertical loading from topography (*Styron and Hetland*, 2015) or sediment burial (Chapter 3)). In summary, probabilistic stress inferences allow for constrained estimates from multiple, uncertain observations of earthquake slip data, reduce bias in interpretations of stress estimates, and hold promise for further development towards constraining Earth's crustal stresses.

BIBLIOGRAPHY

Abdelfattah, A., A. Al-amri, F. K. Z. M. S. Soliman, S. Qaysi, M. Fnais, S. Almadani, and N. Al-Arifi (2020), An analysis of a moderate earthquake, eastern flank of the Red Sea, Saudi Arabia, *Earth Planets Space*, *72*(34).

Alvizuri, C., V. Silwal, L. Krischer, and C. Tape (2018), Estimation of full moment tensors, including uncertainties, for nuclear explosions, volcanic events, and earthquakes, *J. Geophys. Res. Solid Earth*, *123*, 5099–5119.

Angelier, J. (1979), Determination of the mean principal directions of stresses for a given fault population, *Tectonophysics*, *56*, T17–T26.

Angelier, J., A. Tarantola, B. B. Valette, and S. S. Manoussis (1982), Inversion of field data in fault tectonics to obtain the regional stress — I. Single phase fault populations: a new method of computing the stress tensor, *Geophys. J. Int.*, *69*, 607–621.

Arnold, R., and J. Townend (2007), A Bayesian approach to estimating tectonic stress from seismological data, *Geophys. J. Int.*, *170*, 1336–1356.

Atzori, S., C. Tolomei, A. Antonioli, J. P. M. Boncori, S. Bannister, E. Trasatti, P. Pasquali, and S. Salvi (2012), The 2010–2011 Canterbury, New Zealand, seismic sequence: Multiple source analysis from InSAR data and modeling, *J. Geophys. Res.*, *117 B08305*.

Ayele, A. (1998), *Seismicity and earthquake source mechanism study in the East African rift*, PhD dissertation, Uppsala University, Sweden.

Ayele, A., and R. Arvidsson (1998), Fault mechanisms and tectonic implications of the 1985–1987 earthquake sequence in south-western Ethiopia, *J. Seismol.*, *1*, 383–394.

Bai, Y., T. Lay, K. F. Cheung, and L. Ye (2017), Two regions of seafloor deformation generated the tsunami for the 13 November 2016, Kaikoura, New Zealand earthquake, *Geophys. Res. Lett.*, *44*, 6597–6606.

Balfour, N. J., M. K. Savage, and J. Townend (2005), Stress and crustal anisotropy in Marlborough, New Zealand: evidence for low fault strength and structure-controlled anisotropy, *Geophys. J. Int.*, *163*, 1073–1086.

Baumgardner, R., and P. O. Frederickson (1985), Icosahedral Discretization of the Two-Sphere., *SIAM Journal on Numerical Analysis*, *22*(6), 1107–1115.

Beavan, J., M. Motagh, E. Fielding, N. Donnelly, and D. Collett (2012), Fault slip models of the 2010–2011 Canterbury, New Zealand, earthquakes from geodetic data and observations of postseismic ground deformation, New Zealand, *J. Geol. Geophys.*, *55*, 207–221.

Belachew, M., C. Ebinger, D. Coté, D. Keir, J. V. Rowland, J. O. S. Hammond, and A. Ayele (2011), Comparison of dike Intrusions in an Incipient Seafloor-Spreading Segment in Afar, Ethiopia: Seismicity Perspectives, *Journal of Geophysical Research: Solid Earth*, *116*, 1–23.

Berryman, K., A. F. Cooper, R. J. Norris, P. Villamor, R. Sutherland, T. Wright, E. R. Schermer, R. Langridge, and G. Biasi (2012), Late Holocene rupture history of the Alpine Fault in south Westland, New Zealand, *Bull. Seismol. Soc. Am.*, *102(2)*, 620–638.

Boese, C. M., J. Townend, E. Smith, and T. Stern (2012), Microseismicity and stress in the vicinity of the Alpine Fault, central Southern Alps, New Zealand, *J. Geophys. Res.*, *117*, B02,302.

Bosworth, W. (2008), *Geology of East Libya*, chap. ”North Africa – Mediterranean present-day stress field transition and implications for fractured reservoir production in the Eastern Libyan Basins”, Earth Science Society of Libya.

Bosworth, W., and S. Durocher (2017), Present-day stress fields of the Gulf of Suez (Egypt) based on exploratory well data: non-uniform regional extension and its relation to inherited structures and local plate motion, *J. Afr. Earth Sci.*, *136*, 136–147.

Bosworth, W., and M. Taviani (1996), Late Quaternary reorientation of stress field and extension direction in the southern Gulf of Suez, Egypt: evidence from uplifted coral terraces, mesoscopic fault arrays, *Tectonics*, *15*, 791–802.

Bott, M. H. P. (1959), The mechanics of oblique slip faulting, *Geol. Mag.*, *96*, 109–117.

Bradley, B. A., S. E. Bae, V. Polak, R. L. Lee, E. M. Thomson, and K. Tarbali (2017), Ground motion simulations of great earthquakes on the Alpine Fault: effect of hypocentre location and comparison with empirical modelling, New Zealand, *J. Geol. Geophys.*, *60(3)*, 188—-198.

Browne, G. H., B. D. Field, D. J. A. Barrell, R. Jongens, K. N. Bassett, and R. A. Wood (2012), The geological setting of the Darfield and Christchurch earthquakes, *New Zeal. J. Geol. Geophys.*, *55*, 193–197.

Bull, W. B. (1996), Prehistorical earthquakes on the Alpine fault, New Zealand, *New Zealand, J. Geophys. Res.*, *101:B3*, 6037—-6050.

Byerlee, J. (1978), Friction of rocks, *Pure Appl Geophys*, *116*, 615–626.

Cesca, S., F. Grigoli, S. Heimann, T. Dahm, M. Kriegerowski, M. Sobiesiak, C. Tassara, and M. Olcay (2016), The Mw 8.1 2014 Iquique, Chile, seismic sequence: a tale of foreshocks and aftershocks, *Geophysical Journal International*, *204*(3), 1766–1780.

Cesca, S., Y. Zhang, V. Mouslopoulou, R. Wang, J. Saul, M. Savage, S. Heimann, S. K. Kufner, O. Oncken, , and T. Dahm (2017), Complex rupture process of the Mw 7.8, 2016, Kaikoura earthquake, New Zealand, and its aftershock sequence, *Earth Planet. Sci. Lett.*, *478*, 110–120.

Chang, K., W.-C. Chi, R.-F. Chen, and R.-J. Rau (2018), Load-induced seismicity near Tsaoling, Taiwan, *Phys. Earth Planet. In.*, *282*, 21–24.

Clark, K. J., E. K. Nissen, J. D. Howarth, I. J. Hamling, J. J. Mountjoy, W. F. Ries, K. Jones, S. Goldstien, U. A. Cochran, P. Villamor, S. Hreinsdóttir, N. J. Litchfield, C. Mueller, K. R. Berryman, and D. T. Strong (2017), Highly variable coastal deformation in the 2016 Mw7.8 Kaikōura earthquake reflects rupture complexity along a transpressional plate boundary, *Earth Planet. Sci. Lett.*, *474*, 334–344.

Coblentz, D. D., S. Zhou, R. R. Hillis, R. M. Richardson, and M. Sandiford (1998), Topography, boundary forces, and the Indo-Australian intraplate stress field, *J. Geophys. Res.*, *103(B1)*, 919–931.

De Pascale, G. P., M. C. Quigley, and T. R. Davies (2014), Lidar reveals uniform Alpine Fault offsets and bimodal plate boundary rupture behavior, New Zealand, *Geology (Boulder)*, *42(5)*, 411–414.

Delvaux, D., and A. Barth (2010), African stress pattern from formal inversion of focal mechanism data, *Tectonophysics*, *482*(1–4), 105–128.

Diederichs, A., E. K. Nissen, L. J. Lajoie, R. M. Langridge, S. R. Malireddi, K. J. Clark, I. J. Hamling, and A. Tagliasacchi (2019), Unusual kinematics of the Papatea fault (2016 Kaikōura earthquake) suggest anelastic rupture, *Science Advances*, *5*, eaax5703.

Dorn, C., A. Green, R. Jongens, S. Carpentier, A. Kaiser, F. Campbell, H. Horstmeyer, J. Campbell, M. Finnemore, and J. Pettinga (2010), High-resolution seismic images of potentially seismogenic structures beneath the northwest Canterbury Plains, New Zealand, *J. Geophys. Res.*, *115*.

Douilly, R., H. Aochi, E. Calais, and A. M. Freed (2015), 3D Dynamic Rupture Simulations Across Interacting Faults: The Mw7.0, 2010, Haiti Earthquake, *J. Geophys. Res. Solid Earth*, *120*, 1108–1128.

Duputel, Z., L. Rivera, Y. Fukahata, and H. Kanamori (2012), Uncertainty estimations for seismic source inversions, *Geophys. J. Int.*, *190*, 1243–1256.

Duputel, Z., P. S. Agram, M. Simons, S. E. Minson, , and J. L. Beck (2014), Accounting for prediction uncertainty when inferring subsurface fault slip, *Geophys. J. Int.*, *197*, 464–482.

Eberhart-Phillips, D., and S. Bannister (2010), 3-D imaging of Marlborough, New Zealand, subducted plate and strike-slip fault systems, *Geophys. J. Int.*, *182*, 73–96.

Ebinger, C. J., D. Keir, A. Ayele, E. Calais, T. J. Wright, M. Belachew, J. O. S. Hammond, E. Campbell, and R. Buck (2008), Capturing Magma Intrusion and Faulting Processes during Continental Rupture, *Seismicity of the Dabbahu (Afar) Rift*, *174*, 1138–1152.

Elliott, J. R., E. K. Nissen, P. C. England, J. A. Jackson, S. Lamb, Z. Li, M. Oehlers, and B. Parsons (2012), Slip in the 2010–2011 Canterbury earthquakes, New Zealand, *J. Geophys. Res.*, *117 B03401*.

Fielding, E. J., A. Sladen, Z. Li, J. Avouac, R. Bürgmann, and I. Ryder (2013), Kinematic fault slip evolution source models of the 2008 M7.9 Wenchuan earthquake in China from SAR interferometry, GPS and teleseismic analysis and implications for Longmen Shan tectonics, *Geophys. J. Int.*, *194*, 1138–1166.

Forsyth, D., and S. Uyeda (1975), On the Relative Importance of the Driving Forces of Plate Motion, *Geophys. J. Int.*, *43*, 163–200.

Ghosh, A., W. E. Holt, and L. Wen (2013), Predicting the lithospheric stress field and plate motions by joint modeling of lithosphere and mantle dynamics, *J. Geophys. Res. Solid Earth*, *118*, 346–368.

Hamling, I. J. (2019), A review of the 2016 Kaikōura earthquake: insights from the first 3 years, J. Roy. Soc. New Zeal., *J. Roy. Soc. New Zeal.*, *50*, 226–244.

Hamling, I. J., S. Hreinsdóttir, K. Clark, J. Elliott, C. Liang, E. Fielding, N. Litchfield, P. Villamor, L. Wallace, T. J. Wright, E. D'Anastasio, S. Bannister, D. Burbidge, P. Denys, P. Gentle, J. Howarth, C. Mueller, N. Palmer, C. Pearson, W. Power, P. Barnes, D. J. Barrell, R. V. Dissen, R. Langridge, T. Little, A. Nicol, J. Pettinga, J. Rowland, and M. Stirling (2017), Complex multifault rupture during the 2016 Mw 7.8 Kaikōura earthquake, New Zealand, *Science*, *356*, eaam7194.

Hardebeck, J. L., and A. J. Michael (2006), Damped regional-scale stress inversions: Methodology and examples for southern California and the Coalinga aftershock sequence, *J. Geophys. Res.*, *111*, B11,310.

Hastings, W. K. (1970), Monte Carlo sampling methods using Markov chains and their applications, *Biometrika*, *57*, 97–109.

He, P., E. Hetland, Q. Wang, K. Ding, and R. Zou (2017), Coseismic slip in the 2016 Ecuador Mw 7.8 earthquake imaged from Sentinal-1A radar interferometry, *Seismol. Res. Lett.*, *88*, 277–286.

Herman, M. W., R. B. Herrmann, H. M. Benz, and K. P. Furlong (2014), Using regional moment tensors to constrain the kinematics and stress evolution of the 2010–2013 Canterbury earthquake sequence, South Island, New Zealand, *Tectonophysics*, *633*, 1–15.

Hofstetter, R., and M. Beyth (2003), The Afar Depression: interpretation of the 1960–2000 earthquakes, *Geophysical Journal International*, *155*, 715–732.

Holden, C., Y. Kaneko, E. D'Anastasio, R. Benites, B. Fry, and I. J. Hamling (2017), The 2016 Kaikōura earthquake revealed by kinematic source inversion and seismic wavefield simulations: Slow rupture propagation on a geometrically complex crustal fault network, *Geophys. Res. Lett.*, *44*, 11,320–11,328.

Hollingsworth, J., L. Ye, and J.-P. Avouac (2017), Dynamically triggered slip on a splay fault in the Mw 7.8 Kaikoura (New Zealand) earthquake, *Geophys. Res. Lett.*, *44*, 3517–3525.

Holt, R. A., M. K. Savage, J. Townend, E. Syracuse, and C. Thurber (2013), Crustal stress and fault strength in the Canterbury Plains, New Zealand, *Earth Planet. Sci. Lett.*, *383*, 173–181.

Kaiser, A., C. Holden, J. Beavan, D. Beetham, R. Benites, A. Celentano, D. Collett, J. Cousins, M. Cubrinovski, G. Dellow, P. Denys, E. Fielding, B. Fry, M. Gerstenberger, R. Langridge, C. Massey, M. Motagh, N. Pondard, G. McVerry, J. Ristau, M. Stirling, J. Thomas, S. R. Uma, and J. Zhao (2012), The Mw 6.2 Christchurch earthquake of February 2011: preliminary report, *New Zealand Journal of Geology and Geophysics*, *55:1*, 67–90, doi:10.1080/00288306.2011.641182.

Kaiser, A., N. Balfour, B. Fry, C. Holden, N. Litchfield, M. Gerstenberger, E. D'Anastasio, N. Horspool, G. McVerry, J. Ristau, S. Bannister, A. Christophersen, K. Clark, W. Power, D. Rhoades, C. Massey, I. Hamling, L. Wallace, J. Mountjoy, Y. Kaneko, R. Benites, C. Van Houtte, S. Dellow, L. Wotherspoon, K. Elwood, and K. Gledhill (2017), The 2016 Kaikōura, New Zealand, Earthquake: Preliminary Seismological Report, *Seismol. Res. Lett.*, *88*, 727–739.

Kearse, J., T. A. Little, R. J. V. Dissen, P. M. Barnes, R. Langridge, J. Mountjoy, W. Ries, P. Villamor, K. J. Clark, A. Benson, G. Lamarche, M. Hill, and M. Hemphill-Haley (2018), Onshore to offshore ground-surface and seabed rupture of the Jordan–Kekerengu–Needles fault network during the 2016 Mw 7.8 Kaikōura earthquake, New Zealand, *Bull. Seismol. Soc. Am.*, *108*, 1573–1595.

Kebede, F., W.-Y. Kim, and O. Kulhanek (), Dynamic source parameters of the March–May 1969 Serdo earthquakes in Central Afar, Ethiopia, deduced from teleseismic body waves, *J. geophys. Res.*, *94*, 5603–5614.

Keir, D., I. J. Hamling, A. Ayele, E. Calais, C. Ebinger, T. J. Wright, E. Jacques, K. Mohamed, J. O. S. Hammond, M. Belachew, E. Baker, J. V. Rowland, E. Lewi, and L. Bennati (2009), Evidence for Focused Magmatic Accretion at Segment Centers from Lateral Dike Injections Captured beneath the Red Sea Rift in Afar, *Geology*, *37*, 59–62.

Kleffmann, S., F. Davey, A. Melhuish, D. Okaya, T. Stern, and S. Team (1998), Crustal structure in the central South Island, New Zealand, from the Lake Pukaki seismic experiment, *New Zeal. J. Geol. Geophys.*, *41*, 39–49.

Klima, K., G. Riedmuller, and K. Stattegger (1988), Statistical Analysis of Clay Mineral Assemblages in Fault Gouges, Clay., *Clay Miner.*, *36*, 277–283.

Langer, L., A. S. T. Ragon, and J. Tromp (2020), Impact of topography on earthquake static slip estimates, *Tectonophysics*, *791*, 228,566.

Langridge, R., J. Campbell, N. Hill, V. Pere, J. Pope, J. Pettinga, E. Estrada, and K. Berryman (2003), Paleoseismology and slip rate of the Conway segment of the Hope fault at Greenburn Stream, South Island, New Zealand, *Ann. Geophys.*, *46*, 1119–1139.

Langridge, R. M., W. F. Ries, N. J. Litchfield, P. Villamor, R. J. V. Dissen, D. J. A. Barrell, M. S. Rattenbury, D. W. Heron, S. Haubrock, D. B. Townsend, J. M. Lee, K. R. Berryman, A. Nicol, S. C. Cox, and M. W. Stirling (2016), The New Zealand Active Faults Database, *New Zeal. J. Geol. Geophys.*, *59*, 86–96.

Langridge, R. M., J. Rowland, P. Villamor, J. Mountjoy, D. B. Townsend, E. Nissen, C. Madugo, W. F. Ries, C. Gasston, A. Canva, A. E. Hatem, and I. Hamling (2018), Coseismic rupture and preliminary slip estimates for the Papatea fault and its role in the 2016 Mw 7.8 Kaikōura, New Zealand, *Bull. Seismol. Soc. Am.*, *108*, 1596–1622.

Leitner, B., D. Eberhart-Phillips, H. Anderson, and J. L. Nabelek (2001), A focused look at the Alpine Fault, New Zealand: Seismicity, focal mechanisms, and stress observations, *J. Geophys. Res.: Solid Earth*, *106*, 2193—-2220.

Litchfield, N. J., R. V. Dissen, R. Sutherland, P. M. Barnes, S. C. Cox, R. Norris, R. J. Beavan, R. Langridge, P. Villamor, K. Berryman, M. Stirling, A. Nicol, S. Nodder, G. Lamarche, D. J. A. Barrell, J. R. Pettinga, T. Little, N. Pondard, J. J. Mountjoy, and K. Clark (2014), A model of active faulting in New Zealand, *New Zeal. J. Geol. Geophys.*, *57*, 32–56.

Litchfield, N. J., P. Villamor, R. J. V. Dissen, A. Nicol, P. M. Barnes, D. J. A. Barrell, J. R. Pettinga, R. M. Langridge, T. A. Little, J. J. Mountjoy, W. F. Ries, J. Rowland, C. Fenton, M. W. Stirling, J. Kearse, J. R. Berryman, U. A. Cochran, K. J. Clark, M. Hemphill-Haley, N. Khajavi, K. E. Jones, G. Archibald, P. Upton, C. Asher, A. Benson, S. C. Cox, C. Gasston, D. Hale, B. Hall, A. E. Hatem, D. W. Heron, J. Howarth, T. J. Kane, G. Lamarche, S. Lawson, B. Lukovic, S. T. McColl, C. Madugo, J. Manousakis, D. Noble, K. Pedley, K. Sauer, T. Stahl, D. T. Strong, D. B. Townsend, V. Toy, J. Williams, S. Woelz, and R. Zinke (2018), Surface rupture of multiple crustal faults in the 2016 Mw 7.8 Kaikōura, New Zealand, earthquake, *Bull. Seismol. Soc. Am.*, *108*, 1496–1520.

Little, T. A., R. V. Dissen, J. Kearse, K. Norton, A. Benson, and N. Wang (2018), Kekerengu fault, New Zealand: timing and size of late Holocene surface ruptures, *Bull. Seismol. Soc. Am.*, *108*, 1556–1572.

Liu, C., A. Linde, and I. Sacks (2009), Slow earthquakes triggered by typhoons, *Nature*, *459*, 833–836.

McClusky, S., R. Reilinger, G. Ogubazghi, A. Amleson, B. Healeb, P. Vernant, J. Sholan, S. Fisseha, L. Asfaw, R. Bendick, and L. Kogan (2010), Kinematics of the southern Red Sea–Afar Triple Junction and implications for plate dynamics, *Geophysical Research Letters*, *37*(5).

McKenzie, D. (1969), The relation between fault plane solutions for earthquakes and the directions of the principal stresses, *Bull. Seismol. Soc. Am.*, *59*, 591–560.

McNamara, D., D. Faulkner, and E. Mccarney (2014), Rock Properties of Greywacke Basement Hosting Geothermal Reservoirs, New Zealand: Preliminary Results., *Proceedings Geothermal Reservoir Engineering Workshop, Stanford, California*, *SGP-TR-202*.

Medina Luna, L. (2015), *Constraints on Crustal Stress from Coseismic Slip Models and Focal Mechanisms*, PhD dissertation, University of Michigan.

Medina Luna, L., and E. A. Hetland (2013), Regional stresses inferred from coseismic slip models of the 2008 Mw 7.9 Wenchuan, China, earthquake, *Tectonophysics*, *584*, 43–53.

Metropolis, N., A. W. Rosenbluth, M. N. Rosenbluth, A. A. H. Teller, and E. Teller (1953), Equations of state calculations by fast computing machines, *J. Chem. Phys.*, *21*, 1087–1092.

Michael, A. (1984), Determination of stress from slip data: Faults and folds, *J. Geophys. Res.*, *89*, 11,517–11,526.

Michailos, K., E. Warren-Smith, M. K. Savage, and J. Townend (2020), Detailed spatiotemporal analysis of the tectonic stress regime near the central Alpine Fault, New Zealand, *Tectonophysics*, *775*, 228,205.

Mosegaard, K., and A. Tarantola (1995), Monte Carlo sampling of solutions to inverse problems, *J. Geophys. Res.*, *100*, 12,431–12,447.

Muluneh, A. A., T. Kidane, G. Corti, and D. Keir (2018), Constraints on fault and crustal strength of the Main Ethiopian Rift from formal inversion of earthquake focal mechanism data, *Tectonophysics*, *731-–732*, 172–180.

Nicol, A., N. Khajavi, J. Pettinga, C. Fenton, T. Stahl, S. Bannister, K. Pedley, N. Hyland-Brook, T. Bushell, I. Hamling, J. Ristau, D. Noble, Duncan, and S. McColl (2018), Preliminary geometry, displacement, and kinematics of fault ruptures in the epicentral region of the 2016 Mw 7.8 Kaikoura, New Zealand, earthquake, *Bull. Seismol. Soc. Am.*, *108*, 1521–1539.

Okada, Y. (1985), Surface deformation due to shear and tensile faults in a half-space, *Bull. Seismol. Soc. Am.*, *75*, 1135–1154.

Otsubo, M., A. Yamaji, and A. Kubo (2008), Determination of stresses from heterogeneous focal mechanism data: An adaptation of the multiple inverse method, *Tectonophysics*, *457*(3), 150–160.

Quigley, M., R. V. Dissen, P. Villamor, N. Litchfield, D. Barrell, K. Furlong, T. Stahl, B. Duffy, E. Bilderback, D. Noble, D. Townsend, J. Begg, R. Jongens, W. Ries, J. Claridge, W. Klahn, H. Mackenzie, A. Smith, S. Hornblow, and K. Pedley (2010), Surface rupture of the Greendale Fault during the Darfield (Canterbury) earthquake, New Zealand, *Bull. New Zeal. Soc. Earthquake Eng.*, *43*, 236–242.

Quigley, M. C., M. W. Hughes, B. A. Bradley, S. van Ballegooy, C. Reid, J. Morgenroth, T. Horton, B. Duffy, and J. R. Pettinga (2016), The 2010–2011 Canterbury earthquake sequence: Environmental effects, seismic triggering thresholds and geologic legacy, *Tectonophysics*, *672*, 228–274.

Radwan, A. E., W. K. Abdelghany, and M. A. Elkhawaga (2021), Present-day in-situ stresses in Southern Gulf of Suez, Egypt: Insights for stress rotation in an extensional rift basin, *Journal of Structural Geology*, *147*, 10,434.

Ragon, T., A. Sladen, and M. Simons (2018), Accounting for uncertain fault geometry in earthquake source inversions – I: theory and simplified application, *Geophys. J. Int.*, *214*, 1174–1190.

Ragon, T., A. Sladen, and M. Simons (2019), Accounting for uncertain fault geometry in earthquake source inversions – II: application to the Mw 6.2 Amatrice earthquake, central Italy, *Geophys. J. Int.*, *218*, 689–707.

Reyners, M. (1998), Plate coupling and the hazard of large subduction thrust earthquakes at the Hikurangi subduction zone, New Zealand, *New Zeal. J. Geol. Geophys.*, *41*, 343–354.

Ruch, J., D. Keir, L. Passarelli, D. D. Giacomo, G. Ogubazghi, and S. Jónsson (2021), Revealing 60 years of Earthquake Swarms in the Southern Red Sea, Afar and the Gulf of Aden, *Frontiers in Earth Science*, *9*.

Sibson, R. H., F. C. Ghisetti, and R. A. Crookbain (2012), ‘Andersonian’ wrench faulting in a regional stress field during the 2010–2011 Canterbury, New Zealand, earthquake sequence, *Geol. Soc. Spec. Publ.*, *367*, 7–18.

Spasojević, S., and R. W. Clayton (2008), Crustal structure and apparent tectonic underplating from receiver function analysis in South Island, New Zealand, *J. Geophys. Res.*, *113*.

Steer, P., L. Jeandet, N. Cubas, O. Marc, P. Meunier, M. Simoes, R. Cattin, J. B. H. Shyu, M. Mouyen, W.-T. Liang, T. Theunissen, S.-H. Chiang, and N. Hovius (2020), Earthquake statistics changed by typhoon-driven erosion, *Sci Rep*, *10*.

Stirling, M. W., G. McVerry, M. Gerstenberger, N. Litchfield, R. V. Dissen, K. Berryman, P. Barnes, L. Wallace, B. Bradley, P. Villamor, R. Langridge, G. Lamarche, S. Nodder, M. Reyners, B. Bradley, D. A. Rhoades, W. Smith, A. Nicol, J. Pettinga, K. Clark, and K. Jacobs (2012), National seismic hazard model for New Zealand: 2010 update, *Bull. Seismol. Soc. Am.*, *102*, 1514–1542.

Styron, R. H., and E. A. Hetland (2015), The weight of the mountains: Constraints on tectonic stress, friction, and fluid pressure in the 2008 Wenchuan earthquake from estimates of topographic loading, *J. Geophys. Res. Solid Earth*, *120*, 2697–2716.

Sue, C., B. L. Gall, and A. M. Daoud (2014), Stress field during early magmatism in the Ali Sabieh Dome, Djibouti, SE Afar rift, *Journal of African Earth Sciences*, *97*, 56–66.

Tan, Y., H. Zhang, J. Li, C. Yin, and F. Wu (2018), Focal mechanism determination for induced seismicity using the neighbourhood algorithm, *Geophysical Journal International*, *214*(3), 1715–1731.

Tarantola, A. (2005), *Inverse problem theory and methods for model parameter estimation*, Society for Industrial and Applied Mathematics.

Townend, J., S. Sherburn, R. Arnold, C. Boese, and L. Woods (2012), Three-dimensional variations in present-day tectonic stress along the Australia–Pacific plate boundary in New Zealand, *Earth Planet. Sci. Lett.*, *353–354*, 47–59.

Van Dissen, R., and R. S. Yeats (1991), Hope Fault, Jordan thrust, and uplift of the Seaward Kaikoura Range, New Zealand, *Geology*, *19*, 393–396.

Walbert, O. L., and E. A. Hetland (2022), Bayesian inference of seismogenic stress for the 2016 Mw7.8 Kaikōura, New Zealand, earthquake, *Bull. Seismol. Soc. Am.*, *112(4)*, 1894–1907.

Wallace, L. M., P. Barnes, J. Beavan, R. V. Dissen, N. Litchfield, J. Mountjoy, R. Langridge, G. Lamarche, and N. Pondard (2012), The kinematics of a transition from subduction to strike-slip: An example from the central New Zealand plate boundary, *J. Geophys. Res.*, *117*.

Wallace, R. E. (1951), Geometry of shearing stress and relation to faulting, *J. Geol.*, *59*, 118–130.

Wang, T., S. Wei, X. Shi, Q. Qiu, L. Li, D. Peng, R. J. Weldon, and S. Barbot (2018), The 2016 Kaikōura earthquake: Simultaneous rupture of the subduction interface and overlying faults, *Earth Planet. Sci. Lett.*, *482*, 44–51.

Ward, J. H. J. (1963), Hierarchical Grouping to Optimize an Objective Function, *Journal of the American Statistical Association*, *58*, 236–244.

Wessel, P., J. F. Luis, L. Uieda, R. Scharroo, F. Wobbe, W. H. F. Smith, and D. Tian (2019), The Generic Mapping Tools version 6, *G-cubed*, *20*, 5556–5564.

Williams, J. N., D. J. A. Barrell, M. W. Stirling, K. M. Sauer, G. C. Duke, and K. X. Hao (2018), Surface rupture of the Hundalee fault during the 2016 Mw7.8 Kaikōura earthquake, *Bull. Seismol. Soc. Am.*, *108*, 1540–1555.

Xu, W., G. Feng, L. Meng, A. Zhang, J. P. Ampuero, R. Bürgmann, and L. Fang (2018), Transpressional rupture cascade of the 2016 Mw 7.8 Kaikoura earthquake, New Zealand, *J. Geophys. Res. Solid Earth*, *123*, 2396–2409.

Zhai, Q., Z. Peng, L. Y. Chuang, Y.-M. Wu, H. Y.-J., and S. Wdowinski (2021), Investigating the impacts of a wet typhoon on microseismicity: A case study of the 2009 typhoon Morakot in Taiwan based on a template matching catalog, *J. Geophys. Res.: Solid Earth*, *126*.

Zhang, G., E. Hetland, X. Shan, M. Vallée, Y. Liu, Y. Zhang, and C. Qu (2016), Triggered slip on a back reverse fault in the Mw6.8 2013 Lushan, China earthquake revealed by joint inversion of local strong motion accelerograms and geodetic measurements, *Tectonophysics*, *672-673*, 24–33.

Zoback, M. D., M. L. Zoback, V. S. Mount, J. Suppe, J. P. Eaton, J. H. Healy, D. Oppenheimer, P. Reasenberg, L. Jones, C. B. Raleigh, I. G. Wong, O. Scotti, and C. Wentworth (1987), New Evidence on the State of Stress of the San Andreas Fault System, *Science*, *238*, 1105–1111.